GEOCHEMISTRY OF PERIDOTITES AND ASSOCIATED MAFIC ROCKS, RONDA ULTRAMAFIC COMPLEX, SPAIN

by

CHI-YEUNG JOHN SUEN

B.Sc. McGill University, 1972

SUBMITTED IN PARTIAL FULFILLMENT
OF THE REQUIREMENTS FOR THE
DEGREE OF

DOCTOR OF SCIENCE

at the

MASSACHUSETTS INSTITUTE OF TECHNOLOGY

February, 1978

Signature of Author . . . . . .
Department of Earth and Planetary Sciences
January, 1978

Certified by . . . . .
Thesis Supervisor

Accepted by . . . . . .
Chairman, Departmental Committee on
Graduate Students

GEOCHEMISTRY OF PERIDOTITES AND ASSOCIATED MAFIC ROCKS, RONDA ULTRAMAFIC COMPLEX, SPAIN

by

CHI-YEUNG JOHN SUEN

Submitted to the Department of Earth and Planetary Sciences on January 13, 1978 in partial fulfillment of the requirements for the Degree of Doctor of Science.

ABSTRACT

Ronda peridotites and mafic layers have undergone subsolidus recrystallization, but their bulk-rock compositions can be explained by igneous processes. Relative to a chondritic average, REE distributions in all the peridotites are depleted in light REE. Furthermore, their major element compositions are remarkably colinear in variation diagrams of CaO-MgO-Al_2O_3-SiO_2. These geochemical data indicate that the peridotites are residues produced by small degrees (< 15%) of partial melting of garnet lherzolite at 30-35 Kb and approximately 1600°C. Trace element models suggest that the melt was extracted in small increments (~ 1%) and that trapped melts comprised less than 1% of the residual mass. These models also demonstrate that the primary source mantle had REE abundances approximately equal to twice those in chondrites and a major element composition close to that of Pyrolite III. The magmatic mafic layers do not represent primary melts, but they are probably high pressure cumulates (Cpx+Opx+Sp and Cpx+Gn). It is envisioned that the melting was due to adiabatic decompression in a rising mantle diapir. The melts migrated through conduits and formed incrustations along the cooler walls as represented by the mafic layers observed in the field. The fractionated liquids, relatively enriched in incompatible elements, escaped from the ultramafic body.

Thesis Supervisor: Dr. Frederick A. Frey
Title: Associate Professor of Geochemistry

TABLE OF CONTENTS

LIST OF FIGURES

LIST OF TABLES

LIST OF ABBREVIATIONS

Amph	amphibole
An	anorthite
CaTs	Ca-tschermak molecule
Cpx	clinopyroxene
Di	diopside
En	enstatite
Fa	fayalite
Fo	forsterite
Fs	ferrosilite
Gn	garnet
Gr	grossular
Ol	olivine
Opx	orthopyroxene
Plag	plagioclase
Py	pyrope
Qz	quartz
Serp	serpentine
Sp	spinel

CHAPTER I

INTRODUCTION

The most reliable sources of information on the composition of the earth's mantle are samples of the mantle itself. Two principal kinds of mantle samples are available for study:

(1) Inclusions of ultramafic rocks brought to the surface by alkali olivine basalts, kimberlites, and other deep seated magmas;

(2) Large masses of ultramafic rocks known as "alpine-type" peridotites (Benson, 1926) which have been tectonically emplaced along Phanerozoic orogenic belts.

Some alpine peridotites are associated with gabbros, sheeted diabase dikes, pillowed basalts, and deep-sea sediments. These igneous rock associations are termed "ophiolites." With the development of plate tectonic theory, ophiolites, which typically (though not always) lack thermal aureoles (e.g., Troodos [Moores and Vines, 1971] and Vourines [Moore, 1970]), are belived to be overthrust segments of oceanic lithosphere, emplaced in the continental margins as a result of crustal obduction (Dewey and Bird, 1970; Coleman, 1971). Another group of alpine bodies are those without volcanic associations. Commonly, these peridotites have high-temperature

metamorphic aureoles (e.g., Lizard [Green, 1964], Beni-Bouchera [Kornprobst, 1969], and Ronda [Loomis, 1972a; Westerhof, 1977]); and these are called "high-temperature peridotite" intrusions (Green, 1967). They are generally thought to originate as hot diapiric masses intruding crustal rocks from the upper mantle. Geochemically, these bodies are usually (though not always) more fertile in magmaphile elements, such as CaO and Al_2O_3, than ophiolitic peridotites. Therefore, their compositions are appropriate for generating basaltic magmas upon melting (Green, 1967). This thesis is a geochemical study of a major high-temperature alpine-type peridotite body: the Ronda ultramafic complex.

I-1: THE RONDA ULTRAMAFIC BODY

The Ronda ultramafic complex is a high-temperature alpine-type peridotite body emplaced in the internal zone of the Betic Cordillera, southern Spain. It is located about 50 km northeast of Gibraltar and is the largest of several major peridotite bodies in the western Mediterranean. Outcropping over an area of about 10 by 30 km, Ronda is the world's largest high-temperature peridotite body. (See Figure I-1.) Its contact metamorphic aureole gives an intrusion temperature of 800°C $\pm$100°C and a final equilibration pressure of 4.3 $\pm$1 kb (Loomis, 1972a).

Its age of emplacement, based on stratigraphic relations, is post-Triassic to pre-Miocene (Dürr, 1967).

90-95% of the Ronda body is composed of peridotites (including serpentinites), and 5-10% are mafic rocks ranging from garnet pyroxenite to olivine gabbro in mineralogy. These mafic rocks occur as "layers" within the peridotites and were interpreted as partial fusion products by Dickey (1970). The body was mapped as 4 metamorphic facies by Obata (1977). From northwest to southeast, they are: garnet lherzolite facies, ariegite subfacies and seiland subfacies of spinel lherzolite facies, and plagioclase lherzolite facies (Figure II-1). Using geothermometry and geobarometry techniques, the earliest (highest in P and T) traceable equilibrium condition is found to be 1100-1200°C and 20-25 kb in the upper mantle (Obata, 1977). The whole body has since undergone subsolidus recrystallization due to decompression and cooling.

I-2: PREVIOUS WORKS

The Ronda body was first subjected to a thorough geological and petrographic investigation by Orueta (1917). In 1970, it was studied again by Dickey (1970) in the context of modern petrologic theories. Later

FIGURE I-1: Locations of the Ronda peridotite body and other major peridotite bodies in the Betic-Rif orocline (taken from Dickey and Obata, 1977). Bouguer gravity anomalies (in mgal.), shown as dashed lines, are from Bonini et al. (1973).

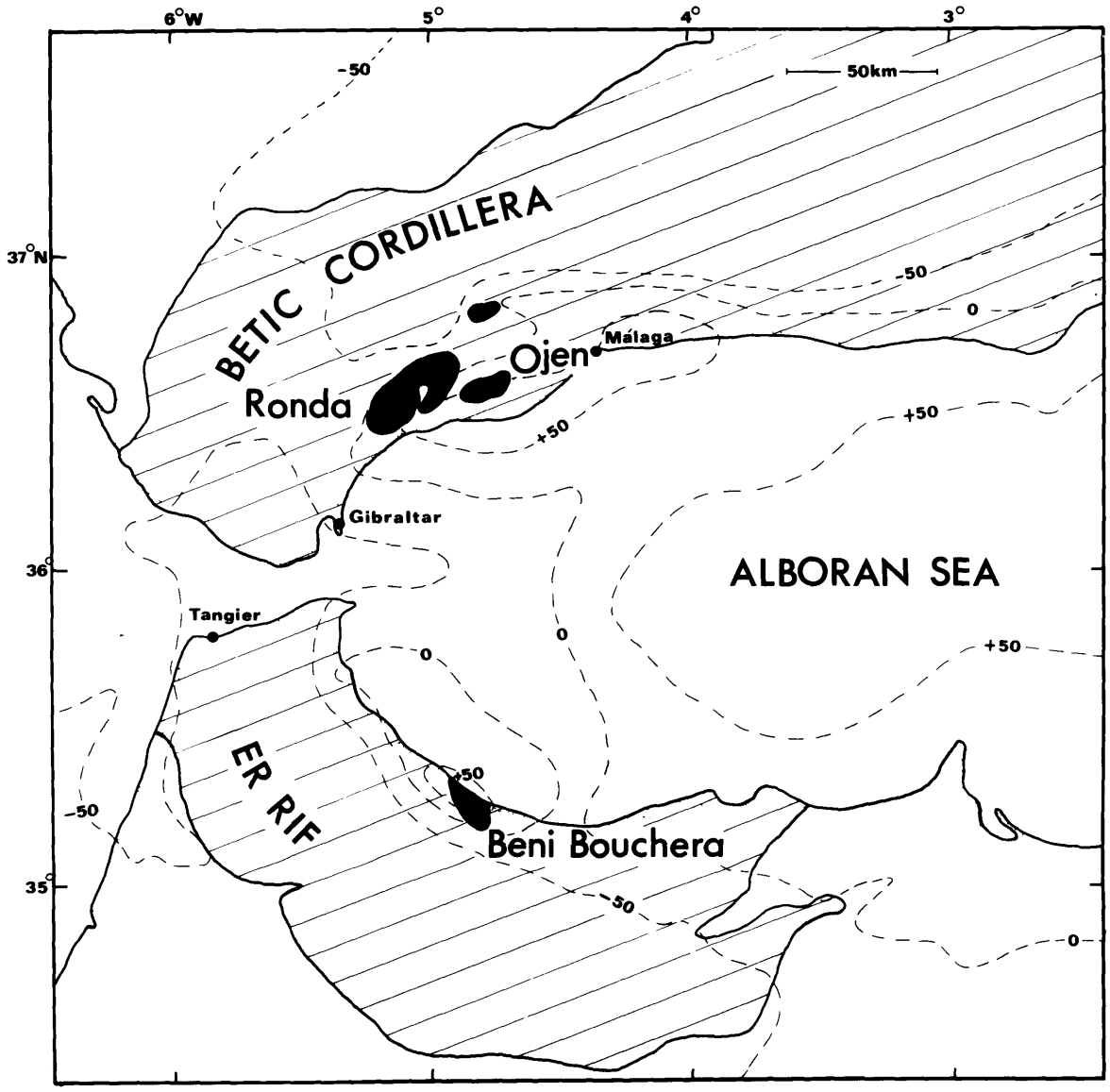
6°W
5°
4°
3°
37°N
36°
35°
50km
-50
0
+50
BETIC CORDILLERA
Ronda
Ojen
Málaga
Gibraltar
ALBORAN SEA
Tangier
ER RIF
Beni Bouchera

Loomis (1972a, b) studied the high-temperature contact aureole and proposed a diapiric mode of emplacement. Darot (1974) and Lundeen (1976) carried out structural and petrofabric analyses of the peridotite body as a nappe rather than a rooted diapir. Obata (1977) studied a large collection of samples in detail using electron microprobe analysis and he applied geothermometry and geobarometry techniques to investigate equilibration pressures and temperatures. Obata also performed high-pressure melting experiments on a mafic rock sample, and mapped the body into different metamorphic facies. Obata's geothermometry and geobarometry was followed by that of Schubert (1977) who obtained similar results. Westerhof (1977) again proposed an emplacement history based on the contact relations.

I-3: OBJECTIVES AND SCOPE FOR THIS WORK

In view of modern petrogenic theories, Dickey's (1970) proposal that the so-called "magmatic" mafic layers in Ronda and other alpine peridotite bodies are products of partial fusion of the mantle peridotites has great significance, because it implies that such occurrences of mafic rocks are examples of in-situ basalt genesis. Dickey's hypothesis was not supported by sufficient whole rock chemical data. This thesis contains the data needed to test the partial fusion hypothesis. The present

study utilizes bulk-rock major and trace element (including REE) abundances and the petrologic results of Obata (1977) to obtain information on:

(1) the origin of the peridotites;

(2) the nature of mantle processes;

(3) the chemical composition of the upper mantle; and

(4) the origin of the mafic layers.

This thesis contains 6 chapters. Chapter II discusses the origin of the peridotites based on bulk chemical compositions. More sophisticated models for trace element fractionation during partial melting are formulated in Chapter III, and are applied to the Ronda peridotite data. Chapter IV estimates the composition of the primary mantle source of the Ronda body and the hypothetical composition of the primary melt produced by melting this source at high pressures. The petrogenesis of the mafic layers is examined in Chapter V where several petrogenetic models are evaluated. The major conclusions of this work are summarized in Chapter VI.

CHAPTER II

GEOCHEMISTRY AND PETROLOGY OF THE RONDA PERIDOTITES

II-1 THE RONDA PERIDOTITES

The peridotites from the Ronda massif have undergone extensive retrograde metamorphism as they came to the surface from upper mantle conditions. These peridotites, therefore, have recrystallized in subsolidus conditions according to the P-T trajectories they followed (Obata, 1977). In this geochemical study, the approach taken is to assume that the metamorphism is isochemical, at least in hand-specimen scale, unless indicated otherwise by field or petrographic observations, or anomalous bulk compositions and mineral assemblages. In a few cases (e.g., R705A and B, plag-gn clinopyroxenite; R896, chromian pyroxenite layer) samples collected from locations close to contacts between peridotites and mafic layers have distinctive bulk chemistry, mineralogy and appearance indicating the possibility of metasomatic processes on a local scale (a few mm. to a few decimeters). However, in general these peridotites are rather homogeneous compositionally, and are close to estimates of primary mantle composition (see Table II-2, Figures II-10a, b, c, d and Figure II-11). There is no evidence that metasomatic or metamorphic reactions have caused changes in bulk composition on a gross scale. Therefore, except for the few samples mentioned above, I assume that the peridotite bulk compositions were determined by igneous processes.

Eight peridotite samples were selected for bulk chemical analyses on the basis of the following criteria:

(1) The least serpentinized specimens (see Appendix II-A).

(2) The freshest-looking rocks without apparent deuteric alteration or surface weathering. Weathered surfaces were sawed off before crushing, and each crushed piece was hand-picked to avoid any veinlets, like calcite and other low-temperature features that might affect the bulk chemistry of the sample.

(3) Specimens from locations free from possible contact metasomatism.

In addition to these criteria, samples were selected to cover a wide range in geographic distribution; hence, also the complete range of metamorphic facies. Sample locations are shown on the location map (Figure II-1). In increasing order of metamorphic grade, they are:

- R131, R224, R893 from plagioclase lherzolite facies;
- R845 from seiland sub-facies of spinel lherzolite facies;
- R243, R855, R717 from ariegite sub-facies of spinel lherzolite facies (R717 lies in the transitional zone between seiland and ariegite sub-facies);
- R501 from garnet lherzolite facies.

Facies names are defined according to O'Hara (1967), and isograds were mapped by Obata (1977). The isograds shown in Figure II-1 differ slightly from Obata (1977) because they are updated with new data obtained in the 1977 field season.

Figure II-1: Sample location map. Open circles are peridotites; solid circles are mafic layers; squares are "tectonic" layers (Dickey, 1970) or chromian pyroxenite layers (Obata, 1977).

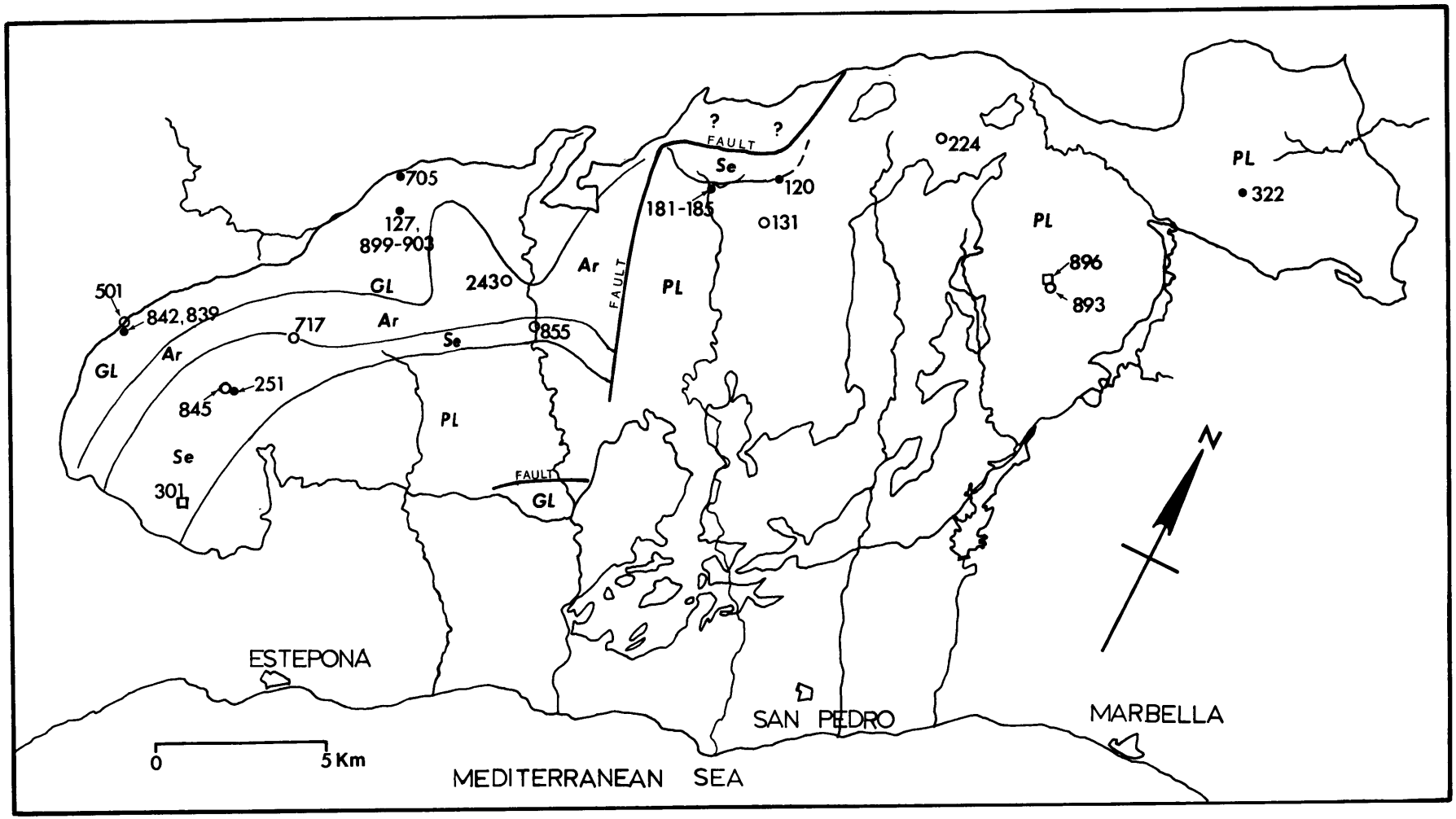
705
127,
899-903
501
842,839
717
Ar
GL
2430
Ar
FAULT
PL
Se
855
181-185
120
131
224
PL
322
PL
896
893
Ar
GL
Se
845
251
301
PL
FAULT
GL
N
ESTEPONA
SAN PEDRO
MARBELLA
0
5 Km
MEDITERRANEAN SEA

Brief petrographic data of the peridotites are given in Appendix II-A. More detailed descriptions of some samples can be found in Dickey (1969), Lundeen (1976) and Obata (1977).

Modal composition of the peridotites were obtained by point-counting thin-sections for at least 1000 counts (Obata, 1977, with some checks by the author). Modally, all samples are lherzolites according to the nomenclature recommended by IUGS Subcommission on the Systematics of Igneous Rocks (1973), with the exceptions of Sample R845 which is classified modally as a harzburgite* and Sample R893 which is a dunite. One other sample, R855, which is included with the peridotites, lies close to the boundary between a peridotite and an olivine websterite. This sample is anomalous in modal mineralogy, texture and bulk chemistry, and it will be discussed separately later in the text. The lherzolites are representative of more than 95% of the peridotites in the Ronda massif. Dunite and olivine websterite samples are extremely rare, and only occur locally.

---

* Some petrologists (e.g., Boyd, 1973; O'Hara et al., 1975) apply the name "lherzolite" to peridotites with the presence of any small amount of clinopyroxene. In such case, all samples can be called lherzolites except R893 which has 90% of reconstituted olivine (see Appendix II-B). R845 is included as "the lherzolites" in general in subsequent discussions.

The modes of these peridotite samples are reconstituted into three primary phases: clinopyroxene, olivine and orthopyroxene, according to the method given in Appendix II-B. This method is used in order to estimate the primary garnet-free mineralogy and to eliminate secondary phases, such as serpentine and amphibole. The procedure is partly based on microprobe data of mineral compositions (Obata, 1977). Reconstituted modes are given in Table II-1, and plotted in Figure II-2.

II-2 GEOCHEMICAL METHODS

Sample Preparation

Field samples (10 x 10 x 10 cm. to 30 x 20 x 20 cm.) were cut with a diamond saw into slabs 1 - 2 cm. thick with a surface area of approximately 20 - 40 $cm.^2$. The samples were examined for inhomogeneity and to ensure that the slabs taken were representative of the whole-rock specimens. Care was also taken to avoid weathered surfaces and late-stage veins; e.g., calcite veinlets. Saw marks on the slab surfaces were cleaned by polishing with carborundum on rotating wheels. The slabs were then wrapped in a clean laboratory cotton towel and crushed into pebble-size with a hammer. Crushed samples were put into a beaker of distilled water and cleaned by an ultra-sonic cleaner for more than 15 minutes. Then these pebbles were dried under an infra-red lamp and hand-picked to avoid calcite veinlets, etc. The hand-picked pebbles were further crushed into pea-size and smaller grains

Table II-1: Modal analyses of the Ronda peridotites

percent	Ol	Serp	Opx	Cpx	Sp	Gn	Plag	Amph	Opaque	Ol*	Opx*	Cpx*	Σpx*
1. R845	70	7	20.2	2.4	0.4	-	-	tr	tr	77.4	20.2	2.7	22.9
2. R131	70	3	17	7	0.2	-	3	tr	tr	70	19	11	30
3. R224										66	21	12.4	33.4
4. R501	40	31	17	2	1	7	-	1	1.7	72.7	22.6	4.3	26.9
5. R243	60	-	23	15	3	-	tr	tr	tr	62	23	15	38
6. R717	46	14	27	12	1.8	-	-	tr	tr	61	27	12	39
7. R893	66	23	8	2	0.7	-	-	-	tr	89.7	8	2	10
8. R855										40	35	25	60

Ol*, Opx* and Cpx* are reconstituted nodules according to the method given in Appendix II-B, except for R224 and R855, the numbers are weight norms obtained by the method given in Appendix II-H, because no reliable modes can be obtained.

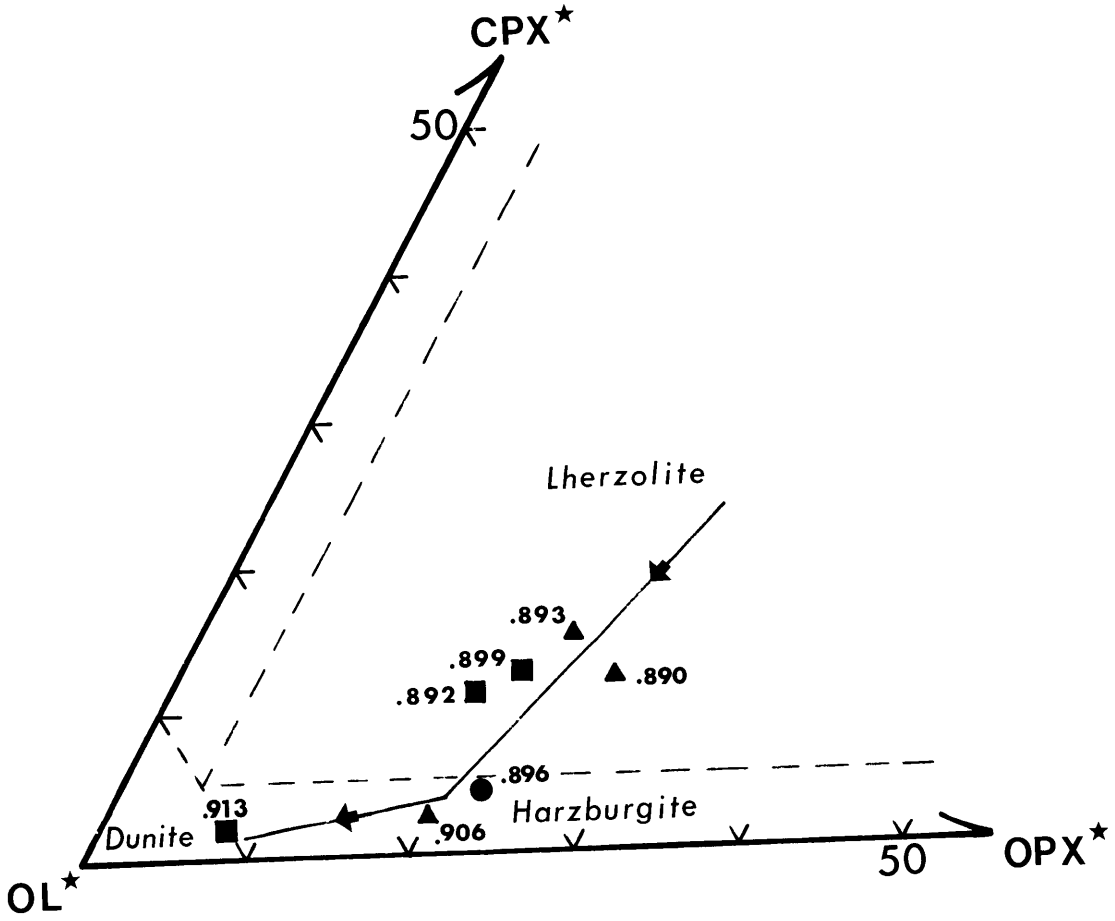

Figure II-2: Reconstituted modal compositions of the Ronda peridotites. Samples from garnet, spinel, and plagioclase lherzolite facies are indicated by circles, triangles, and squares, respectively. The numbers adjacent to each point are Mg/Mg + ΣFe ratios. The indicated trend is a possible residual trend produced by partial melting with increasing degrees of melting from lherzolite to harzburgite to dunite.

in a steel percussion motor. All crushed products were ground down to ∿400 mesh powder by using a tungsten carbide ball-mill, approximately 2.5 cm. in diameter (internal) and 5.5 cm. long with three balls of ∿1.5 cm. in diameter. Run time was about 15 - 20 minutes. These procedures avoided contamination of iron and other transition metals induced by abrasion process between the surfaces of rock fragments and steel tools. The impact action of the percussion motor is believed to introduce negligible contamination because the impact surface relative to the sample volume is small, and in most cases, the sample was crushed in one or two blows. The contamination induced by using a tungsten carbide ball-mill was investigated by Thompson and Bankston (1970) who found no significant contamination except for W and Co. Tungsten addition was obvious because unusually strong W^{187} photopeaks were observed during the neutron-activation analysis. Therefore, as a result of possible accompanying Co addition, the concentrations of Co presented in this work are not useful.

Analytical Techniques

Because the mineral assemblages and mineral compositions of these rocks reflect subsolidus recrystallization conditions (Obata, 1977), mineral composition will not be extensively discussed. Data on bulk rock chemical compositions can be divided into three groups; namely, major elements, rare-earth elements (REE) and other trace elements.

(1) Major element data obtained by x-ray fluorescence spectrometry (fused pellets): Si, Ti, Al, Fe, Mn, Mg, Ca, Na, K, P and S.

(2) Rare-earth element data obtained by radiochemical neutron activation analysis (techniques, discussed later, developed in the course of this work): La, Ce, Nd, Sm, Eu, Gd, Tb, Yb, Lu.

(3) Other trace element data obtained by x-ray fluorescense spectrometry (pressed powder technique): Sc, V, Cr, Co, Ni, Cu, Zn, Ga, Rb, Sr, Y, Zr, Nb and Pb.

In addition, Fe^{2+}/Fe^{3+} ratios were determined by a standard gravimetric method, and CO_2 and H_2O+ by gas chromatography.

(a) X-ray Fluorescence Analysis:

All XRF analyses were done by Dr. B. W. Chappell of the Australian National University. Details of the method employed are described by Norrish and Chappell (1967) and Norrish and Hutton (1969). Major element data on some of the samples in this work have also been obtained by Dickey (1970) using standard wet chemical method from another laboratory. There is no major discrepancy between the two sets of data, with the exception of Fe^{2+}/Fe^{3+} ratios. However, the total Fe content as FeO remains unchanged. Appendix II-C compares these two sets of numbers.

(b) Neutron Activation Analysis:

Both instrumental and radiochemical methods were used for rare-earth element analysis. Instrumental methods were des-

cribed by Gordon et al. (1968), and were used only for some of the mafic rocks discussed in Chapter V. Because in peridotites the REE abundances are one order of magnitude lower than the mafic rocks, radiochemical methods were employed. In most cases, instrumental analyses were carried out to check the La, Sm and/or Nd data.

The radiochemical technique used was developed as part of this research. Approximately 0.5 gm. of rock powder was irradiated in the Massachusetts Institute of Technology Research Reactor II, at a thermal neutron flux of $\sim 6 \times 10^{12}$ n/sec/cm^2. Samples and a standard solution were contained in small quartz vials. Irradiation time is $\sim$100 hours. They were allowed to cool for 3 days, and the activated rock powders were transferred to teflon beakers for dissolution with HF acid. All of the standard solution was transferred directly to a counting tube. Ce^{144} was added to both the samples and the standard as a yield monitor for ion-exchange column chromatography. REE were separated from major elements by using a cation-exchange column similar to that used by Zielinski (1975). Gamma-ray spectra, obtained from a Ge(Li) detector with a resolution of 2·4 KeV FWHM at 1332·5 KeV, and a Canberra Low Energy Photon Scintillation (LEPS) detector for low energy photopeaks, were collected with a 4096-channel analyzer with the output on printed tapes. Peaks were integrated manually using pocket calculators. Integration methods and statistical error estimations are given in Appendix II-D. Appendix II-E is a table of the energies of the photopeaks

used. Detailed radiochemical procedures are given in Appendix II-F together with the counting schedules and duplicate analyses for precision estimate.

II-3 RESULTS

The results of bulk chemical analyses of eight peridotite samples are presented in Tables II-2 and II-3. Calculated Mg/Mg + ΣFe molecular ratios, CaO/Al_2O_3, Al_2O_3/SiO_2 weight ratios are also included. Table II-2 also gives the major element numbers recalculated on volatile-free basis. The lherzolites are tabulated according to the order of increasing concentrations of Al_2O_3 (Columns 1 through 6). The dunite (R893) and the olivine websterite (R855) are compositionally distinct, and are tabulated separately in Columns 7 and 8.

Among the lherzolites (No. 1 through No. 6), strong geochemical trends can be recognized. For example, CaO concentrations vary directly with Al_2O_3, and other major element abundances like MgO and Na_2O vary also roughly in the same order, inversely and directly, respectively. These trends will be discussed later.

Compared to the lherzolites, the dunite (No. 7) is much lower in TiO_2, Al_2O_3, CaO, Na_2O and has higher Mg/Mg + ΣFe, and conversely, the olivine websterite (No. 8) is much higher in these magmaphile* elements with a lower Mg/Mg + ΣFe ratio.

Table II-3 shows the concentrations of REE and other

---

* Refers to major elements which preferentially concentrate in the liquid upon melting of mantle peridotites.

Table II-2(a): Major element compositions of the Ronda peridotites

	(1) R845	(2) R131	(3) R224	(4) R501	(5) R243	(6) R717	(7) R893	(8) R855
SiO_2	42.70	42.45	43.42	40.71	44.13	42.46	38.78	45.52
TiO_2	0.08	0.19	0.06	0.10	0.14	0.16	0.01	0.11
Al_2O_3	2.46	2.52	2.88	3.24	3.56	3.72	0.80	6.30
Fe_2O_3	2.27	3.27	2.51	4.35	2.20	3.73	4.27	1.89
FeO	5.34	5.50	5.74	3.51	6.13	4.46	3.36	5.92
MnO	0.13	0.13	0.13	0.12	0.13	0.13	0.11	0.13
MgO	40.04	39.37	39.70	36.12	38.23	35.71	42.53	31.79
CaO	2.34	2.43	2.65	2.77	3.17	3.37	0.70	5.55
Na_2O	0.19	0.19	0.26	0.25	0.32	0.29	0.03	0.39
K_2O	0.005	<0.003	<0.003	0.01	0.01	0.01	<0.003	0.01
P_2O_5	<0.003	<0.003	<0.003	0.005	0.01	0.01	<0.003	0.01
S	0.02			0.03	0.02	0.03		
H_2O+	2.95	2.94	1.92	6.99	1.14	4.29	7.48	1.52
H_2O-	0.45	0.19	0.14	0.73	0.12	0.64	0.98	0.24
CO_2	0.28	0.22	0.06	0.31	0.25	0.39	0.49	0.21
rest	0.73	0.62	0.66	0.62	0.66	0.64	0.55	0.67
	99.99			99.87	100.22	100.04		
O=S	0.01			0.01	0.01	0.01		
TOTAL	99.98	100.02	100.13	99.86	100.21	100.03	100.09	100.26

Table II-2(b): Adjusted major element compositions on volatile-free basis

	(1) R845	(2) R131	(3) R224	(4) R501	(5) R243	(6) R717	(7) R893	(8) R855	(9) Pyrolite**
SiO_2	44.34	43.92	44.36	44.28	44.81	44.86	42.59	46.43	45.20
TiO_2	0.08	0.20	0.06	0.11	0.14	0.17	0.01	0.11	0.71
Al_2O_3	2.55	2.61	2.94	3.52	3.62	3.93	0.88	6.42	3.54
Cr_2O_3	0.424	0.319	0.350	0.361	0.357	0.368	0.243	0.413	0.43
ΣFeO*	7.66	8.73	8.17	8.07	8.24	8.26	7.91	7.77	8.47
MnO	0.13	0.13	0.13	0.13	0.13	0.14	0.12	0.13	0.14
MgO	41.58	40.73	40.56	39.29	38.82	37.73	46.71	32.43	37.48
CaO	2.43	2.51	2.71	3.01	3.22	3.56	0.77	5.66	3.08
Na_2O	0.20	0.20	0.27	0.27	0.32	0.31	0.03	0.40	0.57
K_2O	0.005	<0.003	<0.003	0.01	0.01	0.01	<0.003	0.01	0.13
P_2O_5	<0.003	<0.003	<0.003	0.005	0.01	0.01	<0.003	0.01	0.06
NiO	0.291	0.284	0.280	0.270	0.261	0.258	0.333	0.213	0.20
CaO/Al_2O_3	0.951	0.964	0.920	0.855	0.890	0.906	0.875	0.881	
Al_2O_3/SiO_2	0.0576	0.0594	0.0663	0.0796	0.0807	0.0876	0.0206	0.138	
$\frac{100Mg}{Mg+\Sigma Fe}$	90.62	89.26	89.84	89.66	89.36	89.06	91.32	88.14	88.74

* Total iron as FeO.

** Pyrolite III (Green and Ringwood, 1967). P_2O_5 abundance from Ringwood (1966).

Table II-3: Rare-earth elements and other trace element abundances in the Ronda peridotites

(ppm)	(1) R845	(2) R131	(3) R224	(4) R501	(5) R243	(6) R717	(7) R893	(8) R855
La	.0890	.0563	.0586	.0808	.188	.198	.009	.0764
Ce	.406	.466	.179	.522	.855*	.833		.494
Nd	.434	.963	.300	.661	.723	.952		.584
Sm	.169	.372	.120	.261	.296	.322	.0115	.249
Eu	.0711	.147	.0595	.116	.118	.135	.0050	.112
Gd		.470			.404*			
Tb	.0514	.0847	.0545	.0844	.0798	.0917		.0834
Yb	.226	.266	.257	.382	.403	.400	.0403	.493
Lu	.0348	.0397	.0398	.0587	.0640	.0611	.0077	.0791

*Values uncertain due to peak interference or poor counting statistics.

Table II-3 (continued): Rare-earth elements and other trace element abundances in the Ronda peridotites

(ppm)	(1) R845	(2) R131	(3) R224	(4) R501	(5) R243	(6) R717	(7) R893	(8) R855
Sc	13	12	13	14	14	16	7	24
V	56	55	54	59	67	73	22	89
Cr	2790	2110	2350	2270	2410	2380	1510	2770
Co	143	136	135	142	139	132	152	155
Ni	2200	2150	2150	1950	2020	1920	2380	1640
Cu	22	17	23	27	26	26	6	10
Zn	53	57	53	53	52	54	47	63
Ga	2.0	2.5	2.0	3.0	2.5	3.5	0.5	4.0
Rb	<0.1	0.1	0.1	0.1	0.4	1.0	0.1	0.9
Sr	7.0	4.5	2.0	6.5	13.0	13.0	0.5	12.5
Y	2	3	2	3	3	4	<1	3
Zr	3	5	1	4	7	7	<1	4
Nb	<1	2	2	1	3	<1	<1	1
Pb	4	4	6	3	5	4	3	4

minor elements in ppm. The REE abundances are normalized to chondritic values (Haskin et al., 1968) and plotted in Figure II-3. Relative to chondrites, all the lherzolites, including the olivine websterite, are light rare-earth (LREE) depleted, with REE abundances close to or within the range of other alpine-type peridotites (Frey, 1969; Philpotts et al., 1972; Loubet et al., 1975). The heavy rare-earths (HREE) are relatively unfractionated (except R131) and generally range from 1 to 2 times chondrites. The dunite (R893) is very LREE depleted and has much lower REE abundances than all other samples. Unlike the rare-earth patterns of peridotite inclusions from kimberlites and alkali-basalts, which commonly have LREE enrichments (Nagasawa et al., 1969; Philpotts et al., 1972; Frey and Green, 1974; Shimizu, 1975), all alpine peridotites analyzed (Frey, 1969; Philpotts et al., 1972; Loubet et al., 1975; and this work) have LREE depletion.

II-4 DISCUSSION AND MODELLING

Gast (1968) and Schilling (1971, 1975) contended that the source mantle of oceanic-ridge or abyssal basalts is depleted in incompatible elements relative to chondrites. One manifestation of this depletion is a LREE depletion relative to REE abundances in chondrites. Recent Nd-Sm isotope data also support this contention (Richard et al., 1976; DePaolo and Wasserburg, 1976(a), (b); O'Nions et al., 1977). Therefore, in view of REE data alone, the Ronda peridotite may be a

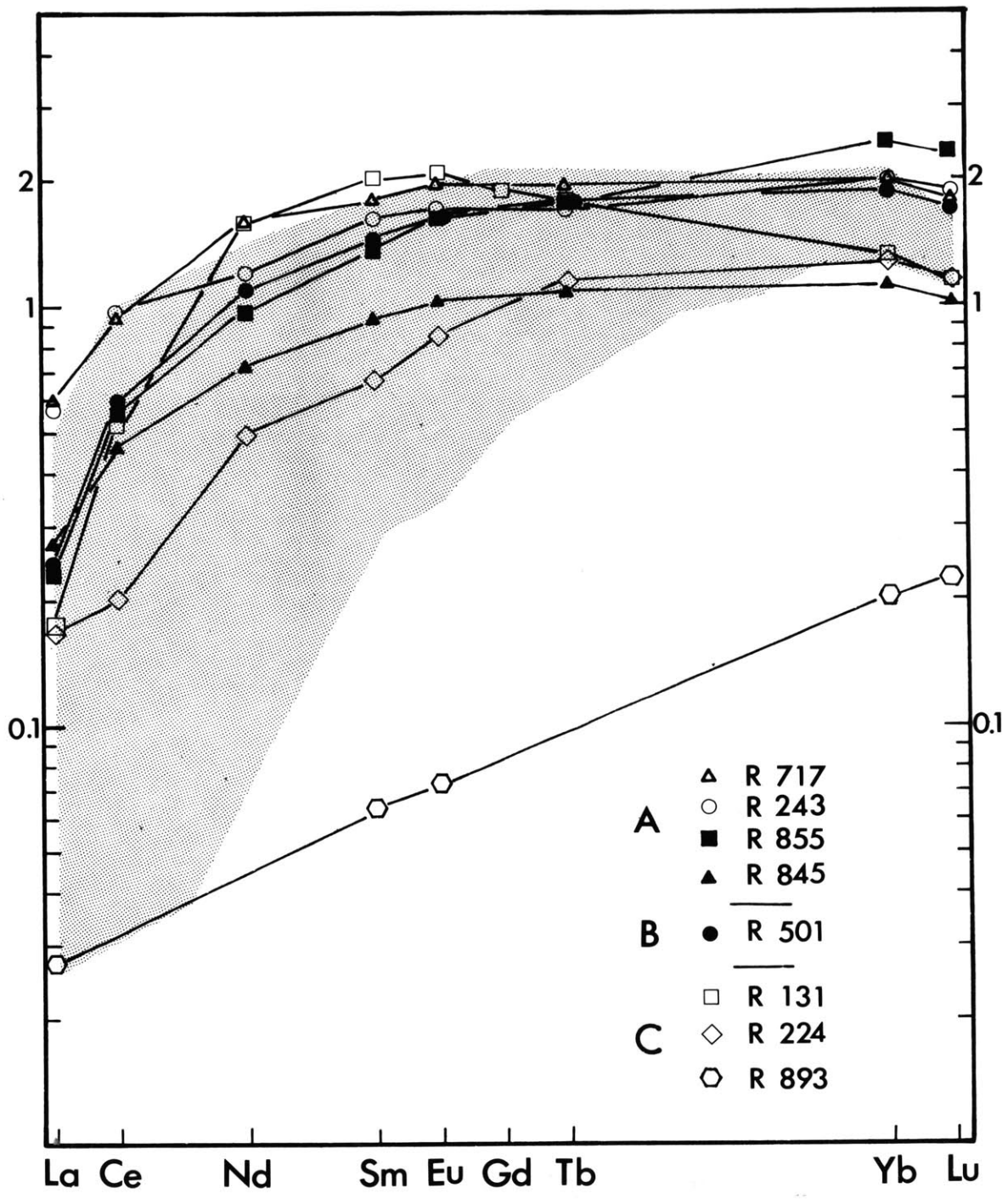

Figure II-3: Chondrite-normalized REE patterns of the Ronda peridotites. Group A samples are from spinel lherzolite facies; B from garnet lherzolite facies; C from plagioclase lherzolite facies. The range of other alpine peridotites analysed (Frey, 1969; Philpotts, et al, 1972; Loubet, et al, 1975) is shown as the shaded area.

section of oceanic upper mantle.

If the most undepleted* lherzolite (No. 6 in Tables II-2 and II-3) is assumed to be a primary mantle rock, the other peridotites (with the exception of olivine websterite No. 8) can be considered as residues remaining after partial melting of this source rock. It can be shown that as melting progresses, the residues would be increasingly depleted, relative to the source rock, in incompatible elements, like LREE, Sr, Zr and K, which preferentially partition into the early melt formed (e.g., Gast, 1968; Schilling, 1975; Menzies, 1976). In addition, CaO and Al_2O_3 would also decrease with increased melting, because clinopyroxene and garnet, if present, are found to be the earliest melting minerals (Ito and Kennedy, 1967; Mysen and Kushiro, 1976). Furthermore, the Mg/Mg + ΣFe ratio in the residue would be expected to increase with increasing percent of partial melting.

The Mg/Mg + ΣFe ratios (adjacent to each point in Figure II-2) are rather uniform in the lherzolites (ranging from 0.890 to 0.899) but increase towards dunite to 0.913. Variations of CaO, Sr and Ni with respect to a LREE are shown in Figures II-4(a), (b) and (c), respectively. Figure II-4(a) shows a strong correlation between CaO and La, as expected from the partial melting model. Sr also exhibits significant

---

* The term "undepleted" (or "depleted") is used in general to describe the concentrations of magmaphile and incompatible trace elements (Ringwood, 1966) relative to a hypothetical primary mantle source rock; for example, pyrolite.

positive correlation with La [Figure II-4(b)], while Ni, a compatible element, shows a negative relationship with Nd [Figure II-4(c)]. Several other similar trends occur among major and minor element abundances. All these trends reflect a systematic fractionation process, such as partial melting, fractional crystallization, or possibly mixing.

It is important to note that although general trends can be observed among the major and minor element abundances, variations among abundances of some minor elements do not necessarily show any correlation trends in the order as arranged in Tables II-2 and II-3 based on the major elements; for example, Yb vs. La (see Figure II-7). In general, the minor element trends are more scattered and much less well defined than the major elements. [For major element variation diagrams see Figures II-10(a), (b), (c) and (d).] This can be readily explained by the fact that during fractionation processes minor elements are much more sensitive to controlling factors like distribution coefficients, the nature of the operating process, the degree of completion of the process, as well as the amounts and the proportions of the mineral phases involved than the major elements. For example, in case of eutectic melting of a four-phase peridotite, the liquid generated would be at constant composition in major elements controlled by the phase diagram; and therefore, the concentrations of these elements in the residue are mainly a linear function of the degree of melting. On the other hand, the minor element concentrations in both the

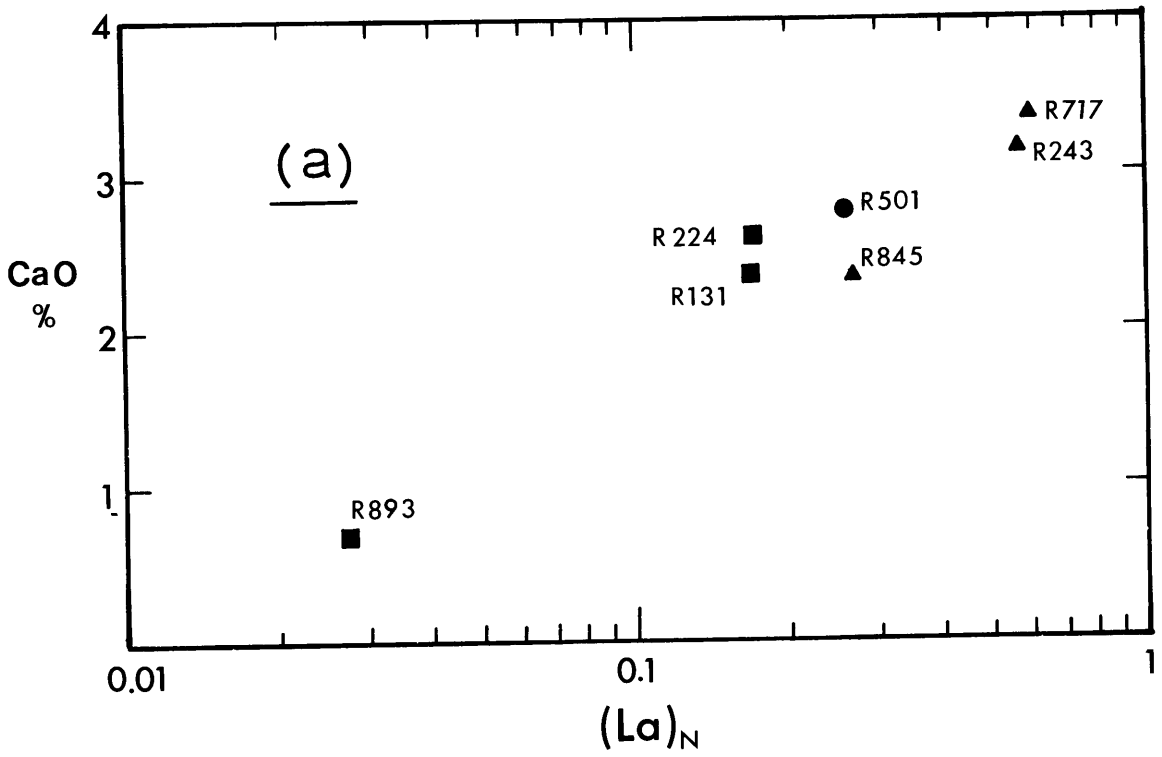

Figure II-4: (a) Semi-log plot of CaO wt.% versus chondrite-normalized La concentration, $(La)_N$. (b) Log-log plot of Sr (ppm) versus $(La)_N$. An apparent straight-line trend with approximately 45° slope would indicate that $D_{Sr} = D_{La}$. (See text) (c) Semi-log plot of Ni (ppm) versus $(Nd)_N$. Note that the maximum variation of Ni content is only 400 ppm.
Symbols are the same as in Figure II-2.

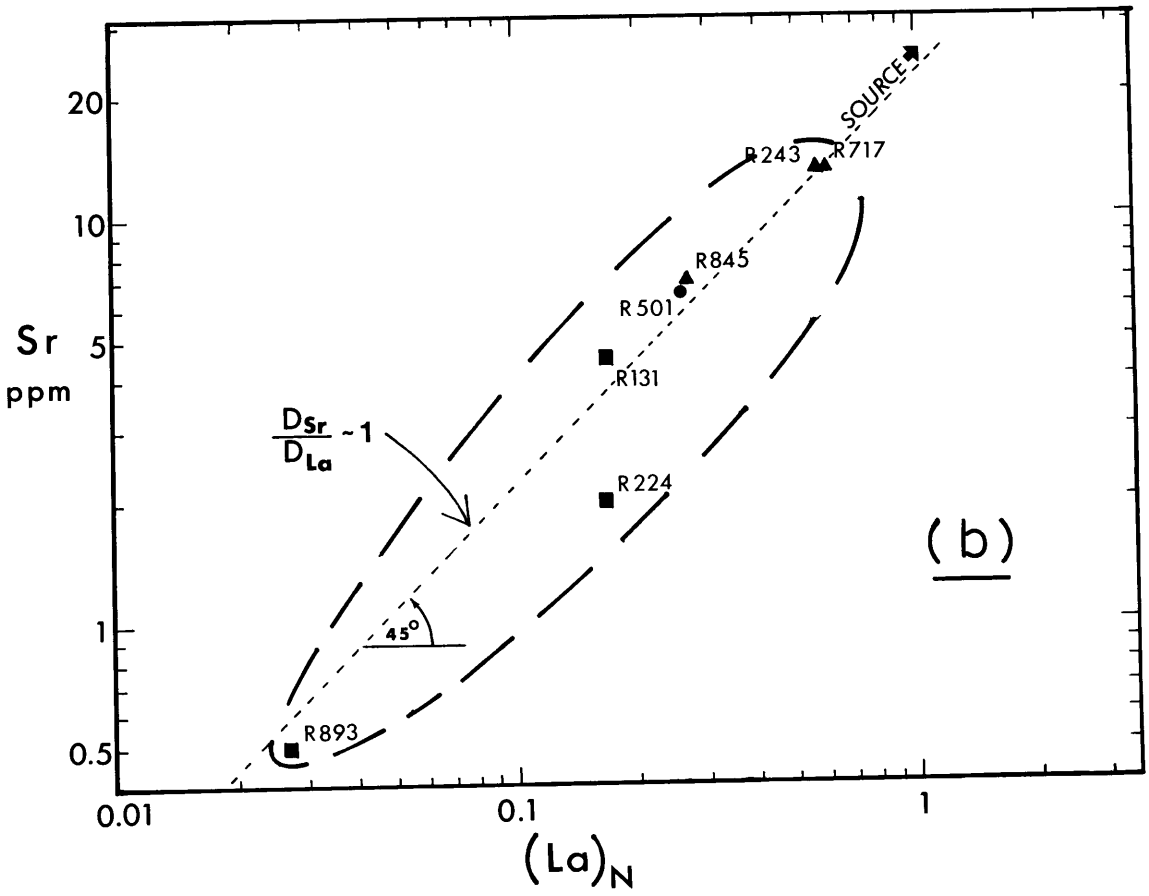
20
10
5
1
0.5
Sr
ppm
SOURCE
R243
R717
R845
R501
R131
R224
R893
$\frac{D_{Sr}}{D_{La}} \sim 1$
45°
(b)
0.01
0.1
1
$(La)_N$

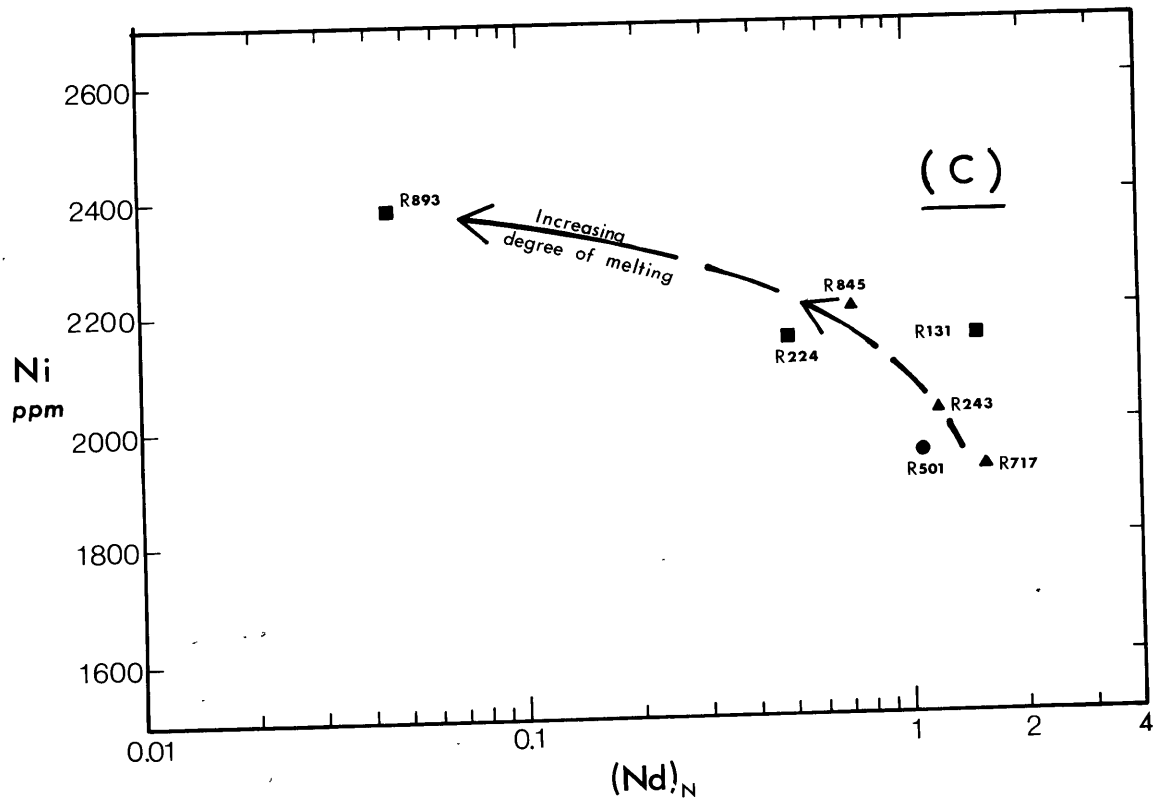
2600
2400
2200
2000
1800
1600
Ni
ppm
(c)
R893
Increasing
degree of melting
R845
R131
R224
R243
R501
R717
0.01
0.1
1
2
4
$(Nd)_N$

liquid and the residue would vary non-linearly as melting progresses; and therefore, linear correlation trends are not expected to exist among various minor elements.

For a model of direct mixing between two components, both minor and major elements should show linear mixing trends as straight lines in linear plots; but this is not observed among the minor elements. This can be easily recognized by the observation that the increasing or decreasing orders of some minor element abundances shown in Table II-3 do not apparently follow the same order as defined by the major elements. Another example can be seen from the complex criss-crossing of the REE patterns in Figure II-3. There is no simple linear relationship among the LREE and the HREE. Hence, the possibility of mixing is very unlikely.

Variation of Nickel in the Ronda Peridotites

Nickel abundance variations among the Ronda samples are particularly important because nickel partitions strongly into olivine. During peridotite melting, olivine is the dominant mineral in the residue, and it also constitutes a large portion of the early cumulates in fractional crystallization of a mafic or ultramafic magma. The distribution coefficient of nickel between olivine and silicate liquid is highly dependent on temperature and composition (Häkli and Wright, 1967; Leeman, 1974; Hart et al., 1976). At high temperatures ($\sim$1500°C) $D_{Ni}^{ol/l}$ is found to be as low as 4 or 5 (Leeman, 1974; Hart et al., 1976; Leeman and Scheidegger, 1977), while at a lower temperature (say, 1200°C) the value of $D_{Ni}^{ol/l}$ in-

creases to ∿16 (Leeman, 1974; Leeman and Scheidegger, 1977; Davis and Hart, 1977) for reasonable basaltic compositions. Therefore, a reasonable range of $D_{Ni}^{ol/l}$ values of 5 to 20 is taken for the modelling calculations of nickel fractionation during melting and crystallization.

Two idealistic models are used: fractional melting and fractional crystallization. In both cases it is assumed that olivine is the only phase involved. Because olivine is the most abundant phase in melting residues and in early cumulates of ultrabasic or basic magma, this simplification will not change the calculated Ni variation significantly from the real situation. Figure II-5 shows how the calculated Ni contents vary with respect to the initial concentration, C_o, as a function of the percent of completion of the process, F. In the case of fractional melting, the curves represent concentrations in the residual solids, and for fractional crystallization, they represent concentrations in the cumulate solids. In both cases three values of $D_{Ni}^{ol/l}$ (5, 10 and 20) were used. Of course, the two cases are assumed ideal, and in reality the processes are probably less effective and therefore the Ni abundance variations would be slightly less.

Variations in Ni concentrations are distinctly different in the sequence of solids generated by melting and crystallization (Figure II-5). For a given interval of degree of completion (percent melted or percent crystallized), the Ni

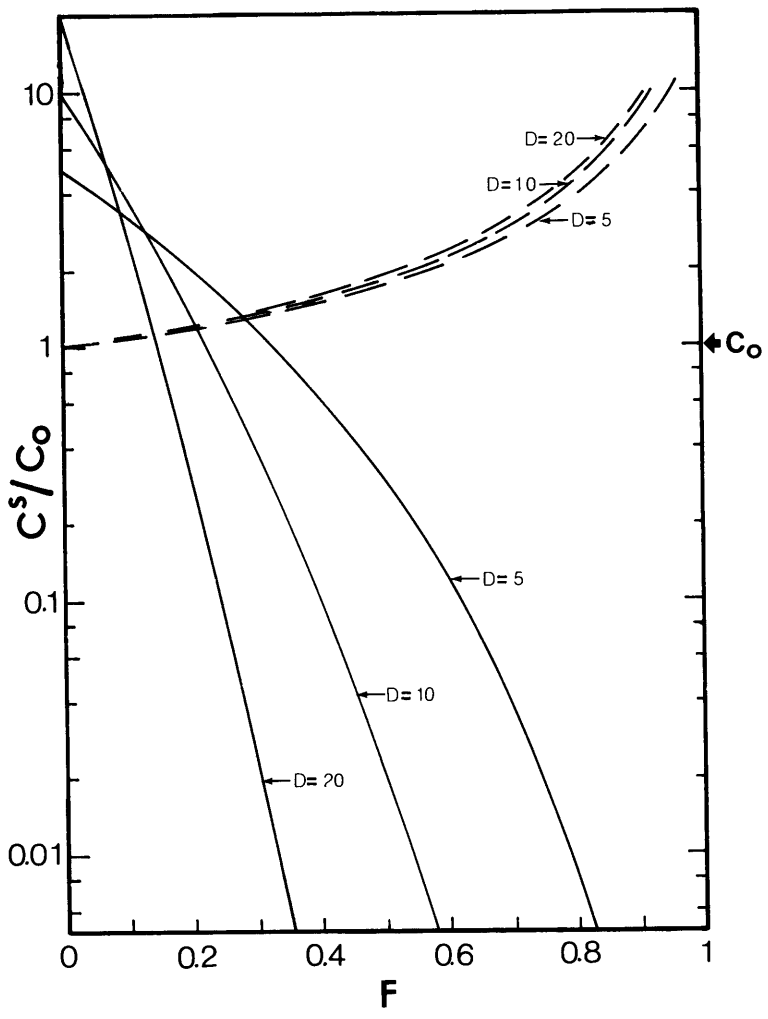

Figure II-5: Variation of Ni content in the solids during fractional melting (dashed lines) and crystallization (solid lines) with the degree of completion (F). C_0 is the initial bulk concentration.

concentration in the cumulate solid from fractional crystallization changes much more rapidly than that of the residual solid from partial melting (see also Frey and Green, 1974, p. 1050). For example, from F ≃ 0 to F = 0.30, 30% of crystallization, the ratio of C^s/C_o changes from 5 to 1.2; i.e., a factor of 4.2, for $D_{Ni}^{ol/l} = 5$. For higher values of $D_{Ni}^{ol/l}$, the change is even more drastic. In contrast to crystallization cumulates, the residual solids from fractional melting change only 33% in Ni content within the same interval (at F ≃ 0, $C^s/C_o = 1$; at F = 30, $C^s/C_o = 1.33$, for $D_{Ni}^{ol/l} = 5$). The Ni concentration varies more rapidly only at high degrees (>60%) of completion; that is, when almost all solid has melted.

The variation in Ni content among Ronda peridotites can be seen in Figure II-4(c). From the most undepleted lherzolite, R717 (1920 ppm. Ni), to the most depleted dunite, R893 (2380 ppm. Ni), the variation is only about 24%, which is equivalent to 20 to 30% of fractional melting from the former to the latter. Since the model assumes an ideal fractional melting case, and also assumes that olivine is the only residual phase, it is expected that in the real case of lherzolite melting, the Ni variation is less for a given interval of melting. Mysen and Kushiro's (1976) experiments on melting of an undepleted spinel lherzolite show that all pyroxenes disappear at about 40% of melting. Dunite R893 has 10% pyroxenes in the mode (Table II-1); thus, the partial melting model prediction of 20-30% melting is in reasonably good agreement.

On the other hand, a fractional crystallization model for Ronda peridotites can be eliminated because crystallization of 30% olivine would change Ni concentration in the solid by a factor of 4 (assuming $D_{Ni}^{ol/l} = 5$). Such large variations in Ni content are common in ultramafic rocks. For example, in the ultramafic rocks of the layered Muskox intrusion a factor of two or more variation in Ni content can be present within a cyclic unit of 300-350 feet (Irvine and Smith, 1967), as compared to a factor of 1.24 over the entire Ronda massif of 10 x 30 km. Therefore, I conclude that: (1) the Ronda peridotites were not formed by crystal fractionation processes similar to those forming layered intrusions, and (2) the Ronda peridotite compositions represent residual solids left after partial melting.*

Behavior of Strontium in the Mantle System

The geochemistry of strontium is believed to be similar to that of Eu^{2+}, a divalent REE ion with similar charge and ionic radius (Philpotts, 1970). Because the Eu^{2+}/Eu^{3+} ratio

---

* However, there remains the possibility that the Ronda massif was originally formed by a crystal fractionation process on a gross scale. For example, the early differentation processes which led to the formation of the crust-mantle-core system. The present work deals only with the fractionation processes after the mantle has been formed; i.e., processes that lead to the generation of basalts, and the formation of the mafic layers in the massif.

is a function of oxygen fugacity, the partitioning of Eu between silicate minerals and liquid strongly depends on f_{O_2}, but the partitioning of Sr does not (Sun et al., 1974; Drake and Weill, 1975). In the presence of cumulate or residual plagioclase, both Eu and Sr are expected to partition strongly into the solid, causing "Eu anomalies" in normalized REE patterns. However, if plagioclase is absent in the residual solid, no Eu anomalies are expected (at normal oxygen fugacities), and the bulk distribution coefficient (solid/liquid) for Sr will be low (<0.5). In Figure 4(b) Sr varies linearly with La on a log-log plot. The slope of the linear regression line is approximately 45° with a correlation coefficient, r = 0.967*. Such a strong correlation suggests that in the mantle system under consideration, Sr and La behave similarly; that is, the bulk $D_{Sr}^{S/l}$ and bulk $D_{La}^{S/l}$ are almost equal†. If this

---

* Calculated slope = 47.3°. If R224 is discarded, r is then 0.995, and the slope would be 46.8°.

† $C_{Sr}^{S} = C_{o_{Sr}} \cdot f(D_{Sr}^{S/l})$
$C_{La}^{S} = C_{o_{La}} \cdot f(D_{La}^{S/l})$
Where C_o is initial concentration. (f means 'a function of'.)

If $D_{Sr}^{S/l} \sim D_{La}^{S/l}$, then $\left(\frac{C^S}{C_o}\right)_{Sr} = \left(\frac{C^S}{C_o}\right)_{La}$

$$\frac{C_{Sr}^{S}}{C_{La}^{S}} = \frac{C_{o_{Sr}}}{C_{o_{La}}} = K, \text{ where K is constant.}$$

$$\therefore \log C_{Sr}^{S} - \log C_{La}^{S} = \log K$$

$$\log C_{Sr}^{S} = \log C_{La}^{S} + \log K$$

For the plot of $\log C_{Sr}^{S}$ vs. $\log C_{La}^{S}$, slope = 1; i.e., 45°.

is true, the bulk $D_{Sr}^{S/l}$ must be very low, since literature values of D_{La} between clinopyroxene and silicate liquid range from approximately 0.05 to 0.10 for a reasonable range of liquid compositions (Onuma et al., 1968; Schnetzler and Philpotts, 1968, 1970; Grutzeck et al., 1974), assuming that, in the absence of plagioclase, $D_{REE}^{S/l}$ between cpx and liquid dominates the value of the bulk distribution coefficient. Because $D_{La}^{cpx/l}$ is lower than $D_{Eu}^{cpx/l}$, $D_{Sr}^{cpx/l}$ is expected to be lower than $D_{Eu}^{cpx/l}$. Shimizu (1974) and Hart and Brooks (1974) found that Sr has a distribution coefficient ranging from $\sim$0.05 to 0.10 in experimental and natural clinopyroxenes. This range for Sr is similar to that found for La. Grutzeck et al. (1974) also reported, from a single experiment, $D_{Sr}^{cpx/l}$ = 0.078, $D_{La}^{cpx/l}$ = 0.069 and $D_{Eu}^{cpx/l}$ = 0.31. According to experiments by Sun et al. (1974), at high temperature ($\sim$1500°C) and low oxygen fugacity ($\sim 10^{-11}$ atm.), Sr has a lower solid/liquid distribution coefficient than Eu for clinopyroxene, while the reverse is true for plagioclase, which has much higher (>1) Sr and Eu solid/liquid distribution coefficients. In addition to the absence of Eu anomalies in the chondrite normalized REE patterns (Figure III-3), the behavior of Sr relative to the REE as discussed above also supports the conclusion that plagioclase was not involved in any fractionation process.

In summary, in the Ronda peridotites Sr behaves like La; that is, it has a very low bulk distribution coefficient, lower than that of Eu, indicating the absence of plagioclase in the mineral assemblage concerned. This observation to-

gether with the lack of a Eu anomaly strongly implies that the peridotites did not melt or fractionate in a P-T range where plagioclase peridotite is stable. This is an important conclusion because 70% of the Ronda massif is composed of plagioclase peridotite. These results support the proposed isochemical retrograde metamorphism which occurred during the cooling and decompression of the massif as it moved to the surface.

Rare-Earth Geochemistry of the Peridotites

Modelling of REE data for the Ronda peridotites can provide additional constraints (e.g., the presence or absence of garnet) on the proposed partial melting model. As a first approximation, Shaw's (1970) non-modal melting equations for trace element fractionation during anatexis are used. However, Shaw did not give the equation for C^S/C_o in the case of total equilibrium (or batch) melting. Using Shaw's equation (12), the following equation can be readily derived:

$$\frac{C^S}{C_o} = [(1 - F)(1 + \frac{F}{D_o - PF})]^{-1} \qquad \text{(II-1)}$$

for batch melting,

where C_o = concentration of trace element in the initial solid

C^S = concentration of trace element in the residual solid

F = degree of melting

D_o = bulk solid/liquid distribution coefficient

$(D_o = \Sigma X^i K^i)$

$P = \Sigma p^i K^i$

X^i = mass fraction of phase i in the initial solid

p^i = melting proportion for phase i

K^i = solid/liquid distribution coefficient for phase i.

In these models, spinel lherzolite R717 (No. 6, Tables 2 and 3), the most undepleted peridotite (e.g., the sample with the least fractionated REE pattern, Figure II-3), was used as the initial composition. Two possible mineral assemblages of the source rock were considered:

(1) Assemblage I which contains garnet, pyroxenes and olivine in proportions similar to the mineral assemblage of the upper mantle in the garnet lherzolite field;

(2) Assemblage II which contains no garnet, but has pyroxenes and olivine, corresponding to the pyroxene lherzolite or spinel lherzolite fields.

Table II-4 gives the mineral proportions in the initial solid and melting proportions for both Assemblages I and II. Note that spinel is not included in Assemblage II because spinel analyses indicate that, like olivine, it has very low solid/liquid distribution coefficients for REE (Kay and Gast, 1973; Allegre, C. J., personal comm., 1976). Therefore, the typical few (<5) percent of spinel in spinel lherzolites would not significantly affect the REE partitioning during melting; hence, spinel can be neglected without changing the modelling results.

To estimate the mineral proportions of the source rock in the garnet lherzolite field (Assemblage I) the major element

Table II-4

	Assemblage I (garnet lherzolite field)	Assemblage II (spinel or pyroxene lherzolite field)
cpx	15%	16%
opx	14%	22%
ol	61%	62%
gn	10%	0%
	Melting Proportions for I cpx:gn ≃3:2 cpx:opx ≃4:1 ol ≃5%	Melting Proportions for II cpx:opx ≃4:1
cpx	50%	74%
opx	12%	18.5%
ol	5%	7.5%
gn	33%	-

composition of R717 (Table II-2, No. 6) was used. A mantle norm calculation procedure devised by J. S. Dickey (personal comm., 1977) was adapted. This method, which is otherwise similar to other mantle norm procedures (e.g., Kushiro and Kuno, 1963), makes use of new experimental data by Akella (1976) on aluminum solubility in enstatite. At a given pressure and temperature condition (e.g., 30 Kb and 1600°C)*, the approach is to saturate the pyroxenes with Al and excess Al is then used to form garnet. The calculated results (shown in Table II-4, Assemblage I) are similar to the modal proportions of undepleted garnet lherzolite nodules found in basaltic rocks and kimberlites (cf. Chen, 1971; MacGregor, 1975).

Assemblage II was derived from Assemblage I by redistributing the components cpx and opx in garnet into the pyroxenes according to Appendix II-B, which is based on the pyrope-grossular contents of garnets in the Ronda peridotites (Obata, 1977). It is important to note that for a relatively small degree of partial melting, slight variations in initial mineral proportions do not drastically change the model results. However, the absence or presence of a mineral phase, for example, garnet, can significantly affect the results.

---

* This P-T condition is a rough estimate using the anhydrous solidus curve of a garnet lherzolite nodule (No. 1611) from a South African kimberlite (Kushiro, 1973). I find that a slight variation of P and T along the solidus does not significantly affect the normative mineral porportions.

Melting proportions were estimated from the eutectic composition in the $MgSiO_3$-$CaSiO_3$-Al_2O_3 plane at high pressure (26 $\sim$ 30 Kb) (Kushiro and Yoder, 1974) for the four-phase assemblage cpx-opx-ol-gn. In the case of the three-phase assemblage cpx-opx-ol, melting would no longer be at the eutectic. However, keeping the same cpx:opx proportion seems to be a reasonable approximation, since the cotectic line is roughly a constant distance from Di_{SS} and En_{SS}.

Because distribution coefficients are strongly compositonal and temperature dependent, no exact values for REE distribution coefficients can be assumed. After a literature survey of REE distribution coefficients for mantle minerals and basaltic liquids, two sets of distribution coefficients were chosen so as to encompass the likely uncertainties: a highest reasonable set of published numbers and a lowest reasonable set of published numbers. These values and references are given in Appendix II-G.

Two different processes, representing extreme cases, were considered: (1) Fractional melting, and (2) Batch melting (or total equilibrium melting). In the former case, liquid is extracted continuously in infinitesimal amount, and therefore, is out of equilibrium with the solid as soon as it is formed from melting. In the latter case, liquid formed is in a continuous equilibrium with the solid until all the liquid is extracted in a single step. Hence, fractional melting can be regarded as repeated steps of batch melting where the number of steps equals infinity. In both

cases, it is assumed that the solid remains homogeneous at all time; that is, the diffusion of trace elements to and from the surface of mineral grains is faster than the loss or "gain" of trace elements to and from the liquid, so that the system is in dynamic equilibrium at all stages.

Calculated REE abundances in residues from various degrees of melting are shown in the chondrite-normalized plot (Figure II-6). As expected, as melting proceeds, all residues are increasingly depleted in LREE with respect to the source. Two contrasting cases are given in Figure II-6. The first case is batch melting of Assemblage I (cpx + opx + ol + gn) and the second case is the batch melting of Assemblage II (cpx + opx + ol with no garnet). It can be seen that the LREE, e.g., La, do not differ significantly, since the distribution coefficients of garnet for the LREE do not differ very much from those of the pyroxenes, especially clinopyroxene, which dominates the bulk solid/liquid distribution coefficients in the absence of garnet. In contrast, the HREE, e.g., Yb, have very different abundances. In the first case (cpx + opx + ol + gn), Yb remains nearly constant during the initial portion of the melting process; i.e., until garnet is gradually consumed. In the latter case (cpx + opx + ol), Yb is removed to the melt much faster as the degree of melting increases. The different behavior of HREE results from garnet's strong affinity for HREE (e.g., $D_{Yb}^{Gn/l} \simeq 4.0$ to 9.8, see Appendix II-G), whereas pyroxenes and olivine have solid/liquid partition coefficients less than unity for HREE.

Therefore, HREE preferentially partition into the residual solid when garnet is present, but they are gradually removed into the liquid as garnet is consumed. In contrast, in the assemblage without garnet, the HREE are preferentially removed from the solid at the onset of melting.

In order to further investigate these two models, the calculated fractionation lines, generated by melting of spinel lherzolite R717, are plotted on a La vs. Yb diagram (Figure II-7). This plot emphasizes the effects of garnet. There are 8 fractionation lines corresponding to the 8 cases considered by combinations of (1) batch and fractional melting, (2) two possible mineral assemblages, and (3) two different sets of distribution coefficients (see legend of Figure II-7). The solid lines correspond to melting of Assemblage I (with garnet), and the dashed lines, to Assemblage II (no garnet). The nearly straight lines are generated by fractional melting, and the curves by batch melting. For each case mentioned there are two lines obtained by using a high set and a low set of distribution coefficients. Residues from melting of garnet lherzolite (Assemblage I) lie within the area enclosed by solid lines, while those from melting of spinel or pyroxene lherzolite (Assemblage II), are in the area enclosed by dashed lines.

Ronda peridotite data (Table II-3) are also plotted in Figure II-7. Only two out of the six peridotites (excluding olivine websterite R855) lie within the range predicted by the models. Therefore, I conclude that melting of peridotite

Figure II-6: Calculated REE patterns in residual solids from various degrees of melting (% indicated by numbers on each curve). Solid lines correspond to batch melting of Assemblage I (cpx + opx + ol + gn), and the dashed lines correspond to Assemblage II (cpx + opx + ol, without garnet).

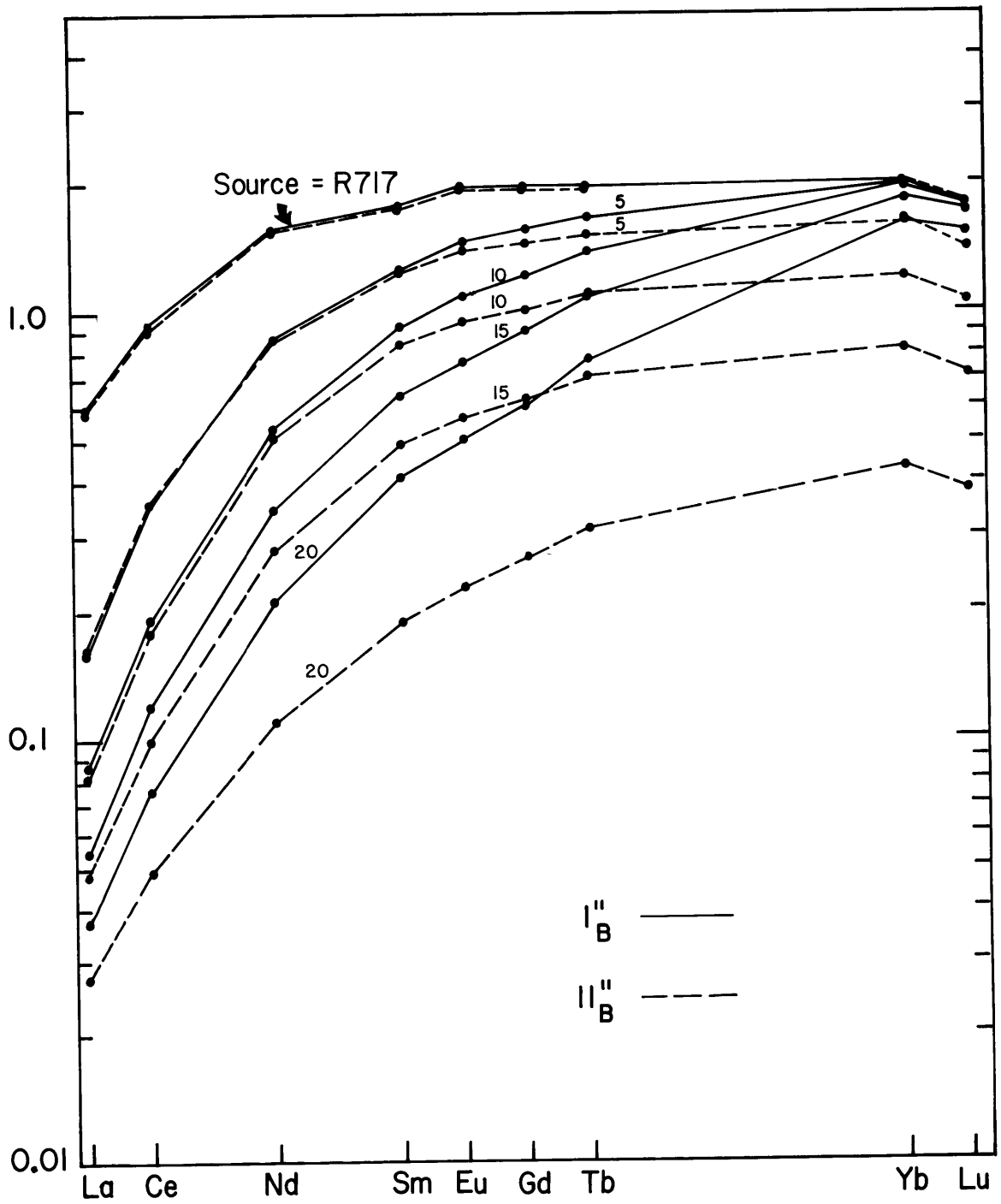
Source = R717
5
5
10
10
15
15
20
20
1.0
0.1
0.01
La
Ce
Nd
Sm
Eu
Gd
Tb
Yb
Lu
I''B
II''B

R717 cannot account for the compositions of most Ronda peridotites. Three peridotite samples from Beni Bouchera, the twin sister of Ronda, are also plotted in Figure II-7 (data from Loubet, M., personal communication, 1977). Note that two of these samples also lie outside of the predicted compositional range. In order to account for the range of La and Yb in the Ronda and Beni Bouchera peridotites, the model source must be more enriched in LREE than spinel lherzolite R717.

In this work, it is assumed that all the Ronda rocks were derived from a homogeneous mantle source. This assumption is the simplest approach, although the possibility of an inhomogeneous mantle on a small (km) scale cannot be ruled out by the data presented in this work. The reasons for a homogeneous source assumption are: (1) There is no evidence to indicate that the portion of the mantle represented by the Ronda body is chemically inhomogeneous. For example, variation diagrams, such as Sr vs. La (Figure II-4, b) and major element variation diagrams (Figure II-10, discussed later), define a single trend. (2) The REE patterns of the Ronda peridotites can be readily modelled by partial melting of a chondritic (on a relative basis) mantle source.

By assuming a homogeneous mantle, the REE compositions of the hypothetical mantle source can be deduced from the Ronda peridotite data . For example, the La and Yb abundances of the source (C_o) must be located in Figure II-7 so

that all Ronda samples (except olivine websterite R855*) lie within the field predicted by the models. In other words, the starting point in Figure II-7 has to be shifted on the diagram, so that the calculated fractionation lines will encompass all the points. Since this diagram is a log-log plot, moving the source compositon to any point in this plot will not affect the shape and orientation of the fractionation lines**. In order to encompass all the sample data, the simplest procedure is to move the source in Figure II-7 to the right towards the chondritic line; i.e., the line indicated by a chondrite-normalized ratio of $(La/Yb)_N = 1$. The result of this transformation is shown in Figure II-8.

If a mantle source with REE concentrations two times chondrites is assumed (Figure II-8), all samples, including those from Beni-Bouchera, fit within the calculated areas. There is little tolerance for the source composition to move along the chondritic line, but a source with $(La/Yb)_N > 1$, i.e., LREE enrichment relative to chondrites, would also encompass all data points. However, major element compositions of these peridotite samples (to be discussed in more detail later) show that these rocks (excluding dunite R893) are not residues from high (>20%) degrees of melting. Therefore, the hypothetical source must be close to the chondritic line, and it cannot have a high degree of LREE enrichment.

---

* See next page for footnote.

** See next page for footnote.

* This rock is believed to have been contaminated with liquid fractions, based on anomalous textural and petrographic observations. Its chemical composition will be discussed in the next section.

**Consider original initial composition at (Co_{La}, Co_{Yb}) then, for a certain process at a certain stage, the residual solid composition is (C^S_{La}, C^S_{Yb}), which can be expressed as:

$$C^S_{La} = Co_{La} \cdot f(F, D^{S/l}_{La}) \qquad (1a)$$

$$C^S_{Yb} = Co_{Yb} \cdot f(F, D^{S/l}_{Yb}) \qquad (1b)$$

If a new initial composition is taken at (Co'_{La}, Co'_{Yb}), so that

$$Co'_{La} = Co_{La} \cdot x \qquad (2a)$$

$$\text{and} \quad Co'_{Yb} = Co_{Yb} \cdot y \qquad (2b)$$

where x and y are some real positive values, at the same stage of the same process, we have the new residual composition:

$$C^{S'}_{La} = Co'_{La} \cdot f(F, D^{S/l}_{La}) \qquad (3a)$$

$$C^{S'}_{Yb} = Co'_{Yb} \cdot f(F, D^{S/l}_{Yb}) \qquad (3b)$$

Combining (1a) and (3a): $\dfrac{C^S_{La}}{C^{S'}_{La}} = \dfrac{Co_{La}}{Co'_{La}}$

Substituting (2a) in $\dfrac{C^S_{La}}{C^{S'}_{La}} = \dfrac{Co_{La}}{xCo_{La}} = \dfrac{1}{x}$

$$\text{or} \quad C^{S'}_{La} = xC^S_{La}$$

Taking log: $\log (C^{S'}_{La}) = \log (C^S_{La}) + \log X$

Also from (2a): $\log (Co'_{La}) = \log (Co_{La}) + \log X$

Similarly, such relationship is also true for $\log C^{S'}_{Yb}$ and $\log Co'_{Yb}$. Therefore, the residual solid composition translates exactly the same amount with respect to the absicca and the ordinate as the new initial composition.

In order to evaluate if a mantle source with REE concentrations of two times chondrites is applicable to other high-temperature peridotite bodies, literature data (Frey, 1969; Philpotts et al., 1972; Loubet et al., 1975) are plotted in a similar diagram* (Figure II-9). Again, this source is sufficient to encompass all the data points.

Another interesting observation from Figure II-8 is that the lherzolite samples can be distinguished into two groups, according to their Yb/La ratios:

(1) Samples that lie within the garnet melting field; namely, R717, R243, R501. These peridotites are

---

* $(Ce)_N$ is chosen because La data are not available for most samples.

Legend for Figure II-7

Assemblage I	Fractional Melting		Batch Melting	
CPX : 15 OPX : 14 OL : 61 GN : 10	HIGH D	LOW D	HIGH D	LOW D
	I''_F	I'_F	I''_B	I'_B
Assemblage II				
CPX : 16 OPX : 22 OL : 62 (NO GARNET)	II''_F	II'_F	II''_B	II'_B

Figure II-7: $(Yb)_N$ versus $(La)_N$ diagram. The curves are calculated fractionation lines of the residual solid compositions generated by melting of spinel lherzolite R717. The solid lines correspond to melting of Assemblage I (with garnet), and the dashed lines, to Assemblage II (no garnet). The nearly straight lines are generated by fractional melting models, and the curves by batch melting models. There are two lines obtained for each case by using a high set and a low set of distribution coefficients (see Appendix II-G), making a total of 8 possible lines. For the meanings of the labels, see legend on page . Numbers on the curves indicate the degrees of melting in percent. Symbols for the samples are the same as in Figure II-2. Open circles are samples from Beni-Bouchera (M. Loubet, per. comm., 1977).

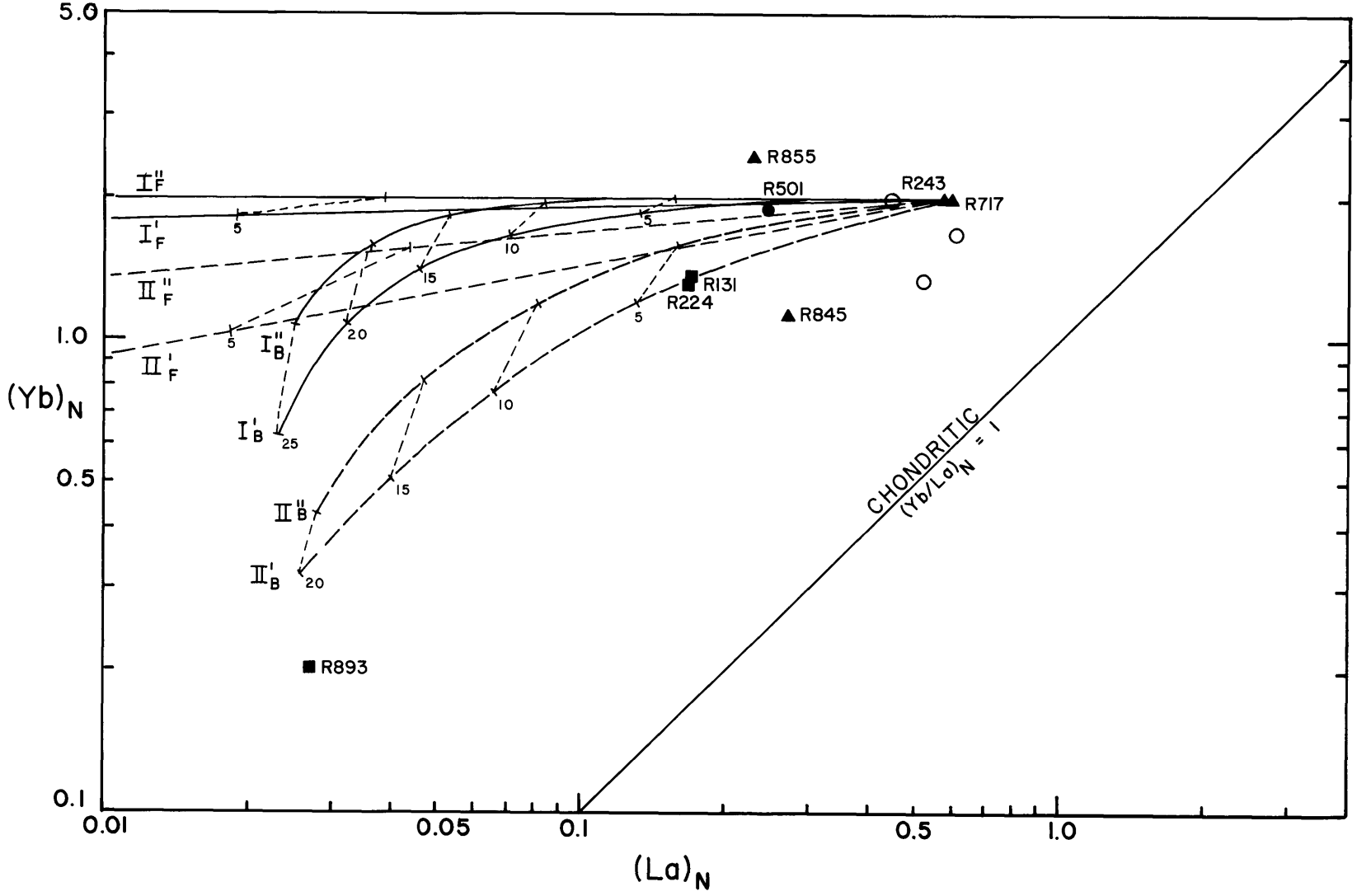
5.0
1.0
0.5
0.1
(Yb)N
0.01
0.05
0.1
0.5
1.0
(La)N
I''F
I'F
II''F
II'F
I''B
I'B
II''B
II'B
5
10
15
20
25
R855
R501
R243
R717
R131
R224
R845
R893
CHONDRITIC
(Yb/La)N = 1

Figure II-8: $(Yb)_N$ versus $(La)_N$ diagram. The fractionation lines are the same as in Figure II-7. The source composition is assumed to be 2 times chondrites, i.e., $(Yb)_N = (La)_N = 2$.

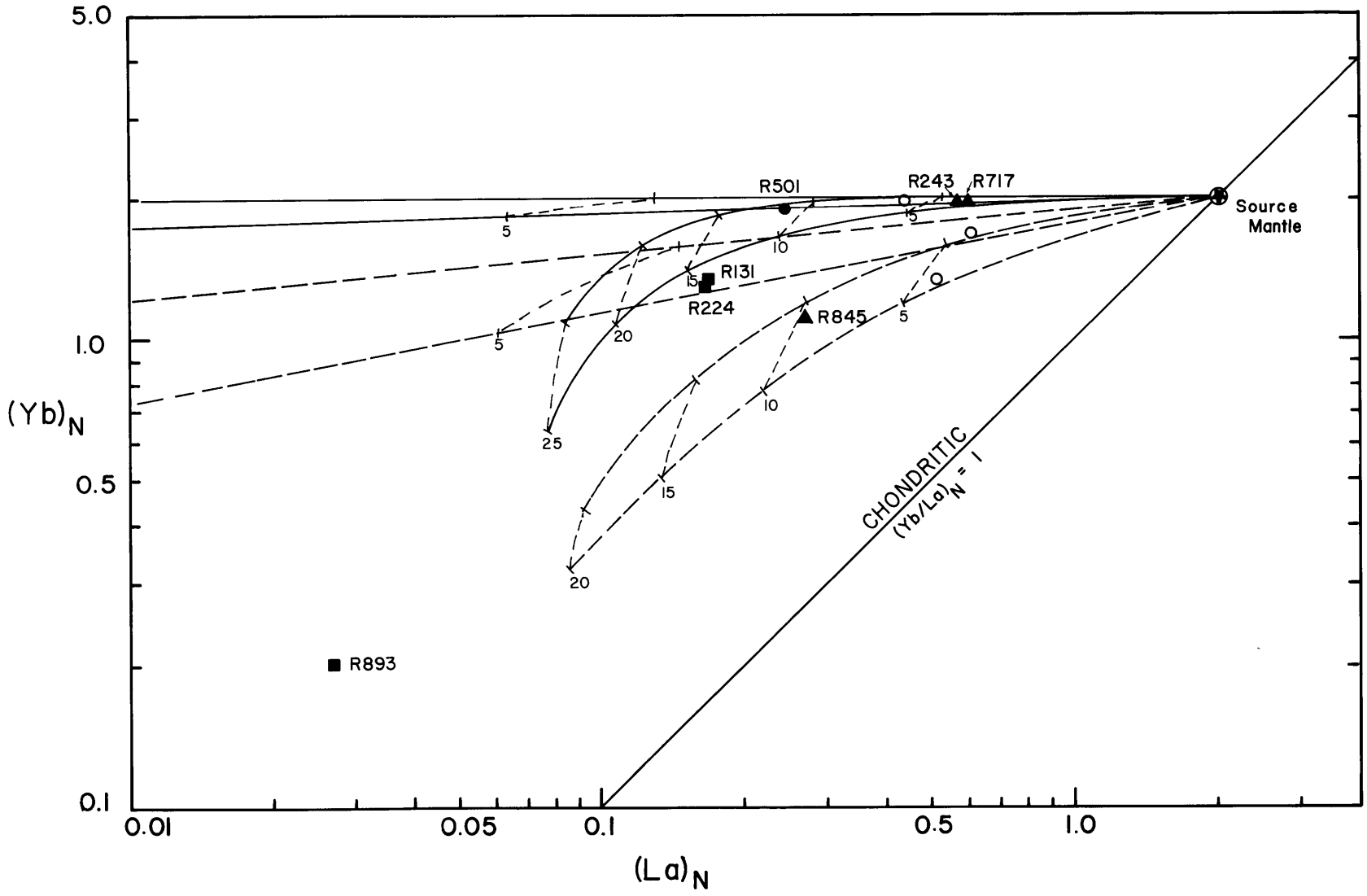
5.0
1.0
0.5
0.1
(Yb)N
0.01
0.05
0.1
0.5
1.0
(La)N
R501
R243
R717
Source
Mantle
R131
R224
R845
R893
5
10
15
20
25
CHONDRITIC
(Yb/La)N = 1

Figure II-9: $(Yb)_N$ versus $(Ce)_N$ diagram similar to Figures II-7 and II-8. A 2 times chondrites source composition is assumed. Data points are from Lizard (Frey, 1969); Tinaquillo (Philpotts, et al, 1972); Beni-Bouchera, Etang de Lers and Alps (Lanzo-North, Lanzo-South, Rivera, Lucana and Badissero) (Loubet, et al, 1975).

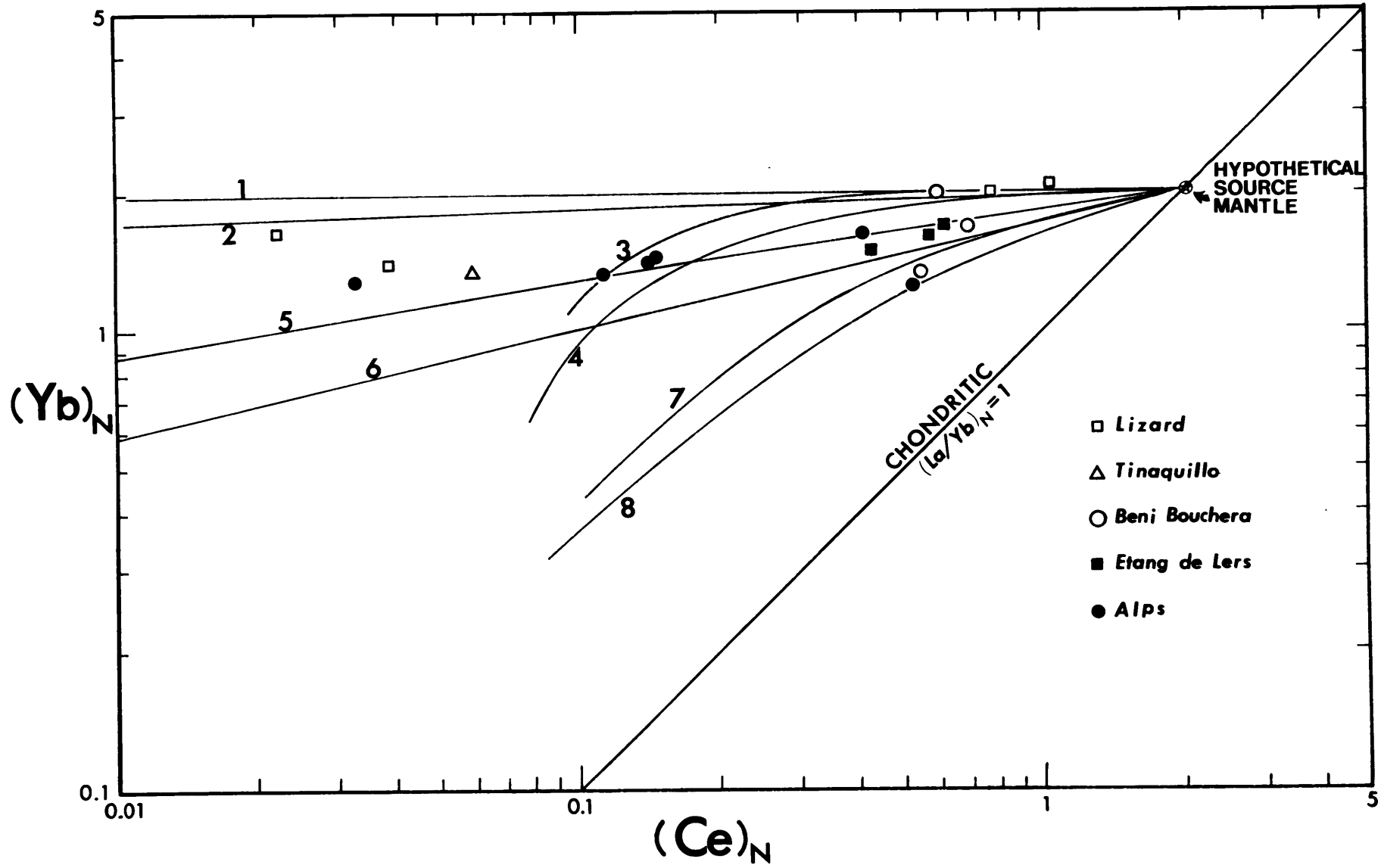
5
1
0.1
0.01
0.1
1
5
(Yb)N
(Ce)N
1
2
3
4
5
6
7
8
HYPOTHETICAL SOURCE MANTLE
CHONDRITIC (La/Yb)N=1
Lizard
Tinaquillo
Beni Bouchera
Etang de Lers
Alps

interpreted as residues from partial melting of a source containing garnet; and

(2) samples that lie outside the garnet field; namely, R845, R131, R224. These peridotites are interpreted as residues from a garnet-free source, or alternatively, a small amount of initial garnet was completely consumed during the early melting stages.

In summary, based on REE data the following conclusions can be drawn:

(1) The Ronda peridotites represent residues resulting from small degrees of partial melting (<10-15%) of the upper mantle.

(2) The melting processes may be approximated by fractional or batch melting models, but most likely the real process is intermediate between the two end-member cases. (A detailed treatment of incremental or multiple-step melting is given in the next chapter.)

(3) Some peridotites contained garnet as a residual phase during melting, while others did not.

(4) The mantle source of these residual peridotites and also other high-temperature peridotites has a near-chondritic REE pattern at approximately two times the chondritic average abundances (values from Haskin et al., 1968).

Compositional Grouping of the Ronda Lherzolites

As described in the last subsection, the Ronda lherzo-

lites can be distinguished into two groups, according to their Yb/La ratios. The grouping is as follows:

				Tables II-2 & 3 column
II.	garnet-absent melting field	R845	spinel lherzolite (seiland subfacies)	1
		R131	plagioclase lherzolite	2
		R224	plagioclase lherzolite	3
I.	garnet melting field	R501	garnet lherzolite	4
		R243	spinel lherzolite (ariegite subfacies)	5
		R717	spinel lherzolite (ariegite subfacies)	6

Since the order from No. 1 to 6 in Tables II-2 and II-3 is according to major element composition, there is an obvious correlation between REE characteristics and major element composition. In subsequent discussions, Nos. 1, 2 and 3 are designated as Group II rocks, corresponding to Assemblage II in the previous subsection, and Nos. 4, 5 and 6 as Group I, corresponding to Assemblage I. Major and minor element characteristics of the two groups are in Tables II-2 and II-3. A summary of the important geochemical characteristics is given below:

(1) Group II has lower concentrations of CaO and Al_2O_3 compared to Group I. Also, CaO/Al_2O_3 ratios of Group II are distinctly higher than those of Group I. The lower CaO/Al_2O_3 of Group I peridotites is consistent with garnet as a primary residual mineral because garnet has much more Al_2O_3 relative to CaO than clinopyroxene even at high temperatures (e.g., Kushiro et al., 1972; Akella, 1976). However, two of the three rocks in Group I lie in the ariegite subfacies of spinel

lherzolite facies, and do not have garnet in the mode (see Table II-1). It follows that Group II rocks did not have a significant amount of garnet as a residual phase. Therefore, the major element implications are consistent with conclusions based on REE data (specifically, conclusion No. 3 of the last subsection).

(2) Sc and Y, like HREE, preferentially partition into garnet during melting of mantle peridotites (Frey et al., 1977). Although Sc and Y abundance differences are small between Groups I and II, the slightly higher abundances in Group I support the previous conclusions based on HREE and CaO/Al_2O_3 data.

(3) The order No. 1 to 6 in Tables II-2 and II-3 is a sequence of increasing enrichment in magmaphile elements. That is, in the context of the partial melting model, Group II samples (Nos. 1, 2 and 3) which are more depleted in magmaphile elements are residues from greater degrees of partial melting than Group I rocks (Nos. 4, 5 and 6) where compositions are closer to the initial source rock. This trend can be observed from the following data:

(a) $Mg/Mg+\Sigma Fe$ ratios decrease from No. 1 to 6, and the abundances of MgO decrease in the same order.

(b) CaO and Al_2O_3 increases in the same order.

(c) In general, TiO_2 contents in Group I are higher than those of Group II, except for No. 2 (R131). Within Group I, TiO_2 content increases in the order of No. 4 - 5 - 6.

(d) Other incompatible trace elements, for example, Sr, Zr, V, Rb, K, Ga and P, also roughly follow this trend. Several of these elements have very low abundances in the peridotites and the small abundance variations may be significantly affected by analytical errors. Nevertheless, the large number of elements which tend to vary systematically from samples 1 to 6 strongly suggests that a single process, varying only in degree, has established the geochemical characteristics of the Ronda peridotites.

Major Element Variations among the Ronda Peridotites

In order to systematically analyze major element trends in the Ronda peridotites, variation diagrams are plotted in Figure II-10 (a), (b), (c) and (d). Because natural peridotites can be approximated by a 4-component system CaO-MgO-Al_2O_3-SiO_2 (herein abbreviated as: CMAS, O'Hara, 1968), variations of CaO, Al_2O_3, SiO_2 and ΣFeO (total Fe as FeO) are plotted against MgO. Because the peridotites are serpentinized to different extents, all values plotted are on volatile-free basis.

In addition to variation diagrams, mantle norm calculations were used to evaluate the bulk rock compositions in terms of three mineral components cpx-opx-ol. The normative calculations adapted and modified slightly from Kushiro and Kuno (1963), are described in Appendix II-H. In brief, the method assigns all Ca, Ti, Na to clinopyroxene molecules and calculates

Figure II-10: Variation diagrams for the Ronda peridotites.
(a) SiO_2 vs. MgO weight percent
(b) Al_2O_3 vs. MgO weight percent
(c) CaO vs. MgO weight percent
(d) ΣFeO vs. MgO weight percent

Open symbols are Ronda samples. The squares are Group I lherzolites; the circles, Group II lherzolites; and the triangles are the olivine websterite and the dunite. Numbers correspond to those in Tables II-2 and 3. The star indicates the estimated hypothetical primary mantle composition.

Solid symbols - Circle: Pyrolite III (Green and Ringwood, 1967); Diamond: Sheared garnet lherzolite nodules (No. 1611) from a South African kimberlite (Nixon and Boyd, 1973); square: composition of the upper mantle based on nodules found at Kilbourne Hole, New Mexico (Carter, 1970) (corresponding to Fa 12%); triangle: Composite bulk composition of Vourinos ophiolite complex (Moores, 1970, Table III-3, average of A and B).

The solid straight line is the "extraction line" obtained by linear regression on the Ronda peridotite samples. The dashed line is a similar line obtained by O'Hara, et al (1975) based on ultramafic nodules in kimberlite. The dot and dash line is obtained by Kuno and Aoki (1970) based on ultramafic nodules in basaltic rocks from various parts of the world.

"L" is the composition of the hypothetical primary magma generated by partial melting of the Ronda peridotites.

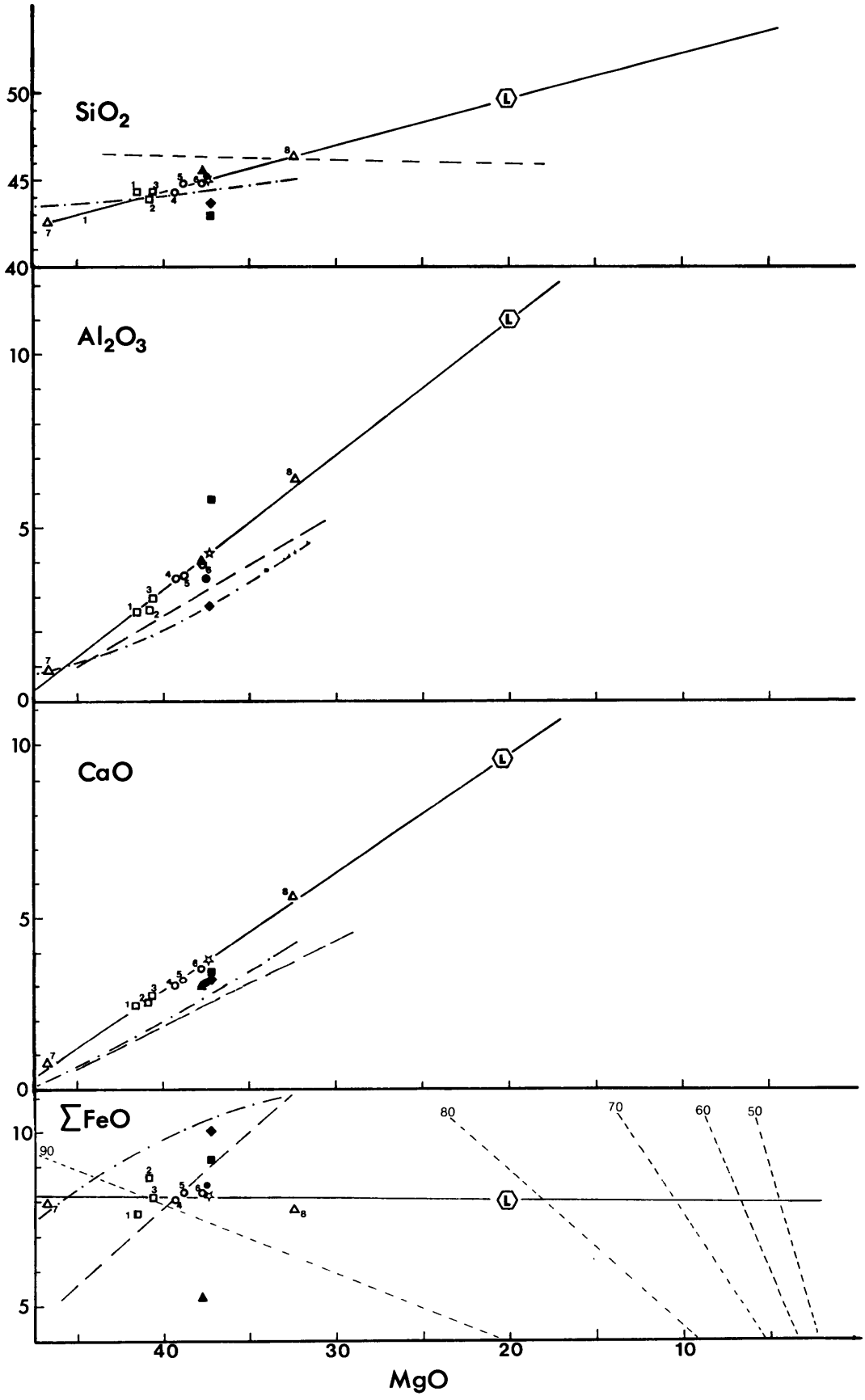
SiO2
50
45
40
Al2O3
10
5
0
CaO
10
5
0
∑FeO
10
5
90
80
70
60
50
40
30
20
10
MgO
L

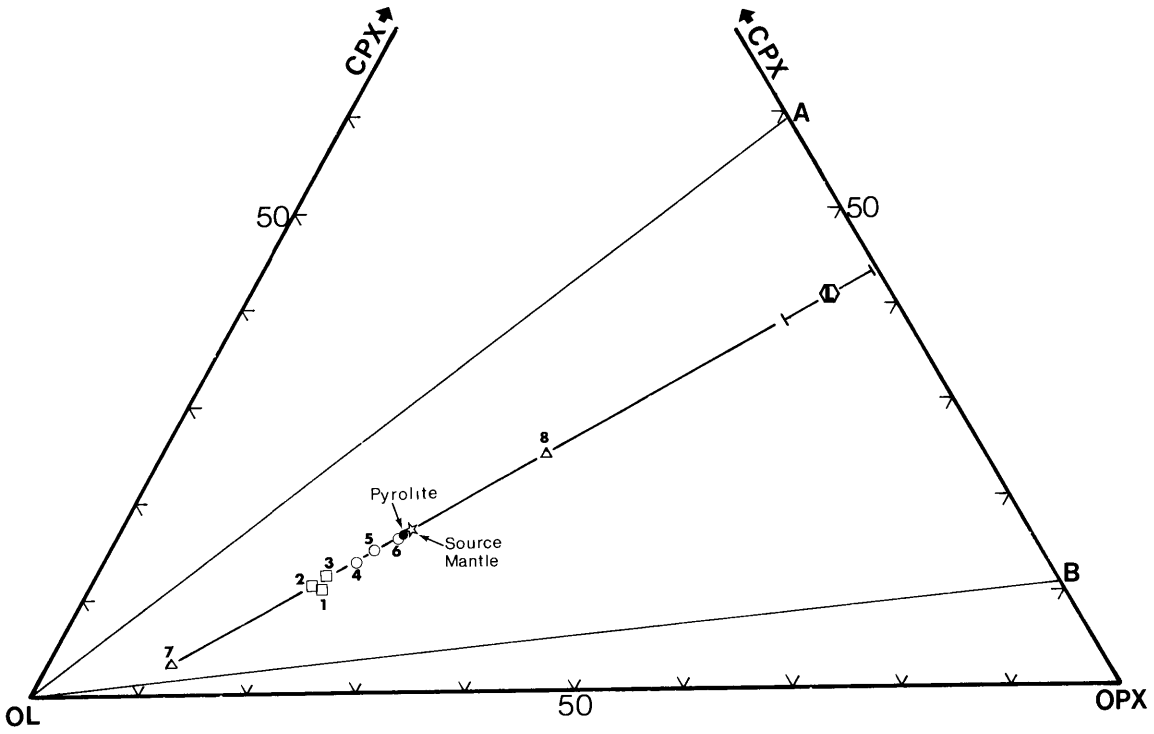

Figure II-11: Plot of Cpx, Opx, Ol normative components (wt. %) of the Ronda peridotites. A and B indicate the position of the pyroxene solvus at 30 Kb., 1500°C (Mori and Green, 1975). Other symbols are the same as in Figure II-10.

the En/Ol ratio according to the amount of SiO_2 left relative to MgO (including FeO) as in the CIPW norm. Al_2O_3 solubilities in En and Di are assumed to be equal. No garnet molecules are formed. The resulting normative plot is shown in Figure II-11.

A prominent relationship in this normative plot is that all peridotites, including the dunite and the olivine websterite, lie on a remarkably straight line. Especially, the Group I rocks are amazingly colinear with the dunite (No. 7) far to the lower left and the olivine websterite (No. 8) far to the upper right. To confirm that the linearity in Figure II-11 is not an artifact of the norm calculation process, the variation diagrams [Figures II-10 (a), (b), (c), (d)] are examined. In each of these plots the peridotites define a nearly linear trend. The poorest correlation is the plot of ΣFeO vs. MgO [Figure 10(d)]. This is probably because Fe and Mg substitute readily for each other, and Fe/Mg ratios of both solid and liquid are changing continuously during melting, as the K_D for Fe/Mg exchange reactions among mantle minerals and liquid is dependent on temperature, pressure, oxygen fugacity and composition (Roeder and Emslie, 1970; Mysen, 1975; Hanson and Langmuir, 1977).

As a result of the strong correlations in the variation diagrams [Figures II-10, (a)-(d)], it is evident that the peridotite compositions lie on a straight line within the CMAS tetrahedron. Such a linear correlation can be explained by two distinct processes: (1) mixing of two end-member

compositions, e.g., liquid and residual solid; (2) a residual trend caused by extracting a liquid of almost constant composition.

It has been concluded on the basis of compositional variations that the model of mixing is not acceptable because trace element variations do not indicate any linear mixing trend, although possible mixing trends are observed in major element variation plots (page 73). In addition to this argument, field and petrographic observations show no indication of liquid contamination in the peridotites (excluding olivine websterite R855). Furthermore, the model of mixing a liquid with a residual solid requires that one end-member composition must be at least as depleted as dunite R893. For this model to be applicable, the whole massif must have melted to a large percent, and the residue must be subsequently remixed in various proportions with the liquid, and then, the mixture must be completely homogenized. Because only approximately 5% of the massif is composed of dykes of mafic rocks with very distinct contacts with the peridotites, a large percent melting followed by complete homogenization is not consistent with field observations. In addition, none of the mafic rocks analyzed have compositions close to the primary liquid required for the end-member composition (see Chapter V).

The linearity observed in Figures II-10 (a)-(d) and II-11 can be explained by a melting model. For example, the REE data of spinel lherzolite R717 indicate that it has undergone

only a very small (2-4%) degree of melting; therefore, the mantle composition prior to melting had a composition close to that of R717 (No. 6 in Tables II-2, II-3). Subsequent melting of this mantle source to various degrees with the extraction of an almost constant composition liquid would produce residues with the observed linear fractionation trend. The extracted liquid composition is therefore expected to lie on or close to the extension of this "extraction line" (Figure II-11) defined by the residue compositions.

Olivine websterite R855 (No. 8, Tables II-2, II-3) is anomalous because it is much more enriched in CaO, Al_2O_3 and other magmaphile elements than any reasonable mantle source. It also exhibits anomalous mineralogy and texture*. However, the composition of sample R855 is colinear in Figures II-10 (a)-(d) and II-11 with other Ronda peridotites. This rock is believed to have formed by contaminating a residual peridotite

---

* In hand-specimen, this rock is not homogeneous. The pyroxenes are slightly darker in color than those in normal peridotites. Both the pyroxenes and the spinels are unevenly distributed, and are concentrated in patches in the scale of a few cm across. In this sample locality, there are many thin mafic layers in the peridotites that have been deformed, disrupted and their boundaries are typically fuzzy, indicating that some mixing between the mafic layers and the peridotites might have occurred.

with a large percent of liquid. Thus, it is the only Ronda "peridotite" studied that is explained by a mixing model.

Another important implication of this trend is that when natural mantle peridotites melt, they probably behave similarly to simple model systems. In other words, since the liquid produced is fairly uniform at the "eutectic" composition of a 4-phase natural peridotite, the behavior during melting of natural rocks can be approximated by the CMAS system. This conclusion agrees with ideas presented by Mysen and Kushiro (1976). In their experiments, they found that the liquid composition is controlled largely by the presence of certain mineral phases, but not by the mineral proportions or small variations in mineral composition. With this simple model established, more detailed melting models (in the next chapter) will be based on experimental data of the CMAS system.

II.5 TECTONIC HISTORY AND PRESSURE-TEMPERATURE TRAJECTORY

REE data indicate that some Ronda peridotites represent residues which contained garnet during melting, and others represent residues that did not contain garnet. These two groups can also be distinguished in terms of major elements (Figures II-10 and II-11). Also, Group I rocks (page 69) which are believed to have contained garnet show less depletion in magmaphile elements, and thus, are residues from a smaller percent of melting than Group II rocks. Since Group II rocks are residues from higher degrees of melting than

Group I rocks, it is possible that garnet was completely melted from the parental peridotite of the Group II residues, whereas primary garnet remained in Group I residues. Group II rocks also show a little more scatter about the extraction line than Group I rocks (Figure II-11). Possibly, the liquid composition for Group II was not as closely controlled as for Group I because only three phases (cpx+opx+ol) coexisted in Group II rocks after garnet was consumed, and the degree of freedom, in the context of the phase rule, would be increased by one in the model 4-component CMAS system.

Another aspect of the grouping is the geographic distribution of the samples (Figure II-1). Note that Group I rocks are from the northwest part of the massif, and the other peridotites are from the southeast and east. This pattern coincides with the metamorphic grades. For examples, the isograd (Obata, 1977) dividing the areigite subfacies and the seiland subfacies of the spinel lherzolite facies may be used as a dividing line between Group I and Group II sample locations (Figure II-1). Although only a few samples have been studied, the coherence of geographic distribution with the peridotite compositional grouping may be very significant.

Obata (1977) proposed a dynamic model in order to explain the geographic proximity of different metamorphic facies corresponding to a large pressure difference which cannot be accounted for by the lithostatic pressure expected from the field relationships. He obtained, from phase relations and

geobarometry, a 10 Kb pressure difference between the garnet lherzolite facies and the plagioclase lherzolite facies which are no more than 5 Km (<1.5 Kb) apart in the field. In view of this discrepancy, Obata proposed that heat conduction within the rising peridotite body was slow relative to the ascent rate. Therefore, the center of the body remained hot while the outer part of the body cooled much faster to a lower temperature at the same pressure. The result is that different parts of the body followed different trajectories in P-T space. Obata suggested that garnet peridotites in the NW part of the massif represent the outermost part of the rising body, while the plagioclase peridotites of the SE represent the center.

Although Obata's (1977) model refers only to the subsolidus recrystallization history of the massif, the positions of the rocks with respect to the whole peridotite massif probably have not changed since melting occurred at high P-T conditions near the solidus. That is, if the NW portion of the massif was near the margin of the peridotite body during subsolidus recrystallization, it is likely to have been in a similar position during the high P-T melting event. Similarly, the SE portion was probably near the center of the body during the melting event. Assuming that this is true, a similar model can be proposed to explain the relationship between compositional data and the field distribution of these peridotite samples.

Figure II-12 is a schematic diagram of the proposed model.

A mantle diapir rises from the geotherm (Point A). Due to the rapid ascent rate and its large size, the outside is cooler than the inside, because the outer part loses heat to the surroundings quickly, while the inner part retains much of its heat. Therefore, the inside (indicated by II*) follows a path A-B close to the adiabat, while the outside (I) follows a path A-C at a lower temperature. Because geochemical data have shown that the outside (Group I rocks) had garnet as a residual phase during melting, both parts must intersect the peridotite solidus inside the garnet lherzolite field. However, the inside intersects the solidus at Point B at a higher P and T than the outside intersection at Point C. As the inside starts to melt, it follows the solidus until one of the four solid phases (cpx+opx+ol+gn) is consumed. Since garnet is likely to be the first phase to disappear with melting†, at a certain point all garnet is exhausted. In the

---

* I and II are chosen to be consistent with mineral assemblages deduced from REE models, and with the previously described geochemical grouping of the peridotites.

† Assuming melting occurs at low pressures within the garnet lherzolite field (Yoder, 1976, pp. 148-9). It is also supported by a more detailed petrologic model presented in the next chapter, and this can be shown directly from the relative position of R717 composition projected into the Al_2O_3-En-Wo plane with respect to the "critical plane" discussed by O'Hara (1970). (See Figure III-2.)

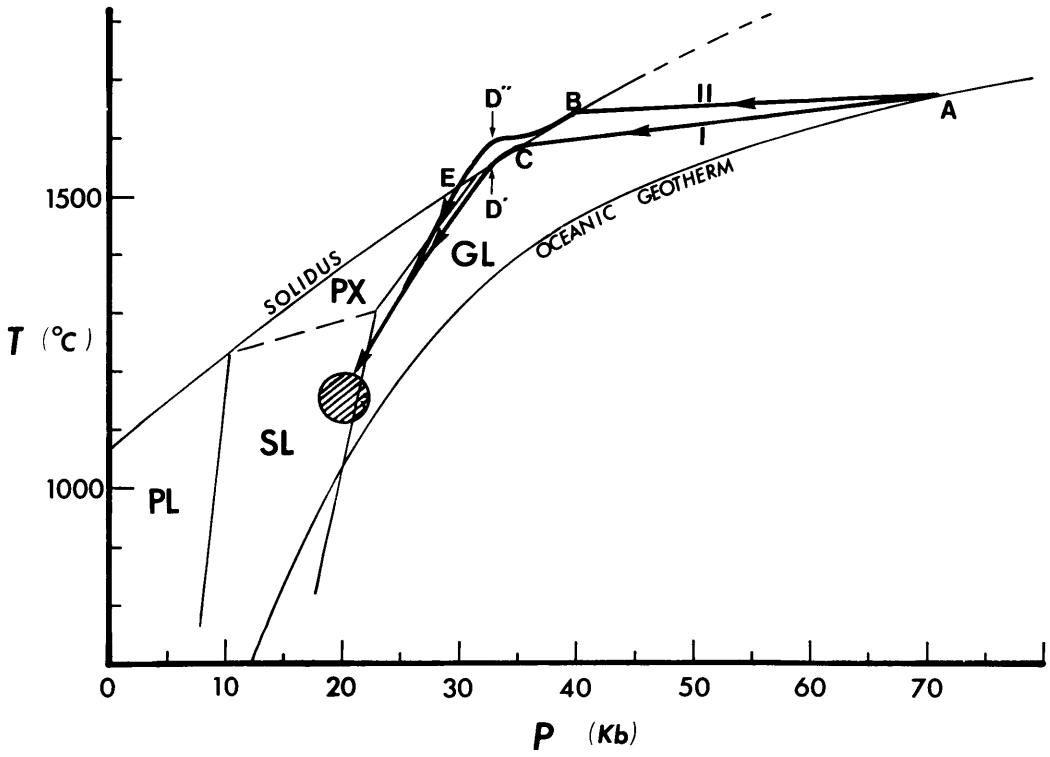

Figure II-12: Hypothetical P-T trajectory of the Ronda intrusion. Phase relations are those of Pyrolite (Green and Ringwood, 1967).

GL: Ol + Opx + Cpx + Gn
SL: Ol + Al-opx + Al-cpx + Sp
PX: Ol + Al-opx + Al-cpx
PL: Ol + Opx + Cpx + Plag
Cross-hatched area: "Primary condition" (Obata, 1977).

second interval of melting, only three phases are present, and thus, the P-T trajectory can leave the 4-phase peridotite solidus, while continuing to melt without garnet as a residual phase. Note that the outside of the diapir starts to melt later than the inside. After intersecting the solidus at C, it also follows the solidus but after only a small degree of melting, with garnet remaining in the residue, the ascending rate of the mantle diapir slows rapidly. The reason for this deceleration is not known*. A consequence of this deceleration is cooling (Points D' and D"). Melting ceases almost instantaneously on the outside (at Point D') and continues on the inside until the center cools from D" to E on the solidus. Since the ascent rate is now slow relative to the conduction of heat, the whole diapir, inside and outside, reaches thermal equilibrium, and finally arrives at the "primary condition" established by Obata (1977) by pyroxene geothermometry and geobarometry.

This model (Figure II-12) explains all the conclusions developed from the geochemical data. In summary, they are:

(1) REE data indicate that Group I rocks had garnet as residual phase, while Group II rocks did not.

(2) Group II rocks are more depleted than Group I rocks in magmaphile and incompatible trace elements.

(3) Group II rocks are more magnesian than Group I rocks. Together, conclusions (2) and (3) indicate Group II rocks

---

* One possibility is that it hits the bottom of the lithosphere, or reaches the top of the asthenosphere.

underwent larger degrees of melting than Group I rocks.

(4) Group I rocks are found in the higher grade metamorphic terrain of the NW part, while Group II rocks are in the lower grade terrain in the SE. According to Obata (1977), the NW probably represents the outer part of the peridotite body, whereas the SE is from near the center.

CHAPTER III

GEOCHEMICAL CONSIDERATIONS FOR THE MELTING OF MANTLE PERIDOTITES

In the last chapter, partial melting, fractional and batch, models were applied to the REE data. However, natural partial melting processes probably lie between the two idealistic end-member models. In this chapter more detailed, realistic models are presented and applied to the Ronda samples.

III-1: HOW LIQUID IS EXTRACTED FROM A PARTIALLY MOLTEN AGGREGATE OF ROCK: POSSIBILITIES AND FACTORS INVOLVED

Fractional Melting Versus Batch Melting

As mentioned in the last chapter, fractional melting and batch melting represent two extreme cases in which liquid is extracted in infinite number of steps and in a single step, respectively. Fractionation of trace elements is most effective during fractional melting; for example, at the same degree of partial melting, fractional melting causes more depletion of LREE in the residual solid and higher enrichment of LREE in the total derived liquid, relative to batch melting. These two cases thus give only the upper and the lower limits for the real case, in which the number of extraction steps must be finite, so that ideal fractional melting is impossible. However, if the number of steps is sufficiently large, that is, the amount of liquid extracted

in each step is sufficiently small, the effect would be close to the ideal case of fractional melting. On the other hand, if the degree of melting is small, it may be feasible to let all the liquid equilibrate with the solid and then be extracted in a single step, or a small number of repeated steps. In this case, the effect would be ideal or close to the ideal case of batch melting. Therefore, it is more realistic to treat the number of steps, N, to be a real positive integral value.

The following table shows the major features of the partial melting models to be considered:

Process		No. of Steps	Way of Extraction	Effectiveness for trace element fractionation
(I)	Fractional melting	∞	continuous	Most effective
(II)	Multiple-step melting (or Incremental melting)	N, real positive integer	discrete	Intermediate between (I) & (III)
(III)	Batch melting (or total equilibrium melting)	1	discrete	Most ineffective

Cases (I) and (III) can be considered as special cases of Case (II) where $N = \infty$ and $N = 1$, respectively.

The Case of Trapped Liquid

During partial melting it is unlikely that complete separation of melt from residual solid is always obtained. Liquid remaining with the residual solid is called "trapped

liquid." Trapped liquid can be present in the three cases listed before, and is assumed to be in equilibrium with the residual solid at all times in all models. The amount of trapped liquid is related to the "efficiency" of the extraction process*. If the process is efficient, only a small amount of the liquid is trapped. However, if the process is inefficient, a considerable amount of trapped liquid is expected.

How much liquid can be trapped in the upper mantle is poorly understood. Theoretical estimations are almost impossible, if not, highly variable, because such estimations depend on poorly known parameters, such as stress conditions, how liquid is aggregated, the shape and size of liquid aggregates, and the viscosity (therefore, the composition) of the liquid at the pertinent P-T conditions (C. Goetze, per. comm., 1977). No direct experiments on melt extraction have been done. However, melting experiments conducted under hydrostatic stress (Waff and Bulau, 1977; Waff and Holdren, 1977) show that the liquid is mainly located at triple grain boundaries with high degree of connectivity without isolated melt pockets, suggesting that the rate of fluid transport would be high. Boudier and Nicolas (1977) also carried out experimental melting of a Lanzo feldspar peridotite at 7 Kb, between 1150°C and 1600°C under uniaxial stress. They found

---

*Not to be confused with the "effectiveness" of the process, which describes trace element fractionation.

that for only small degrees of melting, batches of melt are connected by channels, abundant parallel to the principal stress axis. If such experimental observations are valid for the upper mantle conditions, the separation of the partial melt from the residual solid is expected to be highly efficient.

Experimental measurements of compressional wave velocity and electrical conductivity of peridotite samples as a function of the degree of melting carried out by Murase et al., (1977a, b), also support the above contention. Results indicate that v_p decreases rapidly with increasing melting; for example, for 10% melting v_p decreases by half to approximately 3.5 km/sec. Based on these data, Kushiro (per. comm., 1977) suggested that the low-velocity zone, which is believed to have resulted from partial melting of the upper mantle, corresponds to 1% of melting or less. Furthermore, preliminary modelling of results from electrical conductivity experiments indicates that the liquid must form inter-connected channels, in the shapes of columns or tubes, supporting Waff's findings.

Viscosity measurements of basaltic and andesitic magmas at high pressures (Kushiro et al., 1976) indicate decreasing viscosity with increasing pressure. This correlation probably results from Al coordination number changes (from 4 to 6) in the melt at high pressures (Kushiro, 1976). The viscosity reduction at high pressures, together with the compressional wave velocity and electrical conductivity measurements, strongly support the argument that the process

of magma separation is very efficient, and therefore, the trapped liquid in the upper mantle is less than 1%.

Summary

In short, there are two major factors which must be examined in developing realistic melting models:

(1) The continuity of the liquid extraction process; that is, how small are the discrete melting steps? As the melting increments decrease in size, trace element fractionation increases and the results are best approximated by a fractional melting model. This factor, the size of melting increments, is herein called "effectiveness."

(2) The ability of the process to extract liquid from the partially molten source rock. As the process increases in efficiency, less trapped liquid is left behind in equilibrium with the residual solid. This factor is herein called "efficiency."

Models with various combinations of effectiveness and efficiency will be discussed in the subsequent section.

III-2: MATHEMATICAL FORMULATION FOR TRACE ELEMENT FRACTIONATION DURING PARTIAL MELTING

In general, the efficiency of liquid extraction is believed to be high according to experimental data mentioned in the last section, but there is no direct indication of the effectiveness of the process. It is possible that effectiveness and efficiency are completely unrelated, but this is

unlikely. For example, consider a high efficiency but low effectiveness model, where partial melting equals 10%, but because of low effectiveness, the 10% liquid is in total equilibrium with the residual solid. Simultaneously, factors, such as stress conditions, size and shape of liquid aggregates, viscosity of the liquid, etc., allow a clean and efficient separation of solid and liquid leaving almost no trapped liquid behind after 10% partial melting. Unless the stress conditions, lithospheric pressure, temperature, etc. of the peridotite mass change drastically in one discrete step, this case seems unlikely. On the other hand, these controlling factors (stress, P, T, etc.) in a melting peridotite body are likely to change gradually, and therefore, a high efficiency case is expected to also have high effectiveness, while a low efficiency case probably corresponds with low effectiveness. Therefore, the extraction process is believed to be effective and efficient, that is, liquid is removed from the residual solid in small amounts soon after they are formed, and very little melt is left behind as trapped liquid.

In order to consider all possibilities, mathematical expressions for trace element fractionation are developed for the cases listed in Table III-1. Shaw (1970) has developed the equations for Case I and Case III. Extensions of these two cases to Case I' and Case III' to include the effect of

TABLE III-1

Increasing Effectiveness ←

Increasing Efficiency ↑

process	Fractional Melting	Multiple-Step (or Incremental) Melting	Batch (or Total Equilibrium) Melting
No. of steps	∞	N	1
trapped liquid=none	I (Shaw, 1970)	II This work.	III (Shaw, 1970)
trapped liquid = yes	I' This work.	II' This work.	III' This work.

trapped liquid* will be given in this work, following Shaw's approach, and using the same notations whenever possible. For the purpose of completeness, clarity, and continuity, Case I and Case III will be briefly reviewed. Case II and Case II' are considerably different, and therefore, will be treated last.

Case III: Batch Melting without Trapped Liquid

The following notations apply to all cases, unless redefined specially. Additional notations will be added whenever necessary:

x^i = initial mass fraction of phase i in the source.

p^i = melting proportion of phase i (i.e. fraction of the liquid that is formed by melting of phase i).

K^i = solid/liquid distribution coefficient for phase i.

D_o = bulk distribution coefficient, where

$$D_o = \Sigma x^i K^i$$

$P \equiv \Sigma p^i K^i$

D = bulk distribution coefficient at a certain instant during melting (for modal melting, $D = D_o$).

L = mass of liquid formed.

W_o = initial mass.

---

* The effect of trapped liquid during fractional crystallization has been examined quantitatively by Helmke et al. (1972) and Albarede (1976). This work only deals with the effect of trapped liquid during partial melting and employs a different approach.

F = degree of melting $\equiv L/W_o$

C_o = initial concentration of a trace element in the source.

C^S = concentration in the residual solid.

C^L = concentration in the liquid formed by batch melting.

(a) Modal Melting

In this case, $x^i = p^i$ for all phases, and therefore, the bulk distribution coefficient D is constant during the course of melting, i.e. $D = D_o$. At any instant, we can write

$$D = \frac{C^S}{C^L} \qquad (1)$$

Also, by mass balance:

$$C_o = F \cdot C^L + (1 - F) \cdot C^S \qquad (2)$$

Combining (1) and (2), eliminating C^S, we have:

$$C_o = F \cdot C^L + (1 - F) \cdot D \cdot C^L$$

$$= C^L (F + D - DF)$$

$$\therefore \quad \boxed{\frac{C^L}{C_o} = \frac{1}{D + F(1 - D)}} \qquad (3)$$

(Shaw's Eq. 11)

Similarly, combining (1) and (2), eliminating C^L, we have:

$$C_o = F \cdot \frac{C^S}{D} + (1 - F) C^S$$

$$= C^S \left(\frac{F}{D} + 1 - F \right)$$

$$\therefore \quad \boxed{\frac{C^S}{C_o} = \frac{D}{F + D(1 - F)}} \qquad (4)$$

(b) Non-modal Melting

In this case, D is a function of F. It can readily be shown that (See Appendix III-A):

$$D = \frac{D_o - PF}{1 - F} \qquad \text{Shaw's Eq. 12.}$$

Substituting this relationship into (3), we get:

$$\frac{C^L}{C_o} = \left(\frac{D_o - PF}{1 - F} + F - \frac{FD_o - PF^2}{1 - F} \right)^{-1}$$

$$= \frac{1 - F}{(D_o - PF - FD_o + PF^2 + F - F^2)}$$

$$\therefore \boxed{\frac{C^L}{C_o} = \frac{1}{D_o + F(1 - P)}} \qquad (5)$$

(Shaw's Eq. 15)

Substituting Shaw's Eq. 12 into (4):

$$\frac{C^S}{C_o} = \frac{D}{F + D(1-F)} = \frac{D_o - PF}{1 - F} \cdot \frac{1}{F + (D_o - PF)}$$

$$= \left(\frac{1}{1 - F} \right) \left(1 + \frac{F}{D_o - PF} \right)^{-1}$$

$$\therefore \boxed{\frac{C^S}{C_o} = \left[(1-F) \left(1 + \frac{F}{D_o - PF} \right) \right]^{-1}} \qquad (6)$$

Alternatively, as suggested by Hertogen and Gizbels (1976), using mass balance, as in Eq. (2):

$$C_o = F \cdot C^L + (1 - F) C^S$$

Dividing by C_o: $1 = F \cdot \frac{C^L}{C_o} + (1 - F) \frac{C^S}{C_o}$

$$\therefore \quad \boxed{\frac{C^S}{C_o} = \frac{1}{1 - F}\left(1 - \frac{C^L}{C_o} \cdot F\right)} \qquad (7)$$

Equation (7) is equivalent to Equation 20 of Hertogen and Gizbels (1976). It is easier to use once the value of C^L/C_o is evaluated with Equation (5).

Case III': Batch Melting, Incomplete Liquid Extraction

Only the more general case of non-modal melting is considered in the following.

Redefine: F = fraction of the initial mass that is extracted as liquid.

Define: f = fraction of the residue* which is trapped liquid.

Therefore, the "actual degree of melting," $F' \equiv F + f(1-F)$

$$= F + f - Ff.$$

C^{ST} = average concentration in the residue.

(See diagramatic representation in Figure III-1(a).)

---

* The term "residue" applies to whatever left behind after liquid extraction. If trapped liquid is present, then the residue is composed of residual solid plus trapped liquid.

FIGURE III-1: Diagramatic representations for melting models listed in Table III-1. Cross-hatched areas represent solid; blank areas represent liquid. Notations are defined in the text.

(a) Case III': Batch melting, incomplete liquid extraction.

(b) Case I': Fractional melting, incomplete liquid extraction.

(c) Case I': Same as (b), for non-modal melting.

(d) Case II: Multiple-step melting, without trapped liquid.

(e) Case II': Multiple-step melting, incomplete liquid extraction.

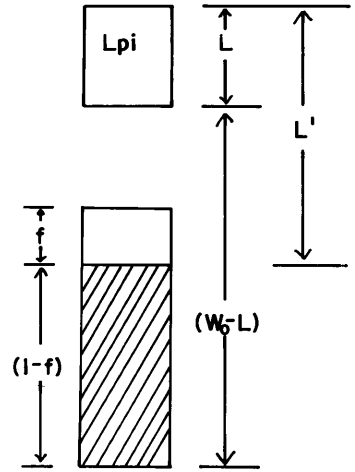
Lpi
L
L'
f
(1-f)
(Wo-L)

(c)

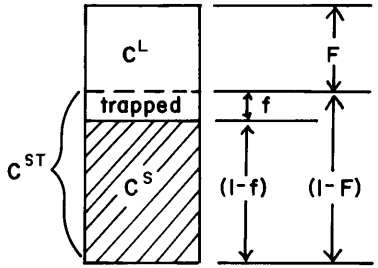
C^L
trapped
f
F
C^ST
C^S
(1-f)
(1-F)

(a)

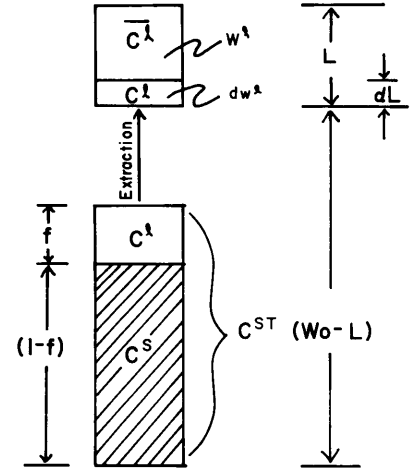
C̄^ℓ
w^ℓ
C^ℓ
dw^ℓ
Extraction
L
dL
f
C^ℓ
(1-f)
C^S
C^ST
(Wo-L)

(b)

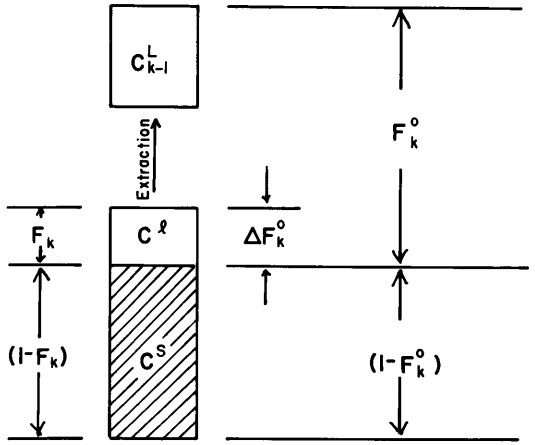
C^L_k-1
Extraction
F^o_k
F_k
C^ℓ
ΔF^o_k
(1-F_k)
C^S
(1-F^o_k)

(d)

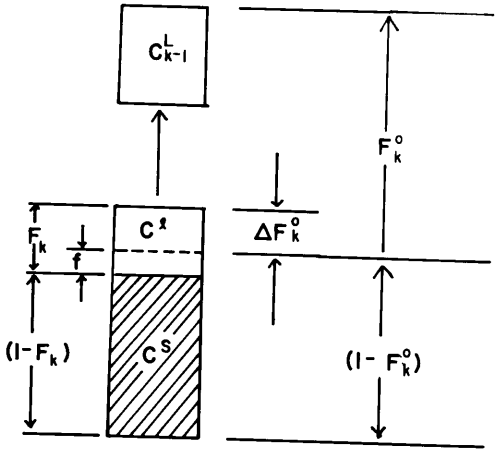
C^L_k-1
F^o_k
F_k
f
C^ℓ
ΔF^o_k
(1-F_k)
C^S
(1-F^o_k)

(e)

We can then directly substitute F' for F in equations (5) and (6):

$$\boxed{\frac{C^L}{C_o} = \frac{1}{D_o + F'(1 - P)}} \qquad (8)$$

$$\boxed{\frac{C^S}{C_o} = \left[(1 - F')\left(1 + \frac{F'}{D_o - PF'}\right)\right]^{-1}} \qquad (9)$$

Using mass-balance, as before,

$$C_o = (1 - F)C^{ST} + F \cdot C^L$$

$$\therefore \quad \boxed{\frac{C^{ST}}{C_o} = \frac{1}{1 - F}\left(1 - \frac{C^L}{C_o} \cdot F\right)} \qquad (10)$$

Equations (8), (9), and (10) are analogous to equations (5), (6), and (7). Notice when f = 0, F' = F. Therefore, Case III can be considered as a special case of Case III'.

Case I: Fractional Melting, without Trapped Liquid

Additional definitions:

w_o = mass of trace element in the initial solid.

w^1 = mass of trace element in the liquid.

$\bar{C}^1$ = average concentration of trace element in the total liquid extracted.

C^1 = concentration of trace element in the infinitesimal increment of liquid formed.

(a) Modal Melting

At any instant

$$C^l = \frac{1}{D_o} C^s \qquad (11)$$

C^l can also be expressed as $C^l = \frac{dw^l}{dL}$

and C^S as $C^s = \frac{W_o - w^l}{W_o - L}$

Substituting into (11), we have

$$\frac{dw^l}{dL} = \frac{1}{D_o} \left(\frac{W_o - w^l}{W_o - L} \right)$$

The solution for this first-order differential equation is

$$\ln(W_o - w^l) = \frac{1}{D_o} \ln(W_o - L) + C$$

where C is a constant.

Putting in the initial condition: L = 0, w^l = 0.

We have: $\ln(W_o - w^l) = \frac{1}{D_o} \ln(W_o - L) + \ln W_o - \frac{1}{D_o} \ln W_o$

This can be simplified and rearranged to get

$$\frac{w^l}{W_o} = 1 - \left(1 - \frac{L}{W_o}\right)^{1/D_o}$$

Differentiating, $$\frac{dW'}{dL} = W_o\left[\frac{1}{D_o}\left(1-\frac{L}{W_o}\right)^{\frac{1}{D_o}-1}\right]\left(\frac{1}{W_o}\right)$$

$$= \frac{W_o}{W_o}\cdot\frac{1}{D_o}\left(1-\frac{L}{W_o}\right)^{\frac{1}{D_o}-1}$$

$$\therefore \boxed{\frac{C'}{C_o} = \frac{1}{D_o}\left(1-F\right)^{\frac{1}{D_o}-1}} \qquad (12)$$

(Shaw's Eq. 8)

Equation (11) is true for all times,

$$\therefore \boxed{\frac{C^S}{C_o} = \left(1-F\right)^{\frac{1}{D_o}-1}} \qquad (13)$$

(Shaw's Eq. 9)

For the average concentration in the extracted liquid as a whole,

$$\frac{\bar{C}'}{C_o} = \frac{\frac{1}{D_o}\int_0^F (1-F)^{\frac{1}{D_o}-1}\cdot dF}{F}$$

$$\boxed{\frac{\bar{C}'}{C_o} = \frac{1-(1-F)^{\frac{1}{D_o}}}{F}} \qquad (14)$$

(Shaw's Eq. 10)

(b) Non-modal Melting

Shaw's (1970) equation 12 can be written as:

$$D = \frac{W_o D_o - LP}{W_o - L} \qquad (15)$$

Substituting (15) into (11), and following similar operations,

$$\frac{dW'}{dL} = \frac{W_o - W'}{W_o D_o - LP}$$

The solution to this equation is

$$\ln(W_o - W') = \frac{1}{P} \ln(W_o D_o - LP) + C$$

For initial condition: L = 0, w^1 = 0, we have

$$\ln\left(\frac{W_o - W'}{W_o}\right) = \frac{1}{P} \ln\left(\frac{W_o D_o - LP}{W_o D_o}\right)$$

or $$\frac{W_o - W'}{W_o} = \left(\frac{W_o D_o - LP}{W_o D_o}\right)^{\frac{1}{P}}$$

By differentiating, we obtain

$$\frac{dW'}{dL} = \frac{W_o}{W_o} \cdot \frac{1}{D_o} \left(1 - \frac{LP}{W_o D_o}\right)^{\frac{1}{P} - 1}$$

Then, the following equations can be obtained by the same operations as in the modal melting case:

$$\boxed{\frac{C'}{C_o} = \frac{1}{D_o} \left(1 - \frac{FP}{D_o}\right)^{\frac{1}{P} - 1}} \qquad (16)$$

(Shaw's Eq. 13)

$$\frac{C^S}{C_o} = \frac{1}{1-F}\left(1 - \frac{FP}{D_o}\right)^{\frac{1}{P}} \qquad (17)$$

(Shaw's Eq. 16)

$$\frac{\overline{C}^l}{C_o} = \frac{1}{F}\int_0^F \frac{C^l}{C_o}\cdot dF$$

$$\frac{\overline{C}^l}{C_o} = \frac{1}{F}\left[1 - \left(1 - \frac{FP}{D_o}\right)^{\frac{1}{P}}\right] \qquad (18)$$

(Shaw's Eq. 14)

Case I': Fractional Melting, Incomplete Liquid Extraction

Diagramatic representation is shown in Figure III-1(b).

Redefine:

L = mass of liquid extracted.

w^l = mass of trace element in the extracted liquid.

$\overline{C}^l$ = average overall concentration of trace element in the total extracted liquid.

C^l = concentration of trace element in the trapped liquid, which is in equilibrium with the solid.

(C^{ST}, F, and f are the same as in Case III'.)

Note that f is assumed to be constant for all values of F. The reason will be discussed in the next section.

(a) Modal Melting

$D = D_o$ = constant

Model calls for f = constant (see next sub-section).

At any instant $C^l = \frac{1}{D} C^s$,

also, $C^l = \frac{dw^l}{dL}$, so $C^s = D \cdot \frac{dw^l}{dL}$ ——— (19)

For mass balance: $C^{ST} = f \cdot C^l + (1-f) C^s$ ——— (20)

and C^{ST} can also be expressed as

$$C^{ST} = \frac{W_o - w^l}{W_o - L} \quad \text{——— (21)}$$

Substituting (21) and (19) into (20), we, therefore, have:

$$\frac{W_o - w^l}{W_o - L} = f \cdot \left(\frac{dw^l}{dL}\right) + D(1-f)\left(\frac{dw^l}{dL}\right)$$

The solution to this differential equation is

$$(D - Df + f) \cdot \ln(W_o - w^l) = \ln(W_o - L) + C$$

For initial condition: L = 0, w^l = 0. We get

$$\ln\left(\frac{W_o - w^l}{W_o}\right) = \frac{1}{D - Df + f} \ln\left(\frac{W_o - L}{W_o}\right) \quad \text{— (22)}$$

For modal melting, $D = D_o$ = constant, therefore, we can introduce the identity of "Effective bulk distribution coefficient," $\boxed{D' \equiv D_o - D_o f + f,}$ which, in fact, is $D' = D_o(1 - f) + f(1)$, a direct linear combination of the "original" D_o plus a "new phase" (the trapped liquid) which has a bulk distribution coefficient equal unity.

Therefore, replacing (D - Df + f) with D' in equation (22), simplify and rearrange, we get

$$\frac{W'}{W_o} = 1 - \left(1 - \frac{L}{W_o}\right)^{\frac{1}{D'}}$$

which is completely analogous to Case I(a) (P. 99), and, therefore, analogous equations can be obtained with D' replacing D_o:

$$\boxed{\frac{C'}{C_o} = \frac{1}{D'}(1 - F)^{\frac{1}{D'} - 1}} \qquad (23)$$

$$\boxed{\frac{\bar{C}'}{C_o} = \frac{1 - (1 - F)^{\frac{1}{D'}}}{F}} \qquad (24)$$

Because $\frac{C^S}{C_o} = D \cdot \frac{C'}{C_o}$ at all times

$$\boxed{\frac{C^S}{C_o} = \frac{D_o}{D'}(1 - F)^{\frac{1}{D'} - 1}} \qquad (25)$$

From equation (20), $C^{ST} = f \cdot C^{l} + (1-f) C^{S}$

Substituting in with equations (23) and (25):

$$\boxed{\frac{C^{ST}}{C_o} = (1-F)^{\frac{1}{D'}-1}} \qquad (26)$$

Alternatively, using initial mass balance,

$$C_o = F \cdot \bar{C}^{l} + (1-F) \cdot C^{ST}$$

$$\therefore \boxed{\frac{C^{ST}}{C_o} = \frac{1}{1-F}\left(1 - \frac{\bar{C}^{l}}{C_o} \cdot F\right)} \qquad (27)$$

Notice that equations (23), (24), (26), and (27) are analogous to (12), (14), (13), and (10), respectively. If there is not trapped liquid, that is, f = 0, then D' = D = D_o, and equations (23) and (24) will be identical to equation (12) and (14). Also, equation (25) will become equation (26) which will then be identical to equation (13).

(b) Non-modal Melting:

This case is more complicated. It is schematically illustrated in Figure III-1(c). All notations used are as in the case of modal melting.

f = constant

p^i and P are constants

$D \neq D_o$, but is a function of L or F.

We can then express D as

$$D = \sum_i \left(K^i \cdot \frac{W_o x^i - L p^i - f(W_o - L)\, p^i}{(W_o - L)(1-f)} \right)$$

$$= \frac{W_o \sum K^i x^i - \sum K^i p^i \left(L + f(W_o - L) \right)}{(W_o - L)(1-f)}$$

$$= \frac{W_o D_o - P\left[L + f(W_o - L) \right]}{(W_o - L)(1-f)}$$

$$\therefore D = \frac{W_o D_o - P\left[L + f(W_o - L) \right]}{W - \left[L + f(W_o - L) \right]}$$

If we define

$$\boxed{L' \equiv L + f(W_o - L)} \quad ,$$

then, we have

$$\boxed{D = \frac{W_o D_o - P L'}{W_o - L'}} \qquad \text{(28)}$$

Note that equation (28) is analogous to Shaw's (1970) equation (12). Therefore, we can follow the similar procedure, using the two basic relationships

$$\begin{cases} C^I = \frac{1}{D} C^S \\ C^{ST} = f \cdot C^I + (1-f) C^S \end{cases}$$

An analogous differential equation as in Case I can be obtained. Using initial condition L = 0, w^1 = 0, the solution of this familar first order differential equation is

$$\ln\left(\frac{W_o - W'}{W_o}\right) = \frac{1}{f+P-Pf} \cdot \ln\left[\frac{fW_o - fL + W_o D_o - PL - PfW_o + PfL}{fW_o + W_o D_o - PfW_o}\right]$$

We can now abandon L' and define

$$\boxed{\begin{aligned} P' &\equiv P(1-f) + f(1) \\ &= P - Pf + f \end{aligned}}$$

Rewriting the solution:

$$\ln\left(\frac{W_o - W'}{W_o}\right) = \frac{1}{P'} \ln\left[\frac{(W_o D_o + fW_o - PfW_o) - LP'}{W_o(f + D_o - Pf)}\right]$$

We can further define

$$\boxed{D_o' \equiv D_o + f(1-P)}$$

We now have,

$$\ln\left(\frac{W_o - W'}{W_o}\right) = \frac{1}{P'} \ln\left[\frac{W_o D_o' - LP'}{W_o D_o'}\right]$$

$$\therefore \quad \left(\frac{W_o - W'}{W_o}\right) = \left[\frac{W_o D_o' - LP'}{W_o D_o'}\right]^{\frac{1}{P'}}$$

Once again, we have exactly analogous equation as in Case I(b), with D_o' replacing D_o, P' replacing P.

We can then write:

$$\frac{C'}{C_o} = \frac{1}{D_o'}\left(1 - \frac{F P'}{D_o'}\right)^{\frac{1}{P'}-1} \qquad (29)$$

which is analogous to equation (16).

And from $\frac{\bar{C}'}{C_o} = \frac{1}{F}\int_0^F \frac{C'}{C_o}\cdot dF$

$$\frac{\bar{C}'}{C_o} = \frac{1}{F}\left[1 - \left(1 - \frac{F P'}{D_o'}\right)^{\frac{1}{P'}}\right] \qquad (30)$$

which is analogous to equation (18),

and $$\frac{C^S}{C_o} = D\cdot\frac{C'}{C_o} = \frac{D}{D_o'}\left(1 - \frac{F P'}{D_o'}\right)^{\frac{1}{P'}-1} \qquad (31)$$

Also,

$$\frac{C^{ST}}{C_o} = \frac{1}{1-F}\left(1 - \frac{\bar{C}'}{C_o}\cdot F\right) \qquad (27)$$

which is equation (27), and it can be applied here. Or, C^{ST} can also be expressed as

$$\frac{C^{ST}}{C_o} = f\cdot\frac{C'}{C_o} + (1-f)\frac{C^S}{C_o}$$

$$\therefore \quad \boxed{\frac{C^{ST}}{C_o} = \frac{D - Df + f}{D'_o}\left(1 - \frac{F P'}{D'_o}\right)^{\frac{1}{P'}-1}} \qquad (32)$$

The value of D in equations (31) and (32) can be obtained by using equation (28), but it is more desirable to express D in terms of the degree of melting or the fraction of extraction, instead of masses as in equation (28). A more convenient way for computation is to express D as

$$D = \frac{W_o D_o - P[L + f(W_o - L)]}{(W_o - L)(1 - f)} \qquad (P.\ 106)$$

which can be simplified, using the relation $F = L/W_o$, down to:

$$D = \frac{D_o - P(F + f - Ff)}{1 - (F + f - Ff)}$$

Using the familar form of substitution, let

$$\boxed{F' \equiv F(1 - f) + f(1)}$$

We have:

$$\boxed{D = \frac{D - PF'}{1 - F'}}$$

This expression is then analogous to Shaw's equation 12.

Multiple-Step Melting: General Considerations

In the formulations of the previous cases, two important points have been implicitly assumed: (1) the proportion of minerals contributing to the melt is a constant, and (2) the amount of trapped liquid is a constant fraction of the residue.

Compositional variations of liquid and residual solid during partial fusion have been analyzed by Presnall (1969) in terms of phase diagrams. The first assumption (i.e., p^i = constant) is correct, if the initial liquid generated is at an invariant (or eutectic) point. In the melting of garnet lherzolite, a total of 5 coexisting phases: 4 solid phases (cpx + opx + ol + gn) plus the liquid phase, can be approximated by the 4-component system (CaO-MgO-Al_2O_3-SiO_2). According to the phase rule, the liquid composition is at an invariant point in the compositional space at constant P. The composition of this liquid remains at the same composition until one phase is consumed. Therefore, in dealing with the first interval of melting, that is, before any of the solid phases is exhausted, the melting proportions should remain constant. The situation is similar for spinel lherzolite, except that spinel replaces garnet as a solid phase.

However, for the second interval of melting, there are two possibilities: (1) batch melting; (2) fractional melting. In batch melting, the liquid leaves the invariant point as soon as one of the solid phases is consumed, and the liquid

composition varies continuously along a univariant line (cotectic) line at constant P. Therefore, say at constant P, the liquid composition varies with temperature, hence, the degree of melting. This variation in liquid composition, also the melting proportions, depends on the position and orientation of the cotectic line with respect to the compositions of the remaining phases. This effect cannot be generalized. In fractional melting, the liquid composition, instead of varying along the univariant line, jumps to another invariant point in the plane which contains the compositions of the three remaining solid phases. So in this case, the trend of liquid composition is discontinuous, and the melting proportions for the second melting interval are constant until a second solid phase is exhausted. For a natural garnet lherzolite, there are other minor components other than CaO-MgO-Al_2O_3-SiO_2, so deviations from ideality are expected. Nevertheless, these deviations may be small, since melting experiments by Mysen and Kushiro (1976) showed that natural peridotites behave similarly to simple model systems when they melt.

The second assumption concerning the proportion of trapped liquid is more uncertain; however, deviations from my assumption are not expected to be significant for trace element fractionation models. The amount of trapped liquid is controlled by the physical factors, e.g. stress condition, P, T, and liquid viscosity, etc., and for a limited degree of

melting, say, the first 10 to 15%, these controlling factors are not likely to change drastically. Therefore, under similar physical conditions, the proportion of trapped melt to residual solid is expected to be fairly constant. Of course, as the degree of melting increases, for example, 70 to 80%, this argument is not valid, but such extensive melting is not of the concern in this work. Because I assume that the amount of trapped melt is a constant proportion of the residue, the absolute amount of trapped liquid decreases as the degree of melting increases. This model is more realistic than a model which calls for a constant amount of trapped liquid at all degrees of melting. In the latter case, the proportion of trapped liquid to residual solid increases steadily as melting proceeds. Ironically, for a small degree of melting, the two approaches have similar effects on trace element fractionation. In fact, the major difference is only in the mathematical manipulations.

Gast (1968) developed mathematical expressions for an incremental melting model, which was used to model the generation of various basalt types by melting of the upper mantle. Smewing and Potts (1976) used this concept to explain the REE concentrations in the basaltic rocks from the Troodos massif. Their model is similar to Shaw's (1970) batch-melting model, but the process was repeated for a second step. The models given in this work are based on the batch-melting expressions presented previously, but the

process can be repeated for N steps*. If N is large, the amount of liquid extracted in each step is small, while if N is small, the amount is large for the same degree of melting or extraction. If N equals one, this special case is batch melting.

The amount of liquid extracted in each step is controlled by the same parameters that control the quantity of trapped liquid. Gast (1968) assumed a constant amount of liquid extracted in each step, that is, the mass of liquid removed in each increment remains the same during melting. Obviously the advantage of this approach is the mathematical simplicity. However, physically, Gast's model is not realistic. As for the case of trapped liquid discussed before, physical considerations support a model with a decreasing absolute amount of liquid extracted in each step as the degree of melting increases. In this model, only a constant proportion of liquid with respect to the residue is removed. Consequently, it is increasingly difficult to remove liquid from the residue as melting proceeds, or in the case of a constant heat supply or adiabatic decompression, the melting steps become smaller and smaller, but are repeated faster and faster.

As with the trapped liquid models, these considerations only make a difference in mathematical handling, and for small degrees of melting, they do not have any major effects

---

* N is any real positive integer.

on trace element fractionation. However, for the purpose of accuracy, the more realistic models are given in this work. Extensions of the multiple-step melting model to include the effect of trapped melt are also presented.

Case II: Multiple-step Melting, without Trapped Liquid

Figure III-1(d) gives a diagramatic representation of this case for easy visualization. Note that additional notations are required:

(1) A superscript ° indicates that the fraction symbol in question applies to a mass fraction with respect to the initial mass before any melting occurs. Therefore, a fraction symbol without this superscript applies only to a mass fraction with respect to the residue mass; that is, the total mass remaining after a particular step.

(2) A subscript k, or any integer (0, 1, 2, 3, . .) designates the symbol corresponding to the value in a specific step. To facilitate mathematical manipulation and machine computation, subscript (n-1) corresponds to the $n^{\underline{th}}$ step. For example, for 1st step, k = 0

2nd step, k = 1

.
.
.

n^{th} step, k = n-1

The above conventions apply to Case II and Case II'. As before, C^S is the solid concentration; C^l, the incremental liquid concentration; C_o, initial concentration; and K^i, p^i,

x^i definitions remain the same. Also, note the slight variations in the following definitions:

C^L = average concentration of a trace element in the total liquid extracted. (This is similar to $\bar{C}^l$ of Case I and Case I'. $\bar{C}^l$ is not used because the liquid in multiple-step melting is a weighted average of discrete batches as in patch melting, not an integral average of C^l as in fractional melting.)

F_k° = total mass fraction of liquid formed, with respect to the initial mass.

F_k = mass fraction of liquid formed in the particular step as indicated by subscript k, with respect to the mass of the residue.

The simplest way to approach the problem is to treat every step discretely as in cases of batch melting (Case III). After melt removal, the residue is considered as a new system which can be treated as before, except that the absolute values of the input parameters must vary according to the model. For example,

STEP 1: $k = 0$

Equations (5), (6), and (7) for batch melting (Case III) are valid. We have:

$$\left.\begin{aligned} \frac{C^l}{C_o} &= \frac{1}{D_o + F(1-P)} \\ \frac{C^s}{C_o} &= \frac{1}{1-F}\left(1 - \frac{C^l}{C_o}\cdot F\right) \end{aligned}\right\} \quad (33a,b)$$

where $F = F_o$.

STEP 2: $k = 1$

The following apply:

(a) Distribution coefficients, K^i, assumed constant;

(b) Melting proportions, p^i, remain the same for reasons previously discussed; therefore, P = constant.

(c) $F_1 = F_o$ = constant (requirement for the model as discussed in the last subsection).

(d) $C_{o_1} = C_o^S$

(e) $$x_1^i = \frac{x_o^i - F_o \cdot p_o^i}{\sum_i (x_o^i - F_o p_o^i)} = \frac{x_o^i - F_o p_o^i}{1 - F_o}$$

(f) Total $$F_1^o = F_o^o + F_o(1 - F_o^o)$$
$$= F_o + (F_o - F_o^2)$$

Then, equations (33a,b) become

$$\left.\begin{aligned} \frac{C_1^l}{C_{o_1}} &= \frac{1}{D_{o_1} + F_1(1-P)} \\ \frac{C_1^S}{C_{o_1}} &= \frac{1}{1-F_1}\left(1 - \frac{C_1^l}{C_{o_1}} \cdot F_1\right) \end{aligned}\right\} \quad (34a,b)$$

where F_1 can be replaced by F_o.

In general, similarly,

STEP (k+1): $k = k$;

$F_k = F_o$;

$C_{o_k} = C_{k-1}^S$;

and

$$X_k^i = \frac{X_{k-1}^i - F_{k-1} p_{k-1}^i}{1 - F_{k-1}}$$

where $p_k^i = p_o^i$; $F_k = F_o$.

It can also be shown that

$$\text{total } F_k^o = \sum_{m=0}^{m=k} \sum_{j=0}^{j=m} (-1)^j \binom{m}{j} (F_o)^{j+1} \tag{35}$$

and the increment for this step

$$\Delta F_k^o = \sum_{j=0}^{j=k} (-1)^j \binom{k}{j} (F_o)^{j+1} \tag{36}$$

where $\binom{k}{j}$ are binominal coefficients. The derivation of equations (35) and (36) is given in Appendix III-B. These two equations can be used for machine computation, but become more troublesome when k gets large. Appendix III-B also gives two equivalent expressions which are slightly simpler and easier to handle:

$$\boxed{\Delta F_k^o = F_o (1 - F_o)^k} \tag{37}$$

$$\therefore \boxed{F_k^o = \sum_{m=0}^{k} F_o (1 - F_o)^m = 1 - (1 - F_o)^{k+1}} \tag{38}$$

Having formulated F_k^o and ΔF_k^o, we now can write

$$\boxed{C_k^L = \frac{1}{F_k^o}\sum_{m=0}^{k} C_m^l \Delta F_m^o = \frac{1}{F_k^o}\left(C_{k-1}^L \cdot F_{k-1}^o + C_k^l \cdot \Delta F_k^o\right)} \qquad (39)$$

Equation (39) can be evaluated by machine computation step by step. The next step is to investigate how C_k^S and C_k^l vary with k, since C_{o_k} and x_k^i are changing in every step.

$p_k^i = p_o^i$ = constant, so that P = constant for all steps.

$$x_k^i = \frac{x_{k-1}^i - F_o p_o^i}{1 - F_o}$$

$$= A\left[A(x_{k-2}^i - F_o p_o^i) - F_o p_o^i\right] \qquad \left(\text{where } A \equiv \frac{1}{1-F_o}\right)$$

$$= A^2 x_{k-2}^i - A^2 F_o p_o^i - A F_o p_o^i$$

$$= A^3 x_{k-3}^i - A^3 F_o p_o^i - A^2 F_o p_o^i - A F_o p_o^i$$

$$\vdots$$

$$= A^k x_o^i - A F_o p_o^i \sum^{k-1} A^m$$

$$= A^k x_o^i - \frac{A F_o p_o^i (1 - A^k)}{1 - A}$$

$$\therefore \boxed{x_k^i = A^k x_o^i + p_o^i - A^k p_o^i} \qquad (40)$$

where $A = \frac{1}{1-F_o}$

$$\therefore D_{o_k} = \sum_i x_k^i \cdot K^i$$

$$= \sum_i A^k \cdot x^i \cdot K^i + \sum_i p^i K^i - \sum_i A^k \cdot p^i \cdot K^i$$

$$= A^k (D_{o_o} - P) + P$$

$$\boxed{D_{o_k} = \left(\frac{1}{1-F}\right)^k (D_{o_o} - P) + P} \qquad (41)$$

Similarly, we can write equations (34a,b) in a more general form:

$$\frac{C_k^l}{C_{o_k}} = \frac{1}{D_{o_k} + F_k(1-P)}$$

$$\boxed{\frac{C_k^l}{C_{o_k}} = \frac{1}{\left(\frac{1}{1-F_o}\right)^k (D_{o_o} - P) + P + F_o(1-P)}} \quad \text{——— (42)}$$

and

$$\boxed{\frac{C_k^s}{C_{o_k}} = \frac{1}{1-F_o}\left(1 - \frac{C_k^l}{C_{o_k}} \cdot F_o\right)} \quad \text{——————— (43)}$$

Or, alternatively, using the form of equation (6),

$$\frac{C_k^s}{C_{o_k}} = \left[(1-F_o)\left(1 + \frac{F_o}{D_{o_k} - PF_o}\right)\right]^{-1}$$

$$\boxed{\frac{C_k^s}{C_{o_k}} = \left[(1-F_o)\left(1 + \frac{F_o}{\left(\frac{1}{1-F_o}\right)^k (D_{o_o} - P) + P(1-F_o)}\right)\right]^{-1}} \quad (44)$$

Equations (42), (43), and (44) express the concentrations in terms of initial parameters, provided that C_{o_k} is known. The simplest way to obtain C_{o_k} is by step-wise process using machine computation as follows:

$$C_o^s = C_{o_o} \times \left(\frac{C_o^s}{C_{o_o}}\right)$$

$$C_1^S = C_{o_1} \times \left(\frac{C_1^S}{C_{o_1}}\right), \qquad \text{where } C_{o_1} = C_o^S$$

$$= C_{o_o} \times \left(\frac{C_o^S}{C_{o_o}}\right) \times \left(\frac{C_1^S}{C_{o_1}}\right)$$

$$\therefore \quad \boxed{C_k^S = C_{o_o} \prod_{m=0}^{k} \left(\frac{C_m^S}{C_{o_m}}\right) = C_{o_{k+1}}} \qquad (45)$$

which can be used in conjunction with equations (42), (43), and (44).

Case II': Multiple-step Melting, Incomplete Liquid Extraction

Trapped liquid is introduced in this case; that is, after each melting step, only part of the liquid is extracted, and trapped liquid is left behind in equilibrium with the residual solid. This trapped liquid is mixed with the new batch of liquid produced in the next step of melting. The liquid mixture is always in total equilibrium with the solid, but only a constant proportion is extracted. Except for the additional complexity of trapped liquid, Case II' is identical to Case II.

Several notations need to be clarified (see Figure III-1 (e)):

(1) Since there is trapped liquid, F_k^o in this case does not include the trapped melt, so that,

F_k^o = total mass fraction of liquid extracted, with respect

to the initial mass, up to and including the $(k+1)^{th}$ step.

On the contrary, F_k includes the trapped liquid and, therefore,

F_k = mass fraction of liquid coexisting and in equilibrium with the solid in the residue of the $(k+1)^{th}$ step, just before any liquid is extracted.

(2) f_k is the mass fraction of the trapped liquid with respect to the mass of the residue left behind by the previous step, (k^{th} step).

(3) The term residue applies, as before, to solid plus trapped melt, after liquid extraction.

Figure III-1(e) gives a diagramatic representation of this model. The assumptions for this model are the same as in previous models. That is, F_k and f_k remain constant throughout, but F_k^o and f_k^o decrease with the increase of melting, so that

$$F_k^o = 1 - (1 - F_o + f_o)^{k+1} \qquad (46)$$

and

$$\Delta F_k^o = (F_o - f_o)(1 - F_o + f_o)^k \qquad (47)$$

These two expressions are derived in Appendix III-C. Notice that equations (46) and (47) are identical to equations (37) and (38) for Case II when f_o goes to zero. In fact, Case II can be regarded as a special case of Case II' where $f_o = 0$, i.e. no trapped liquid.

Similar to Case II, having obtained F_k^o and ΔF_k^o, we can use equation (39) which is also fine for this case,

$$C_k^L = \frac{1}{F_k^o}\left(C_{k-1}^L \cdot F_{k-1}^o + C_k^l \cdot \Delta F_k^o\right) \qquad (39)$$

In order to obtain C_k^S and C_k^l, x_k^i has to be expressed in terms of the initial parameters as in Case II, equation (40). Similar to II, we can write

$$x_k^i = \frac{1}{1 - F_o + f_o}\left[x_{k-1}^i - p_o^i\left(F_o - f_o\right)\right]$$

Notice that this expression is exactly in the same form as in Case II (Page 118) with $(F_o - f_o)$ replacing F_o. Therefore, we can write analogous equations to equations (40) and (41) of II:

$$x_k^i = B^k x_o^i + p_o^i - B^k p_o^i \qquad (48)$$

where $B = \frac{1}{1 - F_o + f_o}$

and

$$D_{o_k} = \left(\frac{1}{1-F_o+f_o}\right)^k (D_{o_o} - P) + P \qquad (49)$$

Similarly,

$$\frac{C_k^l}{C_{o_k}} = \left[\left(\frac{1}{1-F_o+f_o}\right)^k (D_{o_o} - P) + P + F_o(1-P)\right]^{-1} \qquad (50)$$

$$\frac{C_k^s}{C_{o_k}} = \left[(1-F_o)\left(1 + \frac{F_o}{(1-F_o+f_o)^{-k}(D_{o_o}-P)+P(1-F_o)}\right)\right]^{-1} \qquad (51)$$

Equations (50) and (51) are analogous with equations (42) and (44), respectively. Since trapped liquid is present in this case, the concentration of a trace element in the residual solid, C_k^s has to be distinguished from the average concentration in the residue, C_k^{ST}, which includes the trapped liquid. By mass balance,

$$\frac{C_k^{ST}}{C_{o_k}} = \frac{1}{1-F_o+f_o}\left(1 - (F_o - f_o)\cdot\frac{C_k^l}{C_{o_k}}\right) \qquad (52)$$

which is analogous to equation (43).

Alternatively, using C_k^l and C_k^S

$$C_k^{ST} = \frac{f_o \cdot C_k^l + (1 - F_o) \cdot C_k^S}{1 - F_o + f_o} \qquad (53)$$

In this case, the residue concentration, not the solid concentration, is taken to be the initial concentration for the next step. Therefore,

$$C_k^{ST} = C_{o_o} \prod_{m=0}^{k} \left(\frac{C_m^{ST}}{C_{o_m}} \right) = C_{o_{k+1}} \qquad (54)$$

All expressions for this case become identical to those for Case II, when $f_o \to 0$.

Summary and Computation Procedures

Mathematical expressions for several cases of liquid extraction from a partially molten aggregate of rock have been developed. Shaw's (1970) equations for fractional melting and batch melting have been extended to include the possibility of trapped liquid. For the intermediate case of multiple-step melting (or, incremental melting), equations are developed to cover cases with or without trapped liquid. Since the process in this model is in discrete steps, concentrations and other parameters, such as bulk distribution

coefficient, do not vary as continuous functions, but vary as step-functions with the degree of melting. Therefore, machine computation is required as the number of steps increases, and, in addition, error propagations must not be overlooked.

In all models, batch, fractional, or multiple-step melting, the cases with trapped melt are the general cases. The cases without trapped melt are only special cases where f = 0. Therefore, after the extension to the general cases, Cases I, II, and III in Table 1 can be abandoned for practical purposes. Only the equations in Cases I', II', and III' should be used in modelling trace-element fractionation. Two Fortran IV programs have been written to handle the computation*. The first program is for multiple-step melting. The necessary input parameters for this program are:

(1) number and names of the solid phases involved.

(2) initial proportions (x^i) and melting proportions (p^i) for each phase.

(3) number and names of the elements.

(4) solid/liquid distribution coefficients (K^i) of each element for each phase.

(5) initial concentrations of the elements (C_o) in the

---

* Copies of these programs can be obtained from the author upon request. (1) MUSTMELT - for multiple-step melting, and (2) FRACBATM - for fractional and batch meltings.

source rock.

(6) percent (or mass fraction) of melting in each step (F_o), which is constant for all steps.

(7) percent (or mass fraction) of the remaining residue which is trapped liquid (f_o), which is also constant during the course of melting.

(8) the number of steps the computer should do.

Items (1), (2), and (8) are for the computer program only. They are not input data for solving the equations. All real variables and computations are done in double precision, so that error accumulation due to a large number of steps can be neglected.

The second program is written for fractional melting and batch melting. The major difference between these models and the multiple-step melting model is that in the latter case, the concentrations are step-functions. Once the size of the steps is fixed, the program will calculate the concentrations at the end of each step. But in this case of batch and fractional melting, the concentrations are continuous functions with respect to the percent of melting (or extraction). Concentrations can be calculated at any point, or at any given interval desired. Hence, the input parameters for the second program are basically the same from items (1) to (5), but instead of specifying the size of each step and the number of steps to be performed, the interval at which concentrations are to be computed is

specified, together with the termination point for the program. Also note that the percent of trapped melt (f) has a slightly different meaning from the f_o for step-melting as pointed out before (page 121).

The different effects of these models on trace-element fractionation during melting will be discussed in a later section. First, several constraints must be given in order to limit the model parameters to a reasonable range:

(1) As has been discussed, the efficiency and the effectiveness of liquid extraction in the upper mantle are believed to be positively related, and to be high.

(2) The distribution coefficients are limited to the range given in Appendix II-F.

(3) The total degree of melting is small, so that the melting proportions (p^i) are fairly constant during the interval of melting.

(4) A very important constraint is the assumption that the diffusion of the trace elements under consideration in the solid phases is fast relative to liquid extraction, so that equilibrium conditions are maintained at all times.

The last assumption is generally made by trace-element geochemists when modelling partial melting processes, partly because of the absence of strong evidence indicating disequilibrium conditions during melting, although isotopic disequilibrium has been suggested by several workers (Gast et al., 1964; Petermen et al., 1970; Harris et al., 1972;

O'Nions and Pankhurst, 1974) based on isotopic data. It is also partly because data on diffusion are scarce, and the physical melting process is poorly understood. Utilizing recent research on diffusion in silicate minerals and melts, estimates of the applicability of equilibrium melting are feasible. Hofmann and Hart (1978) argue that equilibrium conditions can be attained in a partially molten mantle locally (mineralogical scale) but inhomogeneities may exist in a large scale (Km scale). They base their argument on melting experiments and application of diffusion data.

A similar evaluation of equilibrium melting can be made with respect to REE. No REE diffusion data for mantle minerals at high temperatures are available, but Magaritz and Hofmann (1977) have measured the diffusivity of Eu and Gd in basalt and obsidian glass. Using their empirical equation, La^{3+} and Lu^{3+} are found to have diffusion coefficients (D) equal to 1.0×10^{-7} and 1.4×10^{-7} cm^2sec^{-1}, respectively, at 1300°C, within a factor of 2 to 3 from those of Sr^{2+} and Ca^{2+} (Hofmann, 1975). Above 1500°C, the estimated melting temperature of the Ronda diapir (Chapter II), these diffusion coefficients should be one order of magnitude higher. Judging from diffusion data of other elements such as Sr^{2+} and Ca^{2+} (as summarized by Hofmann and Hart, 1978, Figure 3), a lower limit of $D = 10^{-12}$ cm^2sec^{-1} for temperatures >1500°C may be taken. Assuming that the grain size is 1 cm or less, equilibrium between mineral grains and the surrounding melt can be reached in the order of 8,000 years (using the approximation

$x = \sqrt{Dt}$). Taking 10 cm $year^{-1}$ as the upper limit for ascent of a diapir at a spreading center, the entire melting episode, as estimated from the last chapter (see Figure II-12), occurs in $\sim 4 \times 10^5$ years. Assuming that the extraction process is efficient, so that the liquid is removed in 1% increments, and the total degree of melting is 15-20% as indicated by the REE data, then the residence time for each increment of liquid is in the order of 2×10^4 years, a time sufficient for the equilibrium of REE between melt and mineral grains. Of course, this estimation is for a limiting case. For a slower rising rate of the diapir, and higher diffusion coefficients, equilibrium melting is certain to be attained.

III-3: PETROLOGIC CONSIDERATIONS

In the last chapter, fractionation of REE during melting of a mantle peridotite was treated with simple models of fractional and batch melting. The last section in this chapter gives a more detailed, realistic treatment including the possibility of trapped liquid and models between the two extreme cases of fractional and batch melting. In order to form a more realistic and accurate model, petrologic parameters, such as p^i and x^i, which are needed as input data, must be investigated in more detail. In this section, the petrology of peridotite melting is examined.

The physical conditions (P, T, mineralogy, etc.) for peridotite melting are deduced from the preliminary model

given in the last chapter. Therefore, the first modelling attempt can be considered as a first approximation. The approach used here is similar to an iterative method which converges to a solution. In short, the information deduced from the first modelling attempt will be used to construct the more detailed second model. The results of the second model should be self-consistent with the inputs. If not, it means that the solution is not converging, and a new model with new initial parameters should be tried until a self-consistent model is obtained.

Mineralogy, P-T Condition, and Related Information

The following information obtained from the preliminary model in Chapter II will be utilized.

(1) The Ronda lherzolites are residues after small degrees of melting from an "undepleted" mantle source. This source composition is believed to be very close to that of spinel lherzolite, R717 (Tables II-2, II-3, No. 6).

(2) The P-T trajectory (-ies) of the mantle diapir must hit the undepleted peridotite solidus at a position where garnet is present (see Figure II-12), but, probably, close to the boundary beyond which garnet dissolves in pyroxenes (i.e. boundary between PX and GL fields in Figure II-12). This is because garnet must exist in only small amounts ($\sim$ 10%) if it is to be exhausted by small degrees of melting as deduced by the model given in Chapter II. Furthermore, the lower the pressure at which the

peridotites melt on the solidus, the shorter the adiabatic path would be from the geotherm to the solidus. Because the solidus and the boundary which marks the appearance and disappearance of garnet depend on the composition of the peridotite, there is uncertainty about the P and T at the beginning of melting. However, Figure II-12 is based on Pyrolite III (Green and Ringwood, 1967), and the composition of spinel lherzolite R717 is close to that of Pyrolite III (Table II-2(b)); therefore, an estimate of pressure at ∿35 Kb and temperature at ∿1600°C is believed to be realistic with respect to trace element modelling.

(3) The starting source material has a REE composition close to 2 times chondritic averages.

With the above information, the following parameters must be estimated: (1) mineral proportions in the source rock; (2) the composition of the liquid; and (3) the melting proportions of the mineral phases.

Phase Proportions of the Source Rock

The phase proportions of the source rock depend on composition as well as P-T conditions. The source composition can be approximated by spinel lherzolite R717. At the estimated P-T condition (∿35 Kb, ∿1600°C), this peridotite would be a garnet lherzolite with 4 solid phases: clinopyroxene + orthopyroxene + olivine + garnet. To estimate their proportions, the mantle norm calculation procedure

(Appendix II-H) is used. This method forms molecular components from the chemical composition and distributes them into only three components, i.e. cpx, opx, and ol. Results of such calculations have already been shown in Figure II-11. This triangular plot indicates the compositions of the rocks in terms of end-member components of cpx, opx, and ol. Because the pyroxenes form solid solutions, the actual mineral proportions have to be redistributed in terms of the compositions of cpx_{SS}, opx_{SS}, and ol. The compositions of cpx_{SS} and opx_{SS} can be taken from the experimental cpx-opx solvus at high pressures. In this case, the 30 Kb, 1500°C solvus of Mori and Green (1975) is used, as indicated in Figure II-11 by Points A and B. The proportions of cpx_{SS}-opx_{SS}-ol can be then estimated using triangle A-ol-B. The result for R717 is given below:

x^i:	$\frac{cpx_{SS}}{0.25}$	$\frac{opx_{SS}}{0.19}$	$\frac{ol}{0.56}$

The estimation given above only applies to a garnet-free assemblage, in which the rock is not saturated with garnet due to high Al_2O_3 solubilities in pyroxenes (PX field of Figure II-12), or to a spinel lherzolite in which the amount of spinel is small. (As mentioned before, spinel has low and unfractionated REE distribution coefficients, and can be neglected for the purpose of calculation, if spinel occurs only in small amounts.)

In order to estimate the amount of garnet in R717, the alumina solubility in enstatite at 35 Kb, 1600°C is taken from Akella's (1976) experimental data, and Al_2O_3 solubility in diopside is assumed to be the same as in enstatite. Then, the pyroxenes are saturated with Al and the excess Al is used to form garnet. This procedure results in ∿11.5 wt. % of garnet. In order to be consistent with the assemblage estimated from the previous norm, the amount of cpx and opx is systematically decreased by the amounts corresponding to 11.5 wt. % of garnet, using the relationship in Appendix II-B, based on probe data of Obata (1977). The following proportions are obtained:

$$x^i: \quad \frac{cpx_{SS}}{0.23} \qquad \frac{opx_{SS}}{0.095} \qquad \frac{ol}{0.56} \qquad \frac{Gn}{0.115}$$

These two assemblages (Page III-53 and the one above) differ slightly from those given in Table II-4. The major discrepancy is in cpx/opx ratios which are higher than those in Table II-4, because the pyroxene solvus was not taken into consideration in the previous estimation.

Composition of Invariant Liquid

The melting proportion of different solid phases is directly related to the composition of the invariant liquid with respect to the compositions of the solid phases. Because the liquid composition is important to basalt genesis, considerable experimental work has been done in this area.

However, as pointed out by O'Hara (1976), there is no simple way to calculate the precise composition of a liquid formed by partial melting of a given peridotite under a given condition. Nevertheless, an approximation of the composition is sufficient for the purpose of modelling trace element fractionation. There are two important petrologic observations about the behavior of the liquid during melting at high pressures ($\geq$ 30 Kb) that must be considered in more detail:

(1) At high pressures, above 30 Kb, the garnet-pyroxene plane in the model system CaO-MgO-Al_2O_3-SiO_2 is a thermal divide (O'Hara and Yoder, 1967). It follows that the invariant liquid should lie on the silica under-saturated side of the garnet-pyroxene plane, that is, between this plane and olivine.

(2) O'Hara and Yoder (1967) have found the reaction relation opx + liquid → gn + cpx to exist at 30 Kb. That is, the composition of the liquid lies on the other side of the cpx-gn join from En, so that during melting the fractional contribution of En is a negative value in terms of cpx-gn-opx components. This reaction is equivalent to incongruent melting expressed by the equation

$$gn + cpx - opx \rightarrow liquid$$

For these geometrical relations, the fractional contributions of the solid phases (i.e. melting proportions) can be obtained by direct application of the lever rule using the

information on the compositions of the solid phases and the liquid. The procedures used are described below.

From O'Hara (1968), the estimation of the invariant point at 30 Kb gives the fractional contribution of olivine to the liquid of approximately 7-8%. This number is not critical for modelling calculations, as long as it is small, because the amount of olivine in the source rock is large, and the REE distribution coefficients for olivine are low and have a nearly unfractionated pattern. Therefore, this estimate is sufficient for the purpose of modelling REE.

A more accurate estimate for the melting proportions of cpx, opx, and gn is needed, because the bulk solid/liquid distribution coefficients of incompatible elements, especially REE, are mainly controlled by garnet and clinopyroxene. Figure III-2 is a portion of Al_2O_3-Wo-En plane. The position of the invariant point is taken from O'Hara (1968). This diagram shows how the composition of the liquid is related to the compositions of Gn_{SS}, Di_{SS}, and En_{SS} at 30 Kb. The compositions of these solid solutions vary with temperature and pressure, though gn_{SS} seems to be rather insensitive to the change of P and T (Akella, 1976). Mineral compositions are taken from the experimental results obtained by Akella (1976) at 31 Kb, 1500°C*, and by Mori and Green (1975) at

---

* A survey of all the data points in Akella (1976) shows that Al_2O_3 contents in cpx and opx are roughly equal, except for the 31 Kb, 1500°C run. I, therefore, believe that the cpx composition based on this run is erroneous, and Figure III-2 is constructed with the assumption that the Al_2O_3 content in Di_{SS} is the same as that given for En_{SS}.

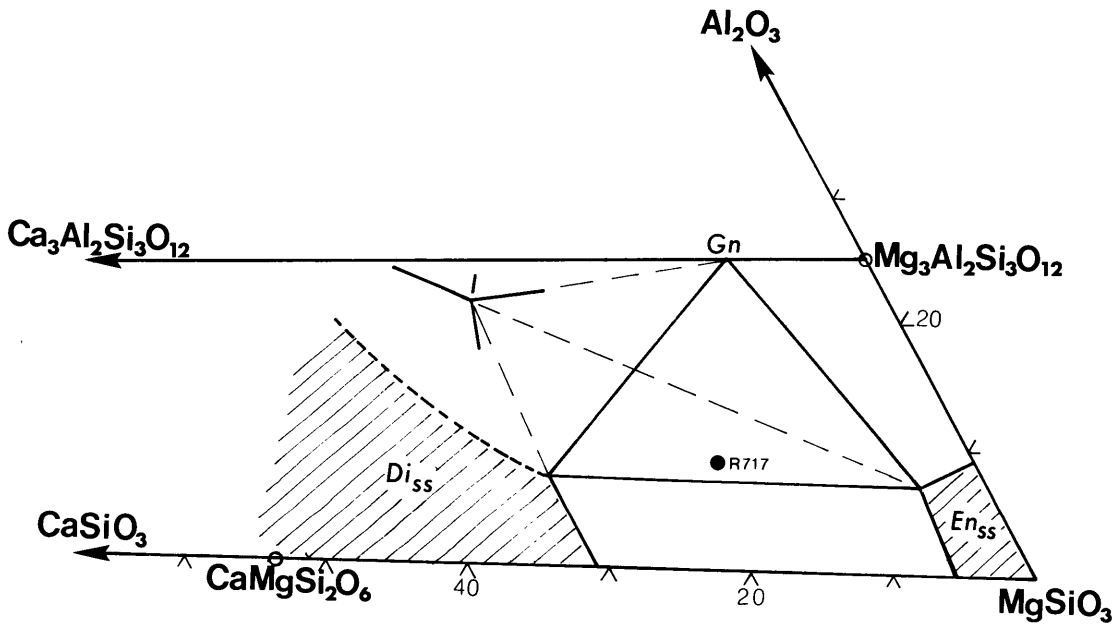

FIGURE III-2: A portion of Al_2O_3-Wo-En plane showing the position of the invariant liquid in relation to the mineral compositions: Gn_{SS}, Di_{SS}, and En_{SS} at ∿30 Kb. Data sources from: O'Hara (1968); Mori and Green (1975); and Akella (1976).

30 Kb, 1500°C. The melting proportions of cpx, opx, and gn are then calculated from the geometric relationship in this diagram. These proportions are normalized to 0.92, allowing 0.08 for olivine. The results are as follows:

p^i:	cpx	opx	ol	gn
	0.73	-0.51	0.08	0.70

When compared with the melting proportions given in the last chapter (Table II-4), there is a major discrepancy for opx, since the reaction relation at high pressure was not considered in the last chapter (notice that $\Sigma_i p^i = 1$)*.

For the 3-phase assemblage, cpx + opx + ol, the melting proportions are more difficult to estimate from experimental phase diagrams. In the case of batch melting of garnet-lherzolite, after garnet is exhausted, the liquid composition does not remain at the invariant point where the 4 primary volumes (cpx, opx, ol, gn) meet, but it varies along the

---

* Hertogen and Gijbels (1976) devised special mathematical formulas for the treatment of incongruent melting. In the author's opinion, this is completely unnecessary and uncalled for. Since for any incongruent melting reaction, for example (taking the example of Hertogen and Gijbels):

Pa(pargasite) → 0.35Di + 0.15Fo + 0.15Sp + 0.35Liquid

can be rearranged, so that it reads:

Pa - 0.35Di - 0.15Fo - 0.15Sp → 0.35Liquid

All the expressions developed in this chapter, including Shaw's (1970) equations, are perfectly valid for negative values of p^i, provided they satisfy the condition of $\Sigma_i p^i=1$. Therefore, the proper equation for this example should read:

2.86Pa - Di - 0.43Fo - 0.43Sp → Liquid

This analysis applies to the melting of peridotites under consideration as well as all other cases of incongruent melting or reaction.

cotectic line where cpx, opx, and ol volumes join (as a function of temperature if pressure is assumed constant). There is no accurate data on the position of this cotectic line in the C-M-A-S tetrahedron from experiments, and, therefore, it is almost impossible to describe the compositional variation of the liquid in this case.

In the case of fractional melting, the liquid theoretically should stay at the invariant point in the plane of opx_{SS}-cpx_{SS}-ol. However, data on this point at high pressures ($\geq$ 30 Kb) are unavailable.

A more direct approach to this problem is to estimate this liquid composition using the information obtained from the compositional variations among the residual peridotites. Figure II-11 is pertinent for this purpose. There are two conditions that the composition of the liquid has to satisy:

(1) It must lie on or close to the extraction line defined by the residual peridotites. Although there is a little scatter among the Group II rocks, they all lie close to the straight line joining olivine websterite, R855, and dunite, R893. Thus the composition of the liquid does not seem to vary to a large extent during the interval of melting under consideration.

(2) Because the garnet-pyroxene plane is a thermal divide above 30 Kb, the liquid composition should lie on the SiO_2 under-saturated side, i.e. the olivine side, of this plane. In terms of the cpx-opx-ol normative components in Figure II-11, it should lie within the triangle.

Assuming that the Group II rocks (R224, R131, and R845) represent residues from 15-20% of partial melting of a source with a starting composition close to spinel lherzolite, R717, or Pyrolite III of Green and Ringwood (1967), the composition of the extracted liquid can be estimated by using the lever rule. The estimated composition is indicated by the symbol "L" in Figure II-11. Making use of the pyroxene solvus at 30 Kb and 1500°C from Mori and Green (1975) as before, the melting proportions for cpx and opx are estimated. For olivine, it is arbitrarily kept at 8% as in the case of 4-phase melting. As mentioned before, this number is not critical for calculations as long as it is small. Nevertheless, the cotectic line formed by intersection of cpx, opx, and ol volumes at 30 Kb, shown by O'Hara (1968), does not seem to run towards olivine, but rather somewhat parallel to the garnet-pyroxene plane*.

The result of this analysis gives:

$$p^i: \quad \underset{0.63}{\text{cpx}} \quad \underset{0.29}{\text{opx}} \quad \underset{0.08}{\text{ol}}$$

For modelling calculations, all numbers obtained from experimental petrologic data, or direct chemical data in this section will be then used in conjunction with the mathematical expressions obtained in the last section.

---

* It is possible that this line was only drawn schematically in Figure 6 of O'Hara (1968) without quantitative data.

III-4: RESULTS AND DISCUSSIONS OF DETAILED RARE EARTH FRACTIONATION MODELLING

The two computer programs are used in Model II*. Input parameters for Model II as obtained in the last section are summarized in Table III-2. As in Model I, a high and low set of distribution coefficients are used (Appendix II-F). Different combinations of efficiency and effectiveness are examined. They are tabulated in Table III-3. Each case is designated by a letter for future reference. In general, the discussion of Model II can be divided into two parts, the variation of concentration due to (1) different effectiveness, and (2) different efficiency. For clarity, the two will be discussed separately.

Variations in Residual Concentrations as a Function of Effectiveness

In order to simplify the discussion, only results from melting of Assemblage II (without garnet) are presented**. The variations in La concentrations of the residual solid (no trapped liquid) as a function of the mass fraction of liquid extracted (F, in the cases of fractional and batch melting; F^{o} in the case of multiple-step melting) for cases

---

* This second more detailed attempt of REE fractionation modelling during partial melting of mantle peridotites is designated by the name "Model II" as distinguished from the first attempt in Chapter II.

** The reason for choosing Assemblage II instead of Assemblage I will be seen later.

of different effectiveness is shown in Figure III-3. In these models, no trapped liquid is allowed. La is chosen because it has the lowest bulk distribution coefficient among the REE, that is, the highest deviation from unity, and, therefore, La shows the most pronounced fractionation effect among the REE. The fractionation curves in Figure III-3 are generated by using the high set of distribution coefficients. The curves corresponding to the low set of distribution coefficients are shown in Figure III-4.

As expected, fractional melting (curve A) removes La from the residual solid much more effectively than batch melting (curve E). All concentrations generated by multiple-step melting models lie within the area between curves A and E (see Table III-3 for designations). Because of the step-wise process, the curves B, C, and D do not represent continuous functions. They are drawn by joining points at different intervals. The intervals (or steps) for Case B are small (i.e. the effectiveness is high), and hence, curve B follows closely to the ideal fractional melting curve of A, for which the number of steps can be considered as infinite. On the other hand, the intervals for Case D are large (F = 0.10; effectiveness is low), and therefore, the first interval is equivalent to batch melting up to the point F = 0.10, followed by a second interval, at which F^{o} = 0.19, and so on. Similarly, a family of curves can be generated, starting from different points on the batch-melting curve (E), correspond-

TABLE III-2

	Assemblage I	Assemblage II
	x^i	x^i
cpx	23%	25%
opx	9.5%	19%
ol	56%	56%
gn	11.5%	0%
	p^i	p^i
cpx	73%	63%
opx	-51%	29%
ol	8%	8%
gn	70%	0%

Initial concentrations, Co = 2*, for all REE.

Distribution coefficients are given in Appendix II-F.

* Concentrations normalized to chondrites.

TABLE III-3

Increasing Effectiveness →

Increasing Efficiency ↑

Efficiency \ Effectivness	Highest Fractional Melting	High Multiple-Step Small Steps	Medium Multiple-Step Intermediate	Low Multiple-Step Large Steps	Lowest Batch Melting
Highest — No trapped melt	A f*=0	B F*=0.01 f=0	C F=0.05 f=0	D F=0.10 f=0	E f=0
High — Small amount of trapped melt	K f=0.01	L F=0.01 f=0.005	M†	N F=0.10 f=0.01	P f=0.01
Low — Large amount of trapped melt	V f=0.10	W**	X§ F=0.05 f=0.04	Y§ F=0.10 f=0.09	Z f=0.10

* F and f for each case are defined as given in Section III-2.

§ Note that for Cases X and Y, the actual size of each step is 1% or less. Therefore, X and Y are processes of high effectiveness; however, they are classified here systematically under the "medium" or "low"column headings, according to the values of F. It will be seen later that the real effectiveness, i.e. the rate of change of concentrations with melting, depends on the value of F rather than the size of the extraction steps, if a large amount of trapped liquid is present as in these cases.

† The effect of Case M can be readily deduced from those of adjacent cases.

** See Case X and Case Y.

FIGURE III-3: Variations of La and Yb concentrations in residual solids with total percent extraction, F% (or F^{o}, in cases of multiple-step melting), according to Model II for cases of different effectiveness as listed in Table III-3. Each curve is designated by a letter corresponding to a specific case in the table. The upper two curves apply to Yb, and the lower curves are for La. The dashed curves between curves B and C, and curves C and D represent in-between cases of varying effectiveness, i.e. the size of each step, as indicated by the numbers (F%). They are drawn by interpolation only. All curves in this diagram are generated by using the high set of distribution coefficients (Appendix II-G). The Group II lherzolite samples are plotted in such a way that their ordinates are La concentrations, and their abscissae are values of F (or F^{o}) in percent estimated by their Yb concentrations as shown by the dotted lines. Therefore, their positions relative to the lower (La) set of curves can be used to estimate the effectiveness of the extraction process.

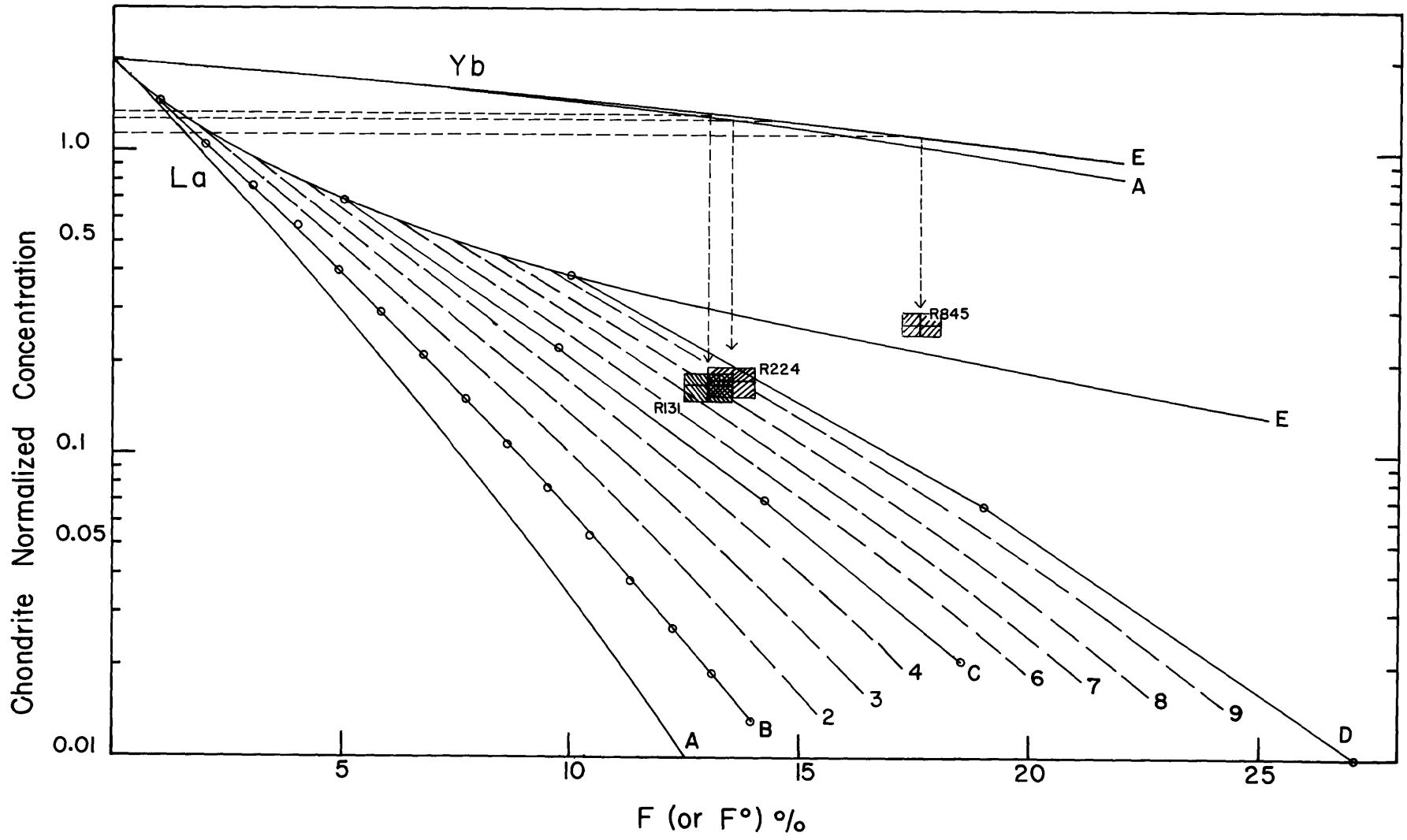
Yb
La
E
A
E
R845
R224
R131
1
2
3
4
C
6
7
8
9
D
A
B
1.0
0.5
0.1
0.05
0.01
5
10
15
20
25
Chondrite Normalized Concentration
F (or F°) %

FIGURE III-4: Same diagram as Figure III-3, except that the curves are generated by using the low set of distribution coefficients.

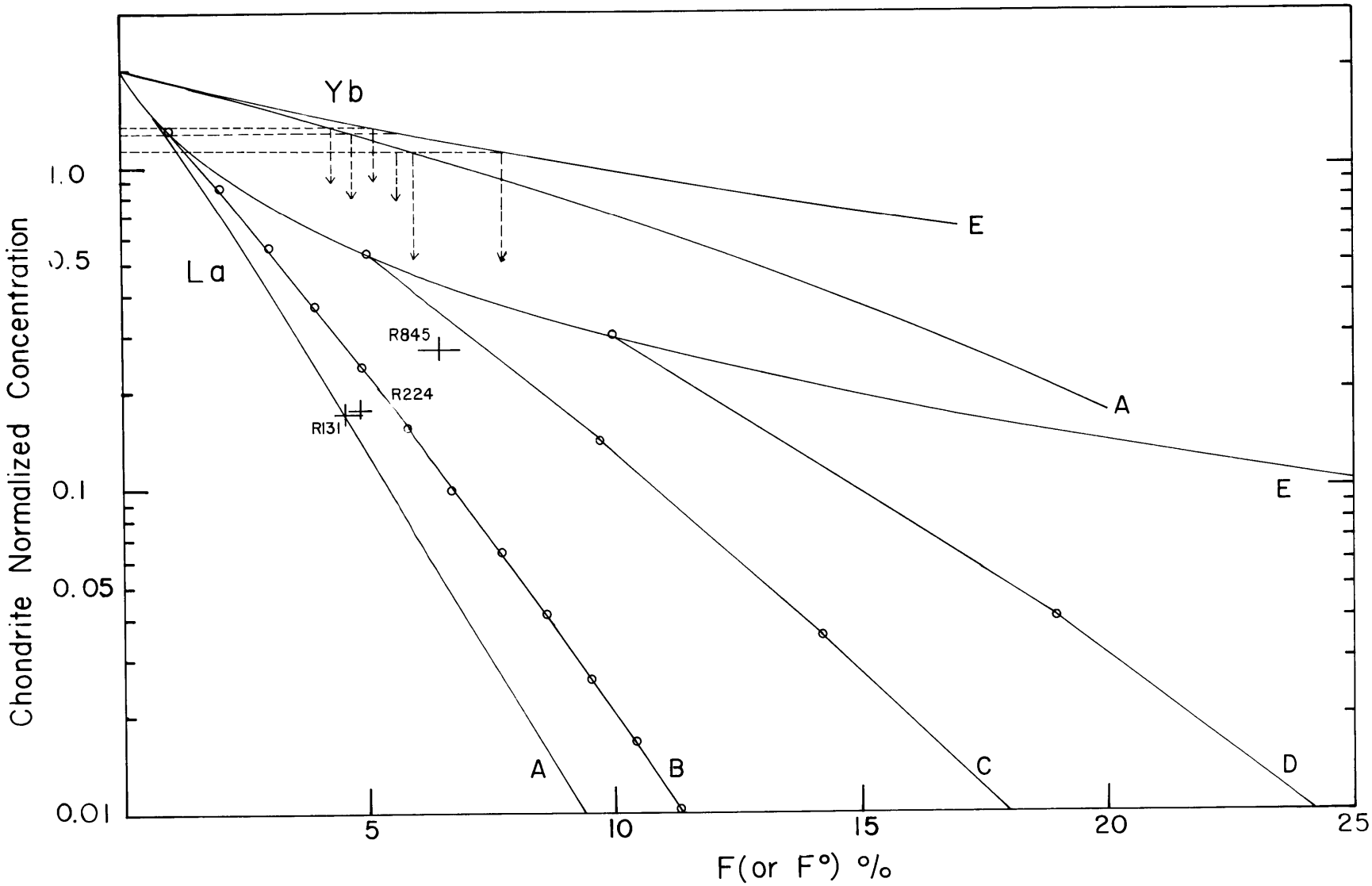
Yb
La
E
A
E
R845
R224
R131
A
B
C
D
1.0
0.5
0.1
0.05
0.01
5
10
15
20
25
Chondrite Normalized Concentration
F(or F°) %

ing to different degrees of effectiveness, that is, different values of F. These curves are drawn in dashed lines (by interpolation) in Figure III-3.

Fractionation curves for Yb, a HREE, are also plotted on the diagram. In contrast to La, Yb varies little with effectiveness, because its bulk solid/liquid distribution coefficient is close to unity. In Figure III-3, the variation of Yb concentration is shown only as a narrow band between curves A and E. Therefore, theoretically, information about the effectiveness of the real mantle melting process can be obtained by using La-Yb concentration pairs in Ronda samples, assuming that little or no trapped liquid is present. For example, the values of F (or F^{O}) can be estimated with the Yb concentrations using the Yb curves, and then, using the La concentrations, the effectiveness of the extraction process can be read directly from the positions of the points relative to the set of curves shown in Figure III-3. However, in practice, there are a number of problems such as:

(1) Although the assumption that the amount of trapped liquid is small (a highly efficient extraction process) can be justified by indirect experimental data, a major difficulty is caused by the considerable amount of uncertainty, associated with the distribution coefficients used in modelling calculations.

(2) For the garnet lherzolite assemblage (Assemblage I), the HREE in the residual solid are held rather constant by the presence of garnet during the initial portion of the

melting process. In other words, the Yb curves are flat, and they are insensitive to the degree of melting, F (or F^{O}). Possibly, another element may be used instead of Yb. As for Assemblage II (without garnet), the Yb concentration in the residual solid decreases steadily with increasing melting, and so, the Yb-La pair can be used.

(3) In the model considered, the Group II Ronda lherzolites, which are believed to have had no garnet in the residual solid, represent residues from a source which once had garnet as a solid phase, but due to higher degrees of melting then Group I rocks, all garnet is consumed. Hence, the REE, especially the HREE, would not have simply followed the fractionation curves calculated by using Assemglage II. In reality, they should have followed the trend of Assemblage I, and up to a certain point, after garnet is exhausted, they would leave trend I and follow a direction parallel to trend II, which they would have been following if they had had no garnet from the start. Therefore, a set of model curves directly calculated with Assemblage II may depart from the real situation for the Group II Ronda peridotites.

In spite of these difficulties, an attempt is made to obtain information from the Group II Ronda rocks. They (R845, R224, and R131) are the only samples used in the subsequent discussion.

Group II Ronda lherzolites are plotted on Figure III-3, which is based on the higher set of distribution coefficients,

and melting of Assemblage II. The abscissae are obtained by using Yb concentrations which correspond to a certain value of F (or F^{o}), the amount of liquid melted. The ordinate is La concentration. The Ronda data plotted on this diagram indicate that the process of liquid extraction was highly ineffective. Note that R845 cannot be accounted for by batch melting, and from the positions of R131 and R224, multiple-step melting with 7-10% of liquid extracted at each step is indicated. It must be emphasized that this is the case for the higher set of distribution coefficients.

With the lower set of distribution coefficients (Figure III-4), a drastically different result can be obtained. In this case, it can be shown that both R131 and R224 lie close to the ideal case of fractional melting, while the data of R845 only indicate a multiple-step melting process with $\sim$3% of liquid extracted at each step. Thus if the low set of distribution coefficients is valid, the extraction process is very effective as opposed to the previous conclusion obtained with the high set of distribution coefficients.

The latter case with the low set of distribution coefficients is believed to be more realistic due to the following reasons:

(1) The arguments given in Section III-1 of this chapter based on experimental observations strongly favor a high-effectiveness, high-efficiency model.

(2) The compositions of R845, and also one of the samples from Beni-Bouchera (M. Loubet, per. comm., 1977)

cannot be accounted for by batch melting with the high set of distribution coefficients. This can be seen in Figure II-8 of the first REE modelling attempt, and is also true for Model II (Figure III-7). It is more obvious in Figure III-3 for R845. In all cases, complete extraction without trapped liquid is assumed, and the source rock is assumed to be two times chondrites in concentrations.

(3) The REE abundances of R243 and R717 of the Group I Ronda lherzolites indicate that they have undergone up to and no more than only 5% of melting starting from a source with REE concentrations two times chondrites (see Chapter II). It follows that the liquid extraction process must have each step less than or equal to 5%.

(4) The gap between R845 and the rest of the Group II samples (R224 and R131) is wider in Figure III-3 than in Figure III-4. Since all rocks must have been melted under almost the same physical conditions, the liquid extraction processes operated on them should be more or less the same, and a large discrepancy as shown in Figure III-3 is not likely to occur.

(5) Low sets of REE distribution coefficients are generally believed to be more appropriate then high sets because: (a) incomplete separates in phenocrysts/matrix tend to give high numbers; (b) experimental data usually give lower values; and (c) megacryst data (Frey et al., 1977; Frey, 1977) also indicate low values.

In summary, I obtain the following conclusions:

(1) Multiple-step melting results in concentrations lying between those of ideal fractional melting and batch melting, depending on the size of each step, i.e. the effectiveness. At small degrees of melting, e.g. < 3 or 4%, the area between the batch melting curve (curve E) and the fractional melting curve (curve A) is small. Therefore, there is no pronounced difference between high effectiveness and low effectiveness processes. Then, in this region, all processes can be regarded as effective.

(2) For LREE, e.g. La, the variation in residual concentrations due to different effectiveness is important, while for HREE, e.g. Yb, no significant variation is produced, at least for the region of degrees of melting under consideration.

(3) A set of curves for LREE can be generated for various effectiveness between the fractional and batch melting curves. Since the variation for HREE is small while that for LREE is large, the effectiveness of the liquid extraction process can be estimated using, for example, Yb and La concentrations. This pair works best for rocks without garnet as a residual phase. However, in practice, the result is obscured by the large uncertainties associated with the values of the distribution coefficients. Nevertheless, with conclusions based on other experiments and observations, the Group II Ronda lherzolites are believed to result from an effective process; therefore, the lower set of distribution

coefficients is probably more realistic than the higher set under the mantle condition concerned.

Variations in Residual Concentrations as a Function of Efficiency

In the last subsection, only concentration variations due to effectiveness are discussed with the assumption that efficiency is high; that is, little or no trapped liquid. Now, I will evaluate the significance of trapped melt (i.e. the role of efficiency). In Figure III-5, curves A and E for La and Yb are the same as in Figure III-4 (corresponding to the low set of D's and the melting of Assemblage II). In addition, curves K and P are also shown. They represent the same fractional and batch melting cases with 1% of trapped liquid (see Table III-3). As expected, the K and P curves for Yb do not depart drastically from curves A and E, respectively. However, for La, considerable displacement occurs, and the main effect of trapped melt is to displace the fractionation curves in the direction towards the initial concentration of the source rock (i.e. shifting upward in Figure III-5).

Although in this case the amount of trapped liquid is small (1%, i.e. efficiency is fairly high), this shift is significant in terms of the Ronda data. Using exactly the same procedure as before and the Yb-La concentration pair, the Group II lherzolites are plotted on this diagram. Two of the three samples (R224, R131) lie <u>outside</u> the area between curves K and P (for La). Based on this observation, it can

FIGURE III-5: This diagram is similar to Figure III-4. The curves are generated by using the low set of distribution coefficients. Only the two extreme cases of effectiveness (fractional melting and batch melting) are drawn. The effect of a small amount (1%) of trapped melt (i.e. f=0.01) on these two cases is shown by the dashed lines (K and P). See Table III-3 for letter designations.

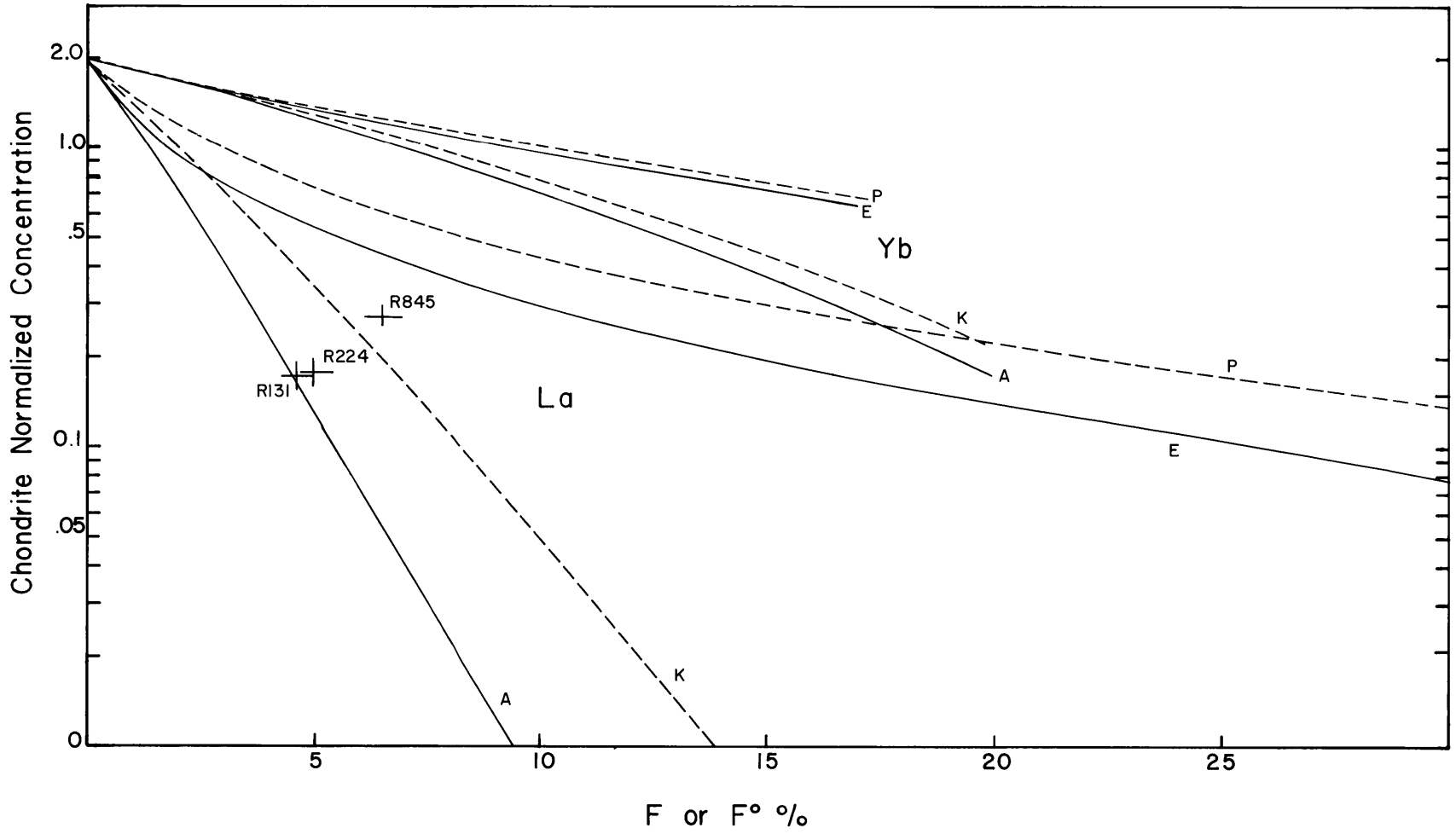
Chondrite Normalized Concentration
2.0
1.0
.5
0.1
.05
0
5
10
15
20
25
F or F° %
Yb
La
P
E
K
A
R845
R224
R131

FIGURE III-6: This diagram is similar to Figure III-3, and corresponds to the high set of D's. The solid curves are the same as in Figure III-3. The dashed curves show the effect of varying amounts of trapped liquid. The curves for Yb are omitted. (See Table III-3 for letter designations.)

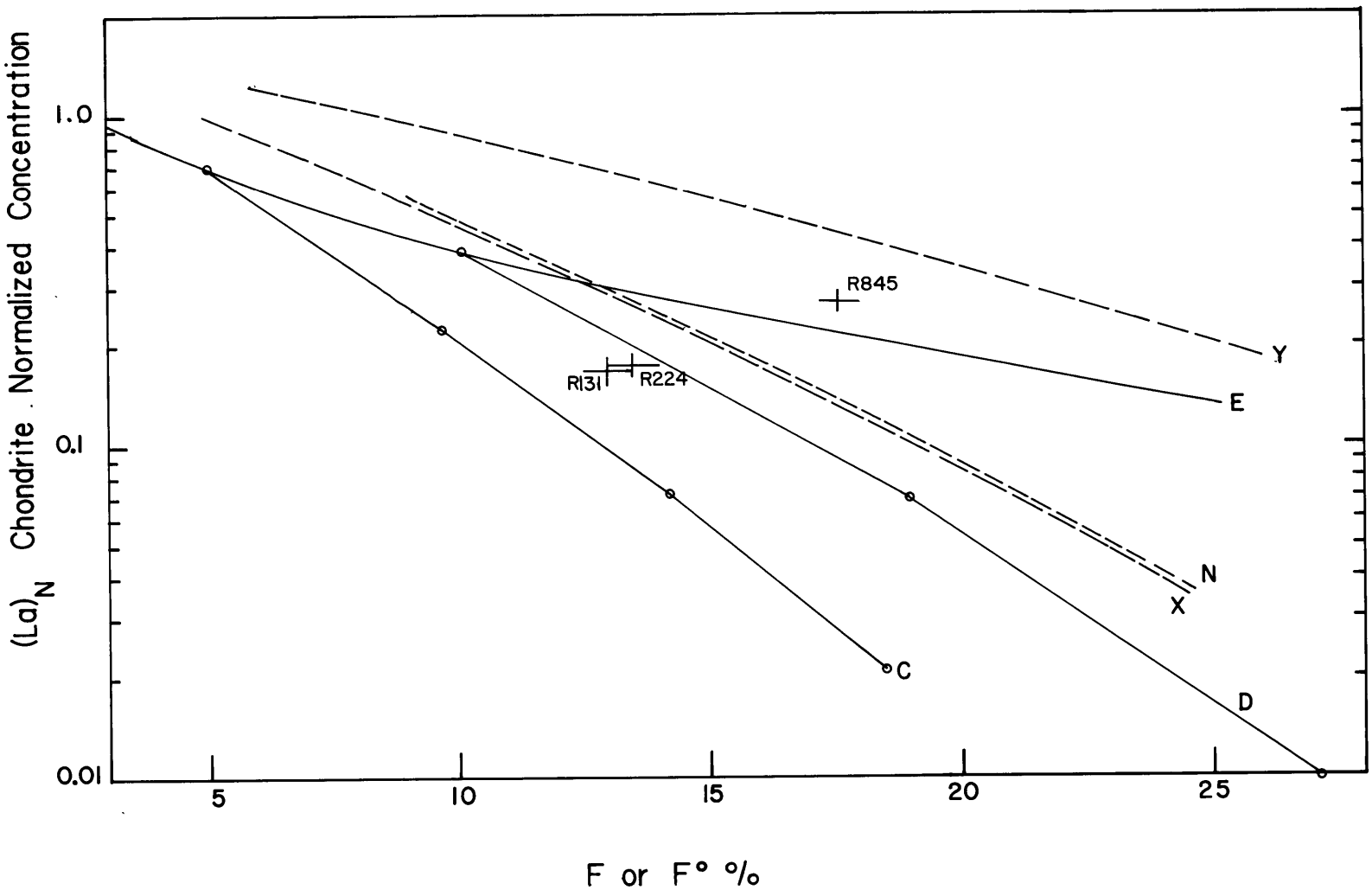
(La)N Chondrite Normalized Concentration
1.0
0.1
0.01
5
10
15
20
25
F or F° %
R845
R131
R224
Y
E
N
X
C
D

FIGURE III-7: Same diagram as shown in Figure II-8. (See Figures II-7 and II-8.) This diagram is generated by using Model II. Curve Z'' corresponds to Case Z in Table III-3, with the high set of D's, and curve P', to case P, with the low set of D's.

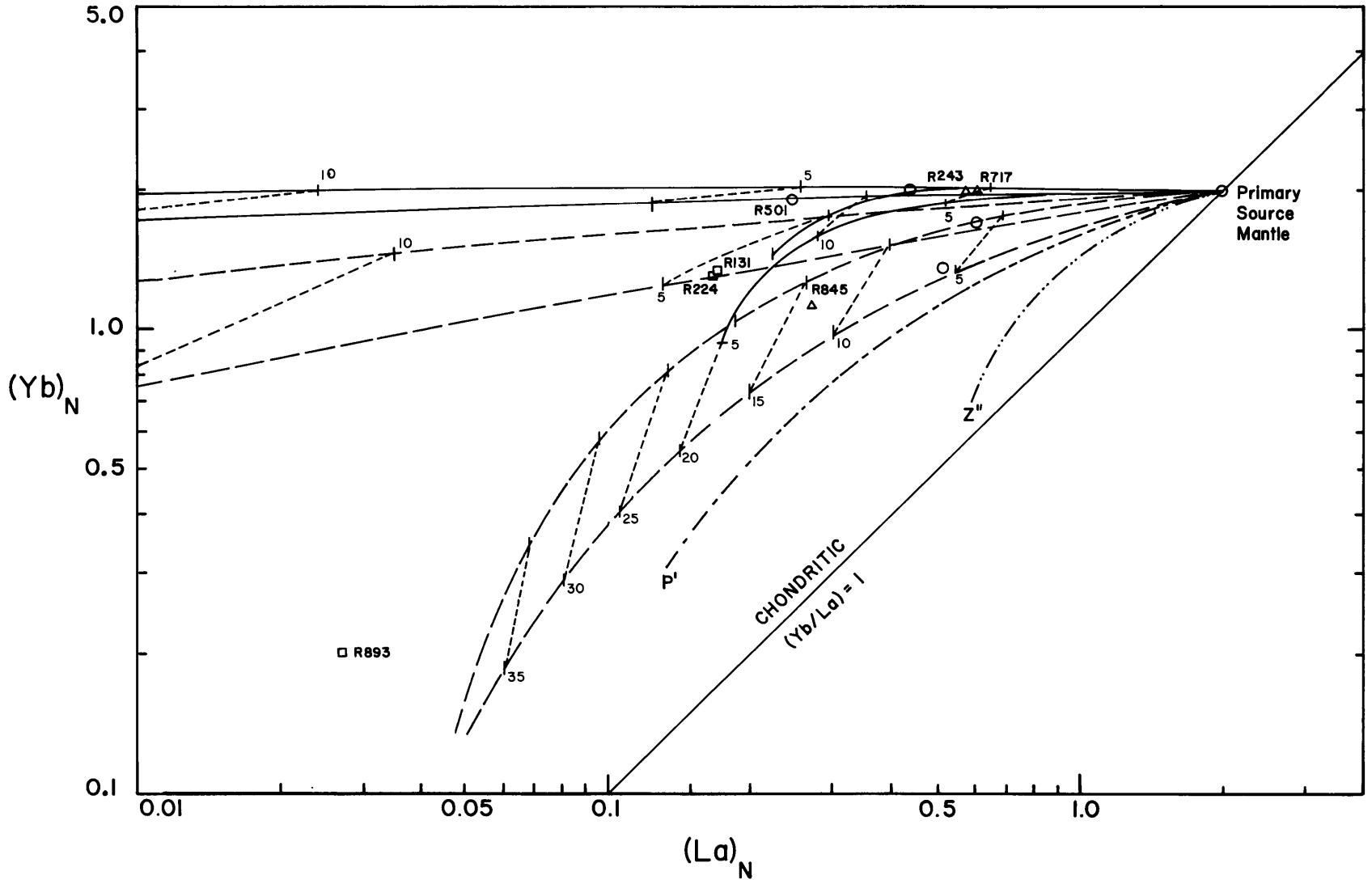
5.0
1.0
0.5
0.1
(Yb)N
0.01
0.05
0.1
0.5
1.0
(La)N
R243
R717
R501
R131
R224
R845
R893
Primary
Source
Mantle
CHONDRITIC
(Yb/La) = 1
P'
Z"
10
5
10
5
10
5
5
10
15
20
25
30
35

be concluded that, if any trapped liquid is present, the amount cannot be more than 1%, assuming that the low D's apply in this case. For R845, a little (< 1%) of trapped melt can be present, assuming a high-effectiveness process.

Although the case of low effectiveness using the high set of D's has been discarded, we will examine the effects of a large amount of trapped melt on the ineffective curves of Figure III-3. In Figure III-6, curves C, D, and E are the same as in Figure III-3. In addition, curves for cases N, Y, and X (see Table III-3) are drawn. Notice that the actual size of the steps for Cases X and Y are small (< 1%). According to the size of the steps, it may be expected that they are high-effectiveness processes. However, due to the large amount of trapped liquid (low efficiency), the actual rate of change of concentrations with respect to melting is small. (That is, Curve X is flatter than Curve C, and Curve Y is flatter than Curve D). Therefore, in cases of low efficiency, with a large amount of trapped melt like these, the "real effectiveness" is controlled not by the size of the steps, but by the value of the parameter F (relative to f).

Since Yb does not show much variation even with the addition of one more factor, efficiency, the Ronda Group II samples can be approximated by the same positions as before in Figure III-3. Provided that the high set of D's is valid, the following possibilities can be drawn from their relative positions to the curves:

(1) To account for R845, trapped liquid must be present. The extraction process is either batch melting with a small amount of trapped melt (highly ineffective, but efficient), or very inefficient (with a large amount of trapped melt), but highly effective (e.g. Case Y).

(2) For R131 and R224, the minimum requirement is a moderately ineffective and a moderately inefficient process. There is a small range of possibilities as the two factors compensate each other in their effects.

Summary of Implications

After such detailed modelling analysis (Model II), it is necessary to recall the REE fractionation modelling of the last chapter which provided the input information for Model II. If Model II agrees with the basic input data, then the more detailed Model II can be accepted as a self-consistent model. However, if it does not agree with the basic input information, another attempt must be made by varying the input parameters until a self-consistent model is found.

Using the new data shown in Table III-2, the results of Model II can be summarized in Figure III-7. When compared to Figure II-8 which illustrates the conclusions of Model I, no major discrepancy can be seen. Therefore, it is true that the conclusions drawn from the former model can be also drawn from Model II.

However, the effect of trapped liquid must be considered before any firm conclusion is made. In the last two sub-

sections, two alternatives have been obtained:

(1) With the low set of distribution coefficients, a process with high effectiveness and small amount ($\geq$ 1%) of trapped melt;

(2) With the high set of distribution coefficients, an ineffective process with moderate to large amount of trapped melt.

It can be argued that option (1) is a much more reasonable case than option (2), but for the moment, let us consider the worst possible case.

Curve Z" in Figure III-7 represents the lowest possible effectiveness (batch melting) and an extremely low efficiency (10% of trapped melt; see Table III-3) for the case with the high set of partition coefficients. Using the same translation operation on the log-log plot as described in Chapter II (page II-43), it can be readily shown that by taking R717 as the source rock, even an extremely improbable case like Z" cannot cover the range of the compositions observed. (R845 is out of the range, together with two samples from Beni-Bouchera). It can also be shown that, with curve Z", the minimum (to encompass all Ronda samples, including those from Beni-Bouchera) required mantle source is at $(La)_N = 1.2$, $(Yb)_N = 2.0$. An extraction process such as Z is not likely to have happened, but this exercise indicates that the effect of even such an extreme case does not significantly alter the conclusions in Chapter II.

Let us now examine the more probable case of the first alternative. Curve P' corresponds to the lower limit generated by batch melting with 1% of trapped melt (see Table III-3). This curve can be taken as the lowest boundary curve for all high efficiency cases. When the same translation operation is performed, it is found that the minimum requirement for the mantle source concentrations is at $(La)_N = 1.55$ and $(Yb)_N = 2.0$.

The conclusions are as follows:

(1) The results of the more detailed modelling show that all major conclusions obtained by the earlier modelling attempt in Chapter II remain valid.

(2) The liquid extraction process in the upper mantle is probably very effective and very efficient. As indicated by the Ronda Group II samples, the amount of trapped melt is no more than 1%, and the size of each extraction step is no bigger than 1 or 2% at a time, that is, the process is close to fractional melting. This contention is also supported indirectly by experimental data (Waff and Bulau, 1977; Boudier and Nicolas, 1977; Murase et al., 1977a,b).

CHAPTER IV

PRIMARY MANTLE AND PRIMARY MELT COMPOSITIONS AS INDICATED BY THE COMPOSITIONS OF THE RONDA PERIDOTITES

IV-1: DERIVATION OF PRIMARY MANTLE COMPOSITION USING THE RONDA PERIDOTITE DATA

It has been shown in Chapter III that the compositions of the Ronda peridotites are remarkably colinear in the Cao-MaO-Al_2O_3-SiO_2 tetrahedron. This colinearity can be seen in Figure II-10 and Figure II-11, and geochemical data, as discussed in Chapter II, indicate that the peridotites are residues after various degrees of partial melting of a hypothetical mantle source. Therefore, the straight line defined by these residual compositions can be taken as an "extraction line" along which the compositions of both the primary source mantle and the primary liquid extracted mantle lie. In Figure II-10, the traces of this line in each variation diagram are calculated using linear regression techniques, and a linear equation is obtained for each case.* The regression line is drawn in each diagram. For the purpose of comparison, two other similar trends are also drawn. One is based on ultramafic nodules in

---

* The linear regression equations are:

$SiO_2 = -0.261\ MgO + 54.84$; $r = -0.987$

$Al_2O_3 = -0.390\ MgO + 18.79$; $r = -0.992$

$CaO = -0.340\ MgO + 16.48$; $r = -0.995$

$\Sigma FeO = 0.00466\ MgO + 8.916$; $r = 0.0557$

Where r is the linear-correlation coefficient.

South African kimberlites (O'Hara et al., 1975) and the other, on ultramafic nodules in basaltic rocks from various localities of the world (Kuno and Aoki, 1970). In the Al_2O_3 and CaO variation diagrams, these trends have about the same slope as the Ronda regression lines, but mantle models based on these lines have less Al_2O_3 and CaO than the Ronda model. In the SiO_2 diagram, there are differences among the slopes of the trends, especially that of the kimberlite nodules. For ΣFeO, the trends are variable, and the Ronda data are much more scattered than in the other diagrams. Since the primary Fe^{2+}/Fe^{3+} ratios are not very well known in most samples, this scatter is not unexpected, and not at all unusual in variation trends of other rock suites.

The trends of O'Hara et al. (1975) are based on average compositions, and Kuno and Aoki's (1970) trend are also based on average compositions of many groups of samples from many different localities of the world. Only the Ronda trend is based on samples from a single locality, and it is the only trend considered in this study.

To estimate the composition of the primary mantle source, the following information is used as constraints:

(1) The composition must lie on the "extraction line".
(2) The most depleted Ronda lherzolite (R845) has undergone no more than 15 or 20% of partial melting,

starting from a chondritic mantle source, and the most undepleted one (R717), nor more than 3-5%. This is based on the REE models. It follows that the primitive mantle composition must be very close to R717.

(3) The composition of the primary "invariant" liquid obtained by using the simple level rule (i.e. mass balance) must lie on the silica undersaturated side of the garnet-pyroxene plane in the Cao-MgO-Al_2O_3-SiO_2 system, if melting occurs above 30 km (Chapter III). In other words, it should 01 in the mantle norm (and lies within the triangle in Figure II-11).

Using these constraints, the result is shown in Figure II-11 and Figure II-10. The primary mantle composition is indicated by the star, and the hypothetical primary liquid, by the symbol "L". Table IV-1 lists this mantle composition based on the Ronda peridotites and other published upper mantle models (Green and Ringwood, 1967; Carter, 1970; Moores, 1970; Nixon and Boyd, 1973) which are also plotted in Figure II-10. All these models are nearly identical in MgO content, but their 100 Mg/Mg+ΣFe values vary from 87-93, with an average of 89.1 which coincides with the Ronda value. The Ronda model also gives about average values for SiO_2 and Al_2O_3, but has

TABLE IV-1: Upper Mantle Compositions According to Different Models (on volatile-free basis).

	Ronda (1)	Pyrolite (2)	Vourinos (3)	Kilbourne Hole (4)	Kimberlite nodule (5)	R717 (6)
SiO_2	45.10	45.20	45.58	42.94	44.59	44.86
TiO_2	> 0.17*	0.71	0.15	0.24	0.26	0.17
Al_2O_3	4.22	3.54	3.86	5.77	2.81	3.93
Cr_2O_3	0.37	0.43	0.28	0.22	0.29	0.368
ΣFeO	8.09	8.47	5.16	9.13	10.25	8.26
MnO	> 0.14*	0.14	0.12	0.13	0.13	0.14
MgO	37.40	37.48	37.71	37.16	37.98	37.73
CaO	3.78	3.08	3.00	3.72	3.33	3.56
Na_2O	0.31	0.57	0.51	0.39	0.34	0.31
K_2O	> 0.01*?	0.13	0.15	0.003	0.14	0.01
P_2O_5	> 0.01*	0.06	0.03	-	trace	0.01
NiO	> 0.26*	0.20	0.24	0.22	-	0.258
	> 99.86					
$\frac{100\ Mg}{Mg+\Sigma Fe}$	89.18	88.75	92.87	87.88	86.85	89.06

(1) Primary source mantle composition estimated by using the Ronda data.
(2) Pyrolite III (Green and Ringwood, 1967). P_2O_5 abundance from Ringwood (1966).
(3) Composite bulk composition of Vourinos ophiolite complex (Moores, 1970, Table III-3, average of A and B).
(4) Composition of the upper mantle based on nodules found at Kilbourne Hole, New Mexico (Carter, 1970)(corresponding to Fa 12%).
(5) Most undepleted sheared garnet lherzolite nodules (No. 1611) from a South African kimberlite (Nixon and Boyd, 1973).
(6) R717. Most undepleted lherzolite sample from Ronda.

* Numbers taken from R717.

the highest CaO concentration. However, the differences in CaO are small and all models show remarkably good agreement within 1%. The only large decrepancy is found in the total iron values, which are more difficult to estimate. Concentrations of the other elements listed in the Ronda model are taken from R717, the most undepleted lherzolite sample from the Ronda body. With the exceptions of K_2O and P_2O_5, these numbers agree well with the other mantle models. An element like K_2O which behaves as a trace element and has very low solid/liquid distribution coefficient in the mantle system (Shimizu, 1974; Hart and Brooks, 1974) can only be estimated by detailed modeling, because the simple lever rule will not apply. The large analytical uncertainties associated with the K_2O and P_2O_5 values preclude any meaningful estimates.

IV-2: DERIVATION OF PRIMARY MELT COMPOSITION

The same procedure is also applied to estimate the composition of the primary ('invariant') liquid melt which is believed to have been generated by the melting of the primary mantle source at high pressures (>30 kb) producing the series of residual peridotite compositions. The resulting hypothetical primary liquid composition, hereafter called "L_o", is shown by the symbol "L" in Figures II-10 and II-11, and is listed in Table IV-2. Only those

elements which show distinct linearity among the peridotite compositions in the variation diagrams are estimated by linear regression methods. The fact that the seven major elements estimated show a total of 99.51% means the fit is statistically very good, with the exception of total iron content.

In Table IV-2, two other inferred primary liquid compositions are also listed. Column (2) is the average composition of the Baffin Island picrites (Clarke, 1970, Group II) which are interpreted as liquids produced by partial melting of garnet peridotite at 30 kb. Column (3) is the composition of a pyroxenite layer from Beni-Bouchera which is thought to be possible primary melt produced by partial melting of garnet peridotite near 1500°C and 28.5 kb (Kornprobst, 1970). Note, that the 100 Mg/Mg+ΣFe value for L_o is considerably higher than the other two. Using K_D values from 0.25 to 0.35 for the partitioning of iron and magnesium between olivine and liquid from Roeder and Emslie (1970), the liquid equilibrated with the most magnesium Ronda lherzolite (R845, 100 Mg/Mg+ΣFe = 90.62) should have 100 Mg/Mg+ΣFe values in the range of 71 to 77 according to calculations. The L_o value of 81.6 is, therefore, too high. This is probably due to the large uncertainty in estimating the ΣFe content, because of the poor statistics associated with the regression line. In the case of FeO vs. MgO

TABLE IV-2: Primary Melt Compositions.

	Ronda (1)	Baffin Island (2)	Beni-Bouchera (3)
SiO_2	49.6	45.1	44.26
TiO_2	0.44*	0.76	0.58
Al_2O_3	11.00	10.8	10.91
Cr_2O_3	***	0.27	0.19
ΣFeO	8.01**	10.26	10.36
MnO	***	0.18	0.15
MgO	20.0	19.7	16.75
CaO	9.69	9.2	12.15
Na_2O	0.77	1.04	1.19
K_2O	***	0.08	0.04
P_2O_5	***	0.09	0.10
NiO	***	0.12	-
CO_2	-	-	0.79
H_2O^+	-	2.14	2.40
H_2O^-	-	-	0.58
Total	99.51	100.0	100.62
$\frac{100\ Mg}{Mg+\Sigma Fe}$	81.6	77.4	74.23

(1) Hypothetical primary melt composition "L_o" obtained by using the lever rule and least-square fit on the Ronda peridotite compositions.

(2) Baffin Island picrite (Clarke, 1970, Table 1, Column 3).

(3) Pyroxenite layer from Beni-Bouchera (Kornprobst, 1970).

* R131 and R855 are excluded from linear regression fit.

** Large uncertainty due to poor statistics associated with the regression line (2σ = 3.05).

*** Not estimated.

(Figure II-10, d) the regression line has a linear correlation coefficient r = 0.056, as compared to the other cases (SiO_2, Al_2O_3, CaO vs. MgO) with $|r| > 0.98$, and the standard error associated with the estimated FeO value is 1.524 (1σ), i.e. FeO = 8.01 $\pm$ 3.05 wt.%. Consequently, the iron content, and the Fe/Mg ratio for the primary liquid composition, L_o, may be higher, in agreement with the general experimental K_D values. The significance of this hypothetical L_o composition in the context of the petrogenesis of the Ronda mafic layers will be discussed in the next chapter.

CHAPTER V

GEOCHEMISTRY AND PETROGENESIS OF THE MAFIC ROCKS

An important petrologic aspect of the Ronda ultramafic complex is the occurrence of mafic rocks within the peridotite body. These rocks range from picritic to basaltic in compositions, and they occur as layers or "dikes" from a few mm to a few meters thick, parallel to the mineralogical banding of the peridotite; rarely, they are oblique to younger foliations. Some layers form lenses and boudins, but they never cross-cut each other. Although their thickness is not always uniform, the mafic-ultramafic contacts are usually distinct. Detailed structural descriptions were given by Lundeen (1976). Petrology and petrogenesis were studied by Dickey (1970), Obata (1977), and Schubert (1977).

V-1: MINERALOGY AND PETROLOGY

Dickey (1970) distinguished two different types of mafic layers: the "tectonic-type" and the "magmatic-type" layers. Obata (1977) renamed the former type as "chromian pyroxenite layers," a purely descriptive name without any genetical implications. They are mainly websterites with abundant green chromian diopside. Compared to "magmatic layers," these layers are characterized by lower Al_2O_3 and higher Cr_2O_3 contents and higher Mg/Fe ratios near

those of the peridotites (with 100 Mg/Mg + ΣFe ∿90). Their field occurrences are similar to other layers (magmatic-type), but chromian pyroxenite layers are less abundant. However, chromian pyroxenite layers also occur at the margins between magmatic-type layers and adjacent peridotites. Dickey (1970) interpreted the chromian pyroxenite layers as solid segregations of pyroxenes and spinel formed during tectonic deformation of a hot solid peridotite body. However, Obata (1977) suggested they they are wall rock reaction products formed by the reaction between peridotites and the escaping mafic melts. Regardless of their origin, these layers have distinctly different bulk and mineral compositions from the majority of the "magmatic-type" layers. Chemical compositions of two of these layers with short discussions are given in Appendix V-A. In this chapter, I will only deal with the geochemistry and petrogenesis of "magmatic-type" layers, which are believed to have formed by igneous processes*. Although these rocks have undergone subsolidus recrystallization under different P-T conditions, similar to the approach taken for the peridotites in Chapter II, it is assumed that the metamorphism is isochemical unless

---

* The unspecified terms "mafic layers" or "mafic rocks" apply hereafter to only the magmatic-type mafic layers.

otherwise indicated by bulk chemistry, mineralogy, and appearance.

Dickey (1970) recognized a sequence of five metamorphic mineral assemblages in the magmatic-type mafic layers, ranging from garnet pyroxenite to olivine gabbro. A later more detailed study by Obata (1977) revealed additional mineral assemblages. Based on petrographic and field mapping data, the stable mineralogy of these mafic layers can be classified as follows:

I. Garnet pyroxenite group:
   a. Cpx + Gn + Plag
   b. Cpx + Opx + Gn
   c. Cpx + Gn
   d. Cpx + Gn + Plag + Qz
   e. Cpx + Opx + Gn + green Sp (ceylonite)

II. Spinel pyroxenite group:
   a. Cpx + Opx + green Sp
   b. Cpx + Opx + green Sp + Plag
   c. Cpx

III. Olivine gabbro group:
   a. Cpx + Ol + Plag + Opx + brown Sp (picotite)
   b. Cpx + Ol + Plag + Opx + opaque Sp (chromite)

Within each group, the assemblages are listed in the order of decreasing abundance. Brown amphibole (pargasite), pyrrhotite, rutile, and ilmenite are common accessory

minerals. Typically, textures of these rocks show incomplete subsolidus reactions and solid deformation. Garnets commonly have kelyphite rims; pyroxenes have exsolution lamellae and Al-rich pyroxenes break down to symplectite consisting of fine-grained mixtures of olivine, plagioclase, spinel, and Al-poor pyroxenes. Detailed petrographic descriptions are given by Dickey (1970) and Obata (1977), and structural implications are considered by Lundeen (1976).

These mineral assemblages reflect the P-T equilibrium conditions during the rising of the Ronda diapir. On the basis of their field occurrence, corresponding isograds can be mapped (Figure II-1). From northwest to southeast, the metamorphic facies are, in the order of decreasing P: (1) garnet lherzolite facies; (2) ariegite sub-facies of spinel lherzolite facies; (3) seiland sub-facies of spinel lherzolite facies; and (4) plagioclase lherzolite facies. All facies names are used according to O'Hara (1967). Group I mafic layers are found in facies (1) and (2); Group II in facies (3); and Group III in facies (4). The isograds in Figure II-1 were mapped by Obata (1977) who also discussed the possible implications of the NW-SE zonation of the Ronda body.

Sample Selection

Eighteen samples, including five samples of Dickey (1970), of magmatic-type layers were chosen for bulk chemical analyses. These samples were selected to include a variety of mineral assemblages, a wide range of geographic distribution, and to investigate the compositional variation within individual thick mafic layers.

In general, most magmatic mafic layers are rather fresh, and they appear to be modally homogeneous in the field. However, there are exceptions to this generalization. Detailed petrographic examination of some layers (especially thick layers, > 20 or 30 cm) show internal banding structures due to variations in modal mineralogy, often accompanied by a change in mineral compositions. These bandings are usually parallel to the peridotite-layer contacts which are typically sharp on a macroscopic scale. As a first-order assumption, most of these zonations are thought to have originated by igneous differentiations, and therefore, several samples from different positions, relative to the contact, from a single mafic layer were also selected for bulk chemical study.

In order of decreasing metamorphic grade, the samples studied are:

A. Thick layer R127: (∿60 cm thick) plagioclase garnet clinopyroxenite; from the garnet lherzolite facies. Sample R127 was collected and analyzed by Dickey (1970),

and studied experimentally at high pressures by Obata and Dickey (1976). Five additional samples from this locality were collected by the author. From bottom to top (present orientation) of the layer, they are: R899, R900, R901, R902, R903. (See Appendix V-B for detailed locations.)

B. Layer R705: plagioclase-garnet clinopyroxenite; from the garnet lherzolite facies. A thin (∿3.5 cm) darker color band is found in the hand-specimen. R705A is the host rock, and R705B is the band. They were analyzed separately.

C. R842*, garnet websterite, and R839*, garnet clinopyroxenite. These samples are from the garnet lherzolite facies close to the western peridotite/country rock contact. They are only ∿15 m apart.

D. R251: spinel plagioclase pyroxenite; from seiland subfacies of spinel lherzolite facies.

E. R181-185: A set of samples from different parts of a thick layer (from "bottom" to "top") R181, R182, R183, R184, R185. They are gabbros (transitional from

---

* R554 and R525 are equivalent sample numbers used by Obata (1977) for R842 and R839, respectively. The former numbers are based on samples collected at the same localities in 1974, while the latter were collected in 1975.

olivine gabbro to spinel plagioclase clinopyroxenite with little olivine); from the plagioclase lherzolite facies.

F. R120, R322: both olivine gabbros from the plagioclase lherzolite facies.

Brief petrographic descriptions of these samples are given in Appendix V-B. More detailed work on some of these samples can be found in Dickey (1969, 1970), and Obata (1977).

V-2: GEOCHEMICAL METHODS

Only bulk rock compositions have been studied in this work. Sample preparations and analytical techniques are given in Chapter II. Similar procedures were used for peridotites and mafic rocks, except that the higher REE concentrations in the mafic rocks enabled the use of instrumental neutron activation analysis (INAA). However, most samples were analyzed by a radiochemical procedure (Appendix II-F) and checked by INAA.

V-3: RESULTS

Major and trace element abundances are given in Table V-1 and Table V-2, respectively. These analyses are grouped A to E as previously described and, thick layer samples R899 to R903, and samples R181 to R185, are arranged according to their relative positions within the layer. The total iron contents are recalculated as FeO (designated by ΣFeO) and only these numbers will be used for further discussions, calculations, and modelling. This is because the present

Fe^{3+}/Fe^{2+} ratios probably do not correspond to the original igneous condition, for they are likely to have been modified by later metamorphism. If the Fe^{3+}/Fe^{2+} ratio in the mantle is assumed to be 0.10 to 0.15, there are no major differences in the results and conclusions. Major and trace element variation diagrams are shown in Figures V-1 and V-2.

The compositions of these mafic layers are somewhat similar within a group (with the exception of R181 of Group E), but overall, they show a wide variation from picritic to basaltic in terms of major elements. Their MgO contents vary from 9.2 to over 22 wt.%, with 100 Mg/Mg + ΣFe ratios, from 58 to 89. Samples with low MgO contents and low Mg/Fe ratios (for example, Group A), have major element compositions similar to basalts, but their K_2O and P_2O_5 contents are much too low for most basaltic compositions, for example, K_2O and P_2O_5 abundances are comparable to but generally lower than K_2O and P_2O_5 abundances in ocean ridge basalts (Melson et al., 1976). In addition, Na_2O and TiO_2 contents are also somewhat lower than in most basalts, although some of these samples (especially those with low MgO contents, e.g., Group A) resemble the "primitive" mid-ocean ridge basalts in SiO_2, Al_2O_3, CaO, MgO, and FeO contents. For the purpose of comparison, the average composition of 101 analyses of abyssal volcanic

TABLE V-1: MAJOR ELEMENT COMPOSITIONS OF THE RONDA MAFIC LAYERS

	GROUP A						GROUP B	
	R127	R899	R900	R901	R902	R903	R705A	R705B
SiO_2	47.32	47.42	47.33	47.62	48.12	48.38	48.34	45.98
TiO_2	0.76	0.68	0.74	0.68	0.57	0.69	0.15	0.96
Al_2O_3	15.79	15.01	15.91	15.10	12.69	15.83	19.60	15.93
Fe_2O_3	1.93]8.57*	1.04]9.85	1.64]10.66	1.48]10.01	1.78]10.62	1.36]7.12	0.63]3.37	1.51]8.17
FeO	6.83	8.91	9.18	8.68	9.02	5.90	2.80	6.81
MnO	0.15	0.19	0.21	0.19	0.18	0.13	0.07	0.16
MgO	10.05	10.44	9.20	10.51	13.03	10.60	10.12	13.90
CaO	14.31	13.29	12.45	13.70	12.65	14.26	15.81	12.48
Na_2O	1.88	1.90	1.77	1.56	1.25	2.00	1.61	1.25
K_2O	0.02	0.01	0.03	0.01	0.01	0.01	0.02	0.01
P_2O_5	0.04	0.05	0.03	0.05	0.03	0.05	0.02	0.04
S	0.04	0.09	0.09	0.08	0.12	0.04	0.04	0.12
H_2O^+	0.39	0.42	0.64	0.20	0.20	0.47	0.27	0.49
H_2O^-	0.04	0.12	0.13	0.08	0.06	0.09	0.09	0.13
CO_2	0.27	0.18	0.63	0.08	0.40	0.10	0.20	0.23
rest	0.17	0.20	0.18	0.20	0.22	0.17	0.27	0.32
	99.99	99.95	100.16	100.22	100.33	100.08	100.04	100.32
O=S	0.02	0.04	0.04	0.04	0.06	0.02	0.02	0.06
TOTAL	99.97	99.91	100.12	100.18	100.27	100.06	100.02	100.26
$\frac{100\ Mg}{Mg+\Sigma Fe}$	67.65	65.40	60.61	65.17	68.62	72.62	84.27	75.20

* Total iron as FeO (ΣFeO)

TABLE V-1: (cont'd)

	GROUP C		GROUP D	GROUP E				
	R839	R842	R251	R181	R182	R183	R184	R185
SiO_2	44.93	46.41	44.08	48.10	46.25	46.24	48.22	46.62
TiO_2	0.58	0.67	1.26	0.43	0.24	0.24	0.33	0.29
Al_2O_3	13.21	12.87	14.28	11.50	15.89	17.63	14.57	15.50
Fe_2O_3	4.03]14.62	2.08]13.40	3.42]7.21	0.73]6.59	1.29]6.00	1.64]6.95	1.01]6.64	1.01]6.85
FeO	10.99	11.53	4.13	5.93	4.84	5.47	5.73	5.94
MnO	0.31	0.27	0.14	0.15	0.12	0.14	0.13	0.14
MgO	11.19	10.73	14.84	19.36	13.09	12.10	12.18	12.97
CaO	12.35	12.58	16.53	11.59	15.38	14.32	15.60	15.37
Na_2O	1.17	1.71	0.91	0.84	1.23	1.35	1.17	1.20
K_2O	0.005	0.03	0.01	0.006	0.03	0.01	0.03	0.02
P_2O_5	0.02	0.03	0.02	0.02	0.04	0.03	0.03	0.03
S	0.02	0.13			0.09	0.02	0.05	0.05
H_2O^+	0.68	0.50	0.18	0.71	1.02	0.49	0.83	0.71
H_2O^-	0.18	0.10	0.06	0.15	0.12	0.04	0.08	0.07
CO_2	0.26	0.56	0.14	0.01	0.21	0.30	0.16	0.13
rest	0.23	0.23	0.20	0.35	0.29	0.20	0.21	0.23
	100.16	100.43			100.13	100.22	100.33	100.28
O=S	0.01	0.06			0.04	0.01	0.02	0.02
TOTAL	100.15	100.37	100.20	99.88	100.09	100.21	100.31	100.26
$\frac{100\ Mg}{Mg+\Sigma Fe}$	57.71	58.80	78.59	83.97	79.54	75.64	76.58	77.14

TABLE V-1: (cont'd)

GROUP F

	R120		R322	
SiO_2	46.58		47.69	
TiO_2	0.50		0.41	
Al_2O_3	12.39		11.47	
Fe_2O_3	1.46	]6.22	1.47	]4.97
FeO	4.91		3.65	
MnO	0.17		0.14	
MgO	20.61		22.24	
CaO	10.36		9.92	
Na_2O	0.99		0.80	
K_2O	0.005		0.005	
P_2O_5	0.01		0.02	
S	0.06		0.03	
H_2O^+	1.32		1.17	
H_2O^-	0.12		0.13	
CO_2	0.18		0.34	
rest	0.43		0.76	
	100.10		100.25	
O=S	0.03		0.01	
TOTAL	100.07		100.24	
$\frac{100\ Mg}{Mg+\Sigma Fe}$	85.51		88.85	

TABLE V-2: RARE-EARTH ELEMENTS AND OTHER TRACE ELEMENT ABUNDANCES IN THE RONDA MAFIC LAYERS

	GROUP A					GROUP B		GROUP C	
(ppm)	R127§	R899	R900	R901	R902	R903	R705A	R705B	R839	R842§
La	0.187	0.388	0.020	0.058	0.047	0.075	0.097	0.278	0.621	1.576
Ce		5.23		0.765	0.993	1.538		2.249	2.827	5.521
Nd	2.334	5.370	0.690	3.004	2.061	2.180	0.738	3.878		3.651
Sm	1.087	1.756	1.389	1.533	0.836	1.639	0.340	1.947	0.817	1.148
Eu	0.536	0.762	0.776	0.776	0.474	0.847	0.291	0.964	0.451	0.381
Gd		2.83	4.131	3.217	2.26	2.78	0.554	3.804	2.883*	2.135
Tb		0.417*	0.783	0.605	0.474	0.286*	0.106*	0.683	0.518	0.572
Yb	1.373	2.230	2.484	1.784	1.533	0.781	0.406	1.795	5.172	4.884
Lu	0.281	0.319	0.329	0.254	0.215	0.102	0.0558	0.239	0.731	0.791

§ HO concentrations obtained by INAA: R127 - 0.667* ppm,
R842 - 1.460 ppm.

* Values uncertain, due to peak interference or poor counting statistics.

	GROUP D	GROUP E					GROUP F	
(ppm)	R251§	R181	R182	R183§	R184	R185	R120§	R322§
La	0.479	0.782	0.649	0.382	0.331	0.323	0.436	0.824
Ce	3.25	4.195	3.145	1.549	1.979	1.823	3.11	3.45
Nd	9.856	4.561	3.142	1.883	2.361	2.398	3.79	3.370
Sm	4.847	1.520	0.914	0.640	0.832	0.772	1.124	1.417
Eu	1.949	0.619	0.385	0.310	0.355	0.348	0.412	0.492
Gd		2.058	1.150		1.121	1.112		
Tb	0.766	0.303	0.143	0.163	0.157	0.182		
Yb	1.503	0.909	0.532	0.649	0.674	0.861	1.075	1.615
Lu	0.286	0.129	0.0755	0.106	0.099	0.125	0.238	0.334

§ HO concentrations by INAA: R251 - 1.031
R120 - 0.275*
R322 - 0.600*

* Values uncertain, due to peak interference or poor counting statistics.

TABLE V-2: (cont'd)

	GROUP A						GROUP B		GROUP C	
(ppm)	R127	R899	R900	R901	R902	R903	R705A	R705B	R839	R842
Sc	41	53	51	50	43	40	36	45	76	69
V	185	292	338	291	270	163	99	223	705	615
Cr	570	430	293	485	505	525	1140	885	209	318
Co	68	138	160	167	128	120	152	152	164	191
Ni	139	153	113	135	325	163	249	560	93	89
Cu	40	90	86	80	139	42	53	152	45	31
Zn	71	70	77	71	84	57	18	45	94	92
Ga	13.0	13.5	13.5	13.0	14.0	12.0	9.5	12.5	13.5	16.0
Rb	1.2	1.7	2.3	1.1	0.9	1.4	0.5	0.7	0.4	1.6
Sr	34.5	93	50	45.5	24.0	37.0	122	110	4.5	30.0
Y	16	21	32	20	20	10	4	26	45	41
Zr	19	34	18	33	14	25	2	42	10	17
Nb	< 3	< 1	< 1	< 1	< 1	< 1	< 1	< 1	< 1	< 1
Pb	10	6	9	7	8	5	5	5	8	10

	GROUP D	GROUP E					GROUP F	
(ppm)	R251	R181	R182	R183	R184	R185	R120	R322
Sc	44	35	37	39	36	40	38	47
V	276	169	133	127	167	168	186	185
Cr	535	1490	985	820	720	890	1790	3990
Co	68	101	109	66	89	84	78	77
Ni	207	500	317	195	245	170	700	810
Cu	5	22	296	35	67	99	81	68
Zn	38	29	44	39	40	42	27	39
Ga	15.0	9.0	9.0	10.0	11.5	10.0	9.0	6.0
Rb	2.3	1.5	2.5	0.7	3.1	1.4	2.9	3.1
Sr	122	46.0	89	50	48.5	44.0	56	45.5
Y	24	7	6	8	7	10	9	14
Zr	52	21	18	16	13	13	21	41
Nb	5	< 1	< 1	1	< 1	< 1	5	4
Pb	7	4	5	6	7	6	5	3

TABLE V-3: High-Pressure Mantle Norms (wt.%)

	GROUP A						GROUP B		GROUP C	
	R127	R899	R900	R901	R902	R903	R705A	R705B	R839	R842
$NaAlSi_2O_6$	12.49	12.58	11.86	10.27	8.26	13.20	10.74	8.28	7.79	11.43
$CaTiAl_2O_6$	2.29	2.05	2.25	2.03	1.70	2.07	0.46	2.89	1.77	2.03
Al_2O_3	11.89	11.18	12.26	11.77	10.04	11.82	16.53	12.87	10.73	9.32
$CaSiO_3$	28.86	26.86	25.13	27.55	25.60	28.81	32.97	24.72	25.14	25.41
$MgSiO_3$	25.31	26.31	23.30	26.33	32.72	26.65	25.55	35.00	25.26	25.71
$FeSiO_3$	16.18	18.65	20.30	18.84	20.00	13.44	6.41	15.47	24.85	24.14
Mg_2SiO_4	0	0	0	0	0	0	0	0	2.15	0.97
Fe_2SiO_4	0	0	0	0	0	0	0	0	2.34	0.99
SiO_2	2.98	2.37	4.90	3.20	1.69	4.02	7.35	0.78	0	0

	GROUP D	GROUP E					GROUP F	
	R251	R181	R182	R183	R184	R185	R120	R322
$NaAlSi_2O_6$	6.02	5.57	8.29	8.94	7.85	7.98	6.60	5.34
$CaTiAl_2O_6$	3.79	1.30	0.73	0.72	0.99	0.86	1.53	1.24
Al_2O_3	11.29	9.84	13.86	15.32	12.40	13.35	10.50	10.22
$CaSiO_3$	32.63	23.69	32.05	29.59	32.18	31.73	21.15	20.36
$MgSiO_3$	25.35	43.87	33.16	30.43	30.67	32.62	40.60	46.92
$FeSiO_3$	9.26	11.25	11.43	13.15	12.56	12.96	9.29	7.95
Mg_2SiO_4	8.32	3.49	0	0	0	0	8.26	6.72
Fe_2SiO_4	3.34	0.99	0	0	0	0	2.08	1.25
SiO_2	0	0	0.48	1.87	3.35	0.49	0	0

FIGURE V-1: Variation diagrams for the Ronda mafic layers.

(a) SiO_2 vs. MgO in wt. %
(b) Al_2O_3 vs. MgO in wt. %
(c) CaO vs. MgO in wt. %
(d) ΣFeO vs. MgO in wt. %

Each group of the Ronda mafic layers is designated by an open symbol as follows:

□ Group A; ◇ Group B; ▽ Group C;

⬡ Group D; ○ Group E; △ Group F.

Each point is labelled with the last digit (or letter) of the sample number. For example; □3 stands for R903. The unlabelled solid circles are the Ronda peridotites (see Figure II-10, Chapter II for details). The regression line and the hypothetical primary magma composition "L_o" (as indicated by [L]) are taken from the results in Chapter IV.

Other symbols are:

- ⧆ R127G: composition of glass coexisting with garnet and clinopyroxene at 25 Kb, 1400-1375°C, obtained by electron microprobe analysis of experimental changes from melting experiments of R127 (Dickey et al., in press)
- ⊕ Average composition of 101 analyses of abyssal volcanic glass from all spreading centers (Melson et al., 1976)
- ⊗ Baffin Island picrite (Clarke, 1970).
- ◒ "Primary melt" from Beni-Bouchera, suggested by Kornprobst (1970).
- + Compositions of the 4 types of garnet pyroxenite from Salt Lake Crater (Beeson and Jackson, 1970). Labels correspond to the type numbers used by Beeson and Jackson.

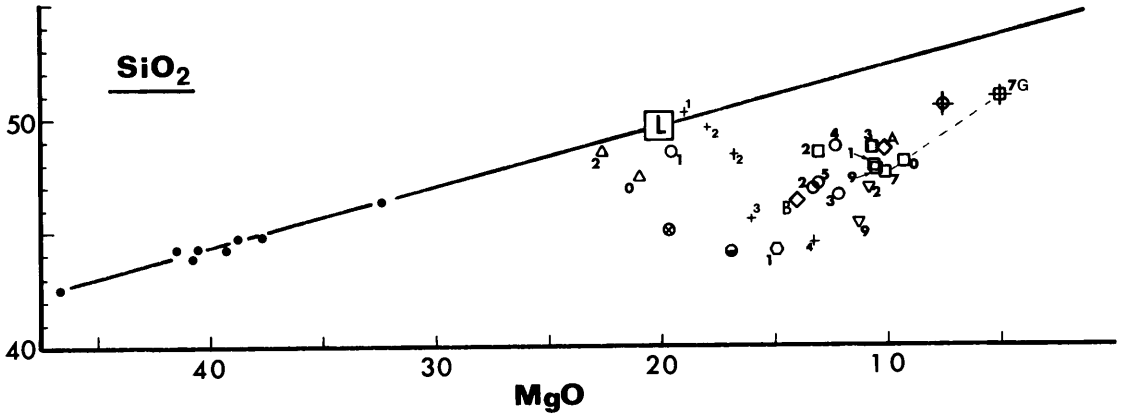
SiO2
50
40
40
30
20
10
MgO

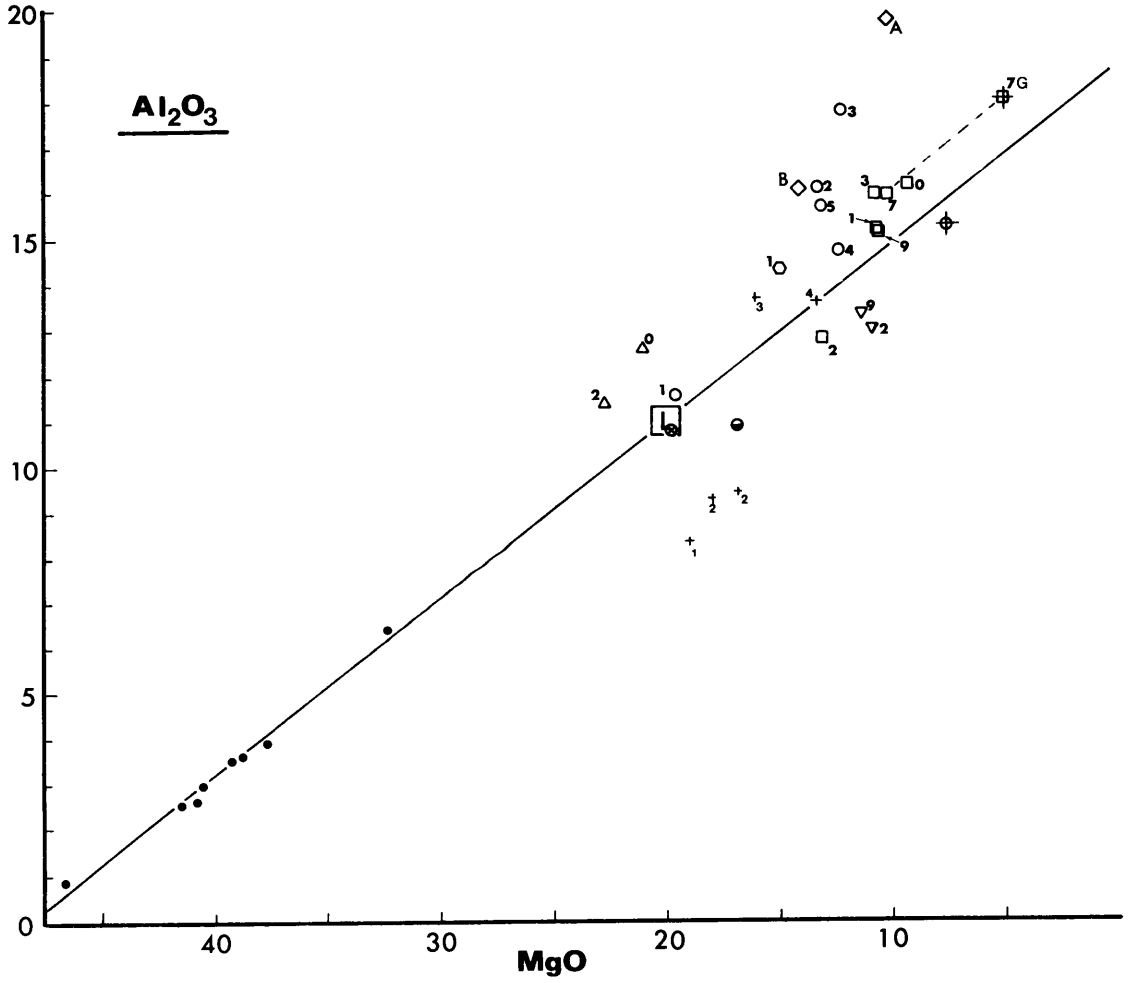
Al2O3
20
15
10
5
0
40
30
20
10
MgO

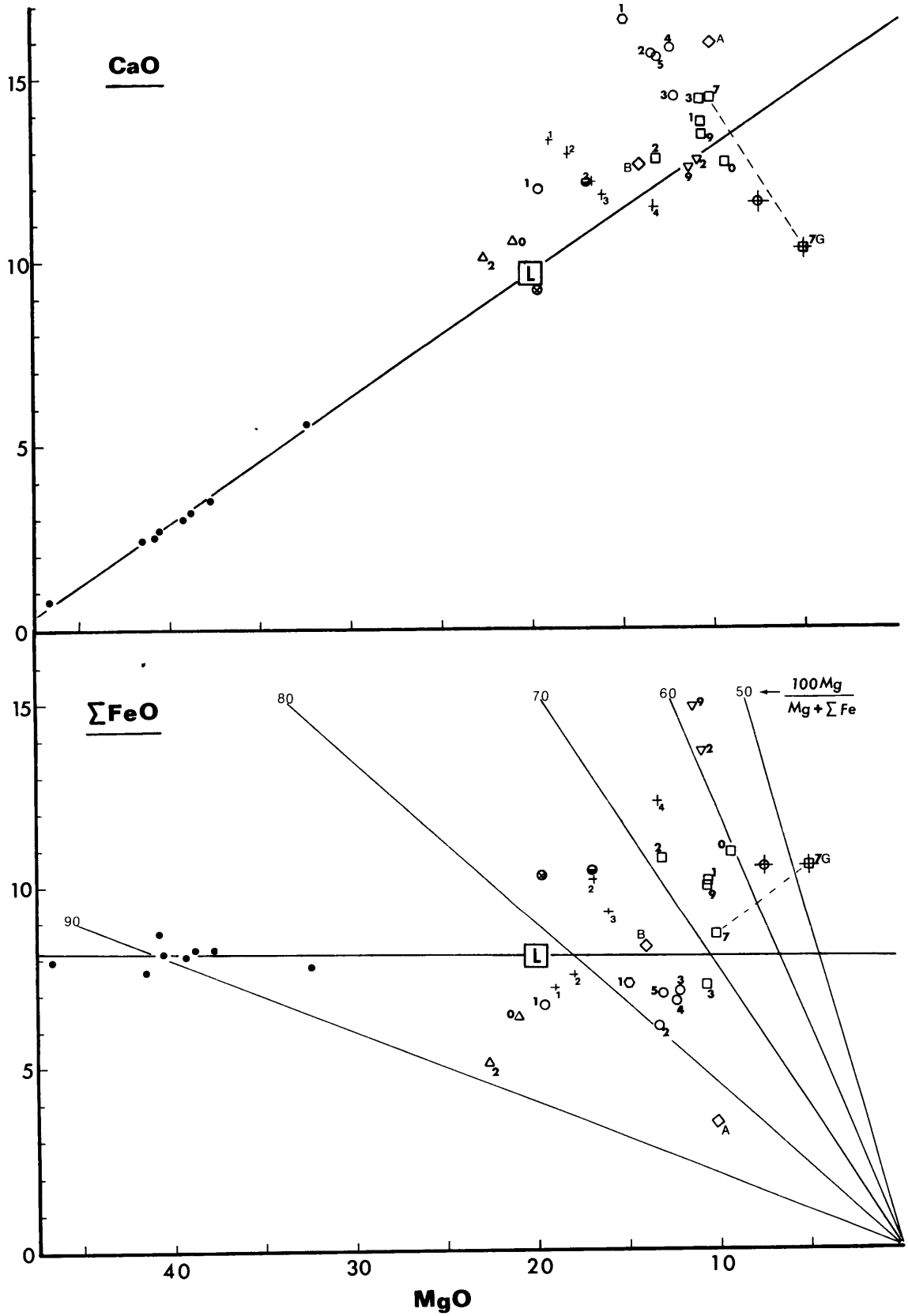
CaO
15
10
5
0
L
7G
ΣFeO
80
70
60
50
100Mg / Mg + Σ Fe
90
40
30
20
10
MgO

FIGURE V-2: Variations of trace element abundances with 100 Mg/Mg + ΣFe. Symbols are the same as in Figure V-1.

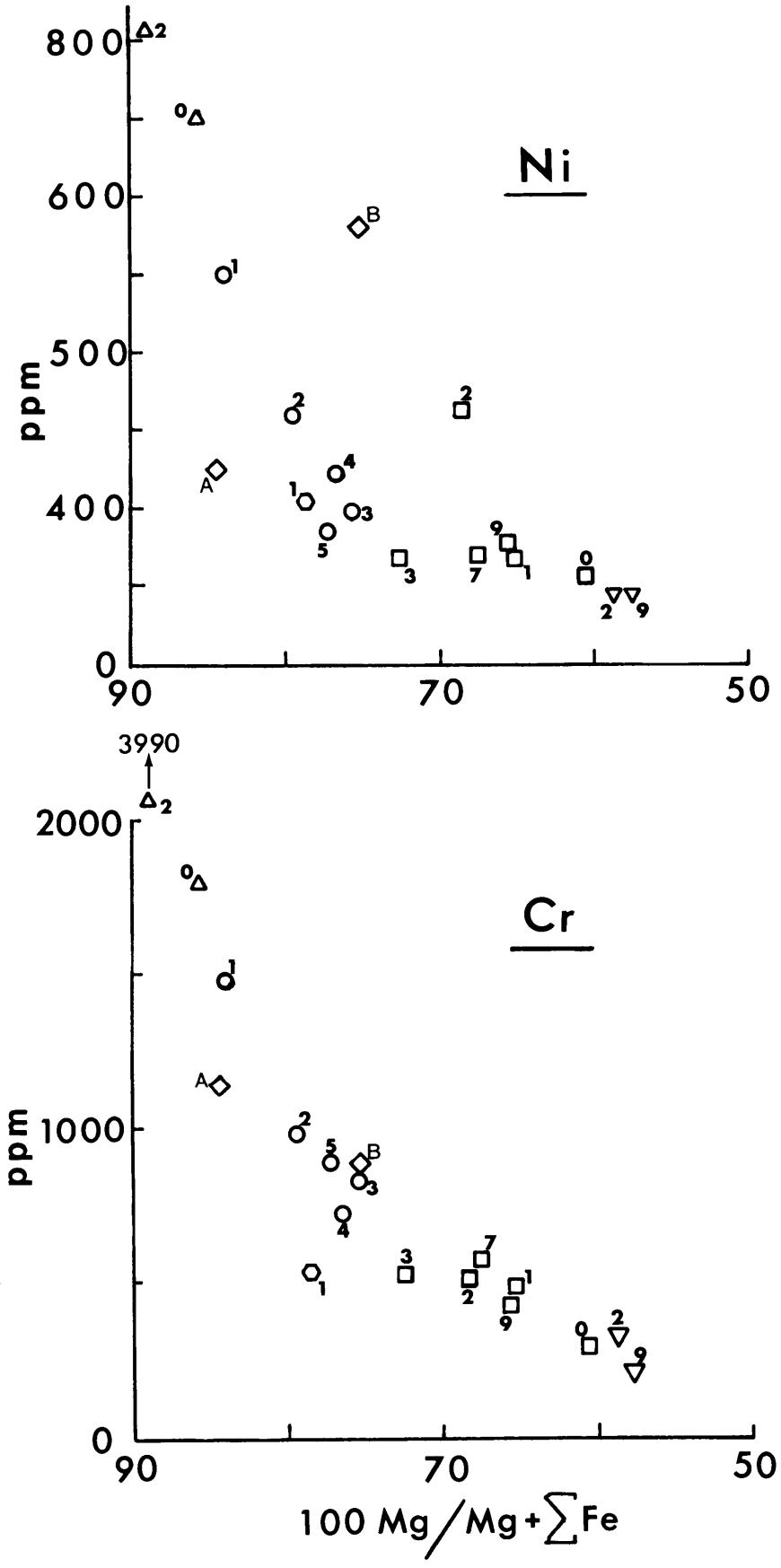
Ni
800
600
500
400
0
ppm
90
70
50
Cr
3990
2000
1000
0
ppm
90
70
50
100 Mg/Mg+∑Fe

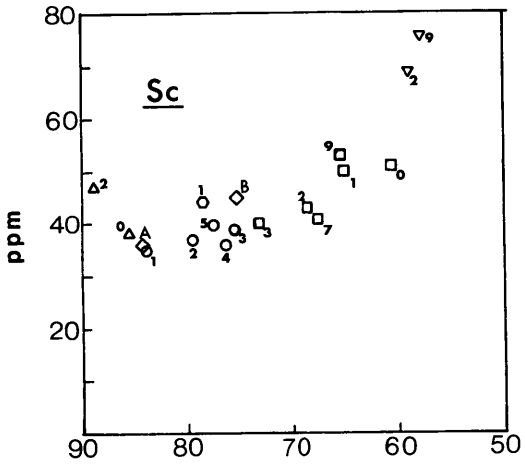
Sc
ppm
80
60
40
20
90
80
70
60
50

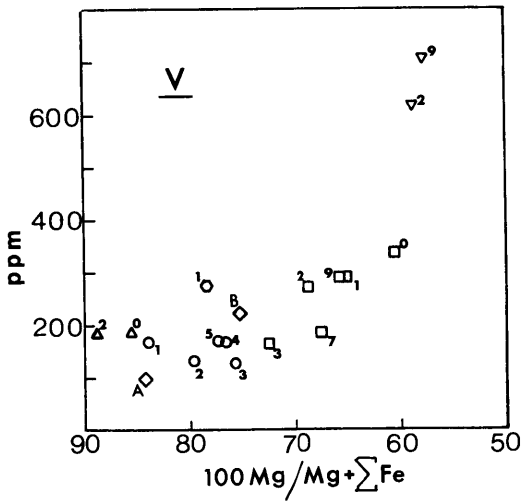
V
ppm
600
400
200
90
80
70
60
50
100 Mg/Mg+∑Fe

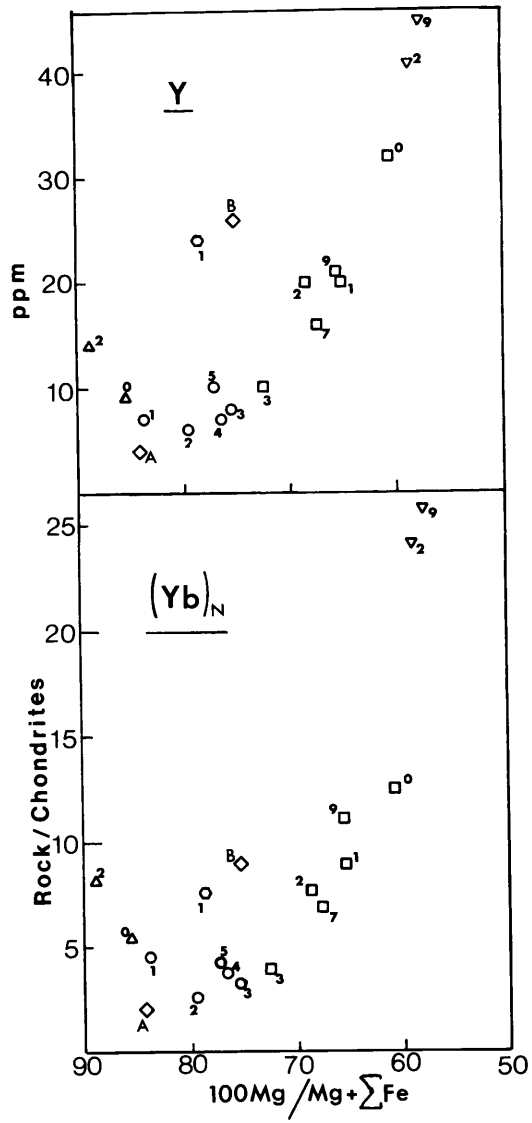
Y
(Yb)N
ppm
Rock/Chondrites
40
30
20
10
25
20
15
10
5
90
80
70
60
50
100Mg/Mg+∑Fe

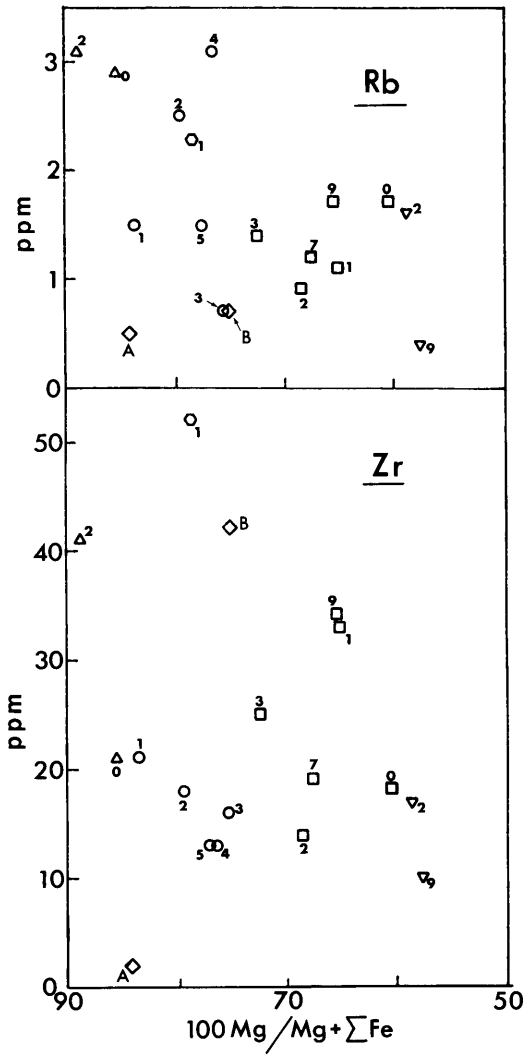
Rb
Zr
ppm
ppm
0
1
2
3
10
20
30
40
50
90
70
50
100 Mg/Mg+∑Fe

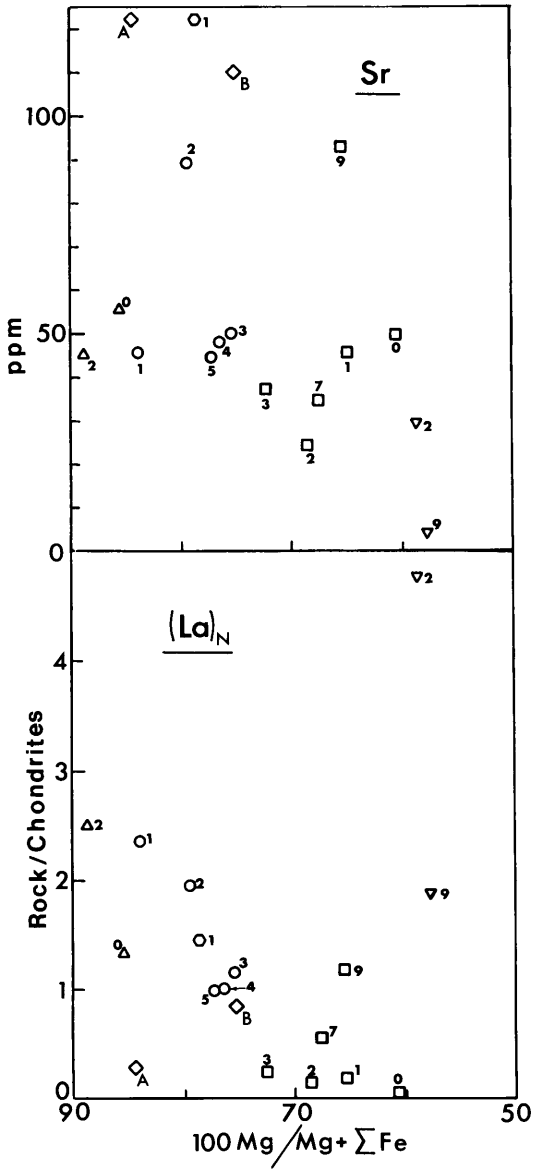
Sr
(La)N
ppm
Rock/Chondrites
0
50
100
1
2
3
4
90
70
50
100 Mg/Mg+∑Fe

FIGURE V-3: Chondrite-normalized REE patterns of the Ronda mafic layers.

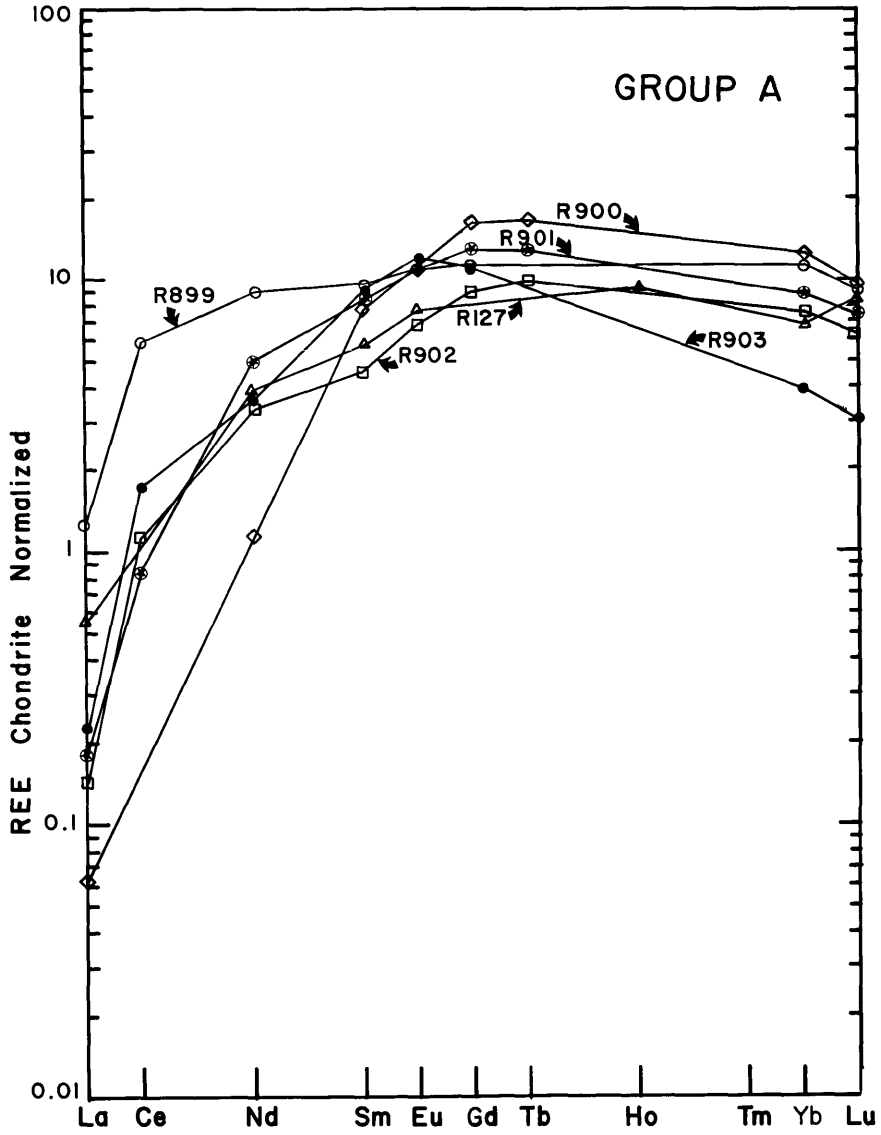
GROUP A
REE Chondrite Normalized
100
10
1
0.1
0.01
R900
R901
R899
R127
R903
R902
La
Ce
Nd
Sm
Eu
Gd
Tb
Ho
Tm
Yb
Lu

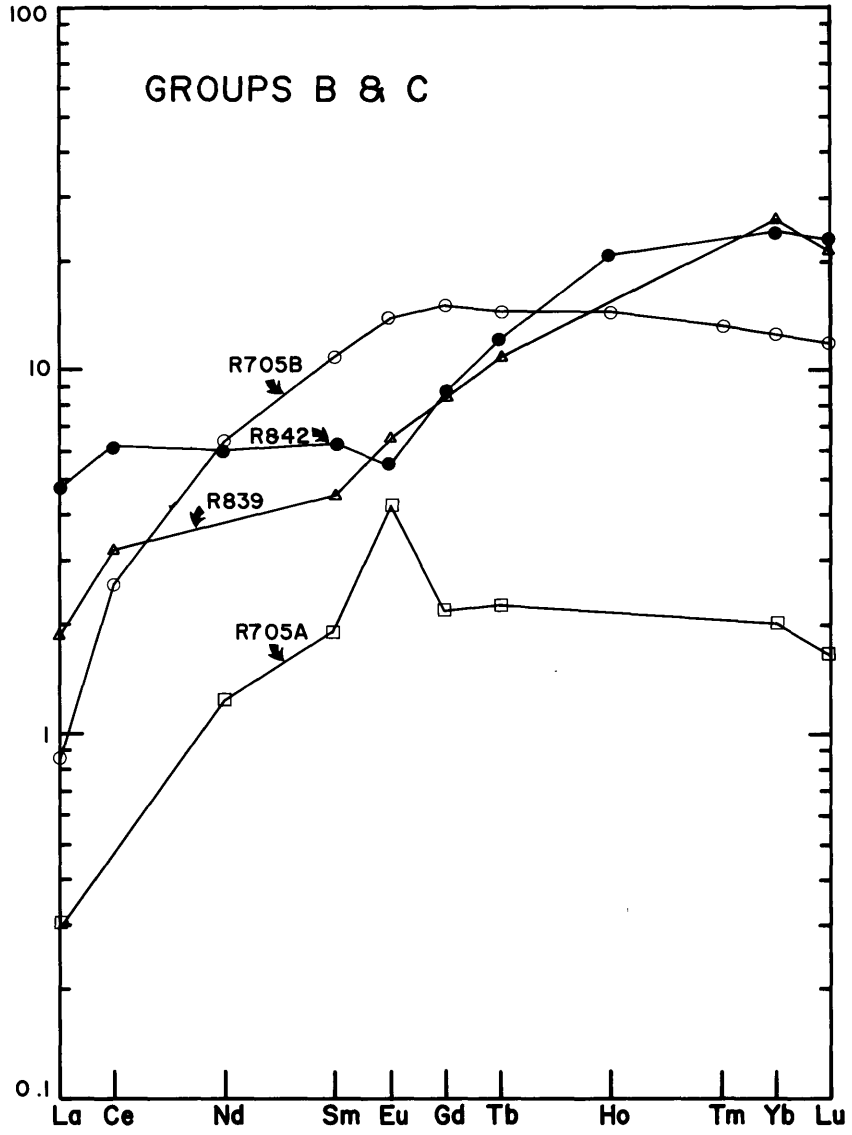
GROUPS B & C
100
10
1
0.1
R705B
R842
R839
R705A
La
Ce
Nd
Sm
Eu
Gd
Tb
Ho
Tm
Yb
Lu

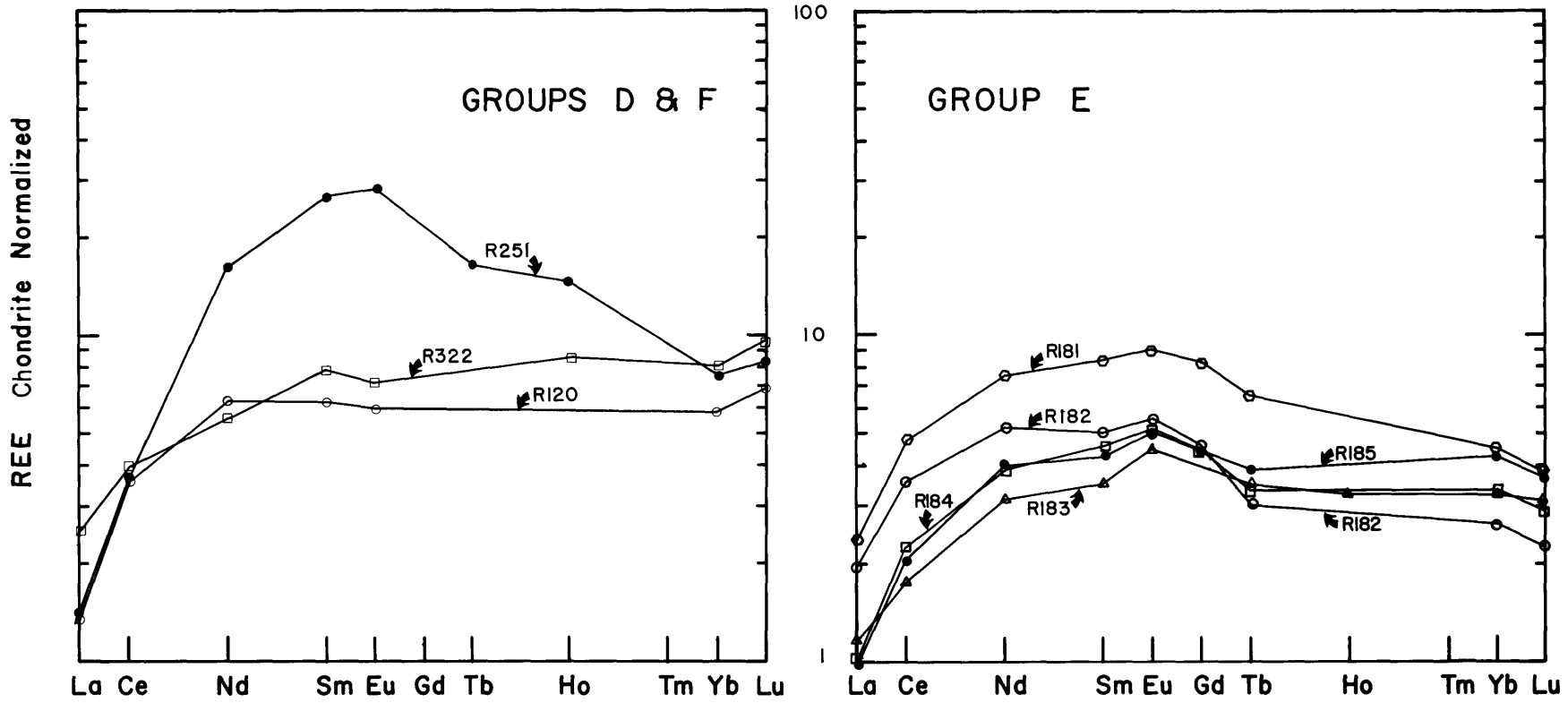
REE Chondrite Normalized
GROUPS D & F
R251
R322
R120
GROUP E
R181
R182
R185
R184
R183
R182
100
10
1
La Ce Nd Sm Eu Gd Tb Ho Tm Yb Lu
La Ce Nd Sm Eu Gd Tb Ho Tm Yb Lu

glasses from Pacific, Atlantic, and Indian Ocean sea-floor spreading centers (Melson et al., 1976) is also plotted in Figure V-1 (and it will also be shown in Figures V-4 and V-10). Note that this is only an average and a considerable amount of compositional spread exists among these glasses (see Melson et al., 1976).

In order to investigate petrogenesis in terms of high pressure mineralogy, a mantle norm calculation procedure (Appendix II-H) was used for the mafic rocks. These norms are listed in Table V-3. Groups A, B, and E (except R181) are quartz normative, and Groups C, D, and F are olivine normative. In context of the CaO-MgO-Al_2O_3-SiO_2 system, they lie close to and on both sides of the pyrope-enstatite-diopside plane. Implications of these results with respect to petrogenesis will be examined later. Also, in terms of CIPW norms, all samples are quartz undersaturated, and contain normative olivine. Also, most are hypersthene normative, with a few exceptions (R251, R182, R185) which have small amounts of normative nepheline (<4 wt.% for R251; <1 wt.% for R182 and R185). Because these rocks are of high pressure origin, only the high pressure mantle norms will be used in further discussions.

Although samples within a group show considerable compositional variation (Figures V-1 and V-2), there are geochemical parameters which distinguish these groups. The most distinct parameter that separates each group is the

100 Mg/Mg + ΣFe molecular ratio (Figure V-1, d). Except for the two samples (R705A and B) of Group B and the single sample (R251) of Group D, all other groups occupy a distinct range of 100 Mg/Mg + ΣFe ratios without overlapping as listed (in decreasing order) below:

Group F (2 samples)	88.9 - 85.5
Group E (5 samples)	84.0 - 75.6
Group A (6 samples)	72.6 - 60.6
Group C (2 samples)	58.8 - 57.7

This sequence will be used as the main trend in further discussions. The remaining 3 samples of Groups B and D have values within the range of Group E rocks.

Using the 100 Mg/Mg + ΣFe ratio as an indicator of igneous fractionation, systematic variations of trace elements can be examined. Figure V-2 summarizes the changes of trace element concentrations with 100 Mg/Mg + ΣFe ratios. Chromium, a compatible element, shows a smooth decreasing trend with decreasing Mg/Fe ratios, as does nickel, another compatible element. Both Cr and Ni have bulk solid/liquid distribution coefficients >1 for mantle mineral assemblages (olivine, pyroxenes, garnet, and spinel). Incompatible elements, which preferentially concentrate in liquids relative to solids, can be divided into roughly two groups: (1) those showing a general increasing trend with decreasing Mg/Fe ratios; and (2) those showing considerably

more scatter without well-defined trends. The first group includes Sc^{+3}, V^{+3}, Y^{+3}, and HREE (as represented by Yb^{+3}), and the second includes Rb^{+1}, Sr^{+2}, Zr^{+4}, and LREE (as represented by La^{+3}). The reason for the scatter shown by the second group of elements is not clear. An important observation is that the first group of elements are all +3 transition metals with solid/liquid distribution coefficients for pyroxenes and garnet greater than or closer to unity than the second group of elements (e.g. $D_{Sc}^{cpx/l} \sim 1.5$ [Lindstrom, 1976]), which have larger ionic radii (or higher charge, in the case of Zr^{4+}) and consequently, their $D^{S/l}$'s for mantle minerals (pyroxenes and garnet) have values much less than unity. With such more extreme values of $D^{S/l}$ (e.g. $D_{Sr}^{cpx/l} = 0.078$ [Grutzeck et al., 1974]) the second group of trace elements must be much more sensitive to fractionation processes and the proportion of the phases involved. In later discussions, wide abundance variations of such elements are expected in melts, especially in the multiple-step melting model. Alternatively, the second group, with larger ionic radius/charge ratios, may be more susceptible to metasomatic alterations. It is not impossible that the scattered data are due to such processes.

Similar to oceanic ridge basalts, the abundances of incompatible trace elements are low. However, except for Sr, which shows concentrations even somewhat lower than oceanic ridge basalts (MORB) (see, e.g., Kay et al., 1970;

Hart, 1971; Frey et al., 1974), other trace elements do not show any significant depletion relative to oceanic basalts, although many of them, e.g. Zr, have abundances in the lower range of the MORB's, corresponding to the "primitive-type" (Frey et al., 1974; DSDP Site 238, Frey, F.A., per. comm., 1977). This is particularly true for Groups A and C which are close to tholeiitic basalts in major element compositions (see, e.g., Hubbard, 1969; Frey et al., 1974; Lambert and Holland, 1977). The chondrite normalized REE patterns are shown in Figure V-3. Also similar to MORB's, all samples are depleted in LREE relative to average chondrites, but unlike them, these samples show a wider range of variations both in absolute abundances and in relative patterns. However, except for Group B (R705A and B), samples within a group have similar REE patterns and concentrations, but each group has a characteristic range of REE patterns and absolute abundances. Some samples, for example, Group C, have distinctly different patterns than common basalts or gabbros, while others, e.g., Group F, are similar to common MORB's in relative patterns.

In summary, these mafic layers range widely in composition, but samples from the same group (i.e., samples of same mineral assemblages from the same metamorphic grade, usually from same locality) are compositionally similar in both major and trace elements with only few exceptions.

Each group can be characterized by its distinct range of Mg/Mg + ΣFe ratios. In terms of mantle norms, they lie close to and on both sides of the garnet-pyroxenes plane. That is, some have normative quartz, and others normative olivine. Although the thick layers are not homogeneous in composition, it is reasonable to assume that rocks from the same group have similar petrogenetic origin, except for the few (R181, R705A and B) whose compositions are distinctly different from other members of their group. These rocks are characterized by low abundances of incompatible elements, especially K, P, and Ti, which are in lower concentrations than most of the common basalt types. Their REE patterns are variable, but consistently depleted in LREE. Both incompatible and compatible trace elements show consistent increases or decreases with increasing Mg/Mg + ΣFe ratios, except for those elements with large ionic radii like Rb, Sr, and La, which show no significant trends.

V-4: DISCUSSIONS

Previous Hypotheses for the Origins of the Ronda Mafic Layers

The significance of these mafic layers in Ronda from the petrogenetic point of view was first recognized by Dickey (1970). Based on limited compositional and field data, he suggested that these rocks are products of partial fusion of the host peridotites. Thus the peridotites

represent residues after partial fusion of the presumably upper mantle, and the mafic layers are melt that could be protobasalts. He also stated that peridotites associated with abundant mafic layers are more depleted in Si, Al, Ca, Na, and S, and more enriched in Mg and Fe relative to those associated with few mafic layers. With more analytical data and field work, this observation is not substantiated. That is, the systematic variations in peridotite compositions (Chapter II) are apparently unrelated to the abundance of mafic layers.

In order to evaluate Dickey's (1970) hypothesis in terms of phase relations, a plagioclase garnet clinopyroxenite (R127) from Group A was chosen for high P-T experimental study by Obata (1977). Experiments were carried out from 850-1500°C, 5-30 Kb using piston cylinder apparatus at the Geophysical Laboratory (Obata and Dickey, 1976; Obata, 1977). The pressure-temperature diagram obtained from these experiments for this composition (R127) indicates that at $P \leq 8$ Kb, olivine (Fo_{85}), clinopyroxene, and plagioclase all crystallize within 25°C of the liquidus, but above 9 Kb olivine is not present above the solidus. These experimental results thus provide the following constraints:

(1) If the mafic layer was formed by partial fusion of the peridotite as suggested by Dickey (1970), the melt-

ing must have occurred at less than 8 Kb, the maximum pressure for olivine as a liquidus phase. In this case, the liquid must have crystallized to olivine gabbro, and later metamorphosed at higher pressures to the present mineral assemblage.

(2) If the melting occurred at pressures greater than 8 Kb, the liquid must have undergone fractionation and its composition must have subsequently been displaced from the olivine field, because of reaction relationships with olivine at pressures between 17 and 30 Kb (Kushiro and Yoder, 1974).

The first case contradicts the conclusions drawn from the peridotite compositional data (Chapters II and III). For example, if melting occurred at pressures below 8 Kb, the peridotite would be plagioclase peridotite, but the Sr and Eu data indicate that the peridotites did not melt or fractionate in a P-T range where plagioclase peridotites are stable (Chapter II). Therefore, the hypothesis that the mafic layers are direct melt products ("orthomagmatic" [Dickey et al., 1977]) can be rejected.

Accepting the second case, Obata (1977) compared the liquidus temperature of R127 with published solidus curves of 4 peridotites. He found that the liquidus temperature of R127 is too high for a melt that has evolved from a primary melt by fractional crystallization. Alternatively,

Obata proposed that these mafic rocks are cumulates formed by such a fractionation process. His model is based on experimental information for liquidus relations at various pressures in the model system $CaO-MgO-Al_2O_3-SiO_2$.

This hypothesis will be discussed in detail in subsequent sections. It is also important to note that Obata's model is based on experimental data for only one rock composition, plagioclase garnet clinopyroxenite R127 of Group A. Because there is a wide range of compositions among these mafic layers, the cumulate model may not be applicable to all the samples studied. Nevertheless, Obata's results provide constraints for the origin of some mafic layers at Ronda.

Other Pyroxenites with Possibly Similar Origins to the Ronda Mafic Layers

Similar occurrences of mafic layers can also be found in other high-temperature peridotite bodies, for example, Etang de Lers in the Pyrenees (Dickey, 1970) and Beni-Bouchera in Morocco (Kornprobst, 1969; Dickey, 1970). The latter has been studied in detail especially by Kornprobst (1969, 1970), who carried out dry melting experiments between 1100-1550°C, from 15 to 30 Kb on four pyroxenites and a peridotite. The pyroxenite sample with the highest Mg/Fe ratio (100 Mg/Mg + ΣFe = 74.23) has the highest liquidus temperatures, which roughly matches the

solidus temperature of the peridotite at ∿28 Kb (at ∿1500°C). All other pyroxenite samples with lower Mg/Fe ratios have lower liquidus temperatures. From these results, Kornprobst (1970) concluded that the sample with the highest liquidus temperatures would be the "primary melt" formed by partial melting of a garnet peridotite, while the other pyroxenite samples with lower liquidus temperatures would be liquids formed by fractionation of the "primary melt." The composition of this "primary melt" is shown in Table IV-2 and plotted in Figure V-1 for comparison with the Ronda samples, and the hypothetical primary liquid (L_o) composition obtained in the last chapter. Note that there are considerable differences in composition between Kornprobst's "primary melt" and Ronda sample R127, and also the L_o composition, although its liquidus almost coincides (within $\pm$ 25°C at 25 Kb) with the R127 liquidus obtained by Obata (1977) in P-T space. Like R127, olivine does not exist as a liquidus phase at high pressures (P > 17 Kb). Therefore, whether it is a "primary" (i.e. orthomagmatic) liquid composition is questionable.

Loubet et al. (1976) studied pyroxenite layer samples from several alpine lherzolite bodies. Using bulk rock geochemical and isotope data, they concluded that pyroxenite layers are of residual nature, formed by melting of

orthomagmatic layers. Their model requires at least two stages of melting. In the first stage, the peridotites partially melted to derive the orthomagmatic layers, and in the second, these layers melted at lower temperatures resulting in residual solids represented by the present mafic layers. This hypothesis would imply a more complicated P-T trajectory for a rising mantle diapir than a one-stage melting and fractionation model.

In addition to pyroxenite layers in alpine peridotite bodies, garnet pyroxenites of similar compositions are found as inclusions in alkali basalt lavas. Examples are Delegate, Australia (Lovering and White, 1969; Irving, 1974); Kakanui, New Zealand (Dickey, 1968; Mason, 1968); and Salt Lake Crater, Oahu, Hawaii (Jackson, 1966, 1968; Jackson and Wright, 1970). Salt Lake Crater samples have been extensively studied by Green (1966), Beeson and Jackson (1970), Reid and Frey (1971), and Wilkinson (1976) using both experimental and geochemical approaches. The hypotheses concerning the origin of these inclusions are:

(1) (a) They originated as cumulates of liquidus clinopyroxene derived from alkali olivine basalt or basanite magmas at a pressure of 13-18 Kb (Green, 1966).
(b) O'Hara (1969) interpreted them as high pressure (close to or above 25 Kb) pyroxene-garnet cumulates from alkali basalt melts.

(2) Beeson and Jackson (1970) suggested that they are liquids (Type 4) and residual solids (Types 1, 2, and 3) resulting from partial fusion of "parental materials" related to the generation of the Honolulu Volcanic Series.

(3) By comparison with the mafic layers in alpine peridotites, Wilkinson (1976) favors the model that these pyroxenite inclusions are accidental xenoliths produced by partial melting of the upper mantle peridotites with possible subsequent fractionation processes.

Hypothesis (1,b) (O'Hara, 1969) corresponds to Obata's (1977) model, while Wilkinson's (1976) hypothesis (3) is related to the models given by Dickey (1970) and Kornprobst (1970). Hypothesis no. 2 is similar to the second stage melting model proposed by Loubet et al. (1976), and it is also supported by Wilshire and Pike (1975) who suggested multiple partial melting episodes, judging from the sequence of cross-cutting relationships of different mafic rock types in ultramafic inclusions from the western United States. However, such relationships are absent in the Ronda body.

The 4 representative type compositions from Beeson and Jackson (1970) are plotted in Figure V-1 for comparisons. Their major element concentrations lie within the

range of the Ronda mafic layer samples. For example, their 100 Mg/Mg + ΣFe values are between Groups E and F of the Ronda rocks. Their chondrite-normalized REE patterns are gently curved and convex upward with abundances between 3 to 10 times chondrites (Reid and Frey, 1971; Frey, per. comm., 1977). These patterns are very similar to those of the Groups E and F samples (especially R181 of Group E). Thus these geochemical data indicate that these pyroxenite inclusions in alkali basalts and Ronda mafic layer samples (especially those with higher Mg/Fe ratios, R181, R322, R130) may have a similar origin.

Possible Petrogenetic Models for the Origin of the Ronda Mafic Layers

The following models will be evaluated using the bulk rock geochemical data:

(1) The mafic layers represent primary melt products (orthomagmatic) from partial fusion of the mantle peridotite at high pressures. This model was suggested by Dickey (1970) and favored by Wilkinson (1976). In this model, I will evaluate the possibility that the compositional variations among these samples may be due to the gradual shifting of the invariant

point* (eutectic or peritectic) with decreasing pressures. That is, the mafic layers may represent a series of orthomagmatic liquids formed by melting of peridotite at different pressures.

(2) They are residual solids left behind after a second stage of melting that modified the compositions of the originally orthomagmatic layers formed by initial melting of the peridotites (Loubet et al., 1976). In this model, some of these layers may also be fractionated liquids produced by this second stage melting of orthomagmatic layers.

(3) The primary melt has undergone fractional crystallization at high pressures (17-30 Kb). These mafic rocks could be:

(a) fractionated liquids (Kornprobst, 1970), or

(b) high-pressure cumulates (Obata, 1977).

In addition to the above models, other possibilities include mixtures of solid and liquid (i.e. solid plus trapped melt), and a multiple-step process which consists of melting, crystal fractionation, solidification, remelt-

* Terms such as "eutectic," "cotectic," and "invariant," etc., which are used in phase equilibria studies, and strictly defined by the phase rule, are also used here in a loose sense to describe the natural rock system under study, with the assumption that it consists of only 4 components (CaO-MgO-SiO_2-Al_2O_3) and no other minor solid phases beside Ol, Cpx, Opx, Gn, or Sp. These terms are applied analogously to the model system, though they are not correct in a strict sense.

ing, etc., as summarized in Dickey et al. (1977) (Figure VI-2). A similar multiple-step process for pyroxenite bands in ultramafic inclusions has been suggested by Wilshire and Pipe (1975). I will confine my initial discussions to the one- or two-stage models listed above.

(1) Mafic Rocks as Orthomagmatic Layers

In previous chapters, the petrogenesis of Ronda peridotites has been examined in detail, and conclusions based on peridotite data provide the following constraints:

(1) As indicated by the residual compositions of the peridotites, the primary liquid (orthomagmatic layer) composition must lie close to the "extraction line" in the vicinity of the estimated liquid composition "L_o" (Chapter IV). (The relations of the "extraction line" and "L_o" to the mafic layers can also be seen in the variation diagrams of Figure V-1.)

(2) The peridotites melted at high pressures above the stability field of plagioclase peridotite. At the estimated P-T condition, ∿35 Kb and ∿1600°C, in the garnet lherzolite field, the invariant liquid should be on the olivine side of the garnet-pyroxene plane (i.e., silica undersaturated) in the CaO-MgO-Al_2O_3-SiO_2 model system, because this plane is a thermal divide above 30 Kb (O'Hara and Yoder, 1967).

(3) Trace element abundances, especially REE patterns, of the primary liquid must agree with those expected from the melting models of mantle peridotites (Chapter III).

First, let us examine the compositions of the mafic rocks in terms of the first constraint listed above. Figure V-1 shows their major element concentrations (SiO_2, Al_2O_3, CaO, FeO, and MgO) in relation to the extraction line defined by the peridotite compositions. For CaO and Al_2O_3, most samples lie above the regression line. That is, they are more abundant in CaO and Al_2O_3 relative to MgO than what is expected for the primary liquid. For ΣFeO, both the peridotites and mafic layers show considerable scatter about the regression line. Thus values estimated with this line may have large errors (Chapter IV). For SiO_2, all samples lie below the regression line, and the samples show a distinct bimodal distribution, especially well in this plot (SiO_2 vs. MgO). The first group, Group F and R181 of Group E, has higher MgO contents (19-22.5 wt.%). These rocks lie close to the regression line and the hypothetical L_o composition. This is also true in the CaO vs. MgO and Al_2O_3 vs. MgO diagrams. The second group includes all other samples which have lower MgO contents (9.2-14 wt.%) and plot away from the regression line in the SiO_2 vs. MgO diagram. In these variation diagrams, compositions of other rocks are also plotted, for example, the average Baffin Island picrite (Table 1, Column 3 of Clarke, 1970)

which was interpreted as the primary liquid produced by partial melting of garnet peridotite at 30 Kb, and also the "primary melt" from Beni-Bouchera (Kornprobst, 1970). The Baffin Island picrite lies close to the first group of Ronda samples, while the Beni-Bouchera sample lies between the first and second groups, but both are richer in Fe relative to Mg than the Ronda high MgO group. In addition, the four compositional types of garnet pyroxenites from Salt Lake Crater (Beeson and Jackson, 1970) are plotted. Their compositions generally lie between the low MgO group and the high MgO group of the Ronda samples, and they also cover a wide range of 100 Mg/Mg + ΣFe ratios.

Using these variation diagrams, the three samples of the high MgO group (namely R181, R120, R322) can be identified as rocks with compositions close to the hypothetical primary melt L_o. Therefore, they are the candidates for possible orthomagmatic layers. However, there are other criteria which they must satisfy.

Considering the second constraint, if these three rocks represent primary liquids, their compositions must lie on the silica undersaturated side of the garnet-pyroxene plane. In order to examine the composition of these mafic rocks in relation to mantle mineral compositions, high-pressure norms (Appendix II-H) are used. These are shown in Figure V-4, CaTs-Ol-Qz plane projected from Cpx; and in Figure V-5, a portion of the Al_2O_3-Wo-Opx plane projected

from Ol. (In both cases, Jd and Ca-Ti pyroxene molecules are discarded.) Also plotted are the Baffin Island picrite, the Beni-Bouchera "primary melt," and the Salt Lake Crater garnet pyroxenites (only in Figure V-4). In Figure V-4, the liquid extraction line, the peridotite compositions, and L_o composition are also shown. The Ronda mafic layers form a continuous trend from close to L_o across the garnet pyroxene plane to the SiO_2 saturated side. The three samples of the high MgO group (R181, R120, R322) lie on the SiO_2 undersaturated side close to L_o. Also plotted close to L_o are the Baffin Island picrite, and Types 1 & 2 of the Salt Lake Crater pyroxenites, which are interpreted by Beeson and Jackson (1970) as residues of fractional fusion. If the trend shown by the Ronda samples in this diagram represents a liquid fractionation trend, these samples of the high MgO group may be ortho-magmatic layers, having compositions of the primary liquid, or at least, only slightly fractionated compositions close to the primary liquid. This contention is further supported by Figure V-5. In this figure, the projection of the invariant point (Liquid + Ol + Opx + Cpx + Gn) at 30 Kb in the natural system is also plotted. The position of this point is estimated from O'Hara (1968), Figure 4, using the Baffin Island picrite (Clarke, 1970, Table 1, Column 3,

FIGURE V-4: Compositions of the Ronda samples projected onto the CaTs-Ol-Qz plane from Cpx. The regression line and "L_o" composition are also shown. All symbols are the same as in Figure V-1. The Salt Lake Crater garnet pyroxenite inclusions (Beeson and Jackson, 1970) are enclosed by the dotted line. The dashed line joins the bulk composition of R127 and R127G, composition of glass obtained from experiments (see text).

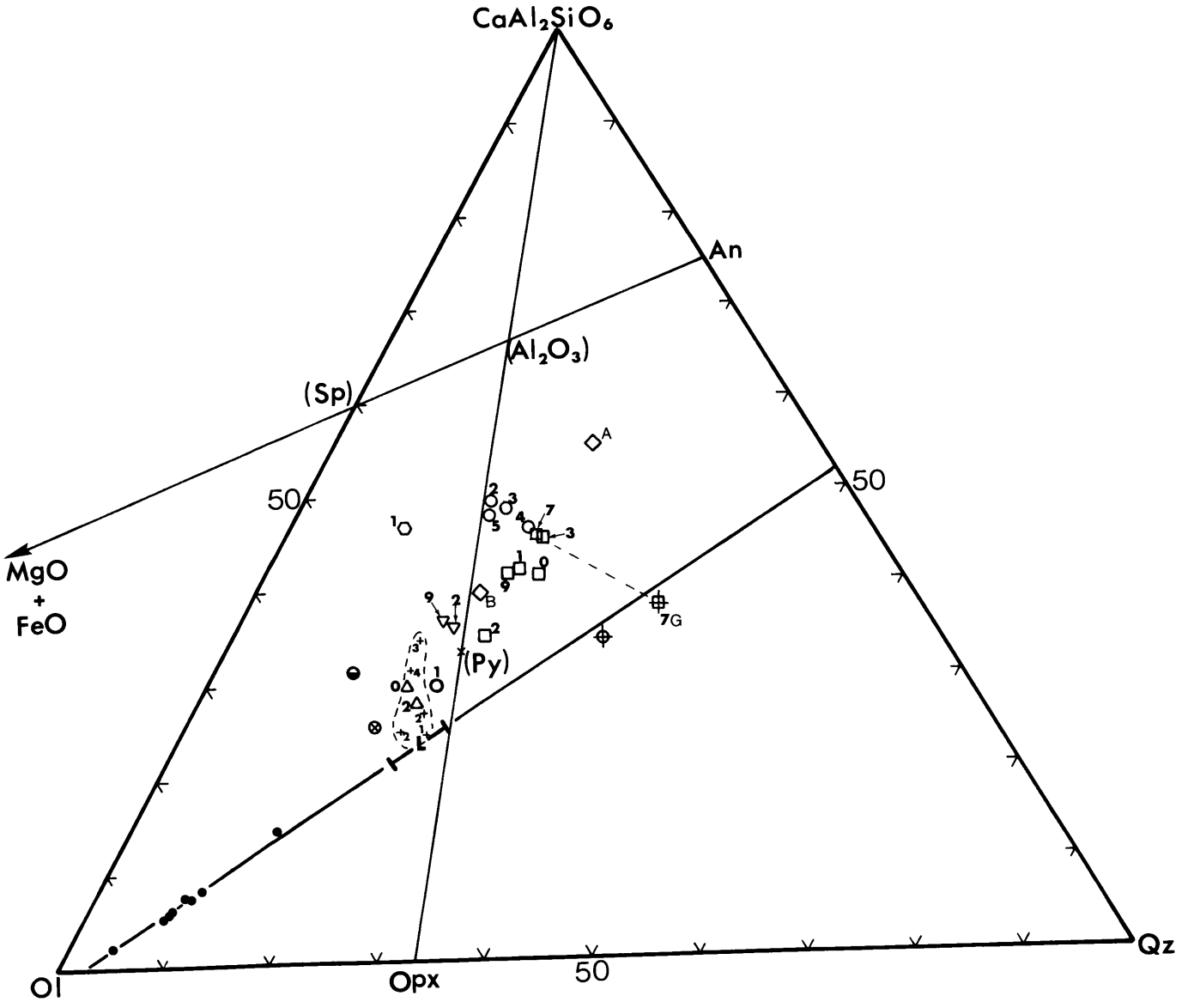
$CaAl_2SiO_6$
An
(Al_2O_3)
(Sp)
50
50
MgO
+
FeO
(Py)
Ol
Opx
50
Qz

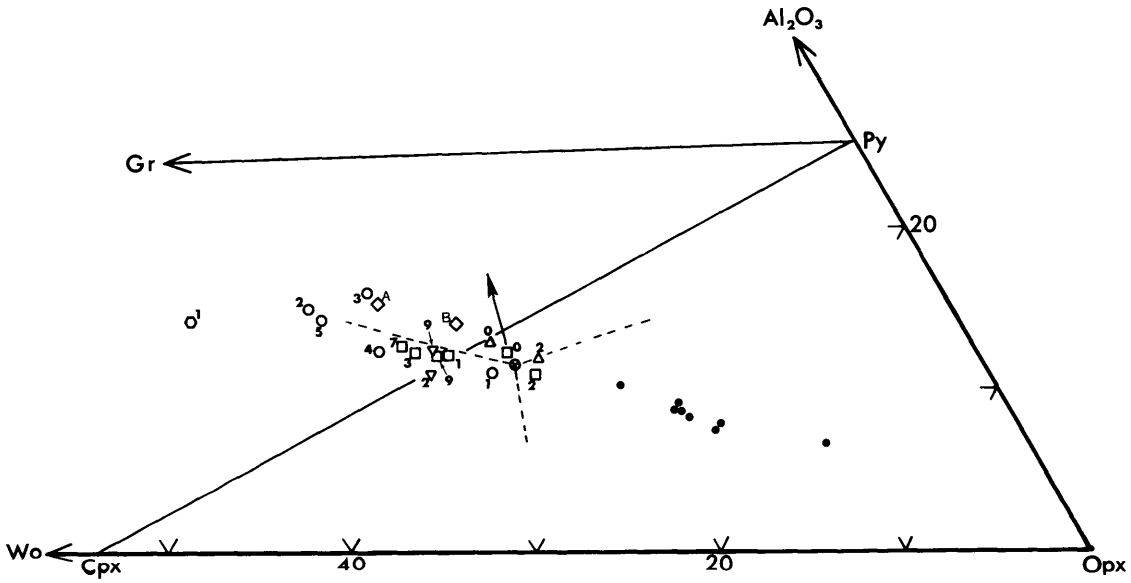

FIGURE V-5: A portion of the Al_2O_3-Wo-Opx plane. The Ronda mafic layers have compositions which lie both on the silica saturated and silica undersaturated sides of this plane. All of them are projected on this plane from olivine (i.e. both forward and backward). Symbols used are the same as in Figure V-1. The estimated invariant point at ∿30 Kb is shown by dotted lines, and it would shift in the direction of the arrow with decreasing pressure (O'Hara, 1968).

and Figure 7) as a reference composition*. The three high MgO samples plot close to this hypothetical invariant liquid composition.

From the above analysis, it can be concluded that the major element compositions of the high MgO group of the Ronda mafic layers lie close to the expected primary liquid composition L_o, and they also satisfy the constraint based on experimental petrology. Furthermore, their compositions agree closely with O'Hara's (1968) invariant composition at 30 Kb in the natural system, similar to the Baffin Island picrite composition, which is interpreted by Clarke (1970) as primary magma from melting of garnet peridotite at 30 Kb. In contrast, Kornprobst's (1970) candidate for primary melt from Beni-Bouchera does not fit well into this model. As mentioned before, his interpretation may be incorrect.

Trace element data provide important independent constraints on the orthomagmatic model because trace element abundances are more sensitive than major elements to solid/liquid fractionation processes (e.g. Gast, 1968).

---

* The compositions of the end-members (C-M-A-S) used by O'Hara (1968) do not correspond exactly to the normative mineral compositions (Al_2O_3-Wo-Opx) used in this work. As a result, the relative positions plotted in O'Hara's projection are different from those shown here. The invariant point in Figure V-5 is estimated by using known reference compositions, e.g., the Baffin Island picrite (Clarke, 1970).

For example, if 90% of the primary liquid crystallized with loss of the last 10% of fractionated liquid, the major element composition would be close to that of the initial liquid, but incompatible trace element abundances would be markedly lower.

In order to evaluate trace element constraints on the orthomagmatic model, I will incorporate the conclusions of Chapter III; that is, the liquid extraction process is efficient and effective, for example, in 1% melt increments with little or no trapped melt, and that the lower set of distribution coefficients are more realistic than the higher set (Appendix II-G). Unlike trace element abundances in residual solids during partial melting (as already discussed in Chapter III), trace element concentrations, and therefore REE patterns, of the liquids produced by fractional or multiple-step meltings may show a wide variation of trace element patterns. This is because each increment of liquid produced has a different REE pattern, and the REE pattern of the total liquid is the integral average of all liquid fractions or increments produced. Note that liquids with strongly varying trace element abundances may have similar major element compositions controlled by the invariant point in the phase diagram. In reality, there are several possibilities. If the melting increments are collected and mixed together, for example, in a magma chamber beneath a volcano, the aggregate liquid

has concentrations equal to those of the total liquid (C_k^L or $\bar{C}^l$, see Chapter III). Alternatively, if the increments remain separate and crystallize without mixing, the concentrations in each increment must equal the instantaneous liquid concentrations (C_k^l for multiple-step melting). Finally, in intermediate cases, the increments may be only partially mixed. For example, in the case of 1% melting increments, if only liquids from step 10 to step 15 are mixed to form one batch of liquid, the trace element pattern of this batch of liquid would be the average of these six increments ($\frac{1}{6}\sum_{k=10}^{15} C_k^l$, assuming each increment is of the same size) resulting in an integral average pattern somewhere between step 10 and step 15. Therefore, if a series of evolving REE patterns are plotted, the REE pattern in the average liquid from steps 10 to 15 must lie conformably between those of earlier and later increments; that is, there are no cross-cutting relationships in the REE distribution.

Using the models developed in Chapter III, calculated REE patterns are plotted in Figure V-6 and Figure V-7, with the assumption of initial REE abundances equal to two times chondrites. In Figure V-6, the cross-hatched area represents a range of REE patterns of total liquids produced by fractional and batch melting of peridotites containing garnet and without garnet. For the garnet absent case, the degree of melting is from 15 to 20%, and

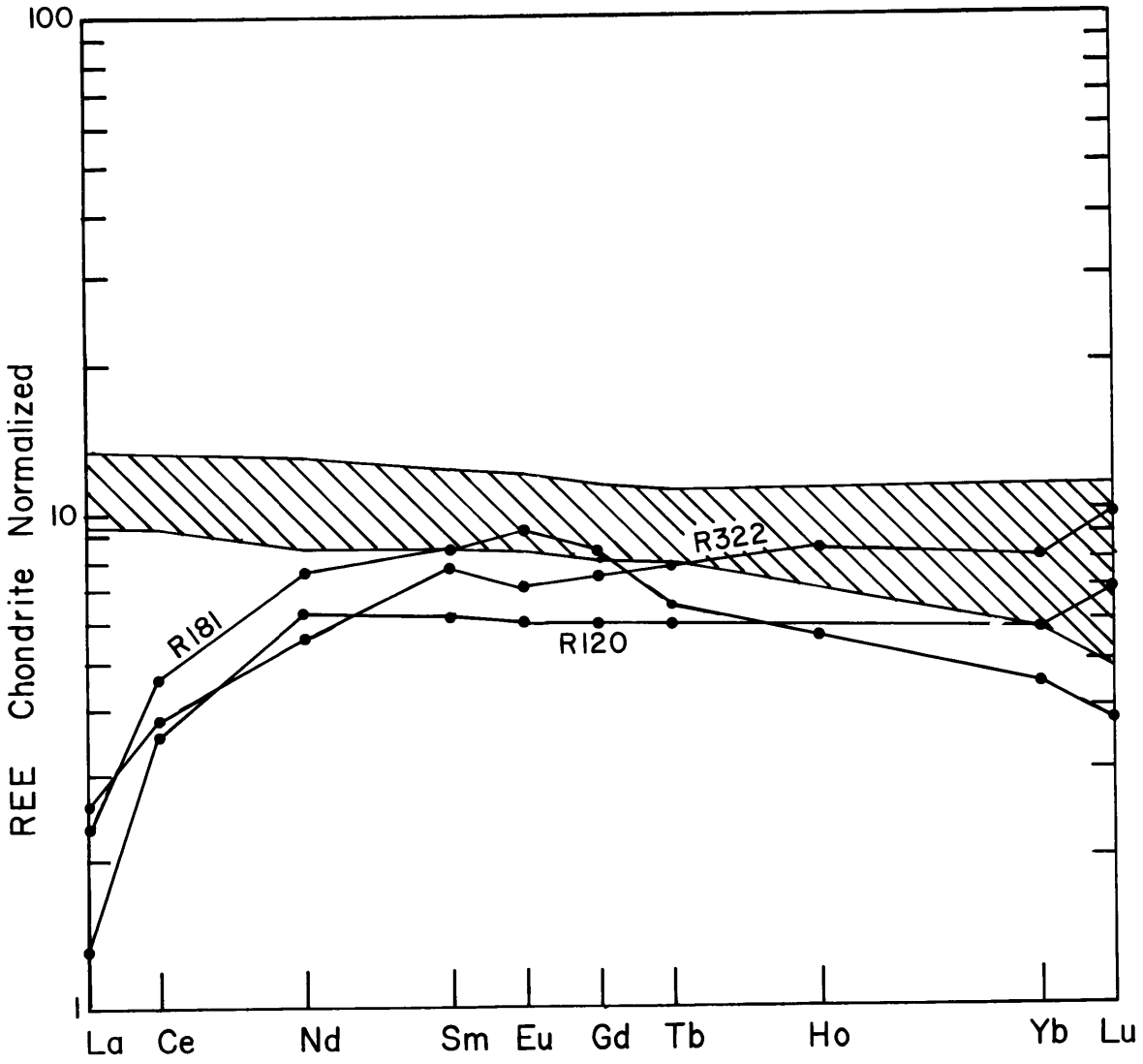

FIGURE V-6: The REE patterns of the high MgO group as compared to the range of calculated total liquid patterns (cross-hatched area) generated by 15 to 20% of melting of a mantle source with initial REE abundances equal to two times chondrites according to Model II given in Chapter III.

for the case with garnet, it is at 15%, because garnet is exhausted at 15.6% in the model (Chapter III). The total liquid patterns produced by the multiple step melting model must lie within this range. Even with this non-discriminating all-out approach, the possible range is rather restricted* as shown in this diagram. REE data for the three samples of the high MgO group are also plotted. The HREE abundances in Group F gabbro (R322 and R120) are within or close to the calculated range, but HREE in R181 are lower than in the calculated total liquid. In contrast, the LREE abundances in these Ronda mafic layer samples are much lower than in the calculated models, and more significantly compared to chondrites, the LREE are depleted relative to HREE. Thus the slope of the REE pattern is opposite to that predicted. The calculated range of REE patterns represents total liquids produced by 15-20% of melting starting with two times chondritic REE abundances. For smaller degrees of melting, the LREE are even more enriched in the calculated total liquids. Therefore, from this figure, the following conclusions can be drawn:

(1) If the Group F gabbros are total liquids from less than

---

* Only the low set of distribution coefficients is considered here. If the high set is included, the lower limit of the HREE will go down by a factor of 2, the upper limit of the HREE and the range of the LREE will remain unchanged.

20% of melting, the source peridotite must have a LREE depleted pattern initially, but this does not agree with the findings in Chapters II and III.

(2) Those rocks do not represent total liquid compositions. They may be incremental liquids or batches of liquid formed by mixing of several consecutive liquid increments (or instantaneous liquid fractions in the case of fractional melting). Considering the field occurrences of these mafic rocks, these possibilities are reasonable, because these layers were probably conduits for liquid transport and not chambers where the liquids could be mixed.

(3) R181 of Group E does not represent any total liquid.

Conclusions (2) and (3) imply an important role for the multiple-step melting model. Figures V-7 (a) and (b) show the evolution of incremental liquid patterns for every 5-step interval. Each line is, therefore, a calculated REE pattern of the liquid extracted in that specified step (Step 5, 10, 15, etc.). It is assumed that the extraction process is both efficient and effective, with $F_o = 0.01$ and $f_o = 0.005$ (Case L, Table III-3). The case with garnet is shown in (a); without garnets, in (b). Garnet affects the HREE and causes HREE abundances to increase with increasing degrees of melting. In contrast, LREE abundances decrease as melting increases, and criss-

crossing REE patterns result (Figure V-7,a). Without garnet, both LREE and HREE decrease sympathetically with increasing degrees of melting. In diagram (7a), R181 is plotted. The calculated patterns of Steps 15-20* are slightly convex upwards with LREE depletion relative to chondrites, and comparable REE abundances to sample R181. Although the match to the calculated REE patterns is not exact, the fit is considered to be good when uncertainties in modelling parameters (e.g., distribution coefficient), and analytical errors are considered. In diagram V-7(b), the calculated liquid patterns are relatively unfractionated in the HREE region and they change from LREE enriched to LREE depleted as melting proceeds. The Group F gabbros (R120 and R322) fit well between Step 20-30**.

The above analysis shows that these rocks with relative LREE depletion can be primary liquids as their major element compositions indicate. As melting progresses, the major element compositions of each liquid increment remains relatively constant at the invariant point (provided that P and T remain constant, and no phase is consumed); however, their trace element contents vary according to the extent of the melting process. This result is very significant when interpreting trace element

---

* Equivalent to approximately 7.5 to 9.5% of total melting.

** Equivalent to approximately 10-15% of total melting.

FIGURE V-7: Comparing the REE patterns of the high MgO group with incremental liquid patterns as obtained by Model II (Chapter III). Diagram (A) corresponds to melting with garnet as a residual phase; diagram (B) corresponds to no garnet. The extraction process is assumed to be both efficient and effective, with $F_o = 0.01$ and $f_o = 0.005$ (Case L, Table III-3). The numbers on each curve are step numbers, not percent of melting or extraction.

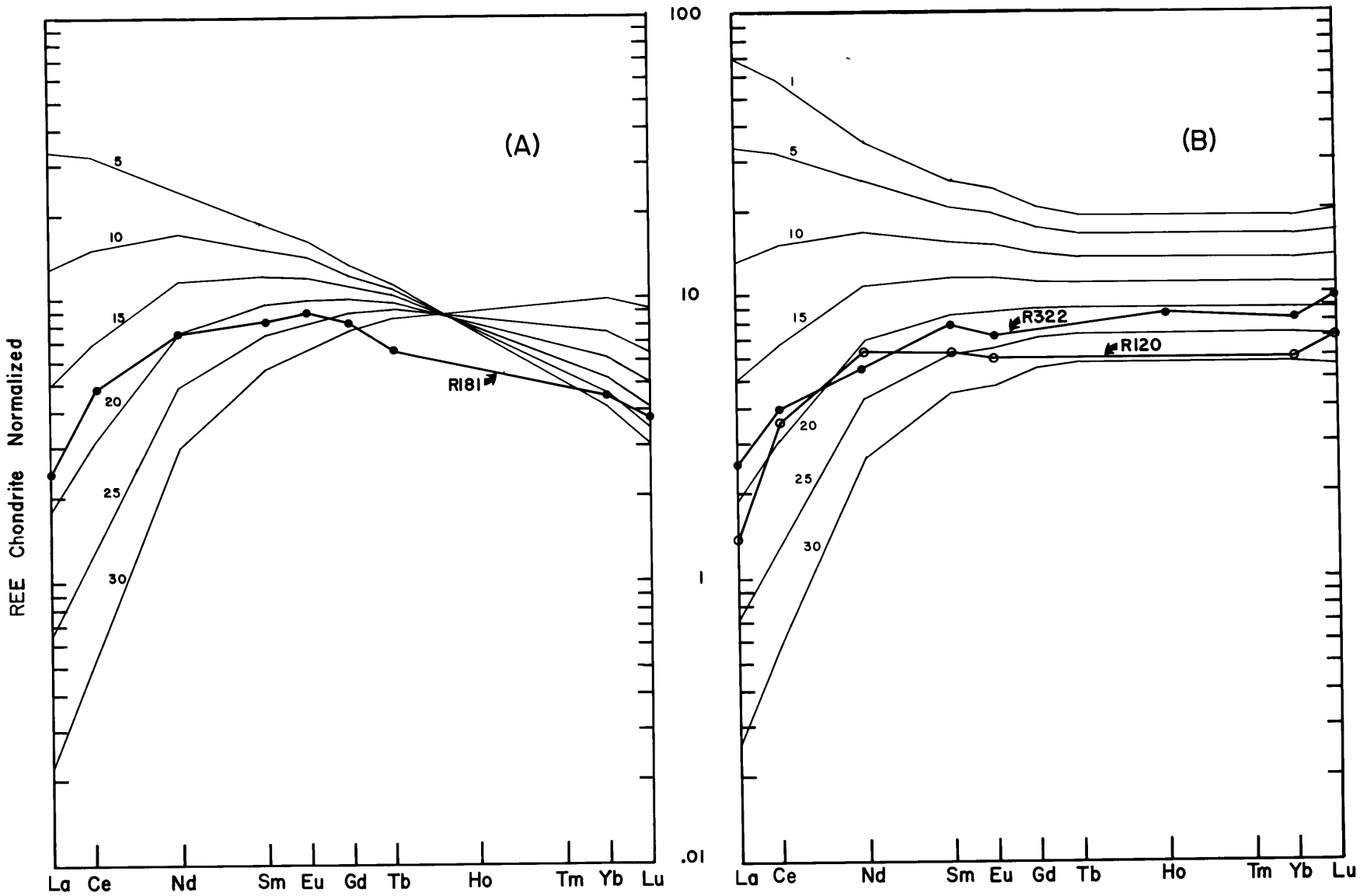
REE Chondrite Normalized
100
10
1
.01
(A)
(B)
1
5
10
15
20
25
30
R181
R322
R120
La Ce Nd Sm Eu Gd Tb Ho Tm Yb Lu

concentrations in liquids.

In the Ronda case, a difficulty with this model is that the earlier increments with relative LREE enrichment have not been found within the Ronda massif (no sample analyzed has the appropriate REE pattern), and we must postulate that all such liquids escaped from the peridotite massif.

Before any firm conclusions are drawn about the ortho-magmatic origin of these 3 samples, the Mg/Fe ratios must also be considered (Figure V-1, d). As discussed in the last chapter, the Mg/Fe ratio of the hypothetical L_o composition is a little too high to satisfy the equilibrium partitioning of Mg and Fe^{2+} between olivine and liquid using the K_D values from Roeder and Emslie (1970). Although L_o is close to the composition of the Baffin Island picrite (Clarke, 1970)(with 100 Mg/Mg + ΣFe = 77.1), it has a lower Fe content (100 Mg/Mg + ΣFe = 81.6). Considering the uncertainties due to a large scatter in the peridotite data of the regression line (Figure II-10, d and Figure V-1, d), the Fe content of L_o could be higher. However, the three samples under consideration have even higher Mg/Fe ratios than L_o. For example, the 100 Mg/Mg + ΣFe of R322 is as high as 88.9. Using the lherzolite with the highest Mg/Fe ratios (R845) as a residual solid in equilibrium with liquid, and a K_D range of 0.25 to 0.35

(Roeder and Emslie, 1970), the acceptable range of 100 Mg/Mg + ΣFe of the coexisting liquids is approximately 70 to 77. Therefore, the high values (84-89) of these rocks preclude an origin as primary liquids. If this is true, why are the REE and major element abundances consistent with primary liquids?

An alternative model is that this high MgO group of rocks are very early high-pressure cumulates from the primary melt. The first cumulates formed by crystal fractionation of such a liquid (between 9 and 25 Kb) would be Sp + Cpx + Opx, which is undersaturated with silica in the mantle norm (Obata, 1977; see also discussion in a later section), and their major element compositions may be close to that of the initial liquid (as shown later in Figure V-10). A cumulate model also explains the depletion in LREE and other incompatible elements, like K and P. However, if an initial liquid produced by 15-20% melting with a REE pattern within the range shown in Figure V-6 is assumed, it can be shown by simple equilibrium models that the early cumulates (i.e. small degree of solidification) of spinel and pyroxenes cannot have their REE abundances as high as the initial liquid as seen in Figure V-6. If these samples do not represent pure cumulate solids, but are mixtures of cumulate minerals and trapped liquid, then their REE abundances are expected to

be higher, that is, displaced closer to the initial liquid pattern. In this case, however, their Mg/Fe ratios must be lowered simultaneously towards the initial liquid value. Alternatively, if the higher set of distribution coefficients is chosen instead of the lower one, these cumulates would have calculated REE abundances closer to the initial liquid. The hypothesis that the Ronda mafic layers are of cumulus origin will be discussed further in a later section.

Finally, consider the trend shown by the mafic layers in Figure V-4. These points may represent the variation of invariant compositions with decreasing pressure, because at lower pressures below 30 Kb, the invariant point is on the SiO_2 saturated side of the garnet-pyroxene plane (Yoder and Tilley, 1962; Yoder, 1974). If the peridotites melted during adiabatic decompression, and all the mafic layers are orthomagmatic, this trend may indicate the trace of the shifting invariant composition with decreasing pressures. This notion is schematically shown in Figure V-8. If this model is valid, the high MgO group (SiO_2 undersaturated) would be earlier melts at high pressures, while the low MgO group (SiO_2 saturated) would be later melts at lower pressures. However, this relationship cannot be true, because melts generated at later times by melting of more depleted peridotites of

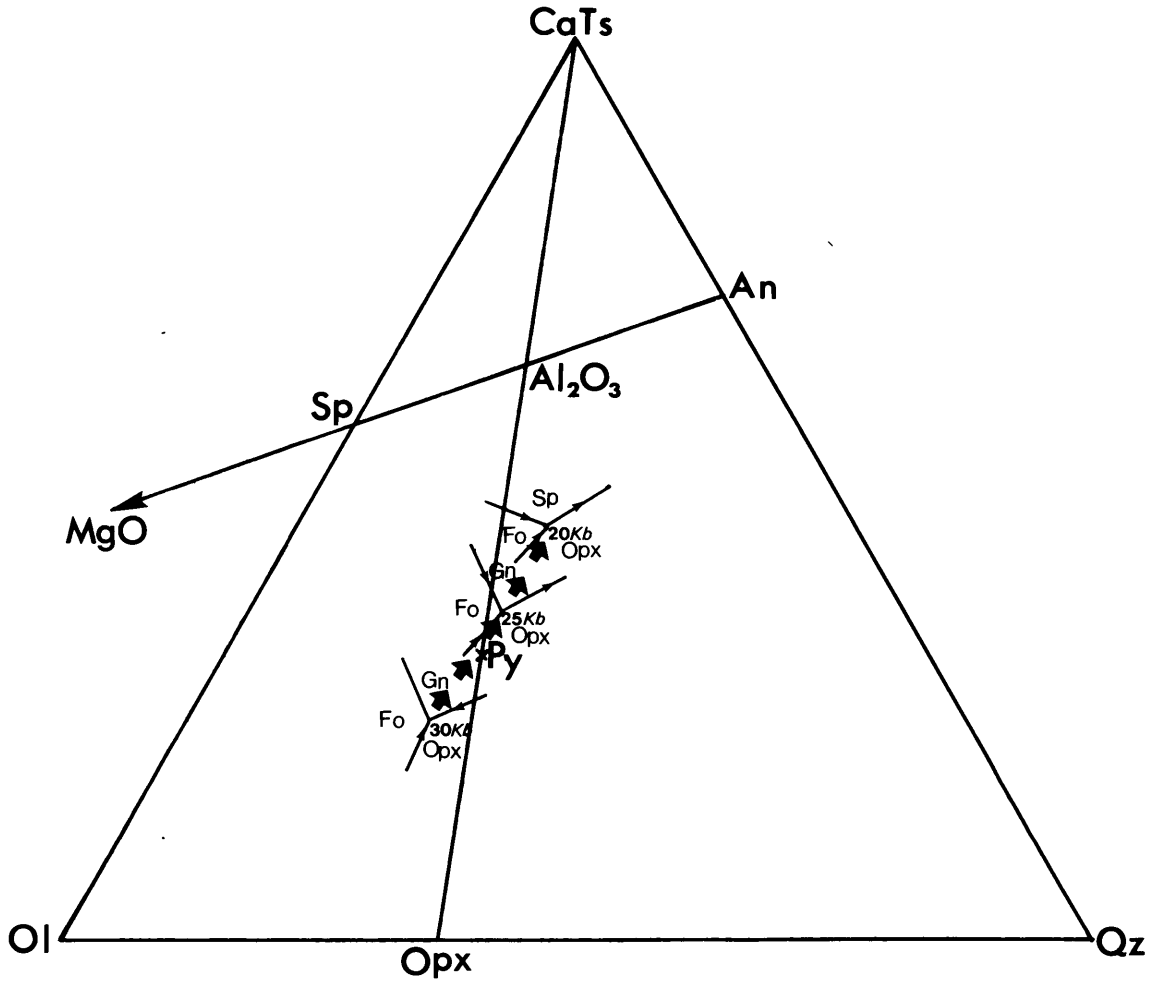

FIGURE V-8: Same projection as in Figure V-4. The possible variation of the invariant composition with decreasing pressure is schematically shown in this diagram.

higher Mg/Fe ratios should have higher Mg/Fe ratios. The relative positions of the mafic layer groups along this hypothetical trace (Figure V-8) do not agree with their Mg/Fe ratios. Also, such a trace as estimated from O'Hara (1968) as shown in Figure V-5 does not coincide with the compositional trend of the Ronda mafic layers. In addition, high P-T experiments by Obata (1977) on the R127 composition are not consistent with this model.

In conclusion, only the high MgO group of the Ronda mafic layers (R120, R322, R181) are possible candidates for orthomagmatic layers. However, their high Mg/Fe ratios indicate a cumulate origin, but in this case either a large percent of trapped liquid must be present or the high set of D's must be taken into account for their trace element patterns.

(2) Mafic Rocks as Products of a Second Stage Melting of Orthomagmatic Layers

Loubet et al. (1976) suggested that the mafic rocks in alpine-type peridotite bodies are residues after a second melting stage affecting only the mafic rocks formed by an earlier stage of melting of the peridotites. Furthermore, Wilshire and Pike (1975) also concluded that composite lherzolite-pyroxenite xenoliths in alkali basalts have undergone multiple partial melting episodes. In this

model, it must be assumed that during the second melting stage, the layers do not equilibrate with the host peridotites. Otherwise, the melt generated would be at the invariant point for peridotite melting at a lower pressure, and this model is identical to the case of shifting invariant compositions as previously discussed. Thus the orthomagmatic layers must behave as closed systems during melting. In this model, the mafic layers may be:

(1) solids left after the second melting stage; or

(2) fractionated liquids formed during this melting.

In the first case, their compositions should show residual characteristics relative to the primary liquid; however, the data are not consistent with this relationship. For example, all members of the low MgO group have lower Mg/Fe ratios than the primary liquid L_o, and at the same time, they have higher CaO and Al_2O_3 contents. Therefore, they cannot be residual solids left by partial fusion of orthomagmatic layers.

Alternatively, if the high MgO group of the mafic layers represent residues, then the low MgO group would be fractionated liquids. The Mg/Fe ratios and magmaphile element abundances indicate that the low MgO layers are more fractionated than the assumed orthomagmatic compositions. However, their REE patterns (e.g. see Group A) are not LREE enriched as expected if they are fractionated

liquids formed by melting of orthomagmatic layers with REE patterns in the range shown in Figure V-6. Of course, an incremental model could be utilized. Because the increments of primary liquid have variable REE patterns (Figure V-7) from LREE enriched to LREE depleted, it is possible that the layers with relative LREE depletion were formed by melting of orthomagmatic layers with extreme LREE depletion. Alternatively, these layers could also be incremental liquids of the second melting episode. Because there are no direct indications to provide controls for simple modelling, direct model calculations are futile. At the same time, such complexities are possible. However, for every sample with a relative LREE depleted pattern, these models require other samples with complementary relative LREE enrichments. We have found no samples with relative LREE enrichment, and these models are valid only if such liquids were completely lost from the peridotite body, or if the analyzed sample population is extremely biased by coincidence. Because <u>all</u> the layers analyzed have relative LREE depletions, these models are unrealistic for statistical reasons.

There are additional arguments demonstrating that the low MgO layers are not fractionated liquids formed by fusion of orthomagmatic layers. For example, this model requires that the layer liquidus temperatures match the

solidus temperatures of the orthomagmatic layers which must be lower than the peridotite solidus. Experimental results of Obata (1977) show that the liquidus temperatures of one sample (R127) either coincides with or is higher than peridotite solidus curves of reasonable mantle compositions (see Figure 6-3 of Obata, 1977). Therefore, the liquidus temperature of R127 (Group A) is not consistent with this model.

In addition to geochemical arguments, two-stage melting requires a more complicated P-T trajectory for the diapir. A drastic change in P-T trajectory slope is required for the temperature to cool below the solidus of the ortho-magmatic layers, and then to intersect the solidus again at a later stage, presumably at lower pressures. While such a trajectory is not impossible, it is tectonically difficult to model. Because similar occurrences of mafic layers are found in several alpine peridotites (Loubet et al., 1976) their origin appears to result from a general phenomenon rather than a set of specific circum-stances.

(3) Mafic Rocks as Products of High-Pressure Crystal Fractionation

If the mafic layers are products of high-pressure crystal fractionation, they may be:

(a) fractionated liquids;

(b) high-pressure cumulates* (solids).

The first hypothesis was suggested by Kornprobst (1970), and the second by Obata (1977). We shall examine these proposals in order.

(a) As suggested by Kornprobst, some mafic layers represent primary melt, while others are liquids formed by fractionation of the primary melt. If this is true, then a necessary corollary is that some layers are fractionated solids, i.e. cumulates. Alternatively, the fractionation process occurred outside the peridotite body, and the liquids are foreign to the massif. We assume that the liquids are generated within the peridotite body because compositional data for the peridotites show that they are residues from partial melting.

Previously, for geochemical and experimental reasons, I concluded that the Ronda mafic layers are not fractionated liquids. Therefore, this model requires that the fractionated liquids, which are enriched in LREE and other incompatible elements, such as K and P, have been extracted from the peridotite body, leaving behind cumulates which may represent mixtures of cumulus crystals and trapped

---

* The term "cumulate" refers to products formed by crystallization from a melt. It does not necessarily infer any settling process due to gravity.

liquids.

(b) Obata (1977) summarized liquidus relations at various pressure intervals in the system CaO-MgO-Al_2O_3-SiO_2 (Figure V-9). Although exact positions and orientations of the cotectic lines are not well known, these schematic diagrams are based on experimental data (Kushiro and Yoder, 1966; O'Hara and Yoder, 1967; O'Hara, 1968; Kushiro and Yoder, 1974), and they are topologically accurate. The projection used in these diagrams are the same as in Figure V-4 where actual rock compositions are plotted in terms of mantle normative mineral compositions. According to this high-pressure cumulate model, the proposed petrogenesis of the Ronda mafic layers is summarized in Figure V-10. In this figure, the liquidus relations are superimposed onto the plotted compositions of the natural rocks. The cotectic lines are constructed according to the topologic relations shown in Figure V-9(c) and (d), between 17 and 15 Kb. The positions and orientations of these curves are partly constrained by the observed compositions to fit the model and partly schematic. This model can be described in several stages:

Stage 1: If the peridotites melt at above 30 Kb as proposed earlier, the primary liquid composition is at L_o, on the SiO_2 undersaturated side of the garnet-pyroxene plane. As the diapir rises, pressure drops below 30 Kb,

the invariant point (Cpx + Opx + Ol + Gn + liquid) is then located on the SiO_2 saturated side of the garnet-pyroxene plane. The liquid at L_o is now within the olivine volume, and must crystallize olivine driving the residual liquid directly away from the olivine corner to L_1. This olivine crystallization process may generate the dunites adjacent to the mafic layers. Such dunites have been commonly observed in the Lanzo peridotites (Boudier and Nicolas, 1977). Below 25 Kb, spinel replaces garnet at the invariant point X. L_1 does not necessarily coincide with point X, but they are close in this diagram.

Stage 2: Eventually, the liquid will reach X by either precipitating Cpx + Opx + Ol, or Cpx + Ol + Sp. If this happens between 25 and 30 Kb, the latter assemblage would be replaced by Cpx + Ol + Gn. This stage of fractionation would be brief, and thus insignificant.

Stage 3: As temperature drops further, the liquid will follow the univariant line X-Y while crystallizing Cpx + Opx + Sp. Note that cumulates formed at this stage are undersaturated with SiO_2. Therefore, the high MgO group of Ronda mafic layers (Group F and R181 of Group E) can be formed by this process.

Stage 4: At point Y, garnet appears as the liquid leaves the spinel field. With decreasing temperature the liquid follows the Gn + Cpx + Opx cotectic line. However,

the liquid can leave this line by the reaction relation Opx + liquid → Gn + Cpx, which was found to exist at 20 and 30 Kb (Tilley and Yoder, 1964; O'Hara and Yoder, 1967). This is shown by the curve Y-Z. Therefore, the predicted cumulates are Cpx + Opx + Gn followed by Cpx + Gn. Judging from the composition of the liquid relative to garnet and ortho-pyroxene, the former assemblage may not be formed because the reaction is likely to occur at or close to point Y. Such cumulates should have compositions on the garnet-pyroxene plane, and plot along the CaTs-Opx line in Figures V-4 and V-10. However, if trapped liquid is present, they would be displaced to the silica saturated side, because the liquids in equilibrium with the crystals are silica saturated. These predicted cumulates can account for the origin of Groups E, A, and C (Figure V-10).

The point R127G in Figure V-10 is the composition of experimental interstitial glasses (Obata and Dickey, 1976) in equilibrium with garnet and clinopyroxene at 25 Kb, between 1400 and 1375°C, for the composition of R127 of Group A (Dickey et al., in press). Therefore, the liquid path, Y-Z, must pass through this point where it is also tangential to the line joining the point and R127 bulk composition, if R127 is formed by cumulating garnet and clinopyroxene.

Mg/Fe ratios and trace element data indicate a fractionation sequence from Group E (except R181) to

FIGURE V-9: Liquidus relations in the system CaO-MgO-Al_2O_3-SiO_2 in different pressure intervals, shown by the same projection as in Figures V-4 and V-8. This figure is taken from Obata (1977, Figure 6-4) who constructed the diagrams according to published experimental data.

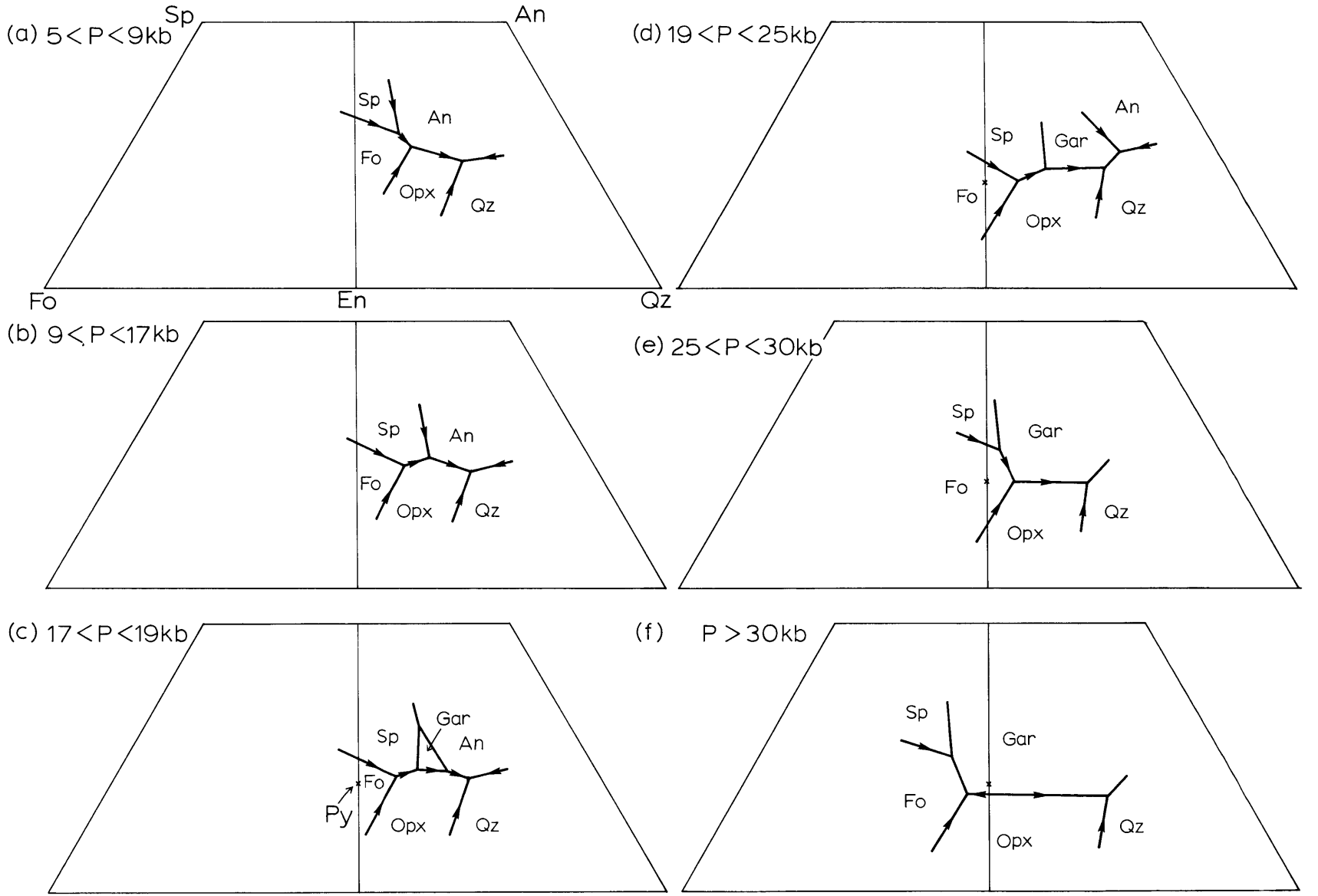
(a) 5<P<9kb
Sp
An
Fo
En
Qz
Sp
An
Fo
Opx
Qz
(b) 9<P<17kb
Sp
An
Fo
Opx
Qz
(c) 17<P<19kb
Gar
Sp
An
Fo
Py
Opx
Qz
(d) 19<P<25kb
An
Sp
Gar
Fo
Opx
Qz
(e) 25<P<30kb
Sp
Gar
Fo
Opx
Qz
(f) P>30kb
Sp
Gar
Fo
Opx
Qz

FIGURE V-10: Same diagram as in Figure V-4. The liquidus relations are constructed according to Figure V-9(c) and (d) together with the constraints of the observed compositions plotted so as to fit the cumulate model. The compositional fields of each sample group are enclosed by dotted lines (see Figure V-4). R127G and the average composition of primitive volcanic glasses from all spreading centers (Melson et al., 1976) are also plotted.

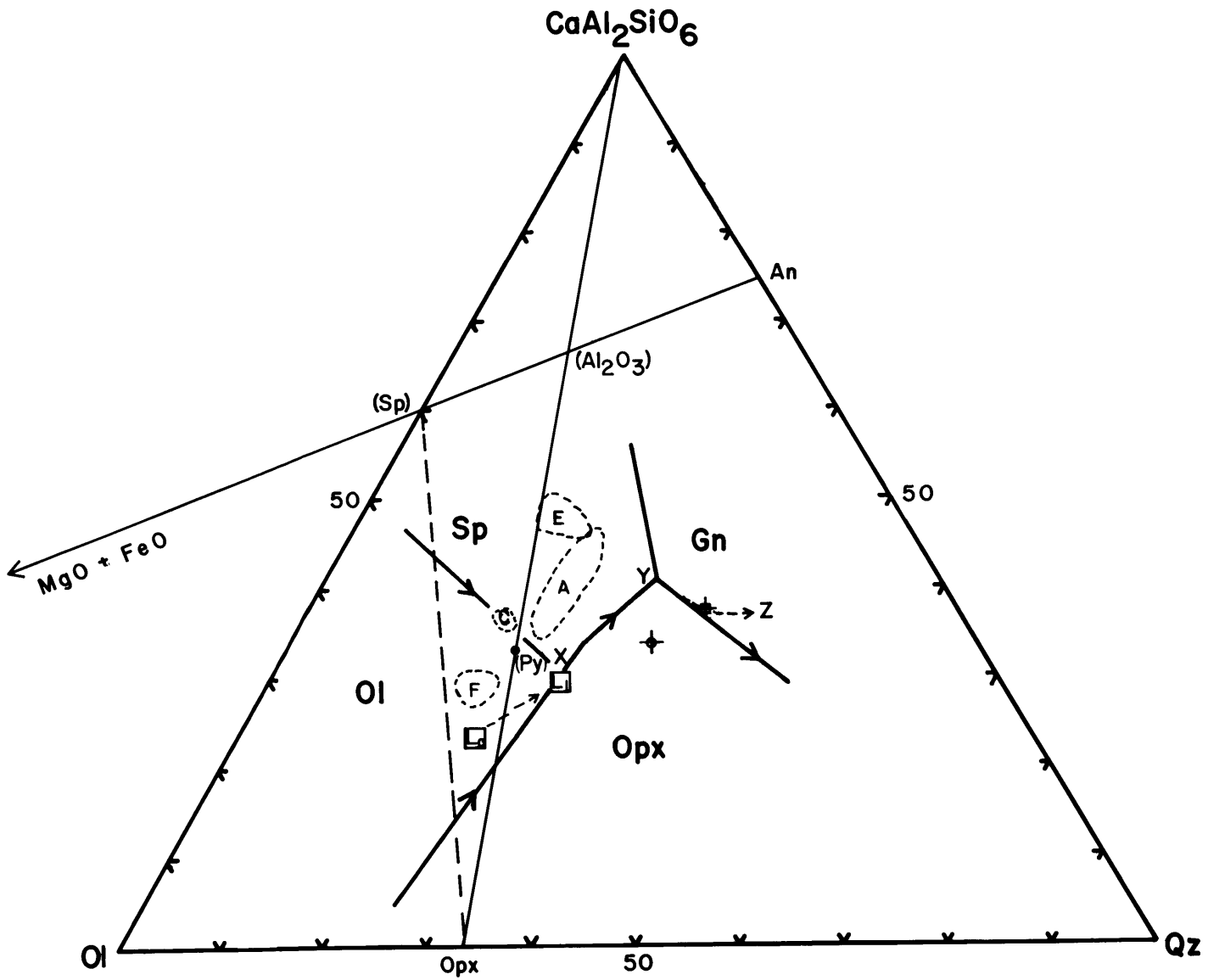
$CaAl_2SiO_6$
An
(Al_2O_3)
(Sp)
50
50
MgO + FeO
Sp
Gn
E
A
C
Y
Z
(Py)
X
F
Ol
Opx
Ol
Opx
50
Qz

Group A to Group C. Group C has the lowest Mg/Fe ratios, and is lowest in Ni and Cr and highest in Sc, V, Y, and HREE (Figure V-2). If this sequence is correct, the liquid path Y-Z must curve upwards as shown in Figure V-10, and the Ca and Al content of the cumulate must decrease with decreasing temperatures. Then the only possibility is that grossular content of garnet decreases with temperature.

This discontinuous cumulate sequence can also explain the apparent compositional gap between R181 and the rest of Group E which are from the same thick layer. According to this model, these samples can form closely in time, because R181 could form just before the liquid reaches Y and the rest of Group E after the liquid passes this point. It also explains why R181 has distinctly high Ni and Cr contents than the rest of Group E.

In summary, the low MgO group can be early stage cumulates of Cpx + Opx + Sp. Groups E (except R181), A, and C are eclogite cumulates (Cpx + Gn), possibly with trapped liquids. The sequence of formation is F→E→A→C in accordance with the Mg/Fe ratios and trace element data.

REE geochemistry: As discussed before, when modelling REE patterns of primary liquids, a wide range of patterns from relative LREE enrichment to relative LREE depletion may result if incremental liquids are not mixed, but are

transported in conduits in the form of mafic layers such as those observed in the peridotite bodies. Note these liquids with widely differing REE abundances may have similar major element compositions. As the conduits cool, the margins will crystallize first, forming incrustations along the walls, while the centers are still molten with influx of new magma passing through, or possibly, the solidified portions of these conduits may later be intruded by magma formed at a later stage. Therefore, within one thick layer, a variety of REE patterns can be expected. A good example is Group E (Figure V-3), whose members are from one thick layer. Because of the many uncertain input parameters required in a multiple-step melting model, it is not fruitful to do direct modelling calculations. However, it is feasible to extract some qualitative information from the observed REE patterns.

If Groups E, A, and C are eclogite cumulates, their REE patterns must reflect the cumulate garnet, because garnet is the only mantle phase that has $D^{S/l}_{HREE}$ greater than unity and $D^{S/l}_{LREE}$ much less than unity (see Appendix II-G). As a result, REE patterns generated involving garnet may criss-cross, for example, as in Figure V-7(a). Earlier cumulates are expected to have higher HREE abundances, but lower LREE abundances than late cumulates

(see also Figure V-11, insets). Such a relationship occurs in the REE patterns of Group E* (Figure V-3); thus the REE data support a eclogite cumulate model. Furthermore, Group C rocks have high abundances of elements that are enriched in garnet, e.g. HREE (>20 X chondrites, Figure V-3), Sc, V, and Y (Figure V-2).

However, variations of REE patterns among the groups cannot be related by just a simple eclogite fractionation model. For example, if the mafic layers formed from a common liquid by various degrees of garnet-clinopyroxene (eclogite) crystallization, then Group C, the most fractionated group, should have the lowest HREE abundances, and conversely Group E should have the highest. However, the observed patterns show the reverse. Apparently unrelated, independent melts are required to form each cumulate group. For example, if the cumulates were composed of 50% clinopyroxene and 50% garnet, using the low set of distribution coefficients in Appendix II-G, the liquids in equilibrium with R839 of Group C and R185 of Group E are calculated and plotted in Figure V-11. Because of the

---

* R181, anomalous member of Group E, which is believed to be early cumulates of Opx + Cpx + Sp, is expected to have lower LREE abundances than the rest of the group (eclogite cumulates). However, its higher LREE abundances is possibly due to trapped liquids, or it may have formed from a slightly earlier liquid increment.

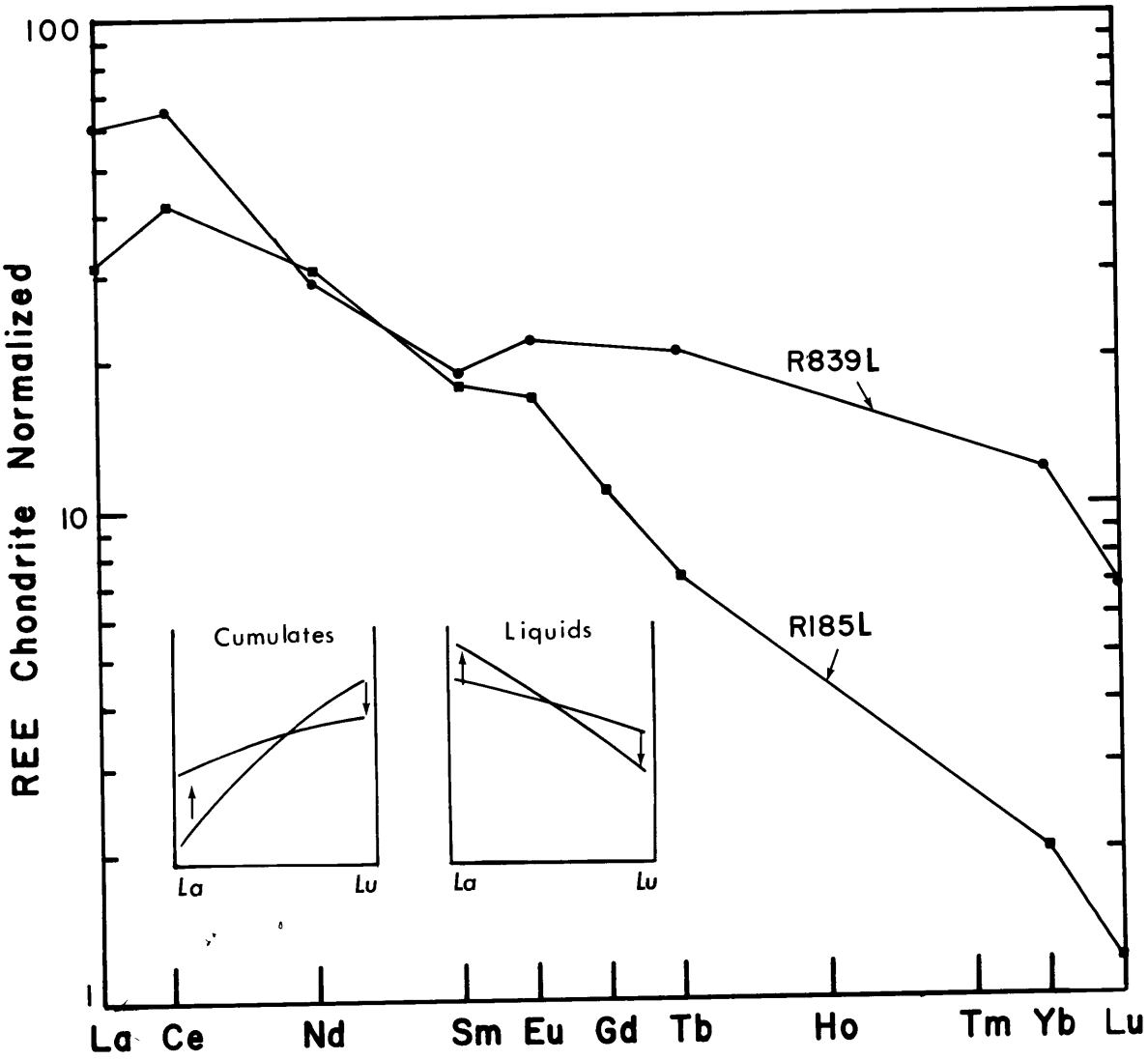

FIGURE V-11: REE patterns of hypothetical liquids in equilibrium with R839 and R185, assuming the cumulates are composed of 50% cpx and 50% gn. The evolution of REE patterns as a result of eclogite fractionation is schematically shown in the insets.

garnet distribution coefficients, it is not possible to generate the former from the latter by simple crystallization of garnet and clinopyroxene, unless the percentage of garnet in the cumulate falls well below 20%. This is not likely, because the compositions of these layers as shown in Figure V-5 require more than 20% garnet, although the high Al_2O_3 solubility in clinopyroxene at high pressures is a complicating factor. In short, REE patterns within a group show signs of eclogite fractionation, but REE variations between groups do not conform to the proposed fractionation sequence.

Why is there a decoupling between HREE, Sc, V, and Y data, and those of Mg/Fe ratios, Cr, and Ni? The multiple-step melting model may provide the answer. The members of each group are found either within a single layer (Groups A and E) or close to each other (Group C). Therefore, they are likely to have been derived from the same parental source, or share the same magmatic line of descent, and also are related closely in space and time. On the other hand, different groups are geographically distinct ($\sim$10 Km from Group C to Group A; $\sim$10 Km from A to E) (see Figure II-1), and it is unlikely that they are as closely related as individual members of a group. Consequently, the parental melts of each group may have had very different incompatible element abundances because

of variations in the extraction process during multiple-step melting. Furthermore, as discussed in Chapter II, some peridotites (Group I) were melted with garnet as a residual solid phase, and others (Group II), without garnet. These peridotite groups are also geographically distinct. Therefore, the primary liquids may be very different in trace element abundances, especially for elements like HREE, Sc, V, and Y, that are greatly affected by garnet. Thus the disagreement between model and the inter-group variations may be attributed to Stage 1, the melting and extraction processes, and not to the final stage of eclogite fractionation.

Group B (R705A and B) and Group D (R251)

So far the origins of R705A, R705B, and R251 have not been discussed. These rocks are anomalous because they do not fall on the main trends established by the Ronda mafic layers.

R705A and R705B of Group B are different portions of one hand-specimen. R705B is a darker color band within R705A, the ligher color "host rock" (petrographic descriptions in Appendix V-B). In terms of major elements, R705B is close to Group A compositions (Figure V-4), except that it has a slightly higher Mg/Fe ratio (Figure V-1). Its REE pattern is very similar to those

of Group A samples (Figure V-3). Furthermore, R705 was collected within 2 km from Group A samples. Except for discrepancies in Mg/Fe ratio and MgO versus Ni and Y abundance trends (Figure V-2), R705B is compositionally similar to Group A rocks and a similar petrogenetic origin is implied. However, R705B occurs as a band or vein inside R705A, which has a composition distinct from Group A samples (Figures V-4 and V-5). Compared to other mafic layer samples, R705A is the lowest in ΣFeo, TiO_2, but the highest in CaO (with the exception of R251) and Al_2O_3 (Figure V-1). It is also the only sample with a strong positive Eu anomaly* (Figure V-3). Surprisingly, R705A has less plagioclase than R705B (Appendix V-A), although modal R705A plots much closer to anorthite in Figure V-4. It is possible that primary plagioclase in R705A recrystallized according to the reaction An + Opx → Gn + Cpx + Qz with increasing pressure (Kushiro and Yoder, 1966), although judging from the bulk composition, this is unlikely to have occurred. In addition, R705B should have also been affected, since they are side by side. Also, the 10%

---

* In some of the Group E samples, there are slight Eu anomalies which are probably due to analystical uncertainties.

of fine-grained recrystallized products found in R705A (Appendix V-B) is not sufficient to account for the major difference in bulk compositions.

If plagioclase was involved in igneous processes, it could either be a cumulus phase in fractional crystallization, or a residual phase in partial melting. In the case of fractional crystallization, it can only appear as a late cumulus phase after garnet disappears (at 17-25 kb; see Figure V-9). In apparent contradiction, the field relations show that R705A is the host rock for R705B. Also, R705A has lower TiO_2, ΣREE contents, and a higher Mg/Fe ratio than R705B. In the second case, if R705A represents residual materials from a second stage of melting, most compositional data agree with this model. However, surprisingly, R705A with a higher Mg/Fe ratio (but lower MgO content) has a lower Ni content (by a factor of two) than R705B, and besides, if R705B, the assumed melt, forms only the lesser portion of the total mass as indicated by the field relations, a strong negative Eu anomaly should occur in R705B.

In view of all these complex geochemical relationships that cannot be easily explained by ordinary igneous processes, metasomatic processes are proposed. Because the whole specimen is only ∿15 cm across and the band is

only 3.5 cm wide, metasomatic processes may have occurred locally. Also, because this sample (R705) is collected only 2 m from the peridotite/country rock contact, metasomatic fluids from the country rock could have easily penetrated the peridotite body for short distances (maybe up to 10 m) modifying the compositions.

Similar metasomatic complexities may have affected R251 whose composition is definitely out of the main trends (Figures V-4, V-5). Among the mafic layers, it has the lowest SiO_2 content, but the highest abundances of CaO and TiO_2. Its REE pattern is convex upwards with a maximum at Eu (28X chondrites) but LREE and HREE has relatively lower abundances similar to Group F samples. Convex REE patterns are typical of incremental melts of garnet peridotites (Figure V-7,a), but the unusual major element composition of R251 is inconsistent with a melt origin.

V-5: CONCLUSIONS AND IMPLICATIONS

Several conclusions regarding the petrogenesis of the Ronda mafic layers can be made by combining constraints derived from the bulk rock compositional data with those from high pressure-high temperature phase relations.

(1) (a) Most, perhaps all, the mafic layers at Ronda, and other alpine peridotite bodies, do not represent direct melts formed by partial fusion of the peridotites

as hypothesized by Dickey (1970). A few mafic layers (Group F and R181) may represent primary liquid compositions, but more likely, they are high pressure cumulates formed by early stage fractional crystallization of the primary liquid.

(b) Although a second melting episode may modify the compositions of orthomagmatic layers, as proposed by Loubet et al. (1976), this process cannot explain most of the compositional variations. Furthermore, this model is difficult to conceive in terms of geophysical and tectonic constraints.

(c) Most mafic layers are probably high-pressure cumulates of garnet and clinopyroxene (with possible trapped melt) formed by fractional crystallization between 17 and 25 Kb. This conclusion supports O'Hara's contention that eclogite fractionation does occur in the upper mantle (O'Hara and Yoder, 1967; O'Hara, 1968). However, the Ronda data do not establish that such fractionation processes are typical of magma generation regions, or that eclogite fractionation is significant for most basaltic magmas.

(d) By analogy, pyroxenite inclusions in alkali basalts may have origins similar to the Ronda mafic layers.

(2) (a) In the upper mantle tectonic environment envisioned for the Ronda peridotite, partial melts are

extracted and transported through conduits soon after they are formed. Because increments of liquid extracted in a multiple-step melting process are unlikely to be mixed, realistic models for trace element abundances of melts are incremental liquid concentrations (or the average of several but not all increments) derived from the multiple-step melting model (Chapter III). A typical result is that REE patterns are variable in incremental liquids with similar major element compositions. If the petrogenetic process involves more than one or two melting and/or crystallization stages, there are too many uncertain inputs for quantitative modelling of trace element abundances. Stochastic inversion techniques (e.g. Press, 1968; Allegre et al., 1977; Minster et al., 1977) may be useful in this case.

(b) Although it is difficult to use REE abundances in cumulates to infer the REE abundances in the equilibrium, presumably lost, liquids, these escaped liquids were probably relatively enriched in LREE. Thus typical oceanic tholeiites are unlikely to be good candidates for the liquid coexisting with these eclogite cumulates. Nevertheless, Dickey et al. (in press) have noted that the major element composition of liquid coexisting with eclogite R127 is similar to oceanic tholeiites (Figures V-1 and V-4).

(3)(a) If the fractionation sequence proposed for

the Ronda groups (F→E→A→C) is correct, it is also correlated with geographical distribution; that is, the sequence F→E→A→C is a geographic trend from east to west (see location map in Figure II-1). This correlation is remarkable, because in Chapter II, I concluded that the north-west part of the Ronda body was the outer part of the diapir, while the south-east portion was the center. This conclusion is based on melting models, and it also agrees with Obata's (1977) conclusions. A natural consequence is that the partial melts were transported from east to west, and as proposed from the mafic layer data, the early cumulates formed in the east with later-stage cumulates formed in the west.

(b) If the proposed fractionation sequence is correct, the grossular content in garnet must decrease with decreasing temperature during eclogite fractionation. This contradicts directly with Yoder and Tilley's (1962, p. 505, Figure 4) conjecture about the compositional relations of garnet, clinopyroxene, and liquid during crystallization. Since there is no hard experimental evidence to support their conjecture, it may not be correct.

(4) "Abnormal" major and trace element compositions of some (three) samples of Ronda mafic layers do tend to indicate that metasomatic processes may have occurred in

local scale, especially near the peridotite/country rock contact. However, there are few indications that such processes affected the bulk compositions on a gross scale.

CHAPTER VI

CONCLUSIONS

The present work provides significant information on the following:

(1) the origin and P-T history of the peridotites;

(2) the generation of magma in the upper mantle;

(3) the chemical composition of the upper mantle; and

(4) the origin of the mafic layers and their significance in the generation of basaltic magmas.

The major conclusions are given below.

VI-1: THE ORIGIN AND P-T HISTORY OF THE RONDA PERIDOTITES

(a) The Ronda peridotites represent residual materials produced by small degrees (<10 to 15%) of partial melting of a primary mantle peridotite. The extracted small increments or batches of primary melt had nearly constant major element compositions.

(b) The melting event occurred in the P-T field where garnet lherzolite is stable, but garnet, being present in small amounts (∿10%), was exhausted before melting ceased in some portions of the body. The initial melting condition is estimated to be 30-35 kb, and ∿1600°C.

(c) The proposed model calls for melting of a rapidly rising mantle diapir by adiabatic decompression. A steep thermal gradient may have existed across the body accounting

for the observed compositional zonation. The northwest portion of the massif is believed to be the outer margin of the diapir, and the southeast portion the center.

VI-2: THE NATURE OF MAGMA GENERATION PROCESSES

Geochemical models agree with the contention of geophysicists that separation of melts from solids in the upper mantle is efficient and effective (Waff and Holdren, 1977). In short, the melt is extracted in small increments, and removed from equilibrium with the residual solid soon after it is produced. Little trapped melt is left behind. It is estimated that each liquid increment averages less than 1 wt.% of the residue, and the trapped melt, if present, is no greater than 1 wt.% of the residue.

VI-3: THE CHEMICAL COMPOSITION OF THE UPPER MANTLE

(a) REE data for the Ronda peridotites indicate that the primary mantle source from which they are derived has REE abundances approximately equal to 2 times chondrites. Modern oceanic upper mantle is believed to be LREE depleted due to an earlier melting event. The melting episode creating the residual Ronda peridotites may correspond to such an event, but the age of this melting is not known for the Ronda rocks.

(b) The major element composition of the primary mantle as deduced from the Ronda peridotite compositions resembles closely that of Pyrolite III proposed by Green and Ringwood (1967).

VI-4: THE ORIGIN OF MAFIC LAYERS AND BASALT GENESIS

(a) The primary melt generated at high pressures (>30 kb) by fusion of 15-20% of Ronda peridotites was picritic in composition and similar to the composition of the Baffin Island picrite (Clarke, 1970). Most of the Ronda mafic layers do not represent primary melts. They are probably high pressure cumulates (sp + cpx + opx, or cpx + gn) formed by incrustation along the conduit walls as the magmas migrated through the peridotite body. The direction of transportation was from east to west (towards the outside of the body).

(b) This conclusion supports the contention of O'Hara (1968) and O'Hara and Yoder (1967) that eclogite fractionation occurs in the upper mantle, but this study does not provide information about the importance of eclogite fractionation in normal basalt genesis. Rather than representing typical, basalt-generating mantle, Ronda may be an anomalous portion of the mantle produced by diapirism.

(c) Under the proposed melting conditions, the

FIGURE VI-1: A schematic example showing the possible complexities involved in the development of a thick mafic layer. Cross-hatched areas represent solid; blank areas within the layer represent liquid. Stage 1: Liquid (1) starts fractional crystallization along the walls of the conduit. Stage 2: The center portion is replaced by Liquid (2) which corresponds to an increment of liquid formed at a later stage of melting. Stage 3: The solids have the compositions of Liquids (1) and (2), and the center is replaced by Liquid (3). Stage 4: Liquids (1), (2), and (3) have solidified, but the solid portion of the layer is later intruded by Liquid (4), which remelts some of the already solidified portions of the layer, and may also force the conduit apart resulting in a thicker layer.

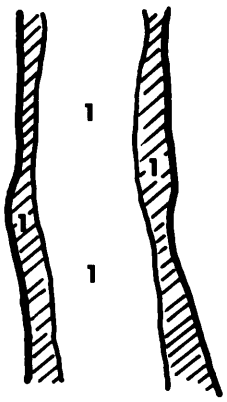

1

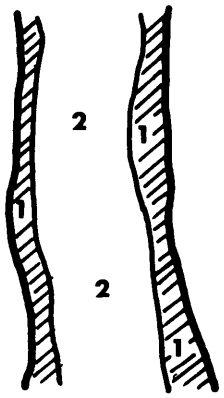

2

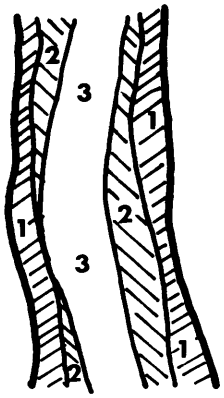

3

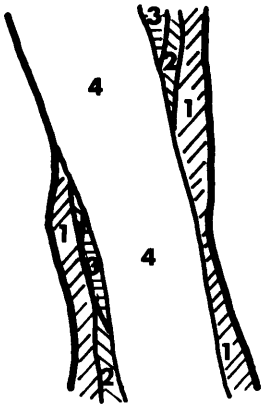

4

FIGURE VI-2: Diagram taken from Dickey *et al.* (1977), showing all possible processes that could have been involved in a multiple-stage model.

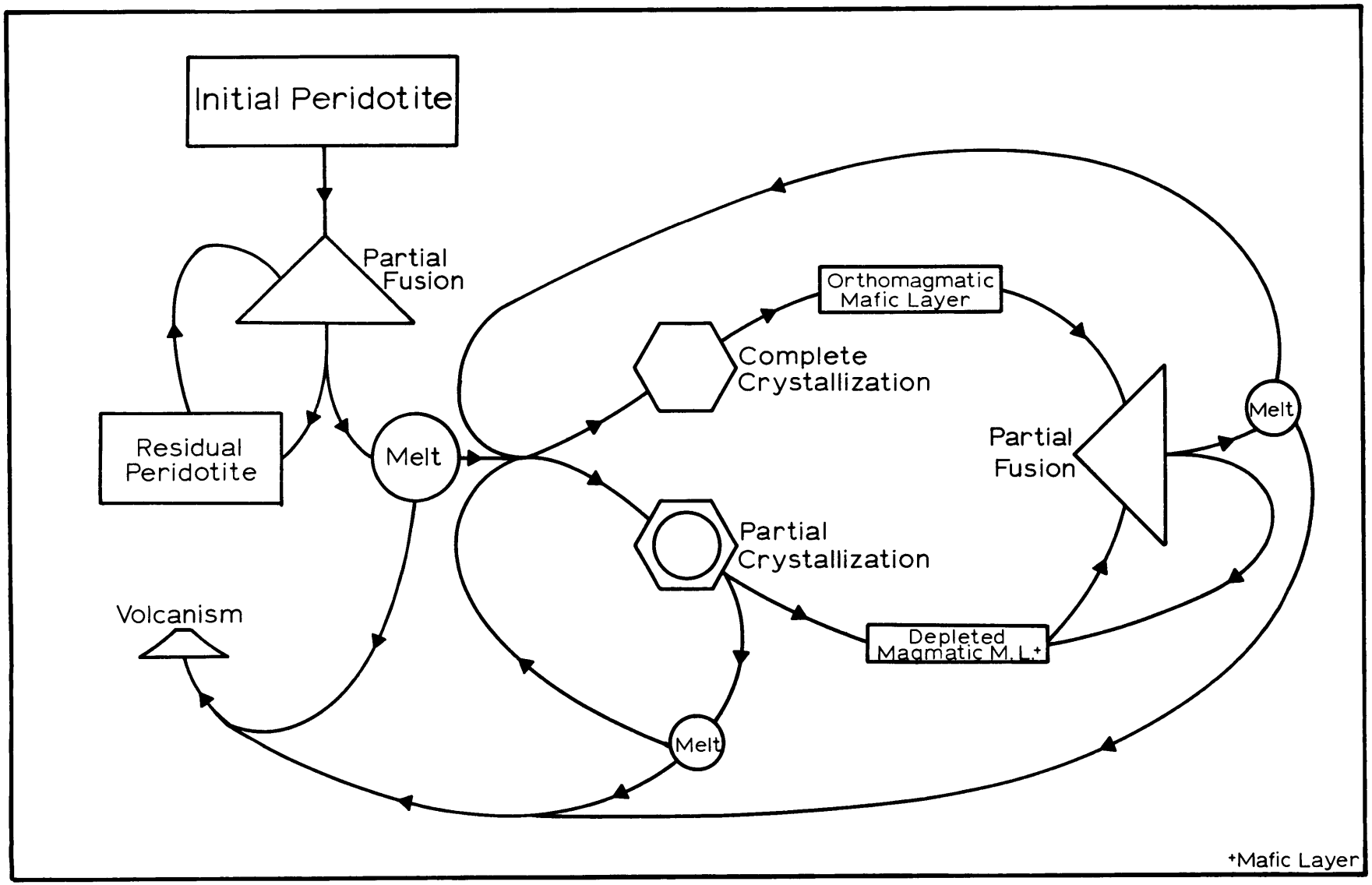
Initial Peridotite
Partial Fusion
Residual Peridotite
Melt
Orthomagmatic Mafic Layer
Complete Crystallization
Partial Fusion
Melt
Partial Crystallization
Volcanism
Depleted Magmatic M. L.+
Melt
+Mafic Layer

increments of primary liquid have a wide range of trace element abundance patterns (e.g., REE), if they were subjected to further fractionation processes without recombination in a magma chamber, the final resulting trace element abundances of the fractionated products could not be uniquely predicted. In such cases, stochastic models may be useful.

(d) The compositions of some Ronda mafic layers have been modified by metasomatic processes and do not fit into the igneous context.

VI-5: SUMMARY

It is envisioned that a thermal anomaly in the earth's mantle triggered the rise of a sizeable (>60 km wide) diapir which rose rapidly along the adiabatic gradient. This body started to melt when it hit the peridotite solidus at >30 kb, but due to the rapid rise of the diapir, a steep thermal gradient was maintained across the body, so different portions of the diapir melted to different degrees according to their position. The melts produced were extracted from the residual solids in small increments, and they were taken out of equilbrium with the peridotites soon after they were formed. As the liquids (probably mixed with crystals) migrated from the inside to the outside of the rising body, they formed incrustations along the cooler walls of the conduits near the outsides of the diapir. These incrustations are

represented by the mafic layers observed in the field. The residual liquid, rich in incompatible elements like the LREE, K, and P, escaped from the body.

The development of the conduits is likely to be more complicated than uniform symmetrical cooling and crystallization from the walls. Processes like remelting with remixing perhaps due to later intrusions by new magmas are likely. A schematic example showing possible complexities is given in Figure VI-1. In addition, if the P-T trajectory of the rising body is more complex, a multiple-stage process as proposed by Dickey et al. (1977) is also possible (Figure VI-2). Unfortunately, such a multiple-stage model cannot be readily evaluated by direct calculation methods. Therefore, stochastic modeling is proposed for further work.

ACKNOWLEDGEMENTS

I gratefully acknowledge the following teachers and friends:

Fred Frey, supervisor of this thesis, for his guidance throughout the whole project;

John Dickey, who introduced me to lovely Ronda and guided me in the field;

Masaaki Obata, whose cooperation is absolutely essential for this work; and

professors, fellow workers and graduate students in M.I.T., who provided me with kind assistance, practical advice , inspiring discussions and constant encouragement, without which this work would have been impossible. They are: Claude Allegre (U. de Paris); Bruce Fegley (for playing tennis with me during the most difficult time, even though he lost most of the time); Ken Goettel; Stan Hart; Rudi Hon; Tony Irving; Ikuo Kushiro (U. of Tokyo); Marc Loiselle; Leopoldo Lopez-Escobar; Michel Loubet (U. de Paris, for unpublished Beni-Bouchera data); Meg Lundeen (Wellesley College); the M.I.T. Research Reactor operation personnel; Dorian Nicol (for field assistance); Eiko Obata (for the food which kept me alive); John Reid (Hampshire College); Steve Roy; Don Skibo; Mark Sneeringer (for those exciting hockey games); Chien-Min Sung; Dave Walker (Harvard University); Earle Whipple; Lori Zarrow; and all

others too numerous to mention here.

I would especially like to thank the members of my thesis committee for the critical examination of the manuscript. I am very much indebted to the late Chris Goetze, one of the original examiners, who has passed away all too soon before the completion of the whole thesis. His expertise in melt segregation from the mantle provides the necessary background for this work.

X-ray fluorescence analyses were performed in the laboratory of Dr. B. W. Chappell (Australian National University) whose generous assistance is greatly appreciated. Neutron irradiations were carried out at the M.I.T. Research Reactor, and the nuclear reactor of Georgia Tech. This thesis was typed by Roxanne Regan and Sandi Hirsch. Many figures were drafted by Ellen Loiselle. This work was supported by the National Science Foundation (Grant Nos: DES 75-02900; EAR 76-84067; DES 73-00264), and my field expenses were partially paid by a grant from the Geological Society of America.

Financial support for my graduate study at M.I.T. was partly provided by my parents, who have waited patiently for 5 and 1/2 years.

REFERENCES

Akella, J., 1976, Garnet pyroxene equilibria in the system $CaSiO_3$-$MgSiO_3$-Al_2O_3 and in a natural mineral mixture. Amer. Mineral., 61, 589-598.

Albarede, F., 1976, Some trace element relationships among liquid and solid phases in the course of the fractional crystallization of magmas. Geochim. Cosmochim. Acta, 40, 667-673.

Allegre, C.J., Treuil, M., Minster, J.F., Minster, B., and Albarede, F., 1977, Systematic use of trace element in igneous process. Part I: Fractional crystallization processes in volcanic suites. Contrib. Mineral. Petrol., 60, 57-75.

Beeson, M.H. and Jackson, E.D., 1970, Origin of the garnet pyroxenite xenoliths at Salt Lake Crater, Oahu. Mineral. Soc. Amer. Spec. Pap., 3, 95-112.

Benson, W.N., 1926, The tectonic conditions accompanying the intrusion of basic and ultrabasic igneous rocks. Mem. Nat. Acad. Sci., 19:1, 1-90.

Bonini, W.E., Loomis, T.P., and Robertson, J.D., 1973, Gravity anomalies, ultramafic intrusions, and the tectonics of the region around the Strait of Gibraltar. J. Geophys. Res., 78, 1372-1382.

Boudier, F. and Nicolas, A., 1977, Structural controls on partial melting in the Lanzo peridotites. Proceedings Chapman Conference on Partial Melting in the Earth's Upper Mantle, in press.

Boyd, F.R., 1973, A pyroxene geotherm. Geochim. Cosmochim. Acta, 37, 2533-2546.

Chen, Ju-Chin, 1971, Petrology and chemistry of garnet lherzolite nodules in kimberlite from South Africa. Amer. Mineral., 56, 2098-2110.

Clarke, D.B., 1970, Tertiary basalts of Baffin Bay: Possible primary magma from the mantle. Contr. Mineral. Petrol., 25, 203-224.

Coleman, R.G., 1971, Plate tectonic emplacement of upper mantle peridotites along continental edges. J. Geophys. Res., 76, 1212-1222.

Darot, M., 1974, Cinematique de l'extrusion, a partir du manteau, de peridotites de la Sierra Bermeja (Serrania de Ronda, Espagne). C.R. Acad. Sci. Paris, Ser. D., 278, 1673-1676.

Davis, K.E. and Hart, S.R., 1977, Partitioning of nickel between olivine and silicate liquid. (abstract) In: papers presented to the International Conference on Experimental Trace Element Geochemistry, pp. 16-17.

DePaolo, D.J. and Wasserburg, G.J., 1976, Nd isotopic variations and petrogenetic models. Geophys. Res. Letts., 3, 249-252.

DePaolo, D.J. and Wasserburg, G.J., 1976, Influences about magma sources and mantle structure from variations of $^{143}Nd/^{144}Nd$. Geophys. Res. Letts., 3, 743-746.

DePaolo, D.J. and Wasserburg, G.J., 1977, Nd in island arc and continental volcanic rocks. (abstract) Transactions, Am. Geophys. Union, 58, 533.

Dewey, J.F. and Bird, J., 1971, Origin and emplacement of the ophiolite suite: Appalachian ophiolites in Newfoundland. J. Geophys. Res., 74, 3179-3206.

Dickey, J.S. Jr., 1968, Eclogitic and other inclusions in the mineral breccia member of the Deborah volcanic formation at Kakanui, New Zealand. Amer. Mineral., 53, 1304-1319.

Dickey, J.S. Jr., 1969, Partial fusion products in alpine-type peridotites: Serrania de la Ronda and other examples. Ph.D. thesis, Princeton University, 101 pp.

Dickey, J.S. Jr., 1970, Partial fusion products in alpine-type peridotites: Serrania de la Ronda and other examples. Soc. Amer., Spec. Paper 3, 33-49.

Dickey, J.S. Jr. and Obata, M., 1974, Graphitic hornfels dikes in the Ronda high-temperature peridotite masif. Amer. Mineral., 59, 1183-1189.

Dickey, J.S. Jr., Obata, M., and Suen, C.J., 1977, Partial fusion versus fractional crystallization: hypotheses for the differentiation of the Ronda ultramafic massif of southern Spain. Proceedings Chapman Conference on Partial Melting in the Earth's Upper Mantle, in press.

Dickey, J.S. Jr., Obata, M., and Suen, C.J., in press, Chemical differentiation of the lower lithosphere represented by the Ronda ultramafic massif, southern Spain. Symposium Volume on the Second Symposium on the Origin and Distribution of the Elements, Paris, May, 1977.

Drake, M.J. and Weill, D.F., 1975, Partition of Sr, Ba, Ca, Y, En^{2+}, En^{3+}, and other REE between plagioclase feldspar and magmatic liquid: an experimental study. Geochim. Cosmochim. Acta, 39, 680-712.

Dürr, S.H., 1967, Geologie de Serrania de Ronda und ihrer südwestlichen Auslaufer. Geologica Romana, 6, 1-73.

Frey, F.A., 1969, Rare-earth abundances in a high-temperature peridotite intrusion. Geochim. Cosmochim. Acta, 33, 1429-1447.

Frey, F.A., 1977, Rare-earth element abundances in megacrysts from alkalic basalts. (abstract) Paper presented to the International Conference on Experimental Trace Element Geochemistry, pp. 31-32.

Frey, F.A., Bryan, W.B., and Thompson, G., 1974, Atlantic Ocean floor: geochemistry and petrology of basalts from Legs 2 and 3 of the Deep-Sea Drilling Project. J. Geophys. Res., 79, 5507-5527.

Frey, F.A. and Green, D.H., 1974, The mineralogy, geochemistry, and origin of lherzolite inclusions in Victorian basalts. Geochim. Cosmochim. Acta, 38, 1023-1059.

Frey, F.A., Green, D.H., and Roy, S.D., 1977. Integrated models of basalt petrogenesis: A study of olivine tholeiites to olivine melilitites from southeastern Australia utilizing geochemical and experimental petrological data. J. Petrol., in press.

Gast, P.W., 1968, Trace element fractionation and the origin of tholeiitic and alkaline magma types. Geochim. Cosmochim. Acta, 32, 1057-1086.

Gast, P.W., Tilton, G.R., and Hedge, C., 1964, Isotopic composition of lead and strontium from Ascension and Gough Islands. Science, 145, 1181-1185.

Gordon, G.E., Randle, K., Goles, G., Corliss, J., Beeson, M., and Oxley, S., 1968, Instrumental activation analysis of standard rocks with high resolution gamma ray detectors. Geochim. Cosmochim. Acta, 32, 369-396.

Green, D.H., 1966, The origin of the "eclogites" from Salt Lake Crater, Hawaii. Earth Planet. Sci. Lett., 1, 414-420.

Green, D.H., 1967, High-temperature peridotite intrusions. In: P.J. Wyllie, ed., Ultramafic and Related Rocks, Wiley, N.Y., pp. 212-222.

Green, D.H. and Ringwood, A.E., 1967, The stability fields of aluminous pyroxene peridotite and garnet peridotite and their relevance in upper mantle structure. Earth Planet. Sci. Letts., 3, 151-160.

Grutzeck, M., Kridelbaugh, S., and Weill, D., 1974, The distribution of Sr and REE between diopside and silicate liquid. Geophys. Res. Letts., 1, 273-275.

Häkli, T.A. and Wright, T.L., 1967, The fractionation of nickel between olivine and augite as a geothermometer. Geochim. Cosmochim. Acta, 31, 877-884.

Hanson, G.N. and Langmuir, C.H., 1977, Use of distribution coefficients for major elements in mantle-melt systems. (abstract) In: Papers presented to the International Conference on Experimental Trace Element Geochemistry, pp. 38-40.

Harris, P.G., Hutchison, R., and Paul, D.K., 1972, Plutonic xenoliths and their relation to the upper mantle. Phil. Trans. R. Soc. London, Ser. A, 271, 313-323.

Hart, S.R., 1971, K, Rb, Cs, Sr, and Ba contents and Sr isotope ratios of ocean floor basalts. Phil. Trans. Royal Soc. London, A268, 573-587.

Hart, S.R. and Brooks, C., 1974, Clinopyroxene-matrix partitioning of K, Rb, Cs, Sr, and Ba. Geochim. Cosmochim. Acta, 38, 1799-1806.

Hart, S.R., Davis, K.E., Kushiro, I., and Watson, E.B., 1976, Partitioning of nickel between olivine and silicate liquid. Geol. Soc. Amer., Abstracts with Programs, 8, 906-907.

Haskin, L.A., Haskin, M.A., Frey, F.A., and Wildeman, T.R., 1968, Relative and absolute terrestrial abundances of the rare-earths. In: Origin and Distribution of the Elements, L.H. Ahrens, ed., pp. 889-912, Pergamon.

Helmke, P.A., Haskin, L.A., Korotev, R.L., and Ziege, K.E., 1972, Rare earths and other trace elements in Apollo 14 samples. Proceedings, Third Lunar Sci. Conf., 2, 1275-1292.

Hertogen, J. and Gijbels, R., 1976, Calculation of trace element fractionation during partial melting. Geochim. Cosmochim. Acta, 40, 313-322.

Hofmann, A.W., 1975, Diffusion of Ca and Sr in a basalt melt. Carnegie Institution of Washington, Year Book 74, 183-189.

Hofmann, A.W. and Hart, S.R., 1978, An assessment of local and regional isotopic equilibrium in the mantle. Earth Planet. Sci. Lett., in press.

Hubbard, N.J., 1969, A chemical comparison of oceanic ridge, Hawaiian tholeiitic and Hawaiian alkalic basalts. Earth Planet. Sci. Lett., 5, 346-352.

IUGS Subcommission on the Systematics of Igneous Rocks, 1973. Plutonic Rocks: Classification and Nomenclature Recommended by the IUGS Subcommission on the Systematics of Igneous Rocks. Geotimes, 18, 26-30.

Irvine, T.N. and Smith, C.H., 1967, The ultramafic rocks of the Muskox intrusion, Northwest Territories, Canada. In: Ultramafic and Related Rocks, Wyllie, P.J., ed., Wiley, New York, pp. 38-49.

Irving, A.J., 1974, Geochemical and high pressure experimental studies of garnet pyroxenite and pyroxene granulite xenoliths from the Delegate basaltic pipes, Australia. J. Petrol., 15, 1-40.

Ito, K. and Kennedy, G., 1967, Melting and phase relations in a natural peridotite to 40 kilobars. Am. J. Sci., 265, 519-538.

Jackson, E.D., 1966, "Eclogite" in Hawaiian basalts. U.S. Geol. Surv. Profess. Papers, 550-D, 151-157.

Jackson, E.D., 1968, The character of the lower crust and upper mantle beneath the Hawaiian Islands. 23rd Int. Geol. Congr., 1, 135-150.

Jackson, E.D. and Wright, T.L., 1970, Xenoliths in the Honolulu Volcanic Series. J. Petrol., 11, 405-430.

Kay, R.W. and Gast, P.W., 1973, The rare earth content and origin of alkali-rich basalts. J. Geology, 81, 653-682.

Kay, R., Hubbard, N.J., and Gast, P.W., 1970, Chemical characteristics and origin of oceanic ridge volcanic rocks. J. Geophys. Res., 75, 1585-1613.

Kornprobst, J., 1969, Le Massif ultrabasique des Beni Bouchera (Rif Interne, Maroc): Etude des péridotites de baute température et de haute pression, et des pyroxénolites, à grenat ou sans grenat, qui leur sont associées. Contr. Mineral. Petrol., 23, 283-322.

Kornprobst, J., 1970, Les péridotites et les pyroxénolites du massif ultrabasique des Beni Bouchera: une étude éxperimentale entre 1100 et 1550°C, sous 15 à 30 kilobars de pression sèche. Contr. Mineral. Petrol., 29, 290-309.

Kushiro, I., 1976, Changes in viscosity and structure of melt of $NaAlSi_2O_6$ composition at high pressures. J. Geophys. Res., 81, 6347-6350.

Kushiro, I. and Kuno, H., 1963, Origin of primary basalt magmas and classification of basaltic rocks. J. Petrology, 4, 75-89.

Kushiro, I., Shimizu, N., Nakamara, Y., and Akimoto, S., 1972, Compositions of coexisting liquid and solid phases formed upon melting of natural garnet and spinel lherzolites at high pressures: a preliminary report. Earth Planet. Sci. Lett., 14, 19-25.

Kushiro, I. and Yoder, H.S. Jr., 1966, Anorthite-forsterite and anorthite-enstatite reactions and their bearing on the basalt-eclogite transformation. J. Petrol., 7, 337-362.

Kushiro, I. and Yoder, H.S. Jr., 1974, Formation of eclogite from garnet lherzolite: liquidus relations in a portion of the system $MgSiO_3$-$CaSiO_3$-Al_2O_3 at high pressures. Carnegie Institution of Washington, Year Book 73, 266-269.

Kushiro, I., Yoder, H.S. Jr., and Mysen, B.O., 1976, Viscosities of basalt and andesite melts at high pressures. J. Geophys. Res., 81, 6351-6356.

Lambert, R. St. J., and Holland, J.G., 1977, Trace elements and petrogenesis of DSDP 37 basalts. Can. J. Earth Sci., 14, 809-836.

Leeman, W.P., 1974, Experimental determination of partitioning of divalent cations between olivine and basaltic liquid. Part 2 of unpublished Ph.D. thesis, University of Oregon, 1974.

Leeman, W.P. and Scheidegger, K.F., 1977, Olivine/liquid distribution coefficients and a test for crystal-liquid equilibrium. Earth Planet. Sci. Lett., 35, 247-257.

Loomis, T.P., 1972a, Contact metamorphism of pelitic rock by the Ronda ultramafic intrusion, southern Spain. Geol. Soc. Am. Bull., 83, 2449-2474.

Loomis, T.P., 1972b, Diapiric emplacement of the Ronda high-temperature ultramafic intrusion, southern Spain. Geol. Soc. Am. Bull., 83, 2475-2496.

Loubet, M., Bougault, M., Shimizu, N., and Allègre, C.J., 1976, Geochemical study (REE, Ba, and partially major and transition elements analysis) of pyroxenolite layers in lherzolite type alpine massives. (abstract) Trans., Am. Geophys. Union, 57, 1025.

Loubet, M., Shimizu, N., and Allègre, C.J., 1975. Rare earth elements in Alpine peridotites. Contr. Mineral. Petrol., 53, 1-12.

Lovering, J.F. and White, A.J.R., 1969, Granulitic and eclogitic inclusions from basic pipes at Delegate, Australia. Contr. Mineral. Petrol., 21, 9-52.

Lundeen, M.T., 1976, Structural evolution of the Ronda peridotite and its tectonic position in the Betic Cordilleras, Spain. Ph.D. thesis, Harvard University, 176 pp..

Lundeen, M.T., 1977, Emplacement of the Ronda peridotite, Sierra Bermeja, Spain. Geol. Soc. Amer. Bull., in press.

MacGregor, I.D., 1975, Petrologic and thermal structure of the upper mantle beneath South Africa in the Cretaceous. In: Physics and Chemistry of the Earth, L.H. Ahrens et al., ed., Vol. 9, Pergamon, New York.

Magaritz, M. and Hofmann, A.W., 1977, REE diffusion in basalt and obsidian. (abstract) Abstracts with Programs, Geol. Soc. Am., 9, 1082-1083.

Mason, B., 1968, Eclogitic xenoliths from volcanic breccia at Kakanui, New Zealand. Contr. Mineral. Petrol., 19, 316-327.

Melson, W.G., Vallier, T.L., Wright, T.L., Byerly, G., and Nelen, J., 1976, Chemical diversity of abyssal volcanic glass erupted along Pacific, Atlantic, and Indian Ocean sea-floor spreading centers. Geophysical Monograph 19, Am. Geophys. Union, pp. 351-367.

Menzies, M., 1976, Rare-earth geochemistry of fused ophiolitic and alpine lherzolites - I. Othris, Lanzo, and Troodos. Geochim. Cosmochim. Acta, 40, 645-656.

Minster, J.F., Minster, J.B., Treuil, M., and Allègre, C.J., 1977, Systematic use of trace elements in igneous processes. Part II: Inversion problem of the fractional crystallization process in volcanic suites. Contr. Mineral. Petrol., 61, 49-77.

Moores, E.M., 1970, Petrology and structure of the vourinos ophiolotic complex of northern Greece. Geol. Soc. Am. Spec. Paper, 118, 1-74.

Moores, E.M. and Vine, F.J., 1971, The Troodos, Cyprus, and other ophiolites as oceanic crust: evaluation and implications. Royal Soc. London Phil. Trans., Ser. A, 268, 443-466.

Mori, T. and Green, D.H., 1975, Pyroxenes in the system $Mg_2Si_2O_6$-$CaMgSi_2O_6$ at high pressure. Earth Planet. Sci. Lett., 26, 277-286.

Murase, T., Kushiro, I., and Fujii, T., 1977a, Compressional wave velocity in partially molten peridotite. Carnegie Inst. Washington Year Book 76, in press.

Murase, T., Kushiro, I., and Fujii, T., 1977b, Electrical conductivity of partially molten peridotite. Carnegie Inst. Washington Year Book 76, in press.

Mysen, B., 1975, Partitioning of iron and magnesium between crystals and partial melts in peridotite upper mantle. Contr. Mineral. Petrol., 52, 69-76.

Mysen, B.O. and Kushiro, I., 1976, Compositional variation of coexisting phases with degree of melting of peridotite under upper mantle conditions. Carnegie Inst. Washington, Year Book 75, pp. 546-555.

Nagasawa, H., Wakita, H., Higuchi, H., and Onuma, N., 1969, Rare earths in peridotite nodules: an explanation of the genetic relationship between basalt and peridotite nodules. Earth Planet. Sci. Lett., 5, 377-381.

Nixon, P.H. and Boyd, F.R., 1973, Petrogenesis of the granular and sheared ultrabasic nodule suite in kimberlites. In: Lesotho Kimberlites, P.H. Nixon, ed., Lesotho National Development Corp., Maseru, Lesotho, pp. 48-56.

Norrish, K. and Chappell, B.W., 1967, X-ray fluoresence spectrography. In: Physical Methods in Determinative Mineralogy, J. Zussman, ed., Academic Press, N.Y.

Norrish, K. and Hutton, J.T., 1969, An accurate x-ray spectrographic method for the analysis of a wide range of geological samples. Geochim. Cosmochim. Acta, 33, 431-453.

Obata, M., 1977, Petrology and petrogenesis of the Ronda high-temperature peridotite intrusion, southern Spain. Ph.D. thesis, M.I.T., 220 pp.

Obata, M. and Dickey, J.S. Jr., 1976, Phase relations of mafic layers in the Ronda peridotite. Carnegie Institution of Washington Year Book 75, pp. 562-566.

O'Hara, M.J., 1967, Mineral paragenesis in ultrabasic rocks. In: P.J. Wyllie, ed., Ultramafic and Related Rocks, Wiley, N.Y., pp. 393-401.

O'Hara, M.J., 1968, The bearings of phase equilibria studies in synthetic and natural systems on the origin and evolution of basic and ultrabasic rocks. Earth Sci. Rev., 4, 69-133.

O'Hara, M.J., 1969, The origin of eclogite and ariégite nodules in basalt. Geol. Mag., 106, 322-330.

O'Hara, M.J., 1970, Upper mantle composition inferred from laboratory experiments and observation of volcanic products. Phys. Earth Planet. Int., 3, 236-245.

O'Hara, M.J., 1976, Partial melting of upper mantle peridotites - a short summary. Extended Abstract, Chapman Conference on Partial Melting in the Earth's Upper Mantle.

O'Hara, M.J. and Yoder, H.S. Jr., 1967, Formation and fractionation of basic magmas at high pressure. Scott. J. Geol., 3, 67-117.

O'Hara, M.J., Saunders, M.J., and Mercy, E.L.P., 1975, Garnet-peridotite, primary ultrabasic magma and eclogite; interpretation of upper mantle processes in kimberlite. In: Physics and Chemistry of the Earth, Vol. 9, T.H. Ahrens et al., eds., Pergamon.

Oka, Y. and Matsumoto, T., 1974, Study on the compositional dependence of the apparent partition coefficient of iron and magnesium between coexisting garnet and clinopyroxene solid solution. Contr. Mineral. Petrol., 48, 115-121.

O'Nions, R.K., Hamilton, P.J., and Evensen, N.M., 1977, Variations in $^{143}Nd/^{144}Nd$ and $^{87}Sr/^{86}Sr$ ratios in oceanic basalts. Earth Planet. Sci. Lett., 34, 13-22.

O'Nions, R.K. and Pankhurst, R.J., 1974, Petrogenetic significance of isotope and trace element variation in volcanic rocks from the Mid-Atlantic. J. Petrol., 15, 603-634.

Onuma, N., Higuchi, H., Wakita, H., and Nagasawa, H., 1968, Trace element partition between two pyroxenes and the host lava. Earth Planet. Sci. Lett., 5, 47-51.

Orueta, D., 1917, Estudio geologico y petrografico de la Serania de Ronda. Mem. Inst. Geol. España, 567.

Peterman, Z.E., Carmichael, I.S.E., and Smith, A.L., 1970, Strontium isotopes in quaternary basalts of south-western California. Earth Planet. Sci. Lett., 7, 381-384.

Philpotts, J.A., 1970, Redox estimation from a calculation of Eu^{2+} and Eu^{3+} concentrations in natural phases. Earth Planet. Sci. Lett., 9, 257-268.

Philpotts, J.A., Schnetzler, C.C., and Thomas, H.H., 1972, Petrogenetic implications of some new geochemical data on eclogitic and ultrabasic inclusions. Geochim. Cosmochim. Acta, 36, 1131-1166.

Presnall, D.C., 1969, The geometrical analysis of partial fusion. Am. J. Sci., 267, 1178-1194.

Press, F., 1968, Earth models obtained by Monte Carlo inversion. J. Geophys. Res., 73, 5223-5234.

Raheim, A. and Green, D.H., 1974, Experimental determination of the temperature and pressure dependence of the Fe-Mg partition coefficient for coexisting garnet and clinopyroxene. Contr. Mineral. Petrol., 48, 179-203.

Reid, J.B. Jr. and Frey, F.A., 1971, Rare earth distribution in lherzolite and garnet pyroxenite xenoliths and the constitution of the upper mantle. J. Geophys. Res., 76, 1184-1196.

Richard, P., Shimizu, N., and Allègre, C.J., 1976, $^{143}Nd/^{146}Nd$, a natural tracer: An application to oceanic basalts. Earth Planet. Sci. Lett., 31, 269-278.

Ringwood, A.E., 1966, The chemical composition and origin of the earth. In: Advances in Earth Science, P.M. Hurley, ed., MIT Press.

Roeder, P.L. and Emslie, R.F., 1970, Olivine-liquid equilibrium. Contr. Mineral. Petrol., 29, 275-289.

Schilling, J.-G., 1971, Sea-floor evolution: rare-earth evidence. Phil. Trans. Royal Soc. London, A268, 663-706.

Schilling, J.-G., 1975, Rare-earth variations acorss 'normal segments' of the Reykjanes Ridge, 60°-53°N, Mid-Atlantic Ridge, 29°S, and East Pacific Rise, 2°-19°S, and evidence on the composition of the underlying low-velocity layer. J. Geophys. Res., 80, 1459-1473.

Schnetzler, C.C. and Philpotts, J.A., 1968, Partition coefficients of rare-earth elements and barium between igneous matrix material and rock-forming mineral phenocrysts. -I. In: Origin and Distribution of the Elements, T.H. Ahrend, ed., pp. 929-938, Pergamon.

Schnetzler, C.C. and Philpotts, J.A., 1970, Partition coefficients of rare earth elements between igneous matrix material and rock-forming mineral phenocrysts-II. Geochim. Cosmochim. Acta, 34, 331-340.

Schubert, W., 1977, Reaktionen im alpinotypen Peridotitmassiv von Ronda (Spanien) und sienen partiellen Schmelzproduktion. Contr. Mineral. Petrol., 62, 205-220.

Shaw, D.M., 1970, Trace element fractionation during anatexis. Geochim. Cosmochim. Acta, 34, 237-243.

Shimizu, N., 1974, An experimental study of the partitioning of K, Rb, Cs, Sr, and Ba between clinopyroxene and liquid at high pressures. Geochim. Cosmochim. Acta, 38, 1789-1798.

Shimizu, N., 1975, Rare earth elements in garnets and clinopyroxenes from garnet lherzolite nodules in kimberlites. Earth Planet. Sci. Lett., 25, 26-32.

Smewing, J.D. and Potts, P.J., 1976, Rare-earth abundances in basalts and metabasalts from the Troodos Massif, Cyprus. Contr. Mineral. Petrol., 57, 245-258.

Sun, C.-O., Williams, R.J., and Sun, S.-S., 1974, Distribution coefficients of En and Sr for plagioclase-liquid and clinopyroxene-liquid equilibria in oceanic ridge basalt: an experimental study. Geochim. Cosmochim. Acta, 38, 1415-1433.

Thompson, G. and Bankston, D.C., 1970, Sample contamination from grinding and sieving determined by emission spectrometry. Applied Spectroscopy, 24, 210-219.

Tilley, C.E. and Yoder, H.S. Jr., 1964, Pyroxene fractionation in mafic magma at high pressures and its bearing on basalt genesis. Carnegie Inst. Wash. Year Book 63, 114-121.

Waff, H.S. and Bulau, J.R., 1977, Fluid distribution in partially molten "pyrolite." Trans. Am. Geophys. Union, 58, 535.

Waff, H.S. and Holdren, G.R. Jr., 1977, The nature of grain boundaries in dunite xenoliths: implications for magma transport in refractory upper mantle material. (abstract) Geol. Soc. Am., Abstracts with Programs, 9, 1214.

Westerhof, A.B., 1977, On the contact relations of high-temperature peridotites in the Serrania de Ronda, southern Spain. Tectonophysics, 39, 579-591.

Wilkinson, J.F.G., 1976, Some subcalcic clinopyroxenites from Salt Lake Crater, Oahu, and their petrogenetic significance. Contr. Mineral. Petrol., 58, 181-201.

Wilshire, H.G. and Pike, J.E.N., 1975, Upper-mantle diapirism: evidence from analogous features in alpine peridotite and ultramafic inclusions in basalt. Geology, 3, 467-470.

Yoder, H.S. Jr., 1974, Garnet peridotite as a parental material for basaltic liquids. Carnegie Inst. Wash. Year Book 73, 263-266.

Yoder, H.S. Jr., 1976, Generation of basaltic magma. National Academy of Sciences, Washington, D.C. 265 pp.

Yoder, H.S. Jr. and Tilley, C.E., 1962, Origin of basalt magmas: an experimental study of natural and synthetic rock systems. J. Petrol., 3, 342-532.

Zielinski, R.A., 1975, Trace element evaluation of a suite of rocks from Reunion Island, Indian Ocean. Geochim. Cosmochim. Acta, 39, 713-734.

APPENDIX II-A: Petrographic notes of the peridotites.

The following descriptions are partly based on those given by Dickey (1969), Lundeen (1976), and Obata (1977; personal communications, 1977) where more details can be found. Modal analyses of the peridotites are listed in Table II-1, and the rock names are based on reconstituted modes.

(1) R845, spinel harzburgite: The texture is xenomorphic granular and porphyroclastic. Olivines (5 mm or less) are only slightly serpentinized. Orthopyroxene porphyroclasts (∿5 mm long) are deformed and kinked. The neoblasts (∿0.3 mm) are partly altered to talc. Clinopyroxenes (∿0.7-1 mm) have thicker lamellae than those in orthopyroxenes. Brown spinels are variable in size (0.7 mm to 0.04 mm). The larger grains are irregular in shape (some with wormy shapes) and some are included in orthopyroxene porphyroclasts.

(2) R131, plagioclase lherzolite: Polygonal olivine grains (0.8 mm) are surrounded by veins of serpentine and magnetite. Orthopyroxenes are in the form of large anhedral grains (2 mm) with abundant clinopyroxene lamellae. Plagioclases occur as rare interstitial grains and in aggregates around embayed brown spinels.

(3) R224, plagioclase lherzolite: Olivines occur as polygonal grains (up to 1 mm), with thin veins of serpentine

and magnetite. Orthopyroxenes form large (up to 3 mm) xenomorphic grains with abundant exsolved clinopyroxene lamellae. Plagioclases occur as rare interstitial grains and as aggregates around embayed brown spinels. Due to the abundant exsolution lamellae, no reliable mode was obtained.

(4) R501, garnet lherzolite (transitional, harzburgite): The texture is porphyroclastic to cataclastic. It has fine grain size (∿0.1-0.2 mm) due to deformation and crushing, and is also heavily serpentinized. Garnets (0.3 mm to 5 mm) are evenly distributed in serpentinized harzburgite matrix, and are rimmed by kelyphites (0.2 to 0.4 mm thick) which are in turn surrounded by pyroxene mosaics. Brown spinels form abundant tiny (∿20μ) grains dispersed in the serpentinie matrix, and rarely, occur as large (0.3-0.7 mm) irregular-shaped grains.

(5) R243, spinel lherzolite: The texture is porphyroclastic. Olivine porphyroclasts form lenticular aggregates (2-3 mm long). The matrix around the porphyroclasts is variable in grain size and appears to be products of cataclastic crushing. Spinels associated with pyroxenes and olivines are rimmed with vermicular-intergrowths of plagioclase and olivine. Large clinopyroxene grains with exsolution textures are surrounded by finer-grained clinopyroxenes and amphiboles.

(6) R717, spinel lherzolite: The texture is porphyroclastic. It is serpentinized in a mesh-like texture forming approximately 1 cm grids. Olivines (∿4 mm) are moderately serpentinized. Orthopyroxenes range from 4 mm (porphyroclasts) to 0.4 mm (neoblasts), and clinopyroxenes, from 2 mm to 0.4 mm, with fine exsolutions. Spinels are greenish-brown and range from 1 mm to 40μ.

(7) R893, dunite: It has coarse granular texture. Olivines (∿7 mm) are moderately serpentinized along veins which form a mesh-like texture. Both orthopyroxenes (<3 mm) and clinopyroxenes (∿1 mm) have exsolution lamellae. Brown spinels have variable grain size (0.7 mm to 0.07 mm). Large grains are irregularly shaped "holly leaves" while the small ones tend to be euhedral.

(8) R855, olivine websterite (or transitional spinel lherzolite): It has a porphyroclastic texture with interlocking grain boundaries. Along the grain boundaries is a recrystallized fine-grained matrix of plagioclase lherzolite assemblage. Olivine (∿2 mm) is slightly serpentinized. Orthopyroxenes (∿4 mm) have clinopyroxene and plagioclase lamellae, like those in R37 (see Obata, 1977, p. 27). They are partly altered to talc along cracks. Clinopyroxenes have abundant orthopyroxene lamellae, and also plagioclase lamellae in some cases. Spinel (≤0.4 mm) is green or brownish green, unlike the usual color for peridotite spinels.

They have irregular amoeboid shape and are always surrounded by plagioclase (∿0.1 mm thick).

APPENDIX II-B: Method of Mode Reconstitution

The following method, taken from Obata (1977), is used to redistribute the observed modes into three component phases: olivine, orthopyroxene and clinopyroxene. All minerals other than these three phases (i.e., garnet, spinel, plagioclase and amphibole [pargasite]), are broken down mathematically into olivine and pyroxene components, and added to the observed mode of olivine and pyroxenes as follows:

Ol* = Ol + serpentine + Sp - Plag + 0.67 pargasite

Opx* = Opx + Plag + 0.12 Gn - 0.17 pargasite

Cpx* = Cpx + Plag + 0.88 Gn + pargasite

The above relations are based on the following stoichiometric equations (The pyrope-grossular content of garnet is based on microprobe data obtained by Obata [1977]):

$$\underset{\text{gn}}{(Ca_{0.12}Mg_{0.88})_3Al_2Si_3O_{12}} = 0.82\ \underset{\text{opx}}{Mg_3Al_2Si_3O_{12}} + 0.18\ \underset{\text{cpx}}{Ca_2MgAl_2Si_3O_{12}}$$

$$\underset{\text{sp}}{MgAl_2O_4} + \underset{\text{opx}}{Mg_2Si_2O_6} = \underset{\text{opx}}{MgAl_2SiO_6} + \underset{\text{fo}}{Mg_2SiO_4}$$

$$\underset{\text{plag}}{CaAl_2Si_2O_8} + \underset{\text{fo}}{Mg_2SiO_4} = \underset{\text{cpx}}{CaAl_2SiO_6} + \underset{\text{opx}}{Mg_2Si_2O_6}$$

APPENDIX II-B (continued):

$$NaAlSi_3O_8 + Mg_2SiO_4 = NaAlSi_2O_6 + Mg_2Si_2O_6$$

plag fo cpx opx

$$NaCa_2Mg_4Al_3Si_6O_{22}(OH)_2 + 0.5\ Mg_2Si_2O_6$$

pargasite opx

$$= CaMgSi_2O_6 + CaAl_2SiO_6 + NaAlSi_2O_6$$

cpx cpx cpx

$$+ 2Mg_2SiO_4 + H_2O$$

fo vapor

APPENDIX II-C: Duplicate Analyses - An interlaboratory comparison

	R131		R224		R243	
	A	B	A	B	A	B
SiO_2	42.45	42.55	43.42	43.61	44.13	44.35
TiO_2	0.19	0.16	0.06	0.06	0.14	0.14
Al_2O_3	2.52	2.50	2.88	2.93	3.56	3.64
Fe_2O_3	3.27	1.72	2.51	1.09	2.20	0.59
FeO	5.50	6.96	5.74	6.74	6.13	7.53
MnO	0.13	0.12	0.13	0.11	0.13	0.13
MgO	39.37	39.89	39.70	39.86	38.23	38.75
CaO	2.43	2.42	2.65	2.66	3.17	3.29
Na_2O	0.19	0.17	0.26	0.26	0.32	0.26
K_2O	<0.003	0.00	<0.003	0.01	0.01	0.00
P_2O_5	<0.003	0.00	<0.003	0.00	0.01	0.00
H_2O+	2.94	2.99	1.92	1.89	1.14	0.67
H_2O-	0.19	0.16	0.14	0.15	0.12	0.06
CO_2	0.22	-	0.06	-	0.25	-
S		-		-	0.02	-
SO_3	-	0.00	-	0.03	-	0.12
rest§	0.62		0.66		0.66	
Cr_2O_3	0.308	0.36	0.343	0.39	0.352	0.33
NiO	0.274	0.26	0.274	0.26	0.257	0.27
	100.02		100.13		100.22	
O=S						
Total	100.02	100.26	100.13	100.05	100.21	100.13

Column (A): This work. Analyst: B.W. Chappell, Australian National University. Method: XRF

Column (B): Dickey (1970). Analyst: E. Jarosewich, U.S. National Museum. Method: Gravimetric

§ "rest" includes Cr_2O_3, NiO and other minor elements.

APPENDIX II-C (continued):

	R120		R127		R183	
	A	B	A	B	A	B
SiO_2	46.58	46.68	47.32	47.73	46.24	46.67
TiO_2	0.50	0.19	0.76	0.73	0.24	0.24
Al_2O_3	12.39	12.91	15.79	16.16	17.63	17.71
Fe_2O_3	1.46	0.99	1.93	0.94	1.64	0.96
FeO	4.91	5.43	6.83	7.84	5.47	6.15
MnO	0.17	0.17	0.15	0.15	0.14	0.14
MgO	20.61	20.81	10.05	9.88	12.10	12.16
CaO	10.36	10.33	14.31	14.15	14.32	14.16
Na_2O	0.99	0.96	1.88	1.89	1.35	1.30
K_2O	0.005	0.00	0.02	0.01	0.01	0.01
P_2O_5	0.01	0.00	0.04	0.00	0.03	0.00
H_2O+	1.32	1.03	0.39	0.35	0.49	0.37
H_2O-	0.12	0.10	0.04	0.06	0.04	0.06
CO_2	0.18	-	0.27	-	0.30	-
S	0.06	-	0.04	-	0.02	-
SO_3	-	0.12	-	0.00	-	0.00
rest§	0.43		0.17		0.20	
Cr_2O_3	0.262	0.25	0.083	0.00	0.120	0.09
NiO	0.089	0.08	0.018	0.01	0.025	0.03
	100.10		99.99		100.22	
O=S	0.03		0.02		0.01	
TOTAL	100.07	100.05	99.97	99.88	100.21	100.04

APPENDIX II-C (continued):

	R251		R301		R322	
	A	B	A	B	A	B
SiO_2	44.08	44.09	53.78	53.93	47.69	48.33
TiO_2	1.26	1.12	0.06	0.02	0.41	0.31
Al_2O_3	14.28	14.51	1.43	1.57	11.47	11.83
Fe_2O_3	3.42	2.47	1.04	0.53	1.47	0.48
FeO	4.13	4.97	1.87	2.49	3.65	4.43
MnO	0.14	0.14	0.10	0.10	0.14	0.12
MgO	14.84	14.80	22.03	22.39	22.24	22.38
CaO	16.53	16.44	16.03	16.05	9.92	9.86
Na_2O	0.91	0.89	0.46	0.43	0.80	0.77
K_2O	0.01	0.01	0.01	0.01	0.005	0.01
P_2O_5	0.02	0.00	0.01	0.00	0.02	0.00
H_2O+	0.18	0.24	0.80	0.52	1.17	0.52
H_2O-	0.06	0.09	0.15	0.10	0.13	0.11
CO_2	0.14	-	0.29	-	0.34	-
S		-		-	0.03	-
SO_3	-	0.04	-	0.00	-	0.06
rest§	0.20		2.01		0.76	
Cr_2O_3	0.078	0.06	1.885	1.83	0.583	0.47
NiO	0.026	0.03	0.095	0.09	0.103	0.11
	100.20		100.07		100.25	
O=S					0.01	
TOTAL	100.20	99.90	100.07	100.05	100.24	99.79

APPENDIX II-D: Standard Counting Errors in Activation Analysis.

The statistical errors associated with gamma-ray counting can be shown to be

$$\sigma_N \simeq \sqrt{N}$$

(where N is the total counts or average count rate)

because in pulse counting, the distribution can be approximated by Poisson distribution. Therefore, the standard errors associated with the resulting calculated concentrations can be estimated by using standard error propagation formulas. The final statistical errors depend on (1) the peak to background ratios in both the sample and the standard; and (2) the method of peak integration.

Half-peak integration method similar to Wassons' (Baedecker, 1971) was used for most peaks, and is summarized below: -

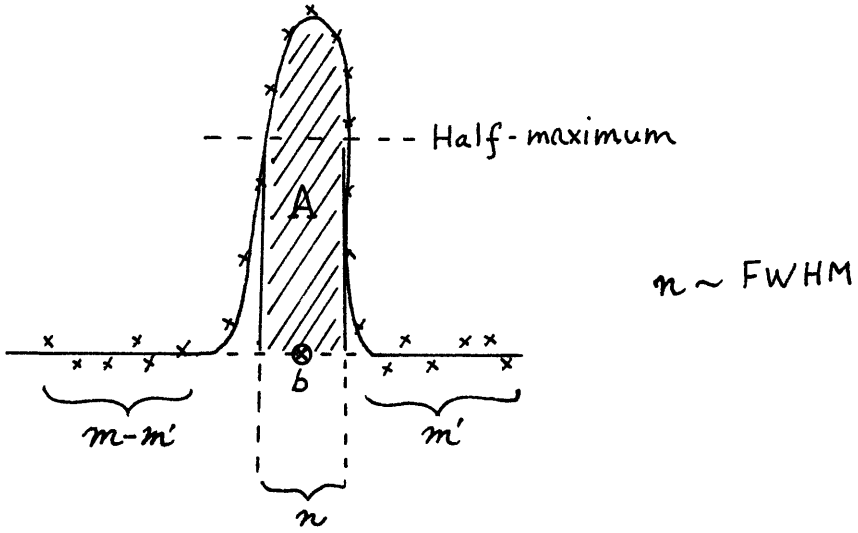

Peak area $A = \Sigma a_i - nb$

where a_i = number of counts in channel i

n = number of channels under the peak integrated (n corresponds approximately to FWHM, but varies from case to case, depending on the situation*.)

b = estimated average background

b is estimated by using a total of m channels on both sides of the peak, and so $\sigma \simeq \sqrt{\frac{b}{m}}$.

Therefore,

$$\sigma_A = \sqrt{\sum a_i + \frac{bn^2}{m}} \quad .$$

When comparing A_{sample} to $A_{standard}$, a time correction factor ϵ is involved, so that

for $A_{corr.}$,

$$\sigma_A = \sqrt{\left(\sum a_i + \frac{bn^2}{m}\right)\epsilon^2} \quad .$$

Then, the standard deviation associated with the ratio A_{samp}/A_{std} is

$$\sigma_R \simeq \frac{A_{samp}}{A_{std}} \sqrt{\left(\frac{\sigma_A}{A}\right)^2_{std} + \left(\frac{\sigma_A}{A}\right)^2_{samp}} \quad .$$

---

*For some cases, total peak area method was also used.

Percent error in final resulting concentrations due to counting errors only is therefore:

$$\sigma\% = \frac{\sigma_R}{Ratio} \times 100$$

$$= \sqrt{\left(\frac{\sigma_A}{A}\right)^2_{std} + \left(\frac{\sigma_A}{A}\right)^2_{samp}} \times 100 \quad .$$

The following table lists the standard errors in percent (1σ%) in measured REE concentrations obtained by radiochemical activation technique for two representative samples (R243, a peridotite and R181, a mafic layer). Only errors associated with counting and integration are given

Nuclide	Peak (Kev)	R243	R181
La140	487.0	3.77	-
La140	1596.5	4.88	1.83
Ce141	145.4	7.92	4.05
Nd147	91.1	6.90	2.83
Sm153	103.2	3.92	1.93
Eu152	121.8	5.35	2.44
Gd153	97.4	11.03	9.86
Tb160	86.8	6.02	-
Tb160	298.5	-	2.64
Yb175	396.1	3.72	1.79
Lu177	208.4	3.71	1.76

Reference:

Baedecker, P.A., 1971, Anal. Chem., 43, 405-410.

APPENDIX II-E: Counting Schedule (RNAA) and Gamma-ray Energies of Photopeaks Used.

Nuclide	KeV	Half-life	Detector & Cooling Time
Ce 144	80.12	284.4 D	3
Nd 147	91.1	10.99 D	1
Gd 153	97.4 *	241.5 D	3
Sm 153	103.2	46.5 H	1
Eu 152	121.8	13 Y	3
Ce 144	133.5	284.4 D	3
Ce 141	145.4 **	32.53 D	3
Lu 177	208.4	6.71 D	2
Tb 160	298.5 §	72.3 D	2
Yb 175	396.1 †	4.19 D	2
La 140	487.0	40.23 H	2
La 140	1596.5	40.23 H	2

(1) 6 to 8 days; LEPS.

(2) 5 to 7 days; Ge(Li).

(3) 19 to 21 days; LEPS.

* Interfered by Sm 153 (46.5 H), same energy.

** Interfered by Yb 175 (4.21 D), 144.85 KeV. Use only the high energy side of the peak if necessary.

§ This peak is more preferable than Tb 160, 86.8 KeV which is interfered by Eu 155, 86.6 KeV.

† This peak gives better results (usually higher concentrations) than Yb 169 (32 D), 63.1 KeV.

APPENDIX II-F: Radiochemical Neutron Activation Procedure (RNAA).

(1) Sample preparation: Approximately 0.5 gram of powder sample was transferred into a quartz tube (~6 in long, 5 mm i.d., 1 mm thick wall) with one sealed end. The exact weight of the rock powder was found by weighing the quartz tube before and after the loading. The tube was sealed at about 2 - 2.25 in from the bottom. The quartz capsule was scratched for identification.

(2) Standard preparation: A dilute standard solution was prepared by mixing standard solutions of individual rare-earth elements and diluted to the desired concentrations, so that 0.5 ml of this dilute solution would contain approximately the same amount of REE as 0.5 gram of the samples. Rare-earth standards were prepared as described in Haskin et al (1968). Exactly 0.5 ml of the dilute standard solution was tranferred into a quartz tube with a micropipette. Before sealing the top, the tube was weighed before and after the loading to check the consistency (which was normally better than $\pm$ 0.2%). Those with abnormally high deviations from the average were discarded. The tube was then centrifuged to ensure all liquid go to the bottom. The closed end was immersed in liquid nitrogen to freeze the solution completely, and was quickly sealed at about 2 - 2.25 inches from the bottom. Care must be taken not to boil the liquid or induce too much strain in the quartz glass. (CAUTION: Quartz

capsules may explode due to pressure build-up. Protective masks or goggle must be worn!)

(3) Irradiation: Before irradiation, all quartz capsules (standard and samples) were heat-tested by subjecting them to a temperature of 265°C in an oven. Approx. 20% of those capsules containing liquid shattered in a violent explosion when heated, but those containing rock powder never did. Four samples and one standard were fitted into an aluminum can which was specially made for the vertical graphite changers of the M.I.T. Research Reactor. Irradiation time was about 100 $\pm$ 10 hours at a thermal neutron flux of approx. 7×10^{12} n cm^{-2} sec^{-1}.

(4) Sample dissolution: The samples were allowed to cool for 3 days, and the capsules were opened carefully. The activated rock powder were completely transfered to 50 ml teflon TFE beakers. The empty capsules were rinsed several times with distilled water to ensure complete transfer. The standard solution was tranfered directly to a polypropylene counting tube (16 X 98.7 mm round bottom centrifuge tube) using a pipette dropper. Both the empty capsule and the pipette were washed at least 3 times with a concentrated REE carrier solution to ensure total transfer. 1 ml of Ce 144 tracer solution (approx. 0.8 μCi/ml) was pipetted into the standard tube and each of the beakers. Dil. HCl acid was added to the standard tube to make up a volume up to about 2.25 in from the bottom. It was then

closed with a rubber stopper and set aside until counting. About 1 ml of perchloric acid and 20 ml of hydrofluoric acid were added to each beaker. They were covered with teflon cover-glass andleft to dissolve on hot-plates under heat-lamps overnight. The mixtures should be agitated occasionally to speed up the reaction. The covers were removed next morning and the rock solutions were evaporated down to near dryness. The residues were redissolved in about 1 - 2 ml of 2N HCl, and agian evaporated to dryness. This was repeated for at least 3 times. The final residues were dissolved in a few ml of 2N HCl, and the solutions were centrifuged to get rid of any precipitates (e.g., chromite and MgF_2 or CaF_2 etc. These ppt. were counted with both Ge(Li) and LEPS detectors, but no REE peaks were detected.) The clear solutions were put through the ion-exchange columns.

(5) Column procedure: Bio-Rad AG50W-X8 resin (100 - 200 mesh, hydrogen form) was used. The resin was washed several times with 6N HCl and equilibrated in 2N HCl. It was loaded into a pyrex glass column tube (10 mm i.d. with fritted disc) up to a length of 21 cm. (The length would shrinked to approx. 19 cm in 6N HCl acid.) The top of the tube was fitted with a 250 ml reservoir made with a separation funnel. The rock solutions was loaded directly into the tube, and the column was eluted with 100 ml of 2N HCl with a drop rate of ~0.97 ml/min. This fraction was discarded into the radioactive waste. 125 ml of 6N HCl

were then added for the second elution (drop rate ≈ 1.03 ml/min). The solution collected was evaporated down to a desired volume (< 10 ml) and transferred to a counting tube. The volumes in the sample tubes were adjusted so as to reproduce the same geometry of the standard solution.

The major drawback of this ion-exchange procedure is that strong Cr or Sc peaks are still present in the gamma spectra with the REE peaks for samples with high Cr or Sc contents, although most of the Al, Si, Na and Fe etc. activities have been removed. This procedure can possibly be improved by using a long column or by extracting Sc with an organic solvent (Garmann et al, 1975).

(6) Counting: All standards and samples were counted at least 3 times:

5 - 6 days	Ge(Li) detector
6 - 7 days	LEPS "
20 days	LEPS "

Each count typically last for 6 -12 hours depending on the concentrations. Gamma spectra were collected by using a 4096-channel analyzer with output on printed tapes. Chemical yields were obtained by comparing the Ce 144 (80.12 KeV; 133.5 KeV) peaks of the sample and the standard. Normally, the chemical yields are 80% or better. However, for some unknown reasons, unreliable values as low as 50% were also obtained, and therefore, the resulting absolute REE abundances may not be correct, although the relative concentrations among the elements can be measured. For all samples, the chemical yield was independently checked by INAA using

La, Sm and/or Nd peaks.

The following table compares the duplicate results from radiochemical and instrumental neutron activation on two samples: R842 and R705B. Note that for R842, the absolute concentrations obtained by RNAA are not correct due to an erroneous chemical yield value. Reported concentrations are adjusted by using the INAA numbers as references.

	R842		R705B	
	(1)	(2)	(1)	(2)
La	2.46 (ppm)	1.58	0.278	-
Ce	8.75	6.33*	2.25	2.98
Nd	5.99	2.99*	3.88	3.87
Sm	1.95	1.15	1.95	1.96
Eu	0.718	0.381	0.964	0.891
Gd	4.17	-	3.80	-
Tb	1.16	0.572	0.683	0.572
Ho	-	1.46	-	1.03
Yb	8.23	4.88	1.79	2.55
Lu	1.21	0.79	0.239	0.401

(1) RNAA

(2) INAA (Precisions are generally lower than for RNAA)

* Poor counting statistics ($2\sigma > 10\%$).

References:

Brunfelt, A. O., Roelandts, I., and Steinnes, E. 1974. Analyst, 99, 277-284.

Garmann, L. B., Brunfelt, A. O., Finstad, K. G. and Heier, K. S. 1975. Chemical Geology, 15, 103-116.

Haskin, L. A., Wildeman, T. R., and Haskin, M. A. 1968. J. Radioanal. Chem., 1, 337-348.

Hooker, P. J., O'Nions, R. K. and Pankhurst, R. J. 1975. Chemical Geology, 16, 189-196.

Strelow, F. W. E. 1960. Anal. Chem., 32, 1185-1188.

Strelow, F. W. E. 1966. Anal. Chim. Acta, 34, 387-393.

Strelow, F. W. E. and Jackson, P.F.S. 1974. Anal. Chem., 46, 1481-1486.

Whipple, E. R. 1974. Chemical Geology, 14, 223-238.

Zielinski, R. A. 1975. Geochim. Cosmochim. Acta, 39, 713-734.

APPENDIX II-G: Distribution Coefficients

	Cpx		Opx	Ol	Garnet	
	High	Low			High	Low
La	0.084	0.052*	.0017*	.010*	0.003*	0.01*
Ce	0.166	0.077	.0026	.009	0.0068	0.021
Nd	0.382	0.174	.006*	.007	0.0327	0.087
Sm	0.736	0.260	.014	.006	0.161	0.217
Eu	0.753	0.273	.023	.006	0.284	0.320
Gd	0.82	0.325§	.0325*	.007*	0.615	0.498
Tb	0.97	0.338*	.046	.008*	1.18*	0.72*
Yb	1.01	0.294	.107	.009*	9.84	4.03
Lu	0.95	0.276*	.111	.009*	12.8*	5.9*
REF	(1)	(3)	(1)	(2)	(4)	(5)

References: (1) Onuma, et al (1968)
(2) Schnetzler and Philpotts (1968), (GSFC No. 25)
(3) Schnetzler and Philpotts (1970), (HHP-66-19)
(4) Philpotts, et al (1972) (Garnet xenocryst 21f)
(5) Shimizu and Kushiro (1975)

*Values by interpolation
§Values by interpolation given by original authors

APPENDIX II-H: Mantle Norm Calculation

The following procedure is adapted from Kushiro and Kuno (1963) with minor changes:

(1) Recalculate Fe^{3+} as Fe^{2+}.

(2) Convert weight percents to atomic proportions.

(3) Add Cr, Mn and K to Al, Fe and Na respectively. Ignore P, S, H_2O and CO_2.

(4) Calculate the components in the following order:

(a) Assign all Na to form Jadeite ($NaAlSi_2O_6$).

(b) Assign all Ti to form Ca-Ti pyroxene ($CaTiAl_2O_6$).

(c) Assign 1/2 of the remaining Al to form Ca-tschermak molecule ($CaAl_2Si\ O_6$), and the other 1/2 to form Mg-tschermak molecule ($MgAl_2SiO_6$).

(d) Use the remaining Ca to form Wollastonite ($CaSiO_3$).

(5) Add Fe to the remaining Mg. Calculate the amounts of either Enstatite (+ Ferrosilite) ($MgSiO_3$) and Forsterite (+ Fayalite) (Mg_2SiO_4), or Enstatite and SiO_2, according to the proportion of Si and Mg(+Fe) as in CIPW norm.

(6) Combine all Wo molecules with En to form Diopside (+Hedenbergite) ($CaMgSi_2O_6$).

For the convenience of plotting certain diagrams, Al can be left as Al_2O_3 without forming Ca - and Mg-tschermak molcules, and Wollastonite is left as it is without forming Diopside.

Appendix III-A: Derivation of Shaw's (1970) Equation (12).

$$D = \sum_i \frac{x^i - F p^i}{1 - F} \cdot K^i$$

$$= \frac{1}{1-F} \cdot \sum_i (K^i x^i - F K^i p^i)$$

$$= \frac{1}{1-F} \left(\sum_i K^i x^i - F \sum_i K^i p^i \right)$$

$$= \frac{D_o - FP}{1 - F} .$$

Phase i is exhausted at $x_i = Fp^i$, and therefore, does not exist, if $Fp^i > x^i$.

Appendix III-B: Derivation of Equations (35) and (36).

$$F_k^o = F_o + F_o(1-F_o) + F_o\left\{1-\left[F_o + F_o(1-F_o)\right]\right\} + \cdots\cdots$$

$$= F_o + (F_o - F_o^2) + (F_o - 2F_o^2 + F_o^3) + (F_o - 3F_o^2 + 3F_o^3 - F_o^4) + (F_o - 4F_o^2 + 6F_o^3 - 4F_o^4 + F_o^5) + \cdots$$

For example, $\Delta F_4^o = F_o - 4F_o^2 + 6F_o^3 - 4F_o^4 + F_o^5$.

In general, $$\boxed{\Delta F_k^o = \sum_{j=o}^{j=k} (-1)^j \binom{k}{j} F_o^{j+1}} \qquad (36)$$

where the binominal coefficient $\binom{k}{j} = \dfrac{k!}{j!\,(k-j)!}$.

$\therefore$ total $F_k^o = \sum_{m=o}^{k} \Delta F_m^o$

$$\boxed{= \sum_{m=o}^{k} \sum_{j=o}^{m} (-1)^j \binom{m}{j} F_o^{j+1} .} \qquad (35)$$

Derivation of Equations (37) and (38):

For k=0, $F_0^o = F_0$

k=1, $F_1^o = F_0^o + F_0(1-F_0^o)$

k=2, $F_2^o = F_1^o + F_0(1-F_1^o)$

$\vdots$ $\vdots$

k=k, $F_k^o = F_{k-1}^o + F_0(1-F_{k-1}^o)$

$$\Delta F_k^\circ = F_k^\circ - F_{k-1}^\circ$$

$$= F_{k-1}^\circ + F_o - F_o F_{k-1}^\circ - F_{k-2}^\circ - F_o + F_o F_{k-2}^\circ$$

$$= (F_{k-1}^\circ - F_{k-2}^\circ)(1 - F_o) .$$

$$\therefore \Delta F_k^\circ = \Delta F_{k-1}^\circ (1 - F_o)$$

$$= \Delta F_{k-2}^\circ (1 - F_o)(1 - F_o)$$

$$\vdots \quad \vdots$$

$$= \Delta F_o^\circ (1 - F_o)^k ,$$

where $\Delta F_o^\circ = F_o^\circ = F_o$.

$$\boxed{\therefore \Delta F_k^\circ = F_o (1 - F_o)^k .} \qquad (37)$$

Thus,

$$F_k^\circ = \sum_{m=o}^{k} \Delta F_m^\circ$$

$$= \sum_{m\ o}^{k} F_o (1 - F_o)^m$$

$$\boxed{= 1 - (1 - F_o)^{k+1} .} \qquad (38)$$

Appendix III-C: Derivation of Quations (46) and (47).

When $k=0$, $F_0^o = (F_0 - f_0^o)$, where $f_0^o = f_0$;

$k=1$, $F_1^o = F_0^o + [F_0(1-F_0^o) - f_1^o]$, where $f_1^o = f_0(1-F_0^o)$;

$\vdots$

$k=k$, $F_k^o = F_{k-1}^o + [F_0(1-F_{k-1}^o) - f_k^o]$, " $f_k^o = f_0(1-F_{k-1}^o)$.

Substituting: $F_k^o = F_{k-1}^o + [F_0(1-F_{k-1}^o) - f_0(1-F_{k-1}^o)]$

$$= (F_0 - f_0) + F_{k-1}^o(1-F_0+f_0).$$

Let $a = F_0 - f_0$;

$b = 1-F_0+f_0$;

$a + b = 1$.

We can then write $F_k^o = a + bF_{k-1}^o$

$$= a + b(a+bF_{k-2}^o)$$

$$= a + ab + b^2F_{k-2}^o$$

$$\vdots$$

$$= a + ab + ab^2 + \cdots\cdots + ab^{k-1} + b^kF_0^o$$

$$= \sum_{j=0}^{j=k-1} ab^j + b^kF_0^o.$$

The sum of the geometric series is $(1-b^k)$,

$$F_k^o = 1 - b^k + b^kF_0^o$$

$$= 1 - b^k(1-F_0^o), \qquad \text{since } F_0^o = F_0 - f_0;$$

$$= 1 - b^{k+1}.$$

$$\therefore \Delta F_k^o = 1 - (1-F_0+f_0)^{k+1}. \qquad (46)$$

$$\Delta F_k^o = F_k^o - F_{k-1}^o$$
$$= 1 - b^{k+1} - 1 + b^k$$
$$= b^k(1-b)$$

$$\therefore \Delta F_k^o = (1-F_0+f_0)^k.(F_0-f_0). \qquad (47)$$

APPENDIX V-A: Chromian pyroxenite layers.

R301: Websterite. Mode: 64% chrome diopside, 35% orthopyroxene, 1% spinel, traces of secondary alteration products. Xenomorphic texture with pyroxenes ranging from 3.5 mm to 0.4 mm.

R896: Websterite. Mode: 59% orthopyroxene, 31% chrome diopside, 7% plagioclase, 2.4% olivine, 0.5% spinel. Xenomorphic granular texture. Large orthopyroxene grains (3 to 5 mm) lie in a matrix of equigranular pyroxene mosaic (0.3 to 0.6 mm).

Their chemical compositions are listed in the following tables. When compared to the "magmatic-type" mafic layers, they are higher in SiO_2, but much lower in Al_2O_3 abundances, with Mg/Fe ratios as high as the peridotites. They are characterized by unusually high Cr concentrations, which are even higher than those of the peridotites, and high Ni concentrations, which are higher than most magmatic layers but lower than the peridotites. Ga, Rb, Sr, Y, Zr, and ΣREE are comparatively low, and they all have concentrations intermediate between the magmatic layers and the peridotites. Both samples have LREE depletions relative to chondrites (R301 has a convex normalized REE pattern with lower HREE abundances than the lherzolites). Considerable differences exist in some element abundances (e.g. Al_2O_3, CaO) between these two analyzed samples, indicating that these layers may

have a wide range of chemical compositions. Their field occurrences are similar to the magmatic layers, but they are also found as the margins of magmatic layers, in contact with the peridotites. Judging from field observations and their unusual mineral and bulk compositions, this type of layer is believed to have formed by diffusional metasomatism between the magmatic layers and the adjacent peridotites, or more likely, by the reaction between the migrating hot liquids (with crystals) and the peridotite walls of the conduits.

	R301	R896
SiO_2	53.78	52.07
TiO_2	0.06	0.13
Al_2O_3	1.43	5.36
Fe_2O_3	1.04]12.81	0.96]14.57
FeO	1.87	3.71
MnO	0.10	0.13
MgO	22.03	23.78
CaO	16.03	11.37
Na_2O	0.46	0.45
K_2O	0.01	0.01
P_2O_5	0.01	0.01
S		0.04
H_2O^+	0.80	0.61
H_2O^-	0.15	0.09
CO_2	0.29	0.16
rest	2.01	1.43
		100.31
O=S		0.02
total	100.07	100.29
$\frac{100\ Mg}{Mg+\Sigma Fe}$	93.33	89.96

	R301	R896
Sc	16	32
V	109	165
Cr	12900	8530
Co	48	119
Ni	745	900
Cu	3	71
Zn	14	26
Ga	1.5	4.5
Rb	0.2	0.7
Sr	12.5	21.5
Y	<1	3
Zr	1	3
Nb	1	<1
Pb	4	4
La	0.177	0.344
Ce	0.535*	1.65
Nd	0.631	1.095
Sm	0.236	0.324
Eu	0.0825	0.141
Gd	0.286*	
Tb	0.055*	0.129
Yb	0.0974	0.404
Lu	0.0213*	0.0559

* Poor counting statistics (2σ > 10%)

APPENDIX V-B: Petrographic notes of the mafic rocks.

The following descriptions are partly based on information in Dickey (1969) and Obata (1977; personal communications, 1977).

(A) Thick layer R127, plagioclase-garnet clinopyroxenite: In general, the samples have a xenomorphic granular texture with garents (0.2-5 mm), pale brown clinopyroxene (0.2-0.7 mm), interstitial plagioclase ($\sim An_{40}$), and with or without quartz. Mineral proportions vary slightly within the layer as shown in the figure on the next page. The samples are typically fresh, except R900, which is slightly altered along cracks. Small amounts of secondary brown amphibole have developed along clinopyroxene grain boundaries in R899. Garnets are partly replaced by kelyphites. Small amounts of quartz occur in form of lenses parallel to the foliation in some samples (R900 and R902). Plagioclase and quartz grains are highly strined and deformed, dismembering into subgrains. Orthopyroxenes (0.3 to 0.7 mm) occur at the very edge of the layer (1 cm from the mafic layer/peridotite contact; this portion not analyzed) where plagioclase is absent.

(B) R705, plagioclase garnet clinopyroxenite: A hand-specimen from the central portion of a thick ($\sim$60 cm) light-color layer, approximately 2 m from the peridotite/country

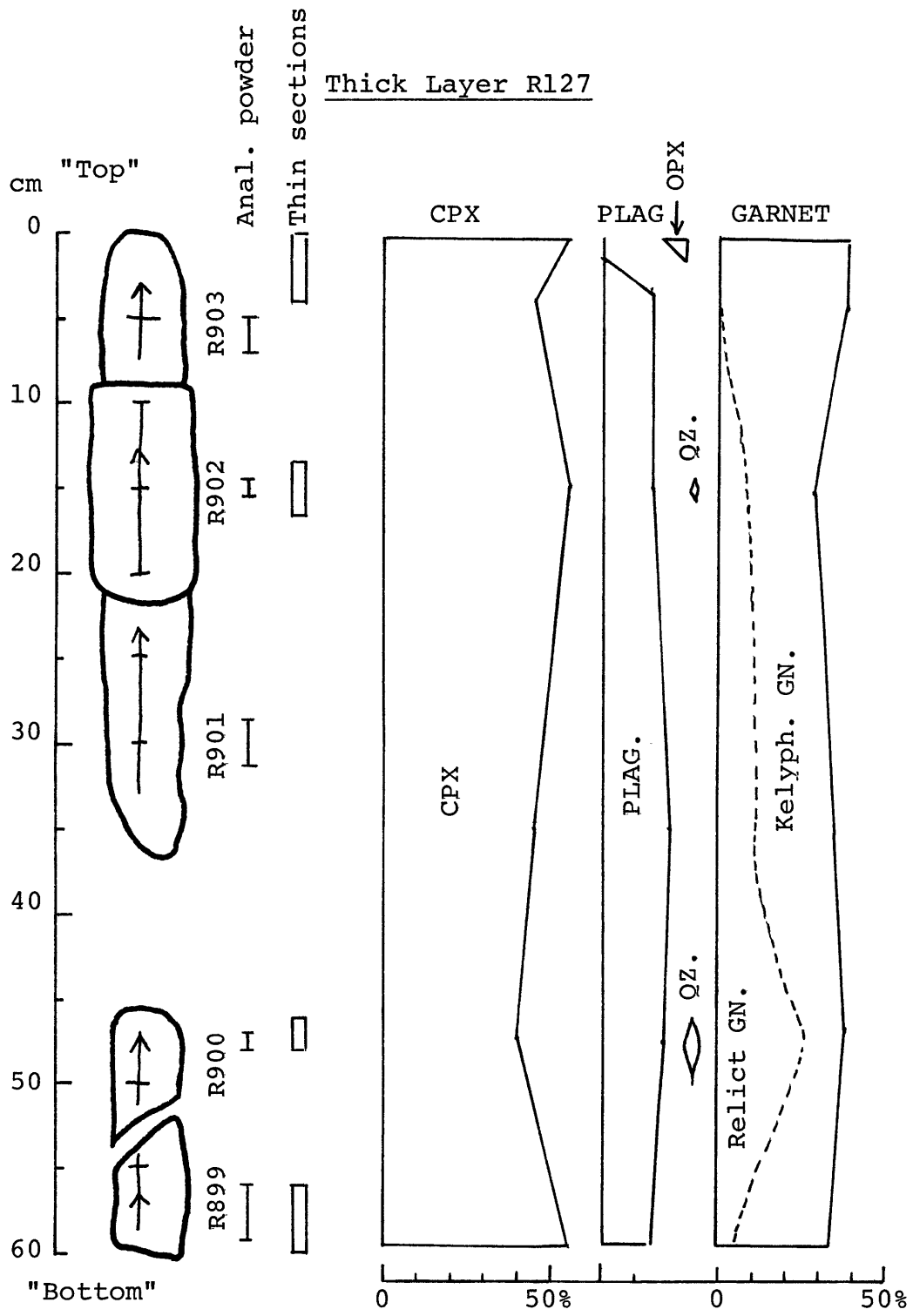
Thick Layer R127
cm
"Top"
0
10
20
30
40
50
60
"Bottom"
Anal. powder
Thin sections
R903
R902
R901
R900
R899
CPX
PLAG
OPX
GARNET
QZ.
QZ.
CPX
PLAG.
Kelyph. GN.
Relict GN.
0
50%
0
50%

rock contact. This hand-specimen has a 3.5 cm wide darker color band in the middle, which is parallel to the foliation of the layer. Sample R705A is the host rock, and sample R705B is the band. They were analyzed separately.
Mode: R705A has 47% cpx, 10% fine-grained recrystallized products after cpx, 7% plagioclase, 36% kelyphite (after garnet), and traces of opaques. R705B has 37% cpx, 6% recrystallized products after cpx, 16% plagioclase, 39% kelyphite (after garnet), 2% opaque, and traces of amphibole. The texture is xenomorphic granular with grain size ranging from 0.2 to 0.4 mm. Primary garnets (up to 1.5 mm) are almost completely kelyphitized. The clinopyroxenes have recrystallized into fine-grained (<40μ) Al-poor pyroxenes, because they are probably very aluminous judging from microprobe data of similar rocks (R410 and R560, Obata, 1977). Some clinopyroxene grains have turbid centers probably due to micro-scale exsolution. The clinopyroxenes are colorless in R705A, but pale brown in R705B, accounting for the color difference in hand-specimens. Small brown amphibole and opaque (ilmenite) grains are closely associated together, because they are secondary alteration products.

(C) R842, garnet websterite; mode: 23% garnet, 58% pyroxenes, 3% opaques, 17% secondary alteration products. The texture is xenomorphic granular with a foliation due to flattening of garnet and pyroxene grains. Large garnet grains (3-4 mm) are surrounded by a mosaic matrix of medium-

sized (0.2-0.4 mm) colorless garnet, orthopyroxene, and clinopyroxene. The garnets do not have kelyphite rims. The pyroxenes are free from exsolution lamellae, but their grain boundaries are fuzzy due to late-stage recrystallization. Small interstitial brown pleochroic amphiboles (0.05 to 0.2 mm) are ubiquitous. Other accessory minerals are ilmenite, rutile, and sulfides.

R839, garnet clinopyroxenite; mode: 20% garnet, 80% clinopyroxene, traces of opaque. Texture and grain-sizes are similar to those of R842. Garnets are free from kelyphitic rims. The grain boundaries in the matrix are clear and sharp. Pyroxene inclusions and rutile needles are common in the large garnet grains. The matrix is an equigranular mosaic of garnet and clinopyroxene with accessory rutile, ilmenite, and sulfides. Orthopyroxene and amphibole are absent.

(D) R251, spinel plagioclase pyroxenite, dark color coarse pyroxenite; mode: 78% clinopyroxene, 3% orthopyroxene, 8% spinel, 7% plagioclase, 4% olivine, traces of ilmenite. It consists of clinopyroxene grains (3-5 mm) and smaller ($\sim$1 mm) kinked orthopyroxene grains with interstitial spinel (<3 mm) and calcic plagioclase ($\sim An_{70}$, 0.5 mm). Clinopyroxenes have abundant lamellae of plagioclase + olivine + ilmenite parallel to (100) (see Figure 7 in Dickey, 1970),

and less commonly lamellae of plagioclase + orthopyroxene + green spinel (see Figure 3-13, Obata, 1977). Fine scale (∿20μ) intergrowths or aggregates of plagioclase + olivine + ilmenite occur in patches and around primary clinopyroxenes. These assemblages are formed by the breakdown of Al-rich pyroxenes.

(E) R181-R185, olivine gabbros. The modes are listed in the following table. Brown clinopyroxene grains (5 mm) have lamellae of olivine + plagioclase + ilmenite parallel to (100) and green spinel lamellae (0.2 mm by 0.03 mm). Plagioclases (An_{76}) form patches (1 mm across) with subhedral olivine (Fo_{75}). Spinels (1 mm) vary from green, associated with large clinopyroxenes, to brown, associated with plagioclases. Smaller clinopyroxene grains (0.3 mm) are free from exsolution lamellae).

(F) R120, olivine gabbro; mode: 23% clinopyroxene, 33% plagioclase, 27% olivine, 3% spinel, 12% orthopyroxene, 2% secondary alterations. It has gnessic texture with plagioclase and pyroxene-rich bands parallel to the layering. Pale brown, large elongated clinopyroxenes (up to 4 mm long) lie subparallel to the foliation in a mosaic matrix of equigranular (∿0.3 mm) olivine, plagioclase (An_{76}), orthopyroxene, clinopyroxene, and greenish brown to brown spinel. The large clinopyroxenes are strongly deformed and have thick (∿40μ) orthopyroxene exsolution lamellae. Small pyroxenes are free from exsolution lamellae.

R322, olivine gabbro; mode: 35% clinopyroxene, 23% olivine, 22% plagioclase, 16% orthopyroxene, 4% opaque + brown spinel, <0.5% secondary brown amphibole. Anhedral clino- and ortho-pyroxenes (up to 5 mm) lie in a medium-grained (0.3 mm) assemblage of olivine ($Fo_{88.3}$), plagioclase (An_{76}), orthopyroxene (En_{86}), and clinopyroxene. Ragged brown spinels (up to 5 mm long) are surrounded by plagioclase. Lamellae of olivine + plagioclase are present in large clinopyroxene grains parallel to (100); plagioclase lamellae parallel to (100) in orthopyroxene grains.

R181 - R185: Table of modal analyses

%	CPX	PLAG	OPX	SP	OL
R181	32	43	2	2	21
R182	65	29	1.6	3	<1
R183	43	42	tr	3	13
R184	63	34	tr	1	2
R185	54	37	1	2	7